An innovative portable detector for the live-monitoring of radionuclides in small terrestrial animals

Ross Fawkes

Supervisors: Prof M.D. Wood, Prof N.A. Beresford, Mr P.H. Burgess

University of
Salford
MANCHESTER

This thesis was submitted to the School of Environment and Life Sciences, University of Salford, in fulfilment of the requirements for the degree of Doctor of Philosophy

2018

Contents

2

Figures

Tables

Acknowledgements

I would like to start by thanking my supervisors: Mike Wood, Nick Beresford and Pete Burgess for their support throughout this research project. Their continued guidance has helped shape this project and has led me through the entire process of designing, building and testing the live-monitor that is described within this thesis.

I would like to further express my gratitude to the people who have made the completion of this project possible. The assistance provided by Oliver Caunt and Paul Schotanus has helped to develop the design of the live-monitor and bring together the main components of the detection system. The production of the animal restraint system and the 3D printed support structures for the detector would not have been possible without the instruction and support of Mike Walsh. Further thanks go to the Ukrainian contacts; Sergey Gaschak for his advice on measuring radiation in wildlife and Dima Bondarkov for transporting me safely (through severe snow and ice!) to and from the testing locations and assisting me with my laboratory and field work. I am indebted to Kelly Milward, not only because she efficiently dealt with my complicated finance requests, but because without her help I would likely still be sat with Ukrainian Customs at Boryspil Airport wondering if I will ever get to test my detector.

Thanks also go out to all my colleagues at Salford University and to those in the TREE research group for their support and advice. Special thanks go to Andjin Siegenthaler with whom I discussed ideas and problems with (also for saving me from many a large spider), Phakphum Arumrun for his support during conferences and supplying me with a range of fantastic (though incredibly spicy) Thai food, Donal Smith for all the cups of coffee and hot cross buns, and also to Charlie Spring and Abdul Abdulghani for supplying me with food during the long days of work in the office. Further thanks go to Adrià López Baucells and Eva Sánchez Gómez for their continued friendship and support.

Finally, I wish to thank my parents: Peter and Marion Fawkes, who have supported me both mentally and financially throughout my PhD and have provided me with the motivation to complete this thesis.

Abbreviations

BR - Branching ratio

CeBr$_3$ - Cerium bromide

CEZ - Chernobyl exclusion zone

CR$_{wo-media}$ - Concentration ratio (can be written as CR)

CsI - Caesium iodide

CZT - Cadmium zinc telluride

DCC - Dose conversion coefficient

EC - European Commission

FWHM - Full width half maximum

HPGe - High purity germanium

HPMT - Hybrid photomultiplier tube

ICRP - International Commission on Radiological Protection

LaBr$_3$ - Lanthanum bromide

LOD - Limit of detection

MCA - Multichannel analyser

MCP-PMT - Microchannel plate photomultiplier tube

MDA - Minimum detectable activity

MLP - Micro leadframe package

MPPC - Multi pixel photon counter

NaI - Sodium iodide

PCB - Printed circuit board

PEP - Poured epoxy packages

PDE - Photon detection efficiency

PMT - Photomultiplier tube

RAP - Reference animal and plant

RBE - Relative biological effectiveness

SCA - Single channel analyser

SiPM - Silicon photomultiplier

TLD - Thermoluminescent dosimeter

TSV - Through-silicone via

Glossary

Absolute efficiency (ϵ_{abs}) - fraction of radiation interactions recorded by a detector as compared to the radiation emitted by the source (Knoll, 2010).

Absorbed dose - energy deposited in a medium due to radiation interactions (Knoll, 2010). Measured in Gray (Gy).

Anthropogenic radionuclide - radionuclides created through artificial processes, e.g. nuclear weapons (Thorne, 2003).

Avalanche initiation probability - probability that a cascade of electrons will be created in a gas-filled detector by electrons moving in its electric field (Knoll, 2010).

Background radiation - contribution to count rate from radiation present in the surrounding environment.

Becquerel (Bq) - unit of radioactivity. One becquerel is defined as one radioactive decay per second (Knoll, 2010).

Biological half-life - time it takes for a particular radionuclide within an organism to reach half of its initial concentration due to biological processes (Whicker and Schultz, 1982).

Branching ratio - the fraction of atoms that decay via a particular decay mode (e.g. alpha, beta, gamma).

Characteristic decay energy - energy of the radiation emitted from a radionuclide when it decays to a lower energy level. The characteristic decay energy can be used to identify the radionuclide present.

Characteristic energy peak - characteristic decay energy of a radionuclide when displayed on an energy spectrum. Also known as the photopeak.

Compliance monitoring - monitoring of radionuclides to ensure a nuclear facility is adhering to regulated emission levels.

Concentration ratio ($CR_{wo\text{-}media}$) - ratio used to relate radionuclide activity concentration within an organism and an activity concentration within a particular medium (e.g. soil) (Howard, 2013). Written as CR for later chances in this thesis.

Count time - amount of time for measuring radiation from a sample.

Critical limit (***L_C***) - the point above which a single count measurement can be classified (with 95% probability) as not being part of the background (Currie, 1968)

Crosstalk event - The occurrence of an electron, created from a radiation interaction in one photodiode, crossing over into another photodiode (Knoll, 2010).

Dead time - time required to separate two radiation events into recordable detections.

Decay time - term used in scintillating detectors. Time required for the fluorescence from a radiation interaction to decay to a level where a second radiation interaction could be identified.

Dose conversion coefficient (DCC) - relates radionuclide activity concentrations to absorbed dose in μGy h^{-1} per Bq kg^{-1} (Vives i Batlle et al., 2011).

Effective dose - total energy deposited across the whole body (Hall and Giaccia, 2006). Sum of equivalent doses multiplied by a tissue weighting factor (i.e. accounts for the radiosensitivity of each organ or tissue). Measured in Sieverts.

Equivalent dose - average energy deposited by radiation interaction over a tissue or organ (Hall and Giaccia, 2006). Absorbed dose multiplied by a radiation weighting factor (i.e. accounts for the properties of the radiation). Measured in Sieverts.

Fill factor - ratio of optically active area to surrounding inactive area (Turchetta, 2016).

Gray (Gy) - unit of absorbed dose. 1 Gy = 1 J kg^{-1} (Knoll, 2010).

Gross count - total count measured during the counting time. Includes the contribution from background and the sample.

Half-value thickness - material thickness required to reduce the intensity of incident radiation by half.

Intrinsic efficiency (ϵ_{int}) - fraction of radiation interactions recorded by a detector as compared to the radiation incident on the detector surface (Knoll, 2010).

Limit of detection (***L_D*** or **LOD**) - point at which a mean number of counts can be differentiated from background counts (Currie, 1968). Also referred to as the minimum detectable activity (MDA) (Knoll, 2010).

Live-monitoring - the non-lethal measurement of radioactivity in a living organism.

Mass attenuation coefficient (**μ/ρ**) - characterises the quantity of radiation attenuated, due to interactions within a medium, from what was initially transmitted (Hubbell and Seltzer, 1996).

Naturally occurring radionuclides - radionuclides that are naturally present in the ground, atmosphere and water. They fall under three categories: primordial, secondary or cosmogenic (Eisenbud and Gesell, 1997).

Net count - the total radioactivity measured above background. Calculated by subtracting the background contribution from the gross count.

Occupancy factor - fraction of time that an organism spends within a particular medium (e.g. on soil, in soil, in air) (Brown et al., 2008).

Phantom - calibration or test substitute for a living organism. Contains a radioactive material inserted or distributed within a tissue equivalent material.

Photodiode - solid state semiconductor that converts incident light exiting from a scintillating material into an electrical signal (Turchetta, 2016).

Photon detection efficiency (**PDE**) - product of fill factor, quantum efficiency and avalanche initiation probability (Turchetta, 2016).

Photomultiplier tube (**PMT**) - device used to convert scintillation light into an electrical signal.

Photopeak efficiency (ϵ_p) - fraction of counts in the characteristic energy peak as compared to the whole spectrum (also termed photopeak ratio) (Knoll, 2010).

Physical half-life ($T_{1/2}$) - time required for a particular radionuclide to reach half of its initial activity by physical decay (Krane, 1988).

Quantum efficiency - photoelectrons emitted per incident photon (Knoll, 2010).

Radionuclide - unstable nuclei that emits ionising radiation when it decays.

Radionuclide activity concentration - quantity of radionuclides present within a medium. Measured in Bq kg^{-1}.

Reference Animal and Plants (RAPs) - a set of hypothetical entities that relate exposure to dose, and dose to radiation effects, for different types of animals and plants (ICRP, 2008)

Relative biological effectiveness - description of the level of damage caused to biological matter from one type of radiation relative to another (Hall and Giaccia, 2006). Uses a weighting factor to compare each type of radiation (e.g. alpha, beta, gamma).

sec - written after a radionuclide as a shorthand method of identifying it and any radionuclides present in its subsequent decay chain (e.g ^{238}U *sec*).

Scintillation detector - a type of detector that works by converting incident radiation into light (Knoll, 2010).

Screening level (or screening dose rate) - dose rate below which populations are unlikely to be significantly harmed (Brown et al., 2008).

Sievert **(Sv)** - unit of radiation absorption that takes into account the RBE (IAEA, 2010b). Used for equivalent or effective dose in humans (but it is not applicable to wildlife).

Silicon photomultiplier **(SiPM)** - an array of photodiodes (Knoll, 2010).

Skyshine - radiation emitted from radionuclides in the ground that is reflected or scattered back down to the ground surface due to interactions in the atmosphere (Mitchell et al., 2009).

Solid state detector - a type of detector that works on the same principles as those of a diode device. It converts incident radiation directly into an electrical signal (Knoll, 2010).

Weighting factor - applied to an absorbed dose to give an estimate of biological damage. Different organs and tissues experience different amounts of biological damage (Hall and Giaccia, 2006).

Abstract

Radionuclide measurements in wildlife are required to demonstrate that the environment is not significantly impacted by radioactivity. Determination of internal radionuclide activity concentrations often requires destructive sampling. Development of alternative (non-lethal) measurement methods is therefore desirable. This thesis presents the design, construction and testing of a new portable live-monitoring detector for measuring radionuclide activity concentrations in small terrestrial animals. The detector is unique in that it enables field-based measurement of both gamma and beta emitting radionuclides (caesium-137 and strontium-90 are tested in this work) in living small animals.

Literature on detector characteristics and radionuclides in the environment informed a modelling approach that was used to optimise the detector design. The optimised design contains two caesium iodide scintillators and two plastic scintillators, which enable the measurement of ^{137}Cs and ^{90}Sr respectively; all four scintillators were shaped and positioned to maximise detection from the organism. Four photomultiplier tubes collect light from the scintillators and a single channel analyser provides signal processing. Surrounding the detection materials is a lead shield designed to give an optimal balance between portability and background reduction. The organism to be measured is put into a card restraint that is designed to humanely secure it during counting.

The portable detector was tested in a laboratory using ^{137}Cs and ^{90}Sr sources to determine suitable operation and detection rates. The variation in detection rate caused by source movement within the restraint was determined to be minimal (standard deviation <5 % for ^{137}Cs and <10% for ^{90}Sr) provided the animal is placed in a restraint of similar size to its body. Field testing was then conducted on small rodent and bird species in the Chernobyl Exclusion Zone. Monitoring of internal activity concentrations for small rodents and birds showed a good correlation to results obtained using an alternative verified method (R^2 > 0.9 for both ^{137}Cs and ^{90}Sr, N = 10 for each species). The field testing demonstrated the utility of this portable detector in a high radiation background environment for measuring radionuclide contamination within a range of different small animals. The results demonstrate the detector could be used for monitoring radionuclides in protected species and reduce the number of animals euthanised for the purposes of radioecological research. The design choices made provide a template for developing a broader range of detectors that could monitor different radionuclides, organism types and sizes.

1 Introduction

1.1 Research purpose

Since the start of this century, there has been growing international recognition of the requirement for wildlife radiological assessments (ICRP, 2007, Pentreath, 1999, Sheppard, 2003). In the UK, radiological environmental assessments are driven by the need for human protection but also by national interpretation of the EC Birds (2009/147/EC) and Habitats (92/43/EEC) Directives, where the focus is on demonstrating that protected species and/or habitats are not significantly impacted by environmental radioactivity (Copplestone et al., 2003, Copplestone et al., 2005).

Various modelling tools have been developed to help with radiological environmental assessments (e.g. Copplestone et al., 2001, Yu et al., 2003, Brown et al., 2008). These tools generally use simple concentration ratios ($CR_{wo-media}$) that predict whole body radionuclide activity concentrations from activity concentrations in environmental media (air, soil or water). Various studies (e.g. Wood et al., 2009a, Johansen et al., 2012) have demonstrated that these $CR_{wo-media}$ values can under or over predict actual whole body radionuclide activity concentrations by several orders of magnitude. Therefore, direct measurement of radionuclide body burdens is preferable, but the conventional approach for achieving this is through destructive sampling of wildlife (IAEA, 1989).

Destructive sampling of protected species for the purposes of demonstrating protection is difficult to justify. Therefore, there is a need to develop non-lethal monitoring techniques, such as live-monitoring (Wood et al., 2011, Bondarkov et al., 2011), that could be used to determine whole-body radionuclide activity concentrations. The creation of a portable live-monitor would be beneficial for the monitoring of protected species and also for the purposes of compliance monitoring for facilities that have radioactive emissions (i.e. it would provide a method for confirming that regulated radionuclide releases are not resulting in radiation exposure to wildlife above levels required for environmental protection). The live-monitor would also be of benefit for measuring non-protected species and environmental media for the purposes of research.

This thesis presents the development of a new portable detector for the live-monitoring of radionuclides in primarily (though not limited to) small terrestrial animals. The necessary background science behind radiation detection and measurement, along with an outline of

currently available monitoring methods and technologies, is provided in chapters two and three. Chapter three further provides an outline for the stages of development given in the remaining chapters: requirements, design, construction, and testing of a bespoke small animal live-monitor.

1.2   Aims and objectives

The aim of this research project was to develop a new detector for measuring radionuclide activity concentrations within wildlife (primarily small animals) without the need to destroy the target organism. This new detector needed to be portable, for use in remote field studies, and have short count times to reduce any stress to the targeted organisms. For the purposes of compliance monitoring, the detector needed to measure within radionuclide activity concentration ranges that are based on screening dose rates applied in UK radiological environmental assessments.

The objectives for meeting this aim were as follows:

1. Critical review of current radiation detection methods and technologies to identify suitable detection solutions for a portable radiation live-monitor (chapter 3).

2. Critical assessment of UK relevant radionuclides and wildlife to identify which radionuclides are most radiologically significant and what wildlife are likely to be most impacted (from a radiological assessment viewpoint) by these radionuclides (chapter 4).

3. Development of computer based models of radiation interaction, between radionuclides within the targeted organisms and an externally placed detector, to determine optimal radiation detector configuration(s) specific to the target organism(s) (chapter 5).

4. Development and construction of a detection device for the live-monitoring of radionuclides present within the targeted organism(s) (chapter 6).

5. Critical evaluation of the constructed device, through a combination of laboratory and field tests using radioactive phantoms and (samples) target organisms, to assess the suitability for field deployment (chapter 7).

6. Development of correlation ratios (between measured and verified activity concentrations) for the selected organism(s) for the estimation of internal radionuclide concentration through external measurement with the constructed detector (chapter 7).

2 Background: radioactivity and radiation detection

In the process of developing a new detector for monitoring radionuclides in wildlife, there is first the important requirement of defining and understanding what it is that needs to be measured. The following chapter provides a description of radioactivity and gives details of the fundamental physics behind radionuclide interaction and detection.

2.1 Radionuclides

Radionuclides are atoms with unstable nuclei that emit ionising radiation when they decay to a daughter nuclide (Knoll, 2010). This radiation is ionising, meaning it will interact with any media it travels through by removing electrons. There are several different types of emission that can occur depending on the condition of what is known as the parent radionuclide. The most common types of emission are alpha, beta and gamma.

Alpha decay occurs primarily in radionuclides with atomic numbers greater than 82 (Whicker and Schultz, 1982). It has the greatest mass of the three types of emission, consisting of two protons and two neutrons. Interaction by alpha particles with a medium occurs primarily by coulomb interaction (Knoll, 2010) and, due to their mass, they experience little deflection through the medium they are travelling. Alpha particles have energies ranging between 4 and 9 MeV (Podgorsak, 2010) which translates approximately to a range of 1 to 10 cm in air or 0.001 to 0.01 cm in soft tissue. This short penetration ability of an alpha particle makes it particularly difficult to detect in live organisms.

Beta decay occurs primarily in radionuclides with atomic numbers less than 82 (Krane, 1988). This decay is categorised into three modes depending on whether there is an excess of neutrons or protons in the nucleus; beta minus, beta plus, and electron capture (Knoll, 2010, Podgorsak, 2010). The most common, beta minus decay, produces a beta particle (electron) and an antineutrino to balance an excess of neutrons. The antineutrino component travels at the speed of light and is difficult to detect. Unlike the well-defined energies of an alpha particle, the presence of the neutrino in the emission means the kinetic energy released is shared between it and the beta particle (Knoll, 2010). This creates an energy spectrum with energies varying between zero and a maximum energy E_{max}, (the mean energy of the beta radiation is approximately a third of E_{max}). This maximum emission energy is under 4 MeV for beta emitting radionuclides with a physical half-life of greater than one day (Ekström and Firestone, 2004). Beta particles have a greater penetration ability than that of alpha particles.

Two approximated equations describe the estimated range for high and low energy beta particles (Evans, 1955). There is some debate, however, as to the boundary between these two equations; whereas Evans (1955) overlaps these equations for energies between 1 and 3 MeV, Stabin (2007) suggests a more definite boundary at 2.5 MeV. The equations given by Stabin (2007) are used in this thesis because they have a definite energy boundary. The range, R, in equations 2.1 and 2.2 is calculated in mg cm^{-2} and therefore needs to be converted to cm using the density of the material of interest. For instance, the maximum range of ^{90}Y (normally the most energetic beta of concern in the environment at 2.27 MeV) in air and soft tissue is 84 cm and 1.1 cm respectively. This is calculated using an air density (ρ) of 1.29 mg cm^{-3} (Bushberg et al., 2011) and a soft tissue density approximately equivalent to water at 1 g cm^{-3} (Berger et al., 2005).

$$R \approx 412E^{1.265-0.0954lnE}$$ For E < 2.5 MeV   2.1

$$R \approx 530E - 106$$ For E > 2.5 MeV   2.2

Gamma radiation, unlike alpha or beta radiation, is categorised as both an electromagnetic wave and a photon (Whicker and Schultz, 1982). It has no mass, travels at the speed of light, and has a wide range of possible energies. The emission of gamma radiation often follows the decay of a radionuclide by alpha or beta radiation that has left the daughter radionuclide in an excited state; i.e. it has excess energy and is therefore still unstable (Knoll, 2010). If there is a delay in an excited radionuclide decaying to a stable state then it is referred to as being in a metastable state (denoted with an *m* next to the atomic mass number. e.g. Ag^{110m}) (Podgorsak, 2010). The parent radionuclide can also undergo a process known as internal conversion (Knoll, 2010). This involves the excess energy being transferred to an orbital electron which is then emitted from the atom at an energy equal to the total energy minus the binding energy of the electron. Of the three radiation types, gamma radiation is the most penetrative. As gamma radiation is attenuated exponentially when it travels through a medium (Krane, 1988, Evans, 1955), its penetrative ability is often described (Equation 2.3, or in terms of range, R_γ, in Equation 2.4) by the distance required to reduce its intensity by half (the half-value thickness). For example, a tissue (of density ρ = 1 g cm^{-3}) thickness (*x*) of 8.2 cm would result in a 50% reduction in gamma intensity (I/I$_0$), for ^{137}Cs (662 keV) with mass attenuation coefficient (μ/ρ) of 0.085 cm^2 g^{-1} (Hubbell and Seltzer, 1996). These equations also

apply in the case of beta emission provided suitable attenuation coefficients can be found (Mahajan, 2012).

$$I = I_0 e^{-\left(\frac{\mu}{\rho}\right)\rho x} \qquad\qquad 2.3$$

$$R_\gamma = -\frac{\ln(0.5)}{(\mu/\rho)\rho} \qquad\qquad 2.4$$

The mass attenuation coefficient characterises the quantity of radiation removed, due to interactions within a medium, from what was initially transmitted (Knoll, 2010). This term is used instead of the linear attenuation coefficient as it does not vary with density and is only dependent on the atomic number of the medium and the energy of the radiation.

There are also other emissions from radionuclides that can occur, such as spontaneous fission and nucleon emission (Knoll, 2010). These emissions are, however, not as common as the above-mentioned decay processes; occurring rarely, or not at all, in the radionuclides discussed in this thesis. These other processes are therefore not considered further.

2.2   Radioactivity

The process of radioactive decay occurs randomly within an individual radionuclide (Knoll, 2010). Radioactive materials, therefore, are treated as having a probability per unit time of decaying. This probability is constant and the effect of applying that constant to each time step results in an exponential relationship. The relationship between the number of initial parent radionuclides and the number of daughter nuclides produced is displayed in Equation 2.5. An initial number of radionuclides (N_0) will decay to a number of daughter products (N) after a length of time (t) according to a decay constant (λ).

$$N = N_0 e^{-\lambda t} \qquad\qquad 2.5$$

The number of decays that occur per second is known as the activity and is measured in becquerel (Bq) (Knoll, 2010). One becquerel is defined as one decay per second. The relationship in Equation 2.5 is useful for determining how much of a radioactive material remains, though is not particularly useful in this form for comparisons between different radionuclides or in determining the potential hazard that they may pose (Whicker and Schultz,

1982). A more useful measure is that of the radionuclides physical half-life, $T_{1/2}$, (Krane, 1988) and is calculated using Equation 2.6).

$$T_{1/2} = \frac{ln2}{\lambda}$$

2.6

The physical half-life is a constant for each radionuclide and describes the length of time it takes for a particular radionuclide to reach half of its activity. Another process, known as the biological half-life, describes the rate of excretion of a radionuclide from an organism through biological processes (Whicker and Schultz, 1982); biological half-life is corrected for physical decay and therefore is for the element and not a given radioisotope. Unless specified as biological half-life, the term half-life will hereafter refer to physical half-life.

2.3   Interaction with organic matter and the calculation of radiation dose

The measurement of the amount of energy deposited in a medium by radiation is defined by the absorbed dose (Knoll, 2010). Absorbed dose (*D*), as shown in Equation 2.7, is the mean energy ($\bar{E}$) deposited per unit mass (*m*) and is measured in gray (Gy). The absorbed dose changes for different materials that the radiation interacts with.

$$D = \bar{E}/m$$

2.7

The physical dose from radiation is not the same as the biological dose. Each type of radiation will cause a different amount of damage for the same amount of energy (Hall and Giaccia, 2006). The Relative Biological Effectiveness (RBE) is used to describe this damage to biological matter, along with a number of weighting factors, as different organs and tissues experience different amounts of biological damage. For human exposure, these help to calculate a set of equivalent doses (average over a tissue or an organ and taking into account the properties of the radiation) and effective doses (sum of all equivalent doses and taking into account the radiosensitivity of each organ or tissue type). These are measured in sieverts (Sv) and are only defined for radiation interactions in humans (IAEA, 2010b). As this is not applicable to wildlife, absorbed or weighted absorbed dose to animals and plants is reported in gray (Pentreath, 2012, ICRP, 2008).

The dose of radiation to an organism depends on the properties of both the organism and the radionuclide producing the radiation. Sets of Dose Conversion Coefficients (DCC) have been

developed that relate radionuclide activity concentrations, in media or biota, to absorbed dose (Vives i Batlle et al., 2011). The total accumulated dose (Equation 2.8), for an organism *b*, is the sum of the internal and external dose that is received from each radionuclide *i* (Brown et al., 2008).

$$D_{Total,\,i,b} = D_{int,i,b} + D_{ext,i,b}$$ 2.8

The internal and external dose rates are calculated as shown in Equations 2.9 and 2.10 respectively. In these equations, *D* is the dose in $\mu Gy\ h^{-1}$ received by a particular organism, *b*, from a radionuclide *i*. *C* is the radionuclide activity concentration in $Bq\ kg^{-1}$, *DCC* is the dose conversion coefficient in $\mu Gy\ h^{-1}$ per $Bq\ kg^{-1}$, *v* is the occupancy factor in media *z (e.g.* on soil, in soil, in air), and *wf* is the weighting factor for an emission type *r (α, β, γ)*.

$$D_{int,i,b} = \sum_{r}\left(C_{wo-biota,\,i,b}DCC_{int,\,i,r}wf_r\right)$$ 2.9

$$D_{ext,i,b} = \sum_{z}\left[v_z \sum_{r}\left(C_{media,\,i}\,DCC_{ext,\,i,b,r,\,z}wf_r\right)\right]$$ 2.10

The relationship between the radionuclide activity concentration in a particular medium and an organism (Equation 2.11) involves a number of complex biological and environmental processes. These processes are generally combined into a single value known as the Concentration Ratio (CR$_{wo-media}$) (Howard, 2013, Hinton et al., 2013). This ratio is used to estimate the radionuclide activity concentration within an organism (on a fresh mass basis) from activity concentration measurements in an environmental medium (C$_{media}$). The units of media radionuclide activity concentration used in Equation 2.11 are $Bq\ m^{-3}$ for air and $Bq\ kg^{-1}$ (dry mass) for soil.

$$C_{wo-biota,i,b} = CR_{i,b}C_{media,\,i}$$ 2.11

The ICRP, amongst others in the international community, has been developing CR$_{wo-media}$ for a set number of Reference Animal and Plants (RAPs) (ICRP, 2008). For terrestrial organisms, these are calculated from measurements of radionuclide (or stable element analogue)

24

concentration in the organism and the corresponding soil concentration in samples collected within the home range of the organism (e.g. Barnett et al., 2014). Historically, $CR_{wo-media}$ have been derived from a limited set of data and have been fragmented in their compilation (Beresford et al., 2008a), meaning there are few or no data for many organism and radionuclide combinations. Further, they assume equilibrium has been reached between the environment and the organism and they therefore do not apply in cases where there is a rapidly changing situation (Howard, 2013). Within the past decade, the available data from around the world have been collated in an international 'Wildlife Transfer Database' (Copplestone et al., 2013). Following reviews of these data, various authors have outlined research directions that would further enhance international understanding of radionuclide transfer in the environment (e.g. Hinton et al., 2013, Howard et al., 2013b). Live-monitoring techniques would assist in part to achieve this understanding by providing a means for monitoring a wider range and number of species.

2.4   Sources of radionuclides

The exposure of living organisms to radiation is a continual occurrence (Thorne, 2003). This radiation is either emitted from radionuclides that occur in the environment naturally or from radionuclides that have been artificially created by humans (i.e. anthropogenic radionuclides) or technologically enhanced naturally occurring radionuclides (i.e. TeNORM).

2.4.1   Naturally occurring radionuclides

Naturally occurring radionuclides can be categorised into primordial, secondary or cosmogenic (Eisenbud and Gesell, 1997) and are present in the ground, atmosphere and water (Thorne, 2003). The average global natural background dose (including radon gas) to humans is $c.2.4$ mSv a^{-1} (UNSCEAR, 2013). Differences in factors such as air flows, altitude, geology, and soil characteristics lead to variation in background exposure (Smith and Beresford, 2005).

Primordial radionuclides have half-lives of the order of the age of the earth; shorter-lived 'secondary radionuclides' are created through the decay of primordial radionuclides (Eisenbud and Gesell, 1997). The most abundant primordial radionuclides in the environment include ^{40}K, ^{232}Th, and ^{238}U (Jones et al., 2009, Thorne, 2003). Also present, but of a lower abundance, is ^{235}U (Kathren, 1984). The daughter products of ^{232}Th and ^{238}U that are often of interest for environmental radionuclide assessments (from a human protection perspective) due to their longevity in the environment and because they are released as teNORM, are ^{234}Th, ^{210}Po, ^{228}Th

^{230}Th, and ^{234}U (Environment Agency et al., 2014). The Radon isotopes ^{220}Rn and ^{222}Rn, while having relatively short half-lives, are classified as high health risks due to their presence in the atmosphere (UNSCEAR, 2000a). Due to the health risk that they pose, ^{226}Ra and ^{228}Ra are also of monitoring interest for humans (IAEA, 2014). Although there are other primordial radionuclides present in the environment, their (individual) contribution to health risks is relatively insignificant compared to the above mentioned radionuclides (Thorne, 2003, IAEA, 2014).

Cosmogenic radionuclides are formed by cosmic-rays bombarding stable nuclides in the atmosphere. These rays are attenuated by the atmosphere and therefore the intensity of cosmogenic radionuclides depends strongly on altitude (Smith and Beresford, 2005). The earth's magnetic field also acts to modulate the intensity of cosmic rays which results in higher level dose rates at the poles than at the equator (Thorne, 2003). The most important radionuclides from cosmogenic sources are ^{3}H, ^{14}C, ^{7}Be, and ^{22}Na (Whicker and Schultz, 1982, UNSCEAR, 2000a). While other cosmogenic radionuclides are present, they are considered as not being abundant enough to add significantly to the total radiation dose from background radiation.

2.4.2   Anthropogenic radionuclides

The discovery of radiation, and the identification of the first radioactive elements, towards the end of the nineteenth century opened new possibilities for medical imaging and therapy and ultimately weapons and power generation, with associated production of artificial (or anthropogenic) radionuclides (Keevil, 2012). During the following century, the increase in use of radioactive materials and their mismanagement has left a lasting legacy of radioactive waste which needs to be managed. Testing of nuclear weapons by several countries during the 1950s and 60s, led to widespread contamination of large areas of the planet (IAEA, 2011). Fallout from these tests is still measurable in the environment for radionuclides with longer half-lives and a large enough initial emission (e.g. a 10-year half-life would result in almost a 97% reduction in concentration since above ground nuclear testing ended), including ^{3}H, ^{14}C, ^{90}Sr, ^{137}Cs, ^{238}Pu, ^{239}Pu, ^{240}Pu, and ^{241}Pu (Thorne, 2003, UNSCEAR, 2000b). Coupled with the production of nuclear weapons came the accidental releases of radionuclides from nuclear weapons facilities. The most significant of these to affect the UK was the Windscale accident in 1957 (Wakeford, 2007) during which substantial quantities of ^{137}Cs, ^{131}I, and ^{210}Po were released (Garland and Wakeford, 2007).

The development of nuclear weapons led to the discovery of nuclear power generation (Eisenbud and Gesell, 1997). The use and transfer of radioactive materials at nuclear power generation, research, and waste management facilities, introduced anthropogenic radionuclides into the environment through planned (authorised) radioactive emissions (e.g. Environment Agency et al., 2014). These emissions are regulated and each facility has a maximum allowable amount of radionuclides they can release each year. Since the introduction of nuclear power facilities, however, there have been two further key accidents that have contributed to elevated levels of radionuclides in the UK. These were the Chernobyl accident in 1986 (Saenko et al., 2011) and (though only a minor contribution to UK levels as compared to Chernobyl) Fukushima in 2011 (Wakeford, 2011). Studies of radionuclide releases, from the nuclear accidents described in this section, are largely focused on ^{134}Cs, ^{137}Cs, ^{131}I and ^{90}Sr due to the fallout measured in the UK as well as the risk they posed to human health through the food chain. Fallout from the Fukushima accident that was measured in the UK included low quantities of ^{131}I and ^{134}Cs (Beresford et al., 2012). Though ^{137}Cs was identified, it was considered that most of the activity present was from previous nuclear weapons and Chernobyl releases.

2.4.3   Radionuclides in the UK

The average background radiation in the UK is 2.7 mSv a^{-1} (Public Health England, 2011). Radiation from radon contributes a large proportion to the annual exposure, with Cornwall experiencing an average radon dose of 7.8 mSv a^{-1} (UK average 1.3 mSv a^{-1}). For cosmogenic radiation, an estimated dose at ground level for the 50th parallel north (UK level) is around 0.35 mSv a^{-1} (Kendall, 2005, Environment Agency et al., 2014). Anthropogenic sources such as nuclear emissions and medical waste contribute a smaller amount; nuclear facilities generally have emissions less than 0.1 mSv a^{-1} and all are below the 1 mSv annual limit for exposure of the public from anthropogenic sources (Environment Agency et al., 2014).

2.5   Detection of radionuclides

2.5.1   Radiation detectors

The interaction of radiation with matter gives rise to a number of detection possibilities. These interactions can be detected and converted to a different form of energy (usually electrical or light) which can then be quantified (Knoll, 2010). There are three main types of detector for instantaneous detection; gas-filled (or ionising), scintillation, and semiconductor (or solid state). **Gas filled** detectors are constructed using an anode and cathode electrode, surrounded

by a gas (Krane, 1988). They utilise electric fields within the gas-filled chamber to count ions that have been formed as a result of a radioactive particle travelling through the detector. **Scintillation** detectors operate on the basis of converting radiation interaction into light (Krane, 1988). Radiation incident on a scintillation detector is converted into a photon of visible, or near visible, light through a process known as fluorescence. The emitted light is collected whereupon it is converted to an electrical signal and amplified (see section 2.5.2). There are two types of scintillators; organic and inorganic (Knoll, 2010). Inorganic scintillators operate on the crystalline structure level, whereas organic scintillators operate at the molecular level and can therefore be formed into liquids or plastics. **Solid state** detectors work on the same principles as those of a diode device, utilising electron hole configurations for the detection of radiation (Knoll, 2010). By combining a n-type (electron rich) and a p-type (electron deficient) semiconductor, an anode and cathode are created with a region of electrical neutrality in between (known as the depletion region). A radioactive particle entering the depletion region can interact and form an electron and hole pair. This then propagates through the material until the electron reaches the p-type material where it forms an electrical pulse that can be measured. A more detailed description of how these detection technologies work is available in Krane (1988) and Knoll (2010).

2.5.2   Scintillator light collection

Unlike gas-filled or solid state detectors, a scintillation detector requires the extra stage of converting light produced from a radiation interaction into an electrical signal. Each interaction typically produces only a few hundred photons and therefore needs to be amplified before it can become a usable signal (Knoll, 2010). The most common method of converting the fluorescence from a scintillating material is to use a **Photomultiplier tube (PMT)**. Light that is incident on a PMT is collected and converted to low energy electrons by means of a photocathode. These electrons are then accelerated and amplified in the next stage of the PMT (the electron multiplier) using a series of dynodes (an electrode that emits one or more electrons when struck by a single electron) that have a high voltage applied to them. The dynodes in the electron multiplier must be contained within a vacuum so the electrons can be accelerated efficiently. At the end of the dynode chain, the resulting electrons have been amplified to a sufficient level (typically between 10^7 to 10^{10} electrons) whereby they can be collected by and anode and output as a useful electrical signal.

The other method for light collection is to use a photodiode. Photodiodes operate under the same principles as semiconductor detectors (Knoll, 2010, Turchetta, 2016) though instead of converting radiation interactions into electrical pulses, it converts incident light exiting from a scintillating material. As such, photodiodes are much smaller in size than a PMT. The most basic form of the photodiode is the **Conventional (PIN)** photodiode. This consists of a p and n-type material with a depletion region forming in between. An incident photon will interact in the depletion region and causes an electron-hole pair to propagate through the material until the electron is collected at the n-type layer, creating an electrical pulse. The electric pulse is equal to the energy of the electron and therefore the output signal needs to be amplified. This causes the input signal to be susceptible to noise; low energy radiation in large detectors can often be of poorer resolution than a standard PMT. Further, the size of each PIN photodiode is typically smaller than 1 cm^2 due to high levels of noise introduced in larger photodiodes; doubling the surface area of a conventional photodiode will double the signal but will also double the noise. By inserting a second p-type material between the depletion region and the n-type layer, a short region of high electrical bias is created. This configuration makes the photodiode work in a similar fashion to gas multiplication in a proportional counter. As such, it is referred to as an **Avalanche (APD)** photodiode. Photons that enter through the first p-type later will be accelerated through the depletion region towards the region of high electrical bias, whereupon further electron-hole pairs are formed. This leads to an avalanche of electrons and therefore increases the measured output signal (proportional to the voltage bias). The gain of this signal is typically around 10^6 which is comparable to standard PMTs.

These two photodiode types are aimed at singular interactions. A more complicated arrangement, consisting of many photodiodes, is required for the spectrographic measurement of radiation emitted from a sample. The **Silicon Photomultiplier (SiPM),** or Multi Pixel Photon Counter (MPPC), consists of an array of avalanche photodiodes. Each avalanche photodiode is operated in the "Geiger" region; the electron avalanche is allowed to saturate the diode. By connecting the diode in series with a large resistor, the electric field over the diode will drop once the diode has saturated and will therefore be quenched within a few nanoseconds. The size of each photodiode is kept small such that, theoretically, only a single photon will be collected during any single detection. The number of incident photons would be proportional to the number of cells that are producing an avalanche. Therefore, large numbers of cells are required due to the number of scintillation events that can be

created within a scintillating material. The size of these arrays is typically 5 to 6 mm though multiple SiPMs can be joined in parallel (creating a larger array) and therefore increase the detection surface area. The efficiency of the SiPM is defined by the photon detection efficiency (PDE). This is a combination of the ratio of the optically active area to the surrounding inactive area (fill factor), the probability that an incident photon will create an electron-hole pair (quantum efficiency), and the probability that an avalanche will be initiated by an electron-hole pair (avalanche initiation probability). There are several advantages and disadvantages to using SiPMs over PMTs. These are discussed in more detail in chapter 3.

2.5.3 Radionuclide decay energy spectrum

The electrical output from the aforementioned detection technologies is processed to produce a readable output that can be used to identify and quantify the radionuclide present in a targeted sample (Knoll, 2010). The nucleus of a radionuclide will often decay to a daughter nuclide through a number of steps or possible routes using a combination of the previously described decay processes (Section 2.1). Each decay path has a characteristic energy that is important for identifying the type of radionuclide. As an example; Figure 2.1 (adapted from Podgorsak, 2010) shows an energy level diagram of the primary decay paths for ^{137}Cs.
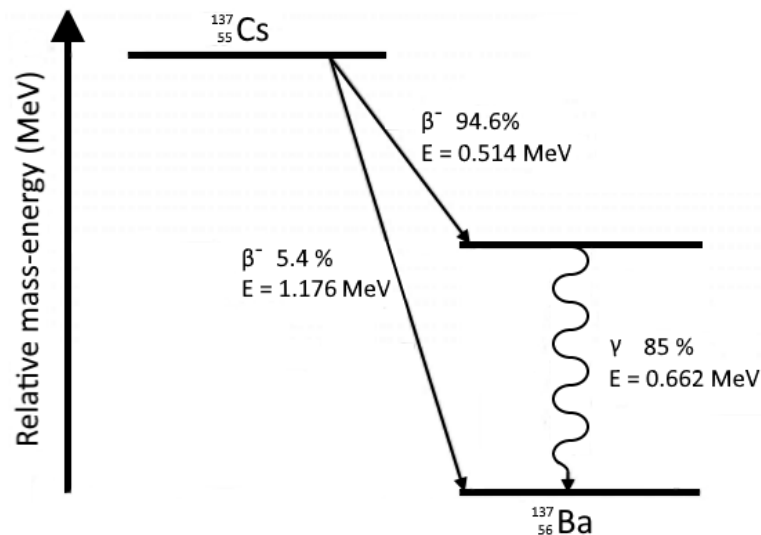
Figure 2.1: Primary decay paths for caesium-137 to barium-137.The most prominent (or main) decay path is by beta minus emission to an intermediate excited state, ^{137m}Ba. From here, it decays to a stable state either through the emission of a gamma photon or by two possible internal conversions (not shown). A secondary path, though of much lower probability, is to decay directly to a stable state by a higher energy beta minus emission. Figure adapted from (Knoll, 2010).

For gamma emitting radionuclides, the emitted gamma photon will interact with any atoms it encounters in the medium it is travelling through (Knoll, 2010). Depending on its energy, a gamma photon will be subject to either photoelectric absorption, Compton scattering, or pair production. A full description of how these secondary processes form is given in Knoll (2010) though a general description is given below.

Photoelectric absorption occurs when a low energy photon is absorbed by an atom resulting in a photoelectron being ejected. The photoelectron energy is equal to its binding energy within the atom and has kinetic energy equal to the difference in energy of the incident photon and ejected photoelectron. Characteristic x-rays may also be emitted when the vacancy left by the photoelectron is filled by a free electron. **Compton scattering** occurs when a photon interacts with an electron. Through this interaction, the photon is deflected by an angle θ and, in doing so, transfers some of its energy as kinetic energy to the electron (defined as a recoil electron). The angle θ determines the energy of the deflected photon and the electron and therefore energies can range from zero to an energy close to that of the incident photon. **Pair production** occurs when the energy of an incident photon exceeds 1.02 MeV. In this process, the gamma photon is converted into an electron-positron pair. Any excess energy above the 1.02 MeV becomes kinetic energy for the emitted electron and positron.

These secondary processes can obscure the characteristic energy peak of a radionuclide and therefore make identification difficult (Knoll, 2010). Compton scattering introduces the largest interference on an energy diagram (pulse height spectrum), creating a plateau known as the Compton continuum. This is visible in Figure 2.2 (adapted from Knoll, 2010) as the higher region shown to the left of the characteristic decay peaks. Backscatter from surrounding materials, such as shielding for the detector, is another source of interference that will be apparent in the lower energies of the spectrum. Pair production can further introduce an 'escape peak' for incident gamma photons of sufficient energy (> 1.02 MeV) though is more likely seen in radionuclides with decay energies above those described in this thesis (see Appendix 10.1). These additional interactions are, however, particularly inconvenient when the measurement of a lower energy decay is desired.

The energy spectrum for beta radionuclides has already been described in Section 2.1 as a range of energies between zero and the maximum energy of the electron, E_{max}, with the spectrum peaking at approximately a third of E_{max}. This energy spectrum means the identification of a single beta emitting radionuclide from a mixture of beta emitting
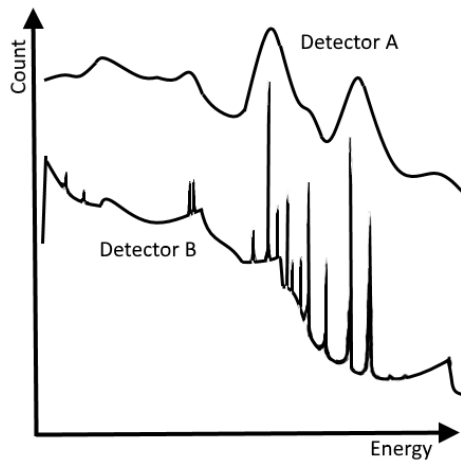
Figure 2.2 Effect of resolution on radionuclide identification. Figure adapted from (Knoll, 2010)
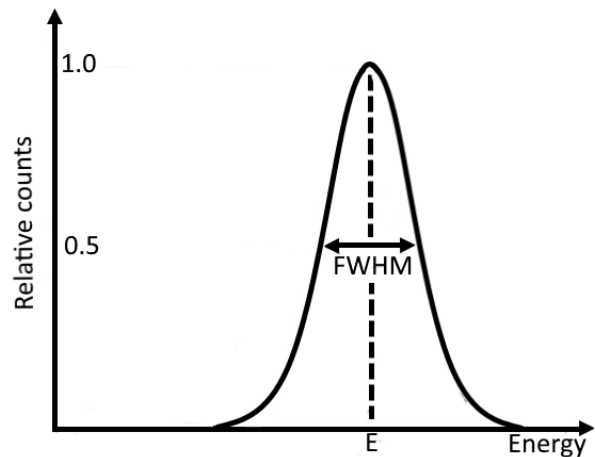
Figure 2.3: Spectrum of energies that define detector resolution. Figure adapted from (Knoll, 2010)

radionuclides is difficult to accomplish with a spectral output like that shown in Figure 2.2. If the beta emitting radionuclide does not have a suitable gamma emission then identification therefore often has to rely on methods that either reject unwanted energies (such as using a thin, low density detector) or chemically separating the expected radionuclide from the sample for analysis (e.g ASTM International, 2014).

2.5.4 Detector properties affecting the identification of individual radionuclides

The pulse height spectrum differs between detectors based on a number of properties; resolution, efficiency, and dead time (Knoll, 2010). These properties determine how suitable a particular detector is for a given task or for measuring a specific radionuclide.

The resolution of a detector indicates how well different energies can be distinguished (Knoll, 2010). For a single energy that is recorded, the responding peak will have a specific height and width which is determined by the statistical variation in individual pulses (as shown in Figure 2.3). The Full Width Half Maximum (FWHM) of this peak, if divided by the energy of the pulse, gives the corresponding resolution. As this is a simple ratio, the value is dimensionless and often reported as a percentage. For different materials that experience the exact same energy and number of pulses, the corresponding peaks will have the same area but can be of two different resolutions. A good resolution will have a tall peak with a small FWHM, whereas a poor resolution will have a short peak with a large FWHM. For a similar count rate on two detectors; one with poor resolution and the other with good resolution, the area under the characteristic peak will be the same. The detector with good resolution, however, will have a much taller (and therefore narrower) peak. Therefore, for a detector with a better resolution,

a much lower count rate can be used to measure a radioactive source. This will give an identifiable peak but will also mean that there is an overall lower signal displayed from any naturally present radiation (background radiation) that the main signal needs to be distinguished from.

For multiple photon detections of varying energies, the peaks will be superimposed through the use of a multichannel analyser (MCA) to form an energy spectrum (Krane, 1988). A higher resolution is critical in being able to differentiate between different energies and hence for identifying specific radionuclides that may have emission energies that are close together (Knoll, 2010). For example, Figure 2.2 illustrates how the resolution can affect the identification of radionuclides. Detector B has a better resolution and is therefore able to identify more radionuclides than detector A. The figure also demonstrates (as described above) that the background measurement is lower for the higher resolution detector.

The detection efficiency of a detector is a measurement of the number of detections made in relation to the number of incident radiations (Knoll, 2010). For lower penetration radiations such as alpha and beta, nearly all the incident particles (that penetrate the detector window) will interact with a detector. In the case of a scintillator or a solid-state detector, this will be nearly 100% efficiency. Gamma photons on the other hand are more penetrative and therefore could travel through the entire detector and make no detectible interactions. Here the detection efficiency will be less than 100%. The efficiency of a detector can be described through a number of different terms. Important to this thesis is the *absolute, intrinsic, and full energy photopeak efficiency* (Knoll, 2010). The *absolute* efficiency (ϵ_{abs}) is a measure of the number of radiation interactions recorded by the detector as compared to the radiation emitted by the source. The *intrinsic* efficiency (ϵ_{int}) denotes the number of radiation interactions recorded by the detector as compared to the radiation incident on the detector surface. The final term used to describe detector efficiency is full energy *photopeak* efficiency (ϵ_p). Also known as the photopeak ratio, this is the fraction of counts in the characteristic energy peak as compared to the whole spectrum.

Between each detectable pulse, there is a short delay before another pulse can be detected (Knoll, 2010). Each interaction takes a minimum amount of time to discharge in the material during which any further interactions will not produce a separately detectable signal (though in some cases the undetected interaction can extend the period of non-detectability). This is known as the dead time and can occur in the material of the detector or in the associated

electronics. This creates a problem for the detection of high activity concentrations for which a correction to account for dead time will need to be made. Shorter dead times are therefore preferable if measuring high count rates (or activity concentrations).

2.5.5   Distinguishing source signal from background

Identifying the quantity of radiation emitted by a target source (Ns) requires the measurement and subtraction of the background (N$_B$) from the gross (or total) signal (N$_T$). There is, however, an uncertainty (σ) associated in the measurement of this signal. For large counts of N$_T$, the uncertainty in the count can be fitted to a gaussian distribution and is approximated to $\sigma_T = \sqrt{N_T}$ (Knoll, 2010). This is the same for measurement of the background; $\sigma_B = \sqrt{N_B}$. Any subsequent propagation of uncertainties, such as the subtraction of background or in calculating the count rate (dividing by total count time), follows the standard rules as shown in Equations 2.12 to 2.14; examples use three variables *a, b, c* and a constant *C*.

$$(a = b + c) \; or \; (a = b - c) \quad \rightarrow \quad \sigma_a = \sqrt{\sigma_b + \sigma_c} \qquad\qquad 2.12$$

$$(a = Cb) \quad \rightarrow \quad \sigma_a = C\sigma_b \qquad\qquad 2.13$$

$$(a = b \times c) \; or \; (a = b/c) \quad \rightarrow \quad \left(\frac{\sigma_a}{a}\right)^2 = \left(\frac{\sigma_b}{b}\right)^2 + \left(\frac{\sigma_c}{c}\right)^2 \qquad\qquad 2.14$$

Because both the background count and the source count have an uncertainty associated with them, there is a need to determine at what point a measurement can statistically distinguish a source from background. For this, limits of detection were outlined (or unified) in 1968 by Currie (1968). Of importance are the critical limit (L_C) which defines the point above which a single count measurement can be classified (with 95% probability) as not being part of the background, and the detection limit (L_D), at which point a mean number of counts can be differentiated from background counts. These two limits, as defined for radioactivity, are given by equations 2.15 and 2.16 (Currie, 1968, Knoll, 2010).

$$L_C = 2.33\sqrt{\sigma_B} \qquad\qquad 2.15$$

$$L_D = 2.71 + 4.65\sqrt{N_B} \hspace{4cm} \text{2.16}$$

More often quoted is the MDA (Minimum Detectable Activity) because this includes the radiation yield per disintegration (BR), absolute efficiency of the system (ϵ_{abs}) and the total count time (t) (Knoll, 2010).

$$MDA = \frac{2.71 + 4.65\sqrt{N_B}}{BR\ \epsilon\ t} \hspace{3cm} \text{2.17}$$

3 Literature review: radionuclide monitoring methods and existing portable detection technologies

3.1 Introduction

This chapter details and discusses the current methods used in radionuclide monitoring for terrestrial wildlife with the purpose of identifying suitable live-monitoring techniques. As a part of this, a description and review, in terms of suitability for portability and field use, is given for currently available materials for radiation detection. This review identifies the direction for the overall project and ends in an outline for the remaining thesis.

3.2 Description and purpose of radiological assessments

Radionuclide monitoring and research programs for terrestrial wildlife have existed since the first use of nuclear weapons (e.g. Kaye and Dunaway, 1962, Garten, 1995, Gaschak et al., 2011, Sazykina and Kryshev, 2006). Their purpose is to measure and assess the concentration of radionuclides that have been introduced to the environment due to human activities such as the generation of nuclear power (Copplestone et al., 2003). Historically, monitoring programs arose primarily due to concern from potential harm to humans through contamination of food sources (Kathren, 1984); for instance, sheep in the uplands of Cumbria and Wales (Horrill and Howard, 1991) and reindeer in Norway (Brynildsen and Strand, 1994) due to fallout from the Chernobyl accident. Until relatively recently, it was considered that the standard of environmental control needed to protect man would ensure that other species were not put at risk (ICRP, 1977, ICRP, 1991). However, by the start of this century, national requirements for the demonstration of wildlife protection began to be introduced (Copplestone et al., 2005) and there was growing recognition that the International Commission on Radiological Protection (ICRP) recommendations may not always adequately protect wildlife (Pentreath, 1999, Sheppard, 2003).

In 2007, the ICRP updated its 'Recommendations' to recognise the need for explicitly demonstrating adequate protection of the environment (ICRP, 2007). In the UK, the regulatory position had already changed due to the interpretation by UK regulatory agencies of the EC Birds and Habitats Directives (Copplestone et al., 2003, Copplestone et al., 2005). The focus of these Directives is on demonstrating that protected species and/or habitats are not significantly impacted by hazardous substances; the UK agencies interpreted 'hazardous substances' to include radionuclides. The measurement of radionuclides within terrestrial

wildlife has typically focused on a specific selection of radionuclides. This is because they have either been the dominant radionuclides dispersed in nuclear accidents (e.g. Chernobyl) or are expected to be present at the site being studied (e.g. a uranium mine). Commonly measured radionuclides include, ^{40}K, ^{90}Sr, ^{99}Tc, ^{131}I, ^{134}Cs, ^{137}Cs, ^{232}Th, ^{238}Pu, ^{238}U, $^{239+240}$Pu and ^{241}Am (e.g. Beresford et al., 2016, Bonisoli-Alquati et al., 2015, Barnett et al., 2014, Chesser and Sugg, 2000, Copplestone et al., 1999, Ishida et al., 2015, Kubota et al., 2015, Maklyuk et al., 2007, Malinovsky et al., 2014, Ryabokon et al., 2005, Semioshkina et al., 2007, Struminska-Parulska et al., 2013, Wood, 2010, Wood et al., 2009b). These radionuclides, however, are not the only ones that require monitoring. The use, storage, and disposal of radioactive materials in the UK covers a broader set of radionuclides and these are required to be monitored as part of the Radioactive Substances Act of 1993 (RSA93). Radiological environmental assessments (for public exposure to radiation from authorised radioactive discharges) are the responsibility of the UK environment agencies (Environment Agency et al., 2014). The levels of radioactivity that have been transferred into environmental compartments (including wildlife) from licenced facilities in the UK have been measured by these agencies and are published[1] as part of the annual Radioactivity in Food and the Environment reports.

3.3   Methods for radionuclide assessment / measurement

The initial process for estimating the exposure (i.e. dose) of wildlife from radionuclides in England and Wales was outlined in the Habitats Regulations for Stage 3 Assessments (Copplestone et al., 2003) and subsequently, international approaches such as the ERICA Integrated Approach (Larsson, 2008) have been developed. A radionuclide assessment will consider all radionuclides that are present within the environment or planned to be released by a licenced facility. The total dose that is estimated to be received from exposure to all present radionuclides is compared to what is often termed a 'screening dose rate' (Brown et al., 2008). This screening dose rate is defined as the dose rate below which wildlife populations are unlikely to be significantly harmed (Howard et al., 2010). Screening dose rates are utilised to indicate if radionuclide emissions from a given facility present negligible risk to wildlife under highly conservative assumptions and if that facility needs a higher degree of assessment or not; they are applied to the additional dose and not natural background radiation. There is, however, no worldwide agreement on a single screening dose rate and therefore different

---

[1] https://www.gov.uk/government/publications/radioactivity-in-food-and-the-environment-rife-reports-2004-to-2016

ones exist in different countries (a summary is provided in Howard et al. (2010)); for the UK, the main modelling tool ERICA has an ICRP defined default of 10 μGy h^{-1} though the screening dose rate used in assessments in England is 5 μGy h^{-1} (Copplestone et al., 2005).

To assist with the radiological assessments that monitor a mixture of radionuclides, a number of tools (e.g. R&D128, RESRAD-BIOTA and ERICA) have been created to model the transfer of radionuclides and estimate exposure and subsequent risk (Copplestone et al., 2001, Yu et al., 2003, Brown et al., 2008). These tools can be used in advance of a facility being built, to assess its impact on the environment, and to review licences that are currently held. These modelling tools are often applied in a tiered way (e.g. Brown et al., 2008). The low-level tiers use conservative assumptions to undertake simple screening assessments, allowing identification and 'screening out' of situations in which it is highly unlikely that wildlife will be impacted significantly. Minimal site data are required for screening assessments, but at higher tiers the assessments become more realistic and these more detailed assessments should be supported by field measurements (Copplestone et al., 2003). Assumptions and simplifications are made in these models (Beresford et al., 2010) and this introduces a high level of conservatism that can cause inconsistencies in the predictions made by different modelling tools when applied in an initial screening level assessment. The transfer element (i.e. the CR) is considered to be the most uncertain aspect of this assessment (Beresford, 2010). Therefore, where possible, a low-cost method to directly measure targeted organisms is desirable.

The standard process for determining radionuclide activity concentrations within an organism is destructive (IAEA, 1989); the body of the organism is either homogenised for a whole-body measurement or is dissected so the radionuclide concentration in each organ can be individually measured (this is employed in cases where the distribution of radionuclides in the body is desired to be known and maybe the only way of processing a larger organism) (e.g. Barnett et al., 2014, Kubota et al., 2015). This destruction of the organism is required because not all types of radiation are penetrative enough (or are not of a sufficient concentration) to be adequately quantified by an external radiation detector. Destructive sampling is, however, difficult to justify (ethically; (Russell et al., 1959)) and there is a drive to reduce the number of animals killed for the purposes of research (Home Office, 2013). Further, this method is undesirable for the monitoring of protected species. Therefore, there has been growing interest in the development of non-lethal monitoring techniques (e.g. Wood et al., 2011, Bondarkov et al., 2011).

There are two main approaches to live-monitoring; directly monitoring the organism using a radiation detector or taking samples from the body of the organism. Direct monitoring has been previously conducted on a limited range of organism and radionuclides (examples of these along with a description of monitoring technology are provided in the next subsection). The limitations of this approach, however, has generally been in requiring the target radiation emission to be both penetrative and in sufficient quantities such that it is detectable by an external radiation detector (and can be distinguished from background radiation). The other approach, of collecting samples from the organism, has been conducted to varying degrees of success. Two main pathways facilitate the entry of radionuclides into the body; absorption via the lungs (inhalation) or via the gastrointestinal tract (ingestion), after which they are transferred through different compartments of the body (ICRP, 1979). The collectable samples from an organisms body are therefore: blood (ICRP, 1979), fur and feathers (McLean et al., 2009, Boryło et al., 2010, Tete et al., 2014, Strumińska-Parulska et al., 2015),faeces and urine (e.g. Mayes et al., 1994, Moss and Horrill, 1996), and for a limited number of radionuclides exhaled air (Didychuk et al., 2014). A final alternative method is to measure the radionuclide content of teeth (IAEA, 2002) or antler (Tiller and Poston, 1999). This is only viable for antler, however, as the use of teeth could be considered too invasive.

An inherent problem with these sampling methods is the requirement to understand body distributions and excretion pathways and to subsequently develop approaches to convert these measurements into whole-organism activity concentrations (ICRP, 1979). Whilst this may be solved over time, the size of some samples that can be collected from an organism severely limits the viability of deploying these methods; blood samples, exhaled air, or urine (urine not possible in birds) would likely not contain sufficient radionuclide concentrations for measurement, especially in smaller organisms. Some of the other above mentioned alternative methods may be suitable to individual species in the event of no other suitable live-monitoring method being available, e.g. antler for deer (Tiller and Poston, 1999) and faeces for large organisms, e.g. grouse (Moss and Horrill, 1996), have all provided good alternatives for some radionuclides. The time required for sample analysis, however, means these sample collection methods are not a rapid process (if immediate results are required), nor can analysis be conducted in the field (e.g. Strumińska-Parulska et al., 2015). Therefore, direct whole-body live-monitoring with a portable radiation detector would be preferred.

3.4 Current technology for terrestrial wildlife monitoring

Radionuclide activity concentrations in animals are often measured on high specification laboratory-based detectors, usually high Purity Germanium (HPGe) detectors, as they offer a high level of spectrometric resolution (IAEA, 1989, IAEA, 2011). The use of these detectors, however, has two main drawbacks; they require the animal to be brought to the detector, and they usually require the animal to be destroyed. The deployment of a portable detection method in the field would therefore be beneficial to monitoring radionuclide concentrations within wildlife.

Previous instances of portable live-monitoring were primarily related to livestock screening in the years following a nuclear accident (Table 3.1). After the Chernobyl accident in 1986, sheep in the UK (Howard et al., 1987) were screened to check which sheep had low enough radionuclide levels for human consumption (Howard et al., 1987). Sheep found to be above the recommended levels were released to await internal levels falling low enough for consumption. This screening ended in 2012 (Wearne, 2012). Similarly, reindeer in Norway were, and still are, routinely monitored for ^{137}Cs levels (Brynildsen and Strand, 1994). Other monitoring programs, such as Canada Geese at the Oak Ridge reservation in America (Middleton, 2011), focus on animals caught by hunters. The Oak Ridge live-monitoring assessed the uptake of ^{137}Cs by geese, those found to be above the limit are still slaughtered for more detailed analysis.

The detection technology used for these studies has commonly been Sodium Iodide (NaI) crystals (e.g. Howard et al., 1987, Mayes et al., 1994, Beresford et al., 1998). The use of this material has remained consistent. Any advancements of the devices used for live-monitoring have typically focused on the detection methods, such as alternative ways of accounting for background radiation (Meredith et al., 1988), or optimal placement of the detector (Brynildsen and Strand, 1994), rather than of the technology itself. Sodium Iodide has primarily been used for portable radiation detection because it is a cost-effective material of good efficiency. Despite its low spectrometric resolution, it has so far been appropriate because only a small number of radionuclides have been targeted at any one time; namely ^{134}Cs and ^{137}Cs, or ^{131}I.

Table 3.1: Examples of portable radiation detectors for animal live-monitoring

Reference	Radionuclide	Animal	Detector	Processing	Shielding	Operation
(Howard et al., 1987)	^{134}Cs, ^{137}Cs	Sheep	15x13 cm NaI	MCA	Partially shielded with lead	Calibrated against polyethylene phantoms filled with aqueous solution of ^{134}Cs and ^{137}Cs
(Meredith et al., 1988)	^{134}Cs, ^{137}Cs	Sheep	4.5 cm NaI(Tl)	SCA	3 mm lead	Background corrected using reading with detector pressed against operators' stomach. Calibrated against slaughtered animals
(Eldridge, 1989)	^{137}Cs	Canada Geese	15x15 cm NaI	-	[thick] Lead	
(Brynildsen and Strand, 1994)	^{134}Cs, ^{137}Cs	Reindeer, Cattle, Sheep	7.6x7.6 cm NaI	Canberra Series 10 MCA	Plastic shield to protect against the environment	Background accounted for by taking measurement with detector held in position but with animal absent
(Moss and Horrill, 1996)	^{137}Cs	Red Grouse	7.6 cm NaI	Canberra Series 20 MCA		Animal placed in box above the detection crystal. Background measured using empty box
(Beresford et al., 1997)	^{131}I	Goats	7.6 cm NaI	Canberra Series 20 MCA		Calibrated against thyroids removed during slaughter.
(Bondarkov et al., 2011)	^{90}Sr, ^{137}Cs	Small mammal	63 mm NaI, 60 x 0.1 mm Plastic scintillator	-	50 - 100 mm lead	Size and weight necessitates detector is transported and used within a mobile laboratory (bus) or static laboratory.

Processing hardware and shielding is detailed for articles where information is provided.

The primary purpose of these detectors has been to monitor gamma emissions. While detectors have been developed for simultaneously identifying gamma and beta emitting radionuclides (e.g. Potapov et al., 2006), these have largely focused on detection within surface soils and are not specifically aimed towards animals. They require a second detector material for the detection of the beta radiation and therefore increase the size requirement for the detector. There is only one instance of a portable gamma / beta monitor for animals that has so far been identified in the literature. The live-monitoring described in Bondarkov et al. (2002) initially required animals to be moved to a laboratory though development (Bondarkov et al., 2011) of this detector led to a mobile laboratory version for use in the Chernobyl Exclusion Zone. This detector uses a sodium iodide crystal for gamma detection and a thin plastic scintillator for beta detection. The beta detector was designed to give it the capability of determining ^{90}Sr content via the measurement of ^{90}Y and has already been utilised for several studies (see reference list for Bondarkov et al., 2011). The size and weight of the detector, however, means it requires a vehicle for transport, meaning it is restricted in how it can be deployed; the detector deployment range is limited to areas accessible by road. If the complexity (i.e. quantification of gamma and beta) of the detector is to be increased, whilst also being made portable, then the use of newer technologies will need to be utilised.

3.5 Technology for portable radiation detectors

A radiation detector comprises (Figure 3.1) of a detection material, a means to collect a signal from the detection material (usually a light guide and PMT if the detector is a scintillator), electronics to amplify and shape the signal, a MCA and a means to display / store the measurement results, and a power supply (Knoll, 2010). The detector may optionally be surrounded by a shield depending on the application. This subsection details the technology that is available for radiation detectors and discusses it in the context of a portable detector
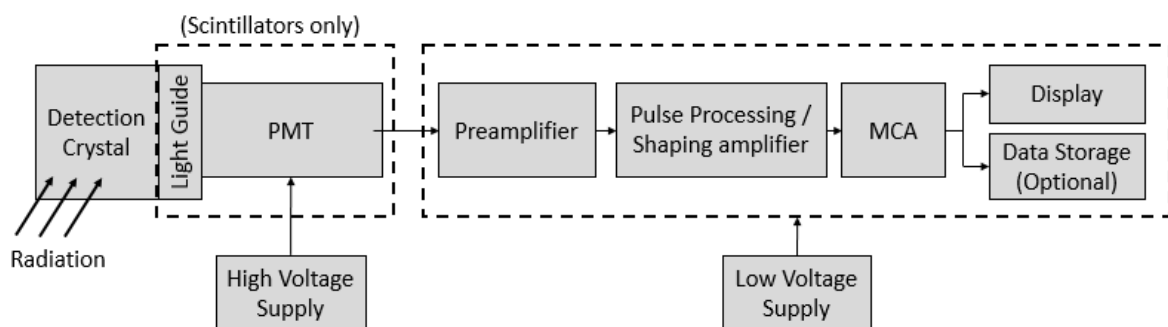
Figure 3.1: Schematic diagram of a radiation detector (Adapted from Knoll, 2010)

3.5.1 Detection materials

There are a wide variety of different materials, each with their own unique properties, that can be used for the detection of radiation. The following description of materials is not intended to be exhaustive but aims to cover some of the more common types of materials that are available for commercial use.

Available since 1948, **Sodium Iodide (NaI)** is an inorganic scintillator that is the dominant material of choice for gamma radiation detection. This is due to it having good availability in large volumes and a low cost compared to other materials (Krane, 1988, Knoll, 2010). Pure NaI will produce a light output of up to 45,000 photons per MeV, though in this form it will only scintillate at liquid nitrogen temperatures (Sakai, 1987, Hine, 2016). It is therefore more commonly seen doped with thallium (as NaI(Tl)) to allow scintillation at room temperatures. In this state, it has a photon output of 38,000 photons per MeV.

The resolutions typically seen in NaI(Tl) detectors are of the order of 8% for decay energies of 662 keV (see Table 3.5). This is towards the lower end of the 3-10% resolutions typically seen in scintillators (Knoll, 2010) although, as already discussed in section 3.4, this resolution has so far been suitable for most uses of portable radionuclide detection involving wildlife. If, however, a larger range of radionuclides require detection, then this low resolution may not suffice. In addition to its low resolution, a NaI(Tl) crystal has a long decay time (time for fluorescence in the crystal to decay after a radiation interaction – see chapter 2.5) at 0.23 µs compared to other detection materials (Knoll, 2010). This makes it less useful for measurement of high activity concentrations. Further, while NaI(Tl) has an effective atomic number (Z_{eff}) of 50 (Tavernier et al., 2006), a low density (compared to other materials) of 3.67 g cm^{-3} means this material does not have as high an intrinsic efficiency as some of the other materials described in this chapter. The efficiency is approximately 50% for ^{137}Cs in a 25 mm thick detector and 75% in a 51 mm detector. The photopeak ratio is also low at 40% for ^{137}Cs in a 25 mm x 25 mm detector and 58% in a 51 mm x 51 mm detector (Hine, 2016). Counting efficiencies and photopeak ratios for a number radionuclide decay energies and crystal sizes are available in Knoll (2010).

While NaI(Tl) crystals can be machined into various shapes and sizes, they are fragile and cannot withstand major mechanical or thermal shock (Hine, 2016). This property should be considered when planning how an animal target will be positioned against it, or if the detector will be used in difficult terrain (i.e. if there is a suitable housing available). Further, as it is

hygroscopic, it requires a surrounding material to stop moisture from reaching the crystal (Knoll, 2010). While this is acceptable for the measurement of gamma rays, the low penetrability of beta rays means that these detectors are generally not suitable (depending on the casing material used) for the measurement of beta radiations of below 0.8 MeV (Hine, 2016)

Caesium Iodide (CsI) crystals, like NaI crystals, have good availability, are available in large volumes (size) and are of relatively low cost (Yoo et al., 2015a). Similar to NaI, CsI is doped with another material and is manufactured as either CsI(Na) or CsI(Tl). Both of these crystal types have very similar properties. They are more durable and malleable than NaI crystals, having a consistency more like lead (Menefee et al., 1967), and so are better suited for demanding fieldwork. Further, as they have a higher density (4.51 g/cm^3), can be made in smaller sizes to the same effect as a larger NaI detector (Knoll, 2010). Combined with a higher atomic number (Z_{eff} = 54 (Tavernier et al., 2006)), this greater density means CsI crystals have a larger gamma ray absorption coefficient and a greater photopeak ratio than NaI (Menefee et al., 1967, Knoll, 2010). This does however, make it less suitable for beta detection (Menefee et al., 1967).

While these properties give it several advantages over NaI, it nonetheless has some disadvantages. CsI(Tl) not as hygroscopic as NaI (Yang et al., 2014), but they still display some clouding at high humidity (CsI(Na) is hygroscopic). In the UK environment, the crystal would still require a casing for use outdoors. They have a variable decay time, which has some advantages (Knoll, 2010), though these times are longer than for NaI and therefore count rates are more limited. When attached to a standard PMT, both CsI(Na) and CsI(Tl) have a photon output lower than NaI (Knoll, 2010) and therefore lower resolution. CsI(Tl), however, operates outputs light in the red wavelength and if coupled to a PMT that also operates at the same wavelength can achieve significantly higher photon outputs than for NaI (up to 65,000 photons per MeV)

Lanthanum Bromide (LaBr$_3$) crystals were discovered at the start of this century, with mass availability around 2005 (Knoll, 2010). Following shortly after, **Cerium Bromide (CeBr$_3$)** properties were first described in 2005 (Shah et al., 2005). Both CeBr$_3$ and LaBr$_3$ crystals share several similar properties and, although more expensive, have several advantages over NaI detectors. Photon output is higher than for NaI and CsI; CeBr$_3$ has an output of 68,000 photons per MeV (Shah et al., 2005) and LaBr$_3$ is slightly higher at 70000 photon output per MeV

(Salacka and Bacrania, 2010). The energy resolution for these detection crystals are improved over NaI and CsI at around 3 to 4 % for 662 keV (Shah et al., 2005, Guss et al., 2009). They have a faster decay time, at approximately 20 ns, and the intrinsic efficiency and photopeak ratios for these detectors both are slightly better than for NaI (Knoll, 2010). They also have a high density at 5.2 g/cm^3 (which reduces the influence of having a lower atomic number ($Z_{eff} \approx 45$) than NaI (Tavernier et al., 2006)). While they are more hygroscopic than NaI, this only presents additional concern during the manufacturing process (Knoll, 2010).

Although LaBr$_3$ has a slight advantage over CeBr$_3$ in the properties mentioned above, its largest disadvantage is the presence of internal radiation from ^{138}La atoms within the detection material (Knoll, 2010, Nilsson et al., 2014). This causes significant problems in measurement e.g. Nilsson et al. (2014). CeBr$_3$ has the same disadvantage, though not as pronounced. This lower internal background radiation often makes CeBr$_3$ the preferred detection material out of the two crystals despite the better detection properties of LaBr$_3$ (Quarati et al., 2013, Guss et al., 2009). These crystals are, however, brittle (Quarati et al., 2013, Iyudin et al., 2013) and would therefore be unsuitable for rugged fieldwork.

Similar to LaBr$_3$ and CeBr$_3$, **Lutetium Yttrium Orthosilicate (LYSO)**, has a number of advantages (Knoll, 2010) that makes it suitable to monitoring gamma radiation (7.1 g cm^{-3} density, relatively cheap, and a similar resolution and photon per MeV output to NaI) but has a high internal background from ^{176}Lu. The crystal size of LYSO is also limited due to non-uniform light yield and self-absorption (Zhang et al., 2014) and is therefore unlikely to be suitable for the requirements of this project.

Organic scintillators that can be dissolved in a solvent can be polymerised to form a **plastic scintillator** (Knoll, 2010). This has generated a number of different types of scintillating detectors, all with their own defining features. This makes it relatively easy to match a detector type to a particular application. Unlike crystals, plastic scintillators are identified using product codes (see Table 3.2). The product code can differ depending on the manufacturer. For example, the same type of material labelled by Saint Gobain as BC-400 is labelled as NE-102A by NE and EJ-212 by Eljen. For simplicity, the materials identified in this thesis will follow the identification scheme used by Saint Gobain (Saint-Gobain, 2015).

Table 3.2: Commercially available plastic scintillators.

Production code	Light output (% anthracene)	Max emission (nm)	Decay constant (ns)	Refractive Index	Density (g/cm^3)	Typical applications
BC-400	65	423	2.4			General purpose
BC-404	68	408	1.8			Fast counting; alpha, beta
BC-408	64	425	2.1			TOF counters; large area; alpha, beta, x-rays, charged particles
BC-412	60	434	3.3			Large area; neutron, gamma, charged particles
BC-416	38	434	4			Large area economy; neutron, charged particcesl
BC-418	67	391	1.4	1.58	1.032	Ultrafast timing; small sizes
BC-420	64	391	1.5			Ultrafast timing, sheet areas
BC-422	55	370	1.4			Very fast timing; small sizes
BC-422Q	<19	<360	0.7			Ultrafast timing; ultrafast counting
BC-428	36	480	12.5			Photodiodes, CCDs; Phoswich detectors
BC-430	45	580	16.8			SiPM, red enhanced PMTs
BC-436	52	425	2.2	1.61	1.13	Thin disks; neutron
BC-440	60	434	3.3		1.03	High temperatre environments (100˚C, M versions 150˚C)
BC-444	41	428	285		1.032	Phoswich detectors; neutron
BC-448	64	425	2.1		1.03	High temperatre environments (100˚C, M versions 150˚C)
BC-452	48	424	2.1	1.58	1.05	X-ray dosimetry (<100 keV)
BC-454	48	425	2.2		1.026	Neutrons
BC-470	46	423	2.4		1.037	Dosimetry
BC-490	55	425	2.3		1.032	General purpose

The resolution of plastic scintillators (at 13%) makes it the worst of the detection materials described in this chapter (van Loef et al., 2015). Similarly, they have a low density ($\approx$1g/cm^3) and atomic number ($Z_{eff} \approx$ 4.5) (van Loef et al., 2015) compared to other detection materials. Their low density makes them better suited to alpha and beta detection rather than gamma (Knoll, 2010), especially if formed as a thin detector as this would better reject the higher energy gammas. The density can be increased by mixing in other higher density materials (a term called "loading"), though this has the effect of lowering the light output of the scintillator and is undesirable as they already have one of the lowest light outputs at approximately 10,000 photons per MeV (Knoll, 2010). Another disadvantage of plastic scintillators is the low softening point. This is generally around 70˚C though there are a couple of specialised materials (BC-440 and BC-448) that can operate in higher temperatures.

Instead, their main advantage over other detection crystals is the ease at which they can be fabricated and shaped. Shaping of the detector can help increase intrinsic efficiency in objects as it can be moulded to a particular shape (Yoo et al., 2015b). Sizes are available from small fibres to large volume detectors and they are relatively inexpensive when compared to other detector materials (Knoll, 2010). If the end user requires other materials to be embedded within the scintillation material, or if they need to be cast into unique shapes, plastic scintillator materials like BC-490 can be used. These materials are delivered partially

polymerised (Saint-Gobain, 2015) and must be hardened by the end user. With a light output of 55%, they are otherwise similar to BC-400. They also have a few other advantages. They have one of the fastest decay times at 2 ns or less (Knoll, 2010) which makes them useful for fast timing applications (e.g. positron emission tomography). Further, as they are non-hygroscopic, this makes them useful for beta and alpha detection as the material does not need any cladding that may otherwise attenuate the radiation before it is measured. For incorporation into a portable detector, the plastic scintillator would be best suited towards beta detection. Without requiring fast timing, the type of plastic scintillator for beta particles can be reduced to BC-400 or BC-430. BC-400 is a general-purpose detector and has an emission wavelength that matches most standard PMTs. BC-430, with emission wavelengths of 580 nm, would be more suited to some types of SiPMs (see section 3.5.2.2).

High Purity Germanium (HPGe) semiconductor detectors were first developed in the 1970s (Knoll, 2010). Due to their high resolution (approximately 1%) they are routinely used in the cases of radionuclide measurement in a wide range of sample types (IAEA, 2011). They have decay times of only a few hundred nanoseconds (Knoll, 2010). Despite having a high density (5.33 g/cm^3), they have a low atomic number (Z = 32) compared to NaI (Z_{eff} = 50) and small crystal volumes (Tavernier et al., 2006, Knoll, 2010). This means that the intrinsic efficiency of HPGe is lower than for NaI. The high resolution of HPGe, however, offsets this disadvantage as is more capable of resolving radionuclides with similar decay energies and detecting weak sources of radiation from background radiation (see chapter 2.5). These properties make HPGe the superior choice for measurements where there is a large radionuclide mix, especially in cases where characteristic decay energies are similar.

While these properties make HPGe the preferred choice in many applications (Khandaker, 2011), they are of relatively high cost (see Table 3.6) and have the limitation of needing to be cooled to liquid nitrogen temperatures to operate (Knoll, 2010). Earlier germanium detectors (e.g. GeLi) required cooling to liquid nitrogen temperatures at all times. Fortunately, the introduction of HPGe meant that the new crystals can be stored at room temperature. Storage at room temperature, however, means that there is a long start-up time (often 4 to 12 hours, see Table 3.6) before the detectors are cool enough to be used. For use of these detectors in portable field applications, advance planning is essential.

Cooling for HPGe detectors was initially only conducted using liquid nitrogen. The use of liquid nitrogen means that portability (i.e. operational range and time usage) is limited (Nilsson et

al., 2014) and also creates safety concerns over the correct transportation and handling of the coolant (Upp et al., 2005). Stirling cycle coolers later became available as an electro-mechanical alternative to liquid nitrogen (Knoll, 2010). Through continued research and development, these detectors have become more portable in size as well as more efficient (Koike et al., 2015). These are now commonly seen in portable HPGe solutions (e.g. CANBERRA Industries Inc., 2015, ORTEC, 2015) though still require a number of hours to cool to an operable level and have limited operational time dependant on a replaceable battery.

While HPGe detectors have the benefit of not requiring a PMT, the addition of a cooling mechanism, such as a liquid nitrogen Dewar, means that these semiconductor detectors are generally heavier than standard scintillators (Nilsson et al., 2014)(also see Table 3.5 and Table 3.6). Having a higher resolution makes HPGe a suitable choice if measuring multiple radionuclides that have decay energies likely to overlap at lower resolutions. When considering the cost and cooling requirements, however, HPGe detectors are best to be only used where the added resolution is required. Several authors have already stressed that the higher specifications do not always make the use of HPGe justifiable (e.g. weight of cooling system for the detection system used by Kock et al. (2014)).

Cadmium zinc telluride (CZT) is a room temperature semiconductor that offers similar specifications to HPGe. It has a higher density (6 g/cm^3) and atomic number (Z_{eff} = 48) than HPGe, which makes CZT a more efficient detection material (Tavernier et al., 2006, Burger et al., 2005). CZT offers the highest resolution for a room temperature material and has decay times of only a few hundred nanoseconds (Knoll, 2010). As no PMT or cooling system is required, it results in smaller and lighter detectors than for HPGe (Burger et al., 2005). The size of a CZT crystal, however, is currently limited to around 1 cm^3 due to manufacturing defects that occur beyond this size. This, along with a small suitable yield, make the manufacturing costs of the CZT crystal relatively more expensive than for other commercially available detection materials (Yang et al., 2013). Further, the small crystal size makes it inefficient for gamma detection; measurement is best at low energies as at higher energies peaks are poorly resolved. Small crystal sizes, poor efficiency, and high cost (Bolotnikov et al., 2015), means CZT is limited in its applications.

There are a number of criteria to consider in assessing which of the above available materials are most suitable for use in a portable radiation detector. Besides requiring a good signal output and low intrinsic background, a portable radiation detector (for field use in potentially

difficult terrain) needs to be robust to mechanical shock damage and have a low weight and size (including extra requirements such as cooling) for transportability. A good resolution is also desired but may not be essential depending on the application. A summary of the above discussed detection materials is presented in Table 3.3.

In comparing the materials, Table 3.3 suggests the most suitable material for a portable detector is likely CsI for gamma detection and a plastic scintillator for beta detection. CsI is a good selection for gamma detection due to its cost to performance ratio and the robust mechanical properties of the material make it suitable for rugged fieldwork. The plastic scintillator is a good selection for beta detection due to its low density and malleability. This means it can be shaped into a thinner detector to reduce detection from higher energy gamma. Having good mechanical properties also means the thinner detector would be more robust for beta detection than an equivalent thin NaI detector.

Table 3.3: Comparison of materials from readily available portable detectors.

Material	Resolution	Density $^{\#}$	Signal output	Cost	Advantages	Disadvantages
NaI	2	3	3	5	Cost and availability	Hygroscopic / brittle
CsI	2	4	5*	5	Malleable	Slightly hygroscopic
CeBr$_3$	3	4	5	4	Good resolution for cost	Internal radiation / hygroscopic / brittle
LaBr$_3$	3	4	5	4	Good resolution for cost	Internal radiation / hygroscopic / brittle
LYSO	2	5	3	5	High density	Internal radiation / self-absorption /non-uniform light yield
Plastic	1	1	1	5	Low density (for gamma rejection in beta detection) / malleable	Low density (for gamma)
HPGe	5	4	2	1	High resolution	Cooling
CZT	5	5	1	1	High density / High resolution	Poor detection >1MeV / Small volume

Properties are ranked from 1 to 5 (5 being superior) to indicate relative performance. * - depends on type of PMT used. $^{\#}$ - rank depends on application, e.g. lower density would be advantageous for beta or alpha detection.

3.5.2 Light collection for scintillators

Radiation interacting with a detection material needs to be converted into an electrical signal in order for a detection to be measured or recorded (Knoll, 2010). Gas and solid state detectors both produce an electrical signal directly from a radiation interaction. Radiation interactions within a scintillating material, on the other hand, must be converted to an electrical pulse through collection, and amplification, of the fluorescence produced within the detection material. Two main technologies are available for the collection of this fluorescence; the standard photomultiplier tube (PMT) and the silicone photomultiplier (SiPM). Advancements in these technologies, along with different manufacturing methods and a combination of the two technologies, means there are several different methods that can be chosen from; the selection of which can have considerable implications to the design of a portable detector. The following section discusses and compares the choices available should a scintillation material be desired for radiation detection. The last subsection demonstrates how these photon collectors are optimally joined to the detection crystal.

3.5.2.1 Photomultiplier tube (PMT)

The **photomultiplier tube** for scintillation counting was developed during the 1940s (Morton, 1975) and, despite the introduction of newer methods, it remains the most widely used device for detecting photon emission (Knoll, 2010). There are many different types of PMTs available that vary in the design of their tube and the materials used for photomultiplication (Knoll, 2010). The standard type of PMT, for use in radiation detection, normally utilises a box-and-grid-type electron multiplier in a head-on arrangement fitted into a cylindrical tube (Knoll, 2010, Hamamatsu Photonics K.K., 2016); essentially the photosensitive surface is at the end of the cylinder. The most common materials used in these PMTs are a bialkali photocathode with a borosilicate glass window; these materials make the PMT more efficient in the blue wavelength (420 nm), which matches the emission from most scintillators. PMTs used in previous and existing animal monitoring studies were of this type (see Table 3.1) and are recommended for radiation detection in field surveys (e.g. Hamamatsu Photonics K.K., 2016). The quantum efficiency (photoelectrons emitted per incident photon) of these PMTs are commonly quoted as between 20 to 30 % (Knoll, 2010) though, depending on the types used, can be up to 45%. A look at available PMTs (e.g. Hamamatsu and Photonis) shows these are (at the time of writing) typically around 30% quantum efficiency. The nature of PMT, however, means it is susceptible to magnetic fields (Knoll, 2010). They therefore need to be magnetically

shielded, though this is usually included within the PMT unit. They are also susceptible to mechanical shock and if the tube is cracked then the vacuum inside is lost. As already shown, however, they are commonly used for portable detectors and therefore, if they do not experience any undue rough handling, they are still usable within a portable detection system.

There are two main limiting factors for the application of PMTs into a portable system. While most portable detectors use PMTs, they constitute a large proportion of the overall detector size (see examples in section 3.5.5). In instances where the detection system would be required to be shielded (as would be wanted for a live-monitor), the use of a PMT could increase the shielding weight requirements considerably as opposed to some of the other options that will be later discussed. This makes it a limiting factor in the operational rage of the detector. The other main limiting factor of the PMT is the high voltage power supply requirement. The PMT requires a high voltage to be placed across the anode and cathode in order to facilitate the acceleration of electrons at each multiplication stage. The requirement of this type of power supply means it impacts the operational time of the detector. Including a larger battery, or using removable backup batteries, further would increase the weight of the detector. A rechargeable system could be used but this means shorter, more frequent trips to allow for recharging if required.

There are other types of PMTs that have different shapes to match different applications. A good description of the various types is given in Knoll (2010). Smaller tube designs are available with diameters as little as 10 mm (e.g. Hamamatsu Photonics K.K., 2016) and lengths of approximately 100 mm. These are much smaller than those used for the studies in Table 3.1 though the smaller tube size does result in a smaller active area for measurement. The smallest available PMT is the Micro PMT from Hamamatsu. This is a multialkali PMT with a size of 21 x 19 x 7 mm (not including a similarly sized voltage divider unit). They are, however, not designed for coupling with scintillators and in addition the small active area size and the higher cost makes it not as cost effective as a standard PMT. Another small PMT type is the MCP-PMT. This uses a microchannel plate, consisting of a cluster of many thousands of tubes a few 10s of um each in diameter. While this device has a faster response time than standard PMTs, it nevertheless has a weaker output, is easier to damage and is more expensive (Knoll, 2010).

3.5.2.2 Silicone photomultiplier (SiPM)

The development of the **silicone photomultiplier** (Renker and Lorenz, 2009) has made photodiode technology useful for incorporation in many applications such as in medical

imaging devices (Sul et al., 2015) and spaced based detectors (e.g. Kryemadhi et al., 2017). The semiconductor properties of the photodiode mean the SiPM has a number of advantages over the PMT. They have a lower power consumption (no high voltage supply is required but gives a similar level of gain as for PMTs), compact size, are insensitive to magnetic fields, and typically have a high efficiency (photon detection efficiency (PDE) is usually used as the main measure due to the influence of avalanche probability and active surface area, known as fill factor) than for a PMT (Turchetta, 2016). These properties make it appealing for use in portable systems. Examples of available SiPMs are listed in Table 3.4.

Because the PMT is often the largest component of a portable scintillation detector (Knoll, 2010), the small footprint of a SiPM (and lower power requirements) is beneficial in reducing the overall size of a detection system. Further, for portable detectors that require shielding against the background radiation, the small size of the SiPM reduces the surface area of the detector that needs to be shielded. This could significantly reduce the weight of the portable system (depending on the design of the detector). Their small size also means they can be embedded directly into the detection crystal. The benefit of this is it would maximise light collection as it removes light loss that would otherwise be introduced through coupling with the detection material (see section 3.5.2.4). The drawback of this is it becomes a permanent feature of the detection crystal; the entire crystal would have to be replaced if the SiPM needed to be relocated or exchanged.

While the SiPM has a number of advantages over the PMT it nevertheless still has a number of disadvantages. These lay primarily in noise introduced to the system and constitutes a complex combination of scintillation, thermal, afterpulse (a random photodiode discharge shortly after a previous discharge), and crosstalk (electrons produced in one photodiode crossing into another photodiode) events (Knoll, 2010, Turchetta, 2016). The size of the SiPM and the size of each microcell (also the ratio of the active to non-active cell area; the fill factor) affects PDE and the amount of noise present. Generally, the larger the SiPM or microcell, the greater the PDE and gain but also the higher the noise. A main limiting factor in their use is the number of microcells available for detection (Renker and Lorenz, 2009); the unit can quickly saturate in the event of high count rates and therefore the types and numbers of SiPMs to use must be carefully selected. Further, while not necessarily a disadvantage, attention should be paid to the choice of detection material the SiPM is coupled to. This is because some

Table 3.4: Comparison of commercially available SiPMs

Manufacturer	Series	Product-Code	Active Area [mm²]	Microcell Size [µm]	No. of Microcells	Fill Factor (%)	Packaging	Package Dimensions [mm³]	Wavelength (nm)	5V overvoltage PDE (%)	5V Dark count rate (kHz/mm²)	5V Crosstalk (%)	5V Afterpulse (%)	5V Gain (x10⁶)	2.5V overvoltage PDE (%)	2.5V Dark count rate (kHz/mm²)	2.5V Crosstalk (%)	2.5V Afterpulse (%)	2.5V Gain (x10⁶)	Terminal capacitance (pF)	Recovery time (ns)	Rise time (ns)	Cost**
Ketek	EB	PM1125-EB	1.2	25	2304		SMD	2.45 x 1.95 x 1.45	430	30	210	16		1.5	19	100	6		0.7	110	43	0.5	50.46
		PM1150-EB	1.2	50	576					38	540	27	3	7.6	28	280	9	1	3.8	140	146	1	
		PM3325-EB	3	25	13408		SMD	3.50 x 3.50 x 1.45		34	500	30		1.7	26	250	10		0.9	790	35		53.94
		PM3350-EB	3	50	3472					38		25		7.2	28				3.6	810	130	1	83.52
		PM6625-EB	6	25	55168		SMD	6.50 x 6.50 x 1.45		34		35		1.7	26		16		0.9	2800	40		
		PM6650-EB	6	50	14272					38		35		7.2	28				3.6	3100	70		
	WB	PM3315-WB	3	15	38800		BGA	3.315 x 3.315 x 0.595	430	31	100	20	1	0.6	22	50	7	1	0.3	750	13	1	53.94
		PM3325-WB	3	25	13920					43		35		1.74	31		15		0.87	800	40		
Sensl	C	MicroFC-10010-SMT	1	10	2880	28	MLP	1.5 x 1.8	420	18					14	30	0.6	0.2	0.2	50	5	0.3	
		MicroFC-10020-SMT	1	20	1296	48				31					24		3		1	90	20		39.27
		MicroFC-10035-SMT	1	35	504	64				41					31		7	0.2	3	100	82		
		MicroFC-10050-SMT	1	50	282	72				47					35		10	0.6	6	110	159		
		MicroFC-30020-SMT	3	20	10998	48		4 x 4		31					24	30	3	0.2	1	770	23	0.6	
		MicroFC-30035-SMT	3	35	4774	64				41					31		7	0.2	3	850	82		51.59
		MicroFC-30050-SMT	3	50	2668	72				47					35		10	0.6	6	920	159		
		MicroFC-60035-SMT	6	35	18980	64		7 x 7		41					31	30*	7	0.2	3	3400	995	1	91.63
	J	MicroFJ-30020-TSV	3	20	14850	62	TSV	3.16 x 3.16	420	42	80	10	1	1.7	31	45	5	0.1	0.91	TBD	12	0.1	62.37
		MicroFJ-30035-TSV	3	35	5676	75				51		22		5.3	38		7		2.8	1000	37	0.3	
		MicroFJ-60035-TSV	6	35	22292	75		6.13 x 6.13												4000	48		100.87
	R	MicroFR-10010-MLP	1	10	4296	43	MLP	1.5 x 1.8	635	30	70	1		0.48						1	10	0.3	
		MicroFR-10020-MLP	1	20	1590	63				39				2					0.7		16		
		MicroFR-10035-MLP	1	35	620	76				47				6							49		60.06
Hamamatsu	S13360	S13360-1325PE	1.3	25	2668	47	SMT	2.63 x 2.1	450	25	41*	1		0.7									
		S13360-1350PE	1.3	50	667	74									40	53*	3		1.7	60			
		S13360-1375PE	1.3	75	285	82									50		7		4				
		S13360-3025PE	3	25	14400	47	SMT	4.35 x 3.85		25	44*	1		0.7									
		S13360-3050PE	3	50	3600	74									40	56*	3		1.7	320			
		S13360-3075PE	3	75	1600	82									50		7		4				
		S13360-6025PE	6	25	57600	47	SMT	7.35 x 6.85		25	44*	1		0.7									
		S13360-6050PE	6	50	14400	74									40	56*	3		1.7	1280			
		S13360-6075PE	6	75	6400	82									50		7		4				
	S13360	S13360-2050VE	2	50	1584		SMT	2.4 x 2.4	450	40	75*									140			
		S13360-3050VE	3	50	3584	74		3.4 x 3.0		50	56*			1.7						320			
		S13360-6050VE	6	50	14336			6.4 x 6.4			56*									1300			
	S1257X	S12571-010P	1	10	10000	33	SMT	2.4 x 1.9	470	10	100			0.135	10					35			
		S12571-015P	1	15	4489	53			460	25				0.23	25								
		S12572-010P	3	10	90000	33	SMT	4.35 x 3.85	470	10	110*			0.135	10					320			
		S12572-015P	3	15	40000	53			460	25				0.23	25								

Sensl and Hamamatsu PDE does not include crosstalk or afterpulse. Hamamatsu overvoltage is set at 4 to 4.5 volts and 3 volts instead of 5 and 2.5 volts respectively. Hamatsu has a second ceramic packaging (larger dimensions than for standard SMT) for all listed MPPC units. *Dark cout recalculated to provide measurement per mm² **A conversion rate of 0.87 was used for Euro to GBP and 0.77 for Dollar to GBP

photodiodes operate in the red wavelength (580 nm) and are therefore better suited to scintillating materials that similarly operate in this region (Knoll, 2010). For example, when coupled with CsI(Tl) the pulse amplitude is typically double that of NaI(Tl) whereas it is typically half when using a standard PMT.

These noise disadvantages mean there are still numerous technological hurdles to overcome. Advances in the manufacturing processes and the packaging options, however, are continually reducing the effect of some of this. SiPMs are currently packaged in three different ways: PEP, MLP, and TSV (Turchetta, 2016). **Poured epoxy packages (PEP)** consist of individual photodiodes joined together in an array using a wire bond. This arrangement is placed onto a ceramic or PCB board and is coated in epoxy for protection. While this is the cheapest construction, it nevertheless has a number of significant disadvantages. The epoxy coating is usually inconsistent in quality and uniformity and therefore means the optical transmission and overall PDE is poor. The materials and build method also means the service life is short compared to the other two methods. A more commonly used construct is the **clear micro leadframe package (MLP)** (or SMT). This involves attaching each photodiode to a large lead frame and covering with a clear compound. This is then cut to size, with typical sizes being 1x1, 3x3 and 6x6 mm^2. Unlike the previous construction method, the process can be automated and therefore fabricated in a larger, more consistent, size. The automated process gives the MLP overall better properties than the PEP. A final construction type is **through-silicon via (TSV)**. Here, photodiodes are left on their production wafer, whereupon a glass substrate is bonded on top of the wafer and the back of the silicon is ground to a thin layer. Gaps are etched into the silicon and metal contacts are inserted before the wafer is cut to size. This process creates the highest specifications out of the three processes due to the use of glass; allowing for better light transmission and removing the failure points that are caused by using epoxy. This increase in specification does, however, come at a higher production cost.

There are currently three main manufacturers for SiPM technology; Hamamatsu (www.hamamatsu.com), Ketek (www.ketek.net), and Sensl (sensl.com). Table 3.4 shows the types of SiPMs available from these companies. Hamamatsu, using the term MPPC, offer four different types of MLP SiPMs (referred to as SMT types on the table) with packaging options for epoxy or silicone resin window materials. Ketek offer two types of MLP (referred to as SMD or BGA types on the table). Sensl provide three series of SiPM: one TSV type and two of MLP (both operating in different peak wavelengths). These three companies have options for SiPMs

to be mounted onto a pin board (easy access to anode and cathode) or onto an evaluation PCB that contains all of the necessary electronics (apart from the display). The dimensions and construct of these evaluation PCBs mean they would not be recommended for incorporation into a portable detector because they limit the design options for the detector and only allow for one SiPM per board to be used. Hamamatsu have ceramic mounted options, but this results in a SiPM unit with a large bezel around the chip. This is not necessarily a drawback unless mounting to the edge of a thin scintillator or requiring more than one fitted in a small space (i.e. in an array). If an array is required, then it would be recommended to instead make use of the custom design array options that Ketek and Sensl provide.

At the time of writing, the cost per unit is *c.*£40 to £100; the TSV option is of the highest cost (see Table 3.4). For small sized detection crystals, the SiPM offers a lower cost solution than for PMT. If using a detection crystal much larger than the size of a single SiPM, then the use of multiple SiPMs becomes necessary and costs could therefore rapidly exceed the cost of the PMT solution. If the SIPM is opted for, instead of the PMT, then the 3 mm appears to have the best trade-off, between cost, PDE and noise if using either a cell size of 50 µm for Ketek or the 20 or 35 µm for the Sensl. Turchetta (2016) recommends the 30035 SiPM as having the best combination of low crosstalk and high PDE. These recommendations, however, will depend entirely on the purpose of the detector.

3.5.2.3   Hybrid Photomultiplier Tube (HPMT)

Hybrid Photomultiplier Tubes (HPMT) combine the properties of a PMT with those of a photodiode (Knoll, 2010). Incident photons are converted to electrons by use of a photocathode whereupon a large voltage bias accelerates the electrons through a vacuum and into a silicone photodiode. The combination of these technologies makes for a detector with a size in between that of a PMT and SiPM. The main advantage in the use of a HPMT is their lower anode capacity and therefore they are better able to discriminate between individual photon interactions than for PMTs or Silicon photodiodes (D'Ambrosio and Leutz, 2003). They are, however, more susceptible to backscattering than the other technologies. Further, they have a lower gain, compared to PMTs, and a poorer energy resolution for larger scintillators (>10mm) (Moszyński et al., 2006). Newer variants of HPMTs are under development such as the incorporation of SiPMs in place of APDs (Russo et al., 2010), but are not at this time commercially available.

3.5.2.4 Coupling and Coatings

For a detection to be recorded, the light exiting the scintillator material needs to enter one of the light detection technologies described above. It is desired, therefore, to reduce the light loss from the sides of the detection material and couple the light collector in such a way as to maximise the light entering the light collector (Knoll, 2010). There are several materials (or components) that can be used to accomplish all this. To assist with describing these, examples are provided for each type of coupling and coating. As Saint Gobain (Saint-Gobain, 2015) provides a full range of what is discussed here, these materials are describe in terms of the codes used by this company to facilitate easy look up (and to match the product codes used in the description of plastic scintillators).

The use of a light guide can help focus the light down to the particular point where the light collector is connected. In some circumstances (e.g. Cherenkov counting) it is beneficial to shift the wavelength of a scintillating material to a longer wavelength so the photons can be more optimally counted. BC-480, BC-482A and BC-484 are bars that can be applied to a particular scintillating material for this purpose.

The scintillation material and the light collector, along with any light guides, all need to be coupled to the scintillator in such a way so as to minimise any light loss or reduction in quality. There are four methods for this. An optical cement (e.g. BC-600), which is a clear epoxy resin, is often used for interfacing the scintillator to a light guide. This material, however, is not recommended for interfacing with the photon collector. For this application either an optical grease (e.g. BC-630), interface (e.g. BC-634A) or coupling (e.g. BC-637) is recommended. BC-630 and BC-637 are both silicon based and permanent. BC-630 is a compound that dries on the interface whereas BC-637 is an adhesive pad that sticks between surfaces. The final material, BC-634A, is a flexible optical disk. It benefits from being non-permanent and therefore can be reapplied to other scintillators or photon collection devices. It does, however, only come in thicknesses of 3 or 6 mm which would require factoring into a design.

Light loss from the scintillator can be reduced by covering it in a reflective material. This can be thin aluminium, though often comes in the form of a tape (e.g. BC-642) or a paint (e.g. BC-620) which are designed to maximise reflectivity and assist in ensuring there are no gaps in the covering. The BC-642 tape is constructed from Teflon (density 2.2 g cm^{-3}) and is 0.08 mm thick. For this particular product, the Saint Gobain website (Saint-Gobain, 2015) recommends three layers of tape for optimum reflectivity. This thickness will need to be considered for the

measurement of beta radiation as it could introduce an attenuation factor greater than for a thin sheet of aluminium. The BC-620 is a reflective paint made using titanium dioxide. It can be applied directly to plastic scintillators, glass, acrylic, and metals. The recommendation from the manufacturer is to only use with scintillators with an emission of 400 nm and to not apply to large area sheets. Because the use of a portable detector in the field would expose it to potentially excessive wear, the paint option may not be appropriate if the detection material is not secured within the detector.

3.5.3 Processing electronics

The electrical signal from the detection material (or light collector) is typically too small to be directly analysed and is therefore amplified and shaped into a usable signal for processing. For the purposes of this project a detailed description of how the signal is amplified and shaped is not required; Knoll (2010) adequately details this information. Instead, the type of unit for processing this signal is important to consider as are the general specifications in terms of field use.

Processing units can be categorised into two types (Knoll, 2010); a single channel analyser (SCA) and a multichannel analyser (MCA). A SCA will discriminate the input signal to identify peak energies between two defined thresholds. This produces a single count for the selected energy range. A MCA is more complex. It measures the counts for a series of selected threshold pairs (in effect a series of SCAs) and produces a histogram of the accumulated counts over a select energy range (see Figure 2.2 for an example). The more channels a MCA has, the more detailed the produced histogram will be. The choice of unit depends on the application. An SCA is more appropriate to use if only a single decay peak needs to be measured. If multiple radionuclides need to be identified and quantified (i.e. more decay peaks) then a MCA needs to be used. A MCA will, however, generally cost more than an SCA due to its complexity.

Another important consideration in selecting either a SCA or a MCA (besides cost) is its suitability for fieldwork. Any unit selected would need to be constructed to withstand a certain degree of mechanical shock and to also be waterproof. Further, for remote fieldwork, it should have a suitable power supply such that the entire system can be powered for the duration of the fieldwork, e.g. a high storage battery or a way to replace or recharge the battery. Portable detector systems containing these elements are already available (see section 3.5.5 for examples) with either a MCA or SCA included. For construction of a new detector (or selection

of suitable components) there are separate processing units available, e.g. digiDART (www.ortec-online.com), InSpector™ 1000 (www.canberra.com), Model 970-X (www.berkeleynucleonics.com) URSA-II (www.laurussystems.com). If appropriate input electronics can be found then a laptop computer or tablet can also be utilised e.g. MAESTRO (www.ortec-online.com). All of these examples, however, only have single inputs and are therefore inconvenient if multiple detection crystals are needed; either multiple processing units will be needed or the sample will need to be re-counted with each detection material. For construction of a portable detector that includes multiple detection crystals, a unit similar to the RMS30 from JCS could instead be employed as it allows the input of two signals. If more inputs are required then the construction of one's own MCA is possible; a number of open source projects detail how to do so (e.g. http://www.theremino.com).

3.5.4 Shielding

Shielding is incorporated into a detection system as a means to remove, or at least reduce, any background radiation that would otherwise interfere with detection from a sample (Knoll, 2010) (see also section 2.4.1 for examples of background radiation). The shield can be any material that can attenuate the incident radiation (attenuation is described in chapter 2.1). Because attenuation occurs due to interactions of the incident radiation with atoms inside the material, the effectiveness of the shielding can be increased by either increasing the thickness of the material or by using a material of a higher density and atomic number. The allowable amount shielding in a portable detector is, however, typically restricted by weight. A thinner shield would also be preferred as a bulky detector could be more difficult to transport if there are space limitations. Therefore, a higher density material would be more suitable.

Because the weight is restricted, the larger the surface area that is required to be shielded (i.e. the detector and organism) the thinner, and hence less effective, the shield will be. In the examples of the large animal monitoring described in section 3.4, the body of the organism itself provided some level of shielding against background radiation. A layer of lead around the rest of the detector provided the remainder for the shielding. For smaller animals, or for deployment in high radiation environments (e.g. Chernobyl), the shield would need to cover either the entire animal or a portion that would suitably reduce the background level. Any gaps or cracks would reduce the effectiveness of the shield.

There are several different materials that are commonly used for the construction of a radiation shield: concrete, lead, steel, and tungsten (Knoll, 2010). The most common shielding

material is lead (most of the portable detectors in section 3.4 use lead). Its high density, large atomic number and malleability make it a suitable material for shielding against radiation. It can be easily shaped around a radiation detector and the density means it generally has a smaller volume than other solutions. Higher density materials such as tungsten can be employed in instances where space is an issue though these are more expensive (a search of material costs shows tungsten is approximately thirty times more than the price of lead per kg). If a large shield is required then steel can also be used, either by itself or in combination with lead, as a way to reduce costs. For larger installations, concrete is commonly used because it is a cheap material that can be easily constructed around the radiation detector. Because of its low density, however, large volumes of concrete are required to effectively shield against gamma radiation. The volumes required therefore mean this material is not suitable for a portable detector. A possible alternative to these materials is the use of water (Kodaira et al., 2014). Its fluidity means it can be easily deployed around a complicated shape (in a container) and, because water could be sourced locally, it would allow for easier transportation of the detector. The disadvantage of this is a large volume of water would be required to provide an effective level of shielding. Further, for use in contaminated areas, the water would need to be sourced from outside of the measurement location and therefore reintroduce the transportation problems. Out of the shielding materials described, the most suitable would be lead due to its good balance between low cost, high density and ease of shaping around a detector.

All of these shielding materials have some form of intrinsic radiation (Sonkawade et al., 2008). This radiation comes from primordial radionuclides or nuclear fallout during the processing stage of the material. Some materials further contain isotopes of the atoms it is made up of, e.g. lead has ^{210}Pb (though low level), and therefore the selection of shielding material may need to consider the radionuclides that will be monitored. In most cases, however, this intrinsic radiation is accounted for by taking measurements of the background count rate.

Other ways of shielding against background radiation include active methods (Knoll, 2010). These methods do not aim to attenuate the external radiation but instead use techniques to selectively remove unwanted detection. Anticoincidence shielding uses an arrangement of two detector systems where a detection is only confirmed when an interaction occurs in one material and not the other. This is often used in reducing the cosmic component of the background but would also be useful for a beta detector as it can be used to selectively remove

any higher energy gammas. It would, however, mean including additional detection materials into the system that would require additional shielding as well as increase the processing requirements. Another method, coincidence shielding, can be applied when a target radionuclide emits two detectable emissions at the same time (e.g. a gamma and beta emission). This method works by selectively removing any single counts that occur within the detector material. Even if the target radionuclide had two such decays, the detector would need to surround the entire organism because the emissions could be in any direction from the decaying radionuclide. The shielding required to achieve this would therefore make this method unsuitable for incorporation into a portable live-monitor.

3.5.5   Currently available detection systems

3.5.5.1   Portable gamma detectors

The availability of higher resolution detector material technology, such as Cadmium Zinc Telluride (CZT) and High Purity Germanium (HPGe) (Knoll, 2010), mean there are more technological possibilities for the detection of radionuclides within organisms than what were available during the early live-monitoring described in Table 3.1. Portable detector systems are already available using these detection materials; Table 3.5 and Table 3.6 detail (as of 2016) the specifications for a range of portable radiation detectors that use scintillator and solid-state materials. The information displayed in these tables is freely available from the respective company websites though the price range given for the detectors is provided as an indication only, as these can change over time, and several companies did not disclose their price ranges. The selection of which portable detector to use for an application depends on a range of criteria; the target radionuclide(s), emission energy, and cost of the detector are all important factors as well as the portability of such a detection system; power requirements, dimensions, and weight all restrict the portability of a detector. The operating temperature of the detector can further restrict the locations (or time of year) where it can be deployed.

Of the detectors listed, scintillators were mainly comprised of Sodium Iodide (NaI), though a few Lanthanum Bromide (LaBr$_3$), Cerium Bromide (CeBr$_3$), and a couple of Caesium Iodide (CsI) detectors were available. The semiconductor detectors were an even mix of Cadmium Zinc Telluride (CZT) and High Purity Germanium (HPGe). Generally, fully inclusive portable detectors are available from *c.*£3,500 to £90,000. NaI detectors are currently available for between *c.*£7000 to £20,000. LaBr$_3$ and CeBr$_3$ detectors are a slightly higher cost at between *c.*£19,000 to £24,500. All of these detectors have detector crystals ranging from 25 x 34 mm

to 76 x 76 mm. Two smaller CsI detectors (scintillators size 18 x 18 mm and 13 x 44 mm) are the lowest cost detectors at between *c.*£3,500 to £4,500. HPGe detection materials averaged 64 x 64 mm in size though these detection systems are the most expensive with costs ranging between *c.*£27,000 for the liquid nitrogen cooled detectors, and up to *c.*£90,000 for the electrically cooled detectors. CZT detectors are the smallest with detection crystals each being around 10 mm^3 in size. These cost approximately *c.*£10,000 (though up to eight crystals are included in some of the detectors).

All the detectors are limited by the range of decay energies that they can detect (also by energy resolution). The lower energy varies from between 10 keV to 90 keV for scintillators, though most are 20 keV. The semiconductors are between 20 keV to 60 keV with most being 30 keV. For most radionuclides, these average lower energy limits allow for detection. The choice of detector (i.e. high or low resolution), however, will depend on the requirement for the detection of radionuclides with low decay energies; such as the gamma emitter ^{241}Am where a high resolution detector is needed to extract the decay peak (though specialised detectors such as the one described by Clark et al. (2011) are often preferred for these instead). For the upper energy limit, the majority of detectors can detect up to 3 MeV. There are a few that have only a maximum energy of 2 MeV, and one at 1.5 MeV. It is not stated if this maximum energy is a hardware limitation or a software limitation (e.g. detector is advertised towards a specific use i.e. lower energy natural background radiation).

For the majority of key environmental radionuclides (see Appendix 10.1), their decay energies are within the 2 MeV detection limit. At 1.25 MeV, detection of radionuclides such as ^{60}Co (main decay energies at 1.17 and 1.33 MeV) would be hindered. What could instead limit the choice of detector is the identification capabilities. All of these detectors use a MCA though there are five detectors (SpiR-ID, SPIR-PACK, Radeagle, RT-30, and RS-220 Super-IDENT) that are limited in their identification of radionuclides from a software viewpoint. Three of these (SpiR-ID, SPIR-PACK, and Radeagle) are limited in the number of radionuclides they can detect at any one time (four radionuclides for one and eight radionuclides for the other two). Two further detectors are limited in the default identification library. Whilst some important radionuclides such as ^{137}Cs are included, others, such as ^{134}Cs, are not in the included database. It is not stated if further radionuclides can be added by the user.

Table 3.5: Portable detector based on scintillator crystals.

Company	Model	Relative cost	Detector Crystal	Crystal Size (mm)	Energy range (keV) Min	Max	Energy resolution (FWHM at 662 keV)	Operating time (hours - single battery)	Battery type (if present)	Charging time (hours - if stated)	Dimensions (cm) Length	Height	Width	Weight (kg)	Operating temperature (°C) Max	Min
amptek	GAMMA-RAD5	ND	NaI	76 x 76	10	3000	<7 %	USB		N/A	31.5	9.2	9.2	3.6	-25	65
atomtex	AT6101			38 x 38			≤7.5 %	12			32	6.2	6.20	1.2		
	AT6101B			64 x 64			≤8 %				35	7.8	7.8	1.9		
	AT6102A	*****(+)	NaI	38 x 38	20	3000	≤7.5 %	25		ND	23	11.5	17.7	1.9	-20	50
	AT6102B			38 x 76			≤8 %							2.15		
	AT1321			25 x 38			≤8 %	14			14.5	10	0.5	0.7		
	AT6101C			64 x 64			≤7.5 %	12			45	33	25	7		
BNC	SAM945	****	NaI	38 x 51	20	3000	ND	8		ND	25.4	12.7	15.2	2.7	-20	50
		****	LaBr₃		ND	ND		ND						ND	ND	ND
		***	CeBr₃													
Canberra	Inspector 1000	ND	NaI	38 x 38 to 76 x 76	50	3000	ND	9		3	19	16.5	6.4	2.4	-10	50
			LaBr₃	38 x 38	30	ND										
Flir	identiFINDER R200	*****	CsI	18 x 18	25		≤7.5 %	36 + 18		6	14.5	5.6	4.8	0.4		50
	identiFINDER R400	****	NaI	36 x 51		3000	≤8 %				24.8 / 27	9.3 / 9.4	7.5 / 8.2	1.1 to 1.4	-20	
	radHUNTER/R500	***	NaI	102 x 19	20	3000	8 %	8		4	12.9	21.2	32.3	2.9		55
			LaBr₃	38 x 38			3.5 %							2.5		
johncaunt	GMS310	ND	NaI	51 x 51	90	2100	ND	ND	2 x C	N/A	50	15	9	1.9	-10	40
	GMS311										33					
Mirion	SpiR-ID#	ND	NaI	76 x 38	25			10		ND	32	14.5	17.5	4.9	-20	50
			LaBr₃	38 x 38										4		
	SPIR-Ace	ND	NaI	35 x 51	20	3000	ND	8		4	20.6	15.3	5.7	1.4		
			LaBr₃	25 x 34												
	SPIR-Pack#		NaI	76 x 76	25			14		ND	45	33	25	6.8	-20	40
Ortec	Radeagle#	***(+)	NaI	76 x 25	11	3000	≤7.2 %	8	AA	N/A	24.8	11.5	15.2	2.5	-20	50
			CeBr₃	51 x 25 to 75 x 21	ND	ND	≤4 %							2.4		
			LaBr₃	38 x 25 to 50 x 25			≤3 %							2.2		
Pico Envirotec	PGIS-2	ND	NaI	ND	ND	ND	ND	ND	ND	ND	ND	ND	ND	5 to 12	ND	ND
Pycko	RT-30&	*****	NaI	51 x 51	20	3000	ND	8	4xAA	N/A	25.9	8.1	9.6	2	-20	50
radcommsystems	SYCLONE	****	NaI	38 x 51	20	3000	8 %	8		ND	18	21	10	1.6	-20	60
	RC2PLUS	****	Plastic	102 x 76 x 51	30	2000	ND	20		2.5				1.5		
	MSpec	*****	CsI	13 x 44	20	3000	9 %	10		4.5	12.1	6.4	3.1	0.2	-10	45
radiationsolutions	RS-220 Super-IDENT&	ND	NaI	51 x 51	30	3000	ND	8	4xAA		25.9	8.1	9.6	2.2	-20	50
Thermoscientific	RIIDEye M-G	*****	NaI	51 x 51	20	3000	ND	8	6xAA	N/A	32	25	15	2.3	-20	50
	RIIDEye M-H	***	LaBr₃	38 x 38												
	RIIDEye™ X-G	*****	NaI	51 x 51										2.6		
	RIIDEye™ X-H	***	LaBr₃	38 x 38												
	PackEye	ND	Plastic	ND			ND	30		ND	58	18	30	6	ND	ND

Star rating indicates relative price (* - high price, *** - low price), ND – not disclosed, N/A – not applicable, USB – universal serial bus, # - Number of radionuclides identified at any one time is limited. & - Radionuclide library is limited in scope. It is not identified if this can be changed by the user. [+] Only the lower quote of a price range was provided.**

Table 3.6: Portable detector based on solid state crystals

Company	Model	Relative cost	Detector Crystal	Crystal Size (mm)	Energy range (keV) Min	Energy range (keV) Max	Energy resolution 122 keV	Energy resolution 662 keV	Energy resolution 1332 keV	Cooling type	Start up time (hours)	Operating time (hours - single battery)	Battery type (if present)	Charging time (hours if stated)	Dimensions (cm) Length	Dimensions (cm) Height	Dimensions (cm) Width	Weight (kg)	Operating temperature (°C) Max	Operating temperature (°C) Min
Canberra	Falcon 5000	ND	HPGe	60 x 30	20	3000	≤1.0 keV	ND	≤2.0 keV	Electronic	3-4	8	2x Li-ion	4	43.9	43	17.4	15.5	-20	50
dtectsystems	Rad-ID	*****	4x/8x CZT + NaI	29 x 38	20	3000	≤3 %	7.50%	ND	NA	NA	12	3x D cell	ND	19	13.5	28.4	3.38	-15	54
Flir	identiFINDER R300	*****	3x CZT	15 x 13 x 5	30	3000	ND	≤3.5 %	ND	NA	NA	24		5.5 (USB)	7	3.3	12.5	0.37	-20	50
kromek	GR1 / GR1-A	ND	CZT	10 x 10 x 10	30	3000	ND	2.0 – 2.5%	ND	NA	NA	USB link		ND	2.5	2.5	6.3	0.06	ND	ND
kromek	RayMon10				60			ND												
kromek	RA4S	*****		ND	ND	ND									ND	ND	ND	ND		
Nats-usa	HAWK HPGe	ND	HPGe	ND	40	3000	≤850 eV	ND	≤1.8 keV	Liquid Nitrogen	1.5	8 (LiN lasts 20h)	Li-ion	ND	15.4	32.4	21.7	4.95	5	35
Nats-usa	HAWK-Electric	ND			ND	ND	ND		ND	Stirling-cooler	ND	6		ND	ND	ND	ND	ND	ND	ND
Ortec	Micro-Detective-HX	*	HPGe	50 x 33	ND	ND	ND	ND	ND	Stirling-cooler	12	5		4	37.4	14.6	27.9	6.9	-10	40
Ortec	Detective-DX-100T	*		65 x 50								3		ND	39.4	16.3	34.9	11.1		
Ortec	Detective-EX-100T	*														18.3		12		
Pycko	NitroSPEC GPD-25300	***	HPGe	ND	30	1500	<600 eV	ND	ND	Liquid Nitrogen	1.5	8 (LiN lasts 20h)		ND				4.59	0	40
Pycko	NitroSPEC GCD-10175	***					≤850 eV		≤1.8 keV						15.4	32.4	21.7	5.9		
Pycko	NitroSPEC GCD-20180	***			40	3000	≤875 eV		≤1.85 keV		2	8 (LiN lasts 18h)						6.1		

Star rating indicates relative price (* - high price, ***- low price), ND – not disclosed, N/A – not applicable, USB – universal serial bus, # - Number of radionuclides identified at any one time is limited. & - Radionuclide library is limited in scope. It is not identified if this can be changed by the user. [+] Only the lower quote of a price range was provided.**

The battery life for the scintillator detectors offer mostly 8 to 14 hours; only 4 detectors can operate longer than this with one offering 36 hours of operation. For the semiconductor detectors, some of the CZT options depend on a link to an external computer and therefore battery time is linked to the specification of the attached computer. The other CZT options ranged from 12 to 24 hours of operating time. HPGe detectors had an operating time of between 3 to 12 hours although, due to the cooling requirements (see chapter 3.5.1), there is an initialisation time of between 1.5 hours to 12 hours before they can be used. Approximately half of the detectors have replaceable batteries whereas the remainder have an internal battery that requires recharging. Recharging time can last from between 2.5 hours up to 4.5 hours. The choice of detector would depend on the locality of an external power supply. For extended fieldwork, the option of having replaceable batteries would likely be the suitable choice. The activation time could likely affect choice as well, the extra power requirements (or availability of liquid nitrogen) for initialisation can restrict the measurement locations (Nilsson et al., 2014). It also limits the time window for measurement which can be a disadvantage due to the unpredictability of animal capture.

Weights of available scintillation detectors average around 1 to 3 kg with two weighing 7 kg. At under 0.5 kg, the CZT detectors weigh the least. The low weight of CZT can be beneficial as multiple CZT crystals can be arranged in a matrix configuration, or be combined with other detection crystals in a single system, whilst still maintaining an overall low weight. HPGe detectors, on the other hand, weigh the most. Weights range from 5 kg up to 15.5 kg which makes them less desirable for remote fieldwork.

The minimum operating temperatures of the scintillator detectors are mostly -20 $^{\circ}$C with only a few at – 10 $^{\circ}$C and one at 0 $^{\circ}$C. For the semiconductor detectors, the minimum operating temperatures are between – 20 and 5 $^{\circ}$C though in general the temperature ranges are more limited than for the scintillator detectors. The maximum operating temperatures are between 40 to 60 $^{\circ}$C. The maximum recorded temperature as recorded in the UK by the UK Meteorological Office (Met Office, 2013) was 38.5 $^{\circ}$C (25.2 $^{\circ}$C highest monthly average) with the minimum being -27.2 $^{\circ}$C (-5.2 $^{\circ}$C lowest monthly average). All the detectors would therefore operate under the maximum temperatures for the UK. The minimum operable temperatures are mostly below the average monthly low temperatures. Most of the listed detectors would, therefore, be operable except in the most extreme of low temperatures.

3.5.5.2 Portable Beta detectors

Detection and identification of beta radionuclides in portable detectors is limited. They are generally detected by the inclusion of a Geiger Muller probe and therefore restricted to gross count instead of identification (e.g. AT1120 from atomtex.com or PM1401K from polimaster.com). There are some portable detectors available, (e.g Microspec Beta Probe from bubbletech.ca), that contain a special phoswich scintillator; two scintillators of different timing properties (e.g. NaI and CsI) sandwiched together to help distinguish between two dissimilar radiation energies (Knoll, 2010). It is therefore capable of distinguishing the required energy spectra components to help identify which beta-emitting radionuclide is present. These beta detection units are, however, fully inclusive separate units that do not include gamma detection. If the requirements for monitoring include emissions it would therefore come at the cost of having to include a sperate detector in whatever detection system is decided upon.

3.5.5.3 Suitability for live-monitoring

Of the detectors described in this section, several could be utilised for certain live-monitoring requirements. They incorporate detection materials that are suitable to gamma detection and are of a specification (e.g. weight and power supply) that makes them adequately portable for field studies. None of these detectors, however, are aimed towards animal monitoring (though do not state that they cannot be used for this purpose) and only a small number of the detectors (at the higher end of the cost scale) state that they can be utilised for the monitoring of specific objects (e.g. PYCKO Scientific Limited, 2014). Further, detector selection depends on a number of factors including the type of radionuclide to monitor and the target organism.

An immediate concern in selection is the cost of any potential live-monitor, especially if more than one detector type or a high resolution detector is required. The technology used for measuring ^{137}Cs in large organisms (e.g. sheep) is already sufficient for the monitoring detailed in section 3.4. Upgrading detectors in these instances is likely only required if a smaller unit with longer battery life is required. If monitoring of smaller organisms (e.g. mice) were required then it would be desirable to shield the organism and detector from background radiation; the smaller internal activity is likely to be difficult to distinguish from background if no shield is used. Here, the current detectors are either too large to sufficiently shield both the detector and any restraint used (due to weight), or the attachment of the display (on

smaller units) is such that is would compromise a part of the shielding. If there is also the added requirement to monitor both gamma and beta emitting radionuclides in both large and small organisms then none of the described available detection systems would be suitable. Multiple detection materials would be required to accomplish this and therefore, aside from finding the optimal configuration of materials, the selection of a suitable MCA (or SCA) to process the signal from detection material also becomes important.

From the materials and technologies identified in this chapter, a likely live-monitor may consist of the following:

1. A CsI(Tl) scintillator for gamma detection and a plastic scintillator (e.g. BC400) for beta (Section 3.5.1), sized and orientated appropriate to the target organism.

2. A small PMT or, if a smaller detection crystal is used, a suitable number of SiPMs (Section 3.5.2). This depends on budget and the radioactivity likely to be encountered.

3. Connection to a MCA if spectral analysis is required for multiple radionuclide identification, or an SCA if single radionuclides where the peak energies can be windowed (Section 3.5.3). The choice must allow for portability of the entire unit.

4. A restraint with a lead shield surrounding it and the detector or another appropriate method of placing the detector against the organism (Section 3.5.4). The design and use of this depends entirely on the size of organism.

From this list, it can be seen that the complete specification of a detector would need to first identify the targets of such a device. The approach to identifying the target radionuclides and organisms, as well as the design process, is outlined in the next section.

3.6 Development of a new detection method / technology

The review of detection methods and technologies in the previous subsections identifies scope (and need) to develop a new detector for the determination of radionuclide content within wildlife. This subsection outlines the design process and the approach taken towards the development of such a new detector.

3.6.1 Approach to detector design

From the conception of an idea to the production of a prototype, there are several development stages to follow (Kamrani and Nasr, 2010). The development process involves a) identifying the needs of the product, b) researching the identified needs to understand the processes of the product, c) developing potential solutions, d) selecting the best solution and

building a prototype(s) and, e) testing the developed prototype(s) to check the desired specifications have been met.

This project had the aim of developing a new method for determining the radionuclide content within terrestrial wildlife (primarily small animals). The literature review chapter has so far discussed the methods and the technologies that are currently available and has identified the development of a portable radiation detector as being the preferred solution for meeting this aim. In planning a design, there are several components to a radiation detector (e.g. detection material, shielding etc) that must be considered in relation to not only the detection of radiation from the target radionuclide but also to what is in the surrounding environment and the properties of the target organism. The variables for these components are identified through considering what will interact with the radiation detector in question.

For a potable detector, positioned at ground level in an unspecified outdoor location, what sources of radiation would the detection material measure? By considering a box (Figure 3.2), of undefined size, that has a detector attached to it at an unspecified point, the possible sources of radiation incident on the detector (described in chapter 2.4) can be identified as follows.

If the box is empty (Figure 3.2a), then the detector will be exposed to radiation from four different sources; radon (along with decay products) from the air, cosmic radiation, intrinsic radiation from the detector (crystal and any shielding), and gamma radiation that is emitted from the ground. By introducing a non-radioactive object (in this case to represent the volume of an animal) into the box (Figure 3.2b), there are two changes that will occur to the radiation that reaches the detector. Firstly, the volume of air will reduce and, in turn, the level of radioactive radon in the box will reduce. Secondly, depending on the orientation of the detector, there will now be a shielding effect from the object meaning a potential reduction from the gamma radiation in the ground (cosmic is too penetrative to be effectively reduced as stated above). If the introduced volume is now substituted with a non-contaminated animal (Figure 3.2c) then a new source of radiation is introduced. An animal that is signified as free from anthropogenic radionuclides will still contain a level of background radiation, the most apparent of this natural internal radiation would be from ^{40}K (Kathren, 1984).
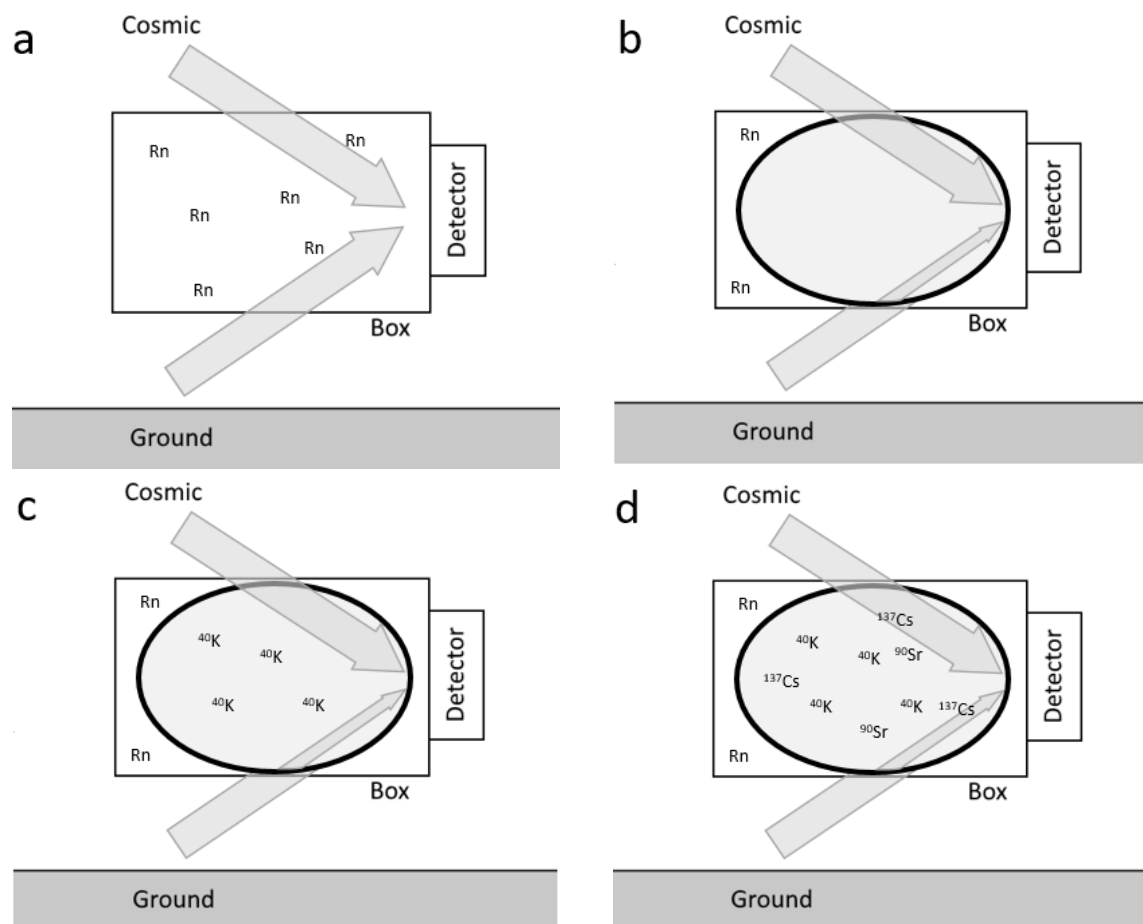
Figure 3.2: Sources of radiation that can interfere with radionuclide measurement. a) Empty box, b) box with blank organism volume, c) box with organism volume containing natural background radiation, d) box with contaminated organism volume.

Accounting for and reducing this background radiation can be accomplished using three methods. First, the background gamma can be reduced by means of a shield. Depending on the size of the animal, this would either surround the animal and the detector or surround only part of the detector with the animal body completing the enclosure (e.g. as for the sheep monitoring methods in section 3.4). This needs to be balanced such that it is still a portable weight but reduces the background gamma such that the target radionuclides can be quantified. Second, the gamma that does penetrate the shield, along with the cosmic, radon, and intrinsic radiation, can be accounted for by taking background measurements at the sampling site and ensuring the count time is long enough to sufficiently reduce the MDA for the target radionuclide. Finally, the introduction of a phantom, with a density of close approximation to the animal target, can account for the difference in volume when measuring the background radionuclide activity levels. This will act to reduce the radioactive radon present in the air, and attenuate the gamma radiation from the ground, to similar levels as if a true animal target was introduced. In designing the shielding, therefore, the factors to

identify are: i) the likely background activity in the measurement location; ii) what the targeted radionuclide(s) are; and iii) the size of the target organism(s).

The last component to be introduced is an animal which is now contaminated with anthropogenic radionuclides (Figure 3.2d). Variables associated with the target animal itself, instead of from the surrounding environment, are now important to consider. These are: (i) the distribution of the target radionuclide within the target organism and its visibility to the detector (e.g. ^{90}Sr is a bone accumulating radionuclide and therefore the emitted radiation would need to travel through soft tissue before it can be detected); (ii) radionuclides contained within the gut; (iii) shielding by, or contamination on, fur (or feathers); (iv) moisture present or trapped on the surface of a wet animal; and (v) movement of the animal.

The target radionuclide has already been identified as an important factor in the environmental variables mentioned above. The type of radionuclide and its distribution with the body, however, also have implications on the type of detector to use as well as its size and orientation (in relation to the animal body). The possible radiation from radionuclides within the gut is likely not problematic for larger animal though would be difficult to account for in smaller animals without removing the whole gut (Beresford et al., 2016) though can be minimised by providing uncontaminated food to the animal if it is held in a trap. The presence of fur (or feathers), surface contamination, and water, all add a shielding effect to the detection of radiation emitted from inside the organism. Removing fur (or feathers) would make the method invasive and the washing of the animal is likely to not remove all contamination (e.g. Ishida, 2015). The final variable, movement of the animal, is one that can be limited by having an appropriate restraint. The true extent as to the effect of movement is one that will be revealed in testing of a prototype detector. In designing the main detector, therefore, the main factors to consider for the animal are: i) the target radionuclide; ii) the size and type of organism; ii) the size and orientation of the detector; and ii) how the movement of the animal affects the measured count.

3.6.2 Organisation of subsequent chapters in this thesis

In considering the main factors identified in the previous subsection, the development stages detailed in section 3.6.1 have been adapted for the design of a radiation detector (shown in Figure 3.3). The stages shown are categorised into the objectives outlined in section 1.2. The structure of the remaining thesis chapters is as follows:

1. Chapter 4 addresses objective 2. It details the selection of the target radionuclide(s) based on their presence in the UK environment and their importance to dose contribution. It also identifies the target organism(s) that would be suitable candidates for measuring with such a detector.

2. Chapter 5 addresses objective 3. It determines the optimal detector material size and orientation (in relation to the animal) by modelling the emission of the target radiation(s) from the target organism(s).

3. Chapter 6 addresses objective 4. It outlines the design and construction of a detector based on the information and conclusions in chapters 2, 4, and 5.

4. Chapter 7 addresses objective 5 and 6. The detector is tested in the laboratory and field to ascertain how it performs in detecting the target radionuclide(s) from the live target organism(s).

A discussion and conclusion is presented in Chapter 8 to draw together the research findings and outline a strategy for further research.
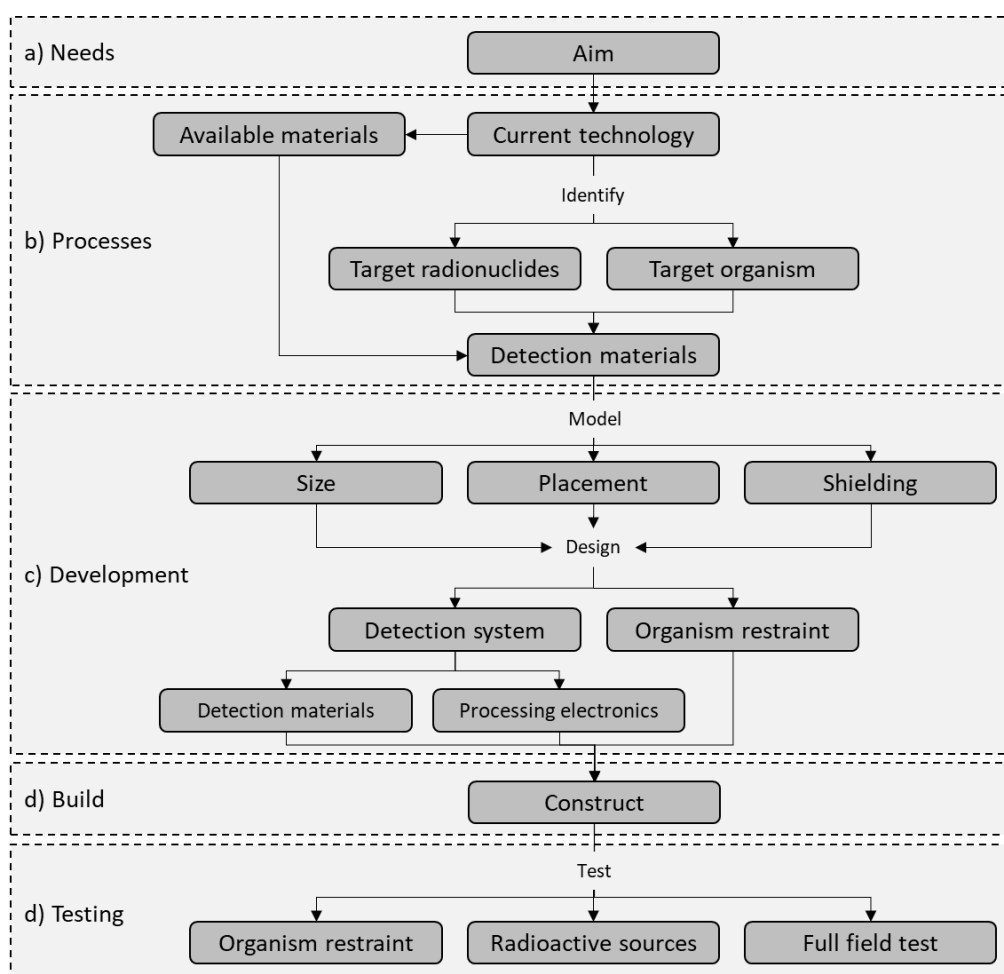
Figure 3.3: Overview of the device design and development methodology

4 Determination of radionuclide measurement requirements.

4.1 Introduction

This chapter identifies organisms and radionuclides to be monitored under a UK regulatory context and evaluates the potential for live-monitoring.

4.2 Methods

4.2.1 Data Sources

The selection of target organisms was based on the requirement to monitor protected species. Because there is a wide variety of different protected species in the UK (see JNCC (2015) for a comprehensive list) a means of categorising similar organisms and estimating internal doses was required. The ERICA tool (Brown et al., 2008), as an approved radiological assessment method for use in UK, was used to accomplish this. It categorises organisms as Reference Organisms, in-effect broad groups (e.g. amphibians, birds, mammals etc.), each of which are assigned a representative size, weight, dose conversion coefficients (DCC) and concentration ratio (CR). The organisms considered were the terrestrial reference organisms (not flora) considered in the ERICA tool (version 1.2 values used for this thesis (Brown et al., 2016)).

The selection of target radionuclides was determined by reviewing what anthropogenic radionuclides are currently authorised for release in the UK. An emphasis was placed on radiological monitoring programs (Environment Agency et al., 2014, Copplestone et al., 2003) as these would give indicative profiles (i.e. information for a set of radionuclides characteristic for a site) for radionuclide releases from facilities across the UK. These are reported, in a consistent manner, as radionuclide activity concentrations in various organisms and environmental media. As measurement methods can vary between studies, it was decided not to supplement the data extracted from the RIFE reports[2] with data from other studies. The set of radionuclides to be assessed within this chapter are those that are required to be monitored within the terrestrial ecosystem. For the UK, these radionuclides are Environment Agency et al. (2014): ^{3}H, ^{14}C, ^{32}P, ^{35}S, ^{41}Ar, ^{60}Co, ^{85}Kr, ^{90}Sr, ^{95}Nb, ^{95}Zr, ^{99}Tc, ^{106}Ru, ^{110m}Ag, ^{125}I, ^{125}Sb, ^{129}I, ^{131}I, ^{134}Cs, ^{137}Cs, ^{144}Ce, ^{155}Eu, ^{210}Po, ^{226}Ra, ^{228}Th, ^{230}Th, ^{232}Th, ^{234}Th, ^{234m}Pa, ^{234}U, ^{235}U, ^{238}Pu, ^{238}U, $^{239+240}$Pu, ^{241}Pu, and ^{241}Am. Although other radionuclides may be released or

---

[2] https://www.gov.uk/government/publications/radioactivity-in-food-and-the-environment-rife-reports-2004-to-2016

present (especially as members of decay chains) only the radionuclides listed are monitored in the RIFE programme.

The RIFE reports contain radionuclide activity concentrations for a range of marine and terrestrial targets (organisms and environmental media). A number of terrestrial animals are included, such as pheasant and rabbit as well as parts of larger animals (namely consumables e.g. deer meat). Data for all reference organisms was not, however, present in RIFE. Instead, because soil data is recorded in RIFE for most sites, it was decided to use soil activity concentrations (Table 4.1) to generate activity concentration estimates (using ERICA CRs) in each reference organism. Some sites (e.g. Capenhurst) report activity concentrations from multiple locations within the area. These individual locations were averaged for each radionuclide (and listed with a standard deviation) to provide a single set of site soil radionuclide concentrations. Radionuclide activity concentrations, as reported in rabbit (Table 4.1) were additionally used in combination with the soil data to verify the calculations that follow hold up when only limited biota data are available i.e. for a single site. Note Capenhurst was ignored due to a poor match between soil and rabbit data.

For the radionuclides that were reported in each site profile (i.e. the set of radionuclides present at that site) there were several assumptions that were made in selecting and converting radionuclide activity concentrations:

a) Only average soil radionuclide activity concentrations that were measured in dry weight were used. Wet weight (as no percentage dry matter was given) and maximum values were ignored.

b) The plutonium radionuclides; ^{239}Pu and ^{240}Pu, are reported in RIFE as $^{239+240}$Pu. As a conservative measure (see: Wood, 2010), these were input as ^{240}Pu to provide an upper estimate of dose for combined $^{239+240}$Pu.

c) Radionuclide activity concentrations that were recorded as being at the limit of detection (LOD) were assumed to be present in the soil at that level. This decision was made so as to not under predict their contributions to dose as compared to the other radionuclides present within the profile. It is noted, however, that the radionuclides not at LOD will as a result be (assumed minimally) under predicted.

Table 4.1: Radionuclide activity concentrations (Bq kg⁻¹) for soil and rabbit as recorded in 2013 (RIFE 2014).

Nuclide	Soil activity ($Bq\ kg^{-1}$)														Rabbit internal activity ($Bq\ kg^{-1}$)			
	Capenhurst	Sellafield	Springfields	Dounreay	Culham	Chapelcross	Hunterston	Torness	Aldermaston	Auchengaich	Lochan Ghlas Laoigh	Amersham	Cardiff	East Northants	Dounreay	Hunterston	Torness	Aldermaston
Ag-110m							7.00E-02	7.00E-02								1.00E-01	1.00E-01	5.00E-02
Am-241		5.80		1.70E-01		4.20E-01	1.80E-01	2.00E-01		1.30	2.60E-01				1.10E-01	1.10E-01	1.20E-01	7.10E-05
C-14					3.74E-03	8.32E-03	6.93E-03	6.93E-03							2.30E-01	1.90E+01	3.40E+01	
Ce-144				5.30E-01														
Co-60		3.40		1.50E-01			5.00E-02			5.00E-02	5.00E-02				5.00E-02	7.00E-02		
Cs-134		7.90E-01		7.00E-02		6.00E-02				6.00E-02	7.00E-02				5.00E-02			
Cs-137		6.30E+01		1.60E+01	4.70	7.60	8.70	3.30	1.26E+01	7.10E+01	1.60E+01	7.97	3.80	3.15	4.10E-01	3.20E-01	5.00E-02	1.10E-01
Eu-155				1.60		1.40	5.70E-01	1.00		2.80	7.10E-01				5.00	5.00	5.00	
H-3				2.31E-03	3.70E-03	4.25E-03	2.31E-03	2.31E-03						1.85E-03				3.20
I-125												5.67E-01						
I-129				5.00E-02											5.00E-02			
I-131												4.07E-01						
Nb-95				2.10E-01				1.00E-01							5.00E-02		7.00E-02	
Pu-238				5.00E-02					2.95E-01					2.00				5.20E-05
Pu-240				4.10E-01					1.02					2.00				3.40E-05
Pu-241																		
Ru-106		3.10		5.60E-01											3.70E-01			
S-35					3.61E-03	1.16E-03	1.99E-03	1.94E-03										
Sb-125		1.60														1.10	6.00E-01	
Sr-90				1.50	2.00	1.10	7.40E-01	5.10E-01							1.00E-01	1.60E-01	1.00E-01	
Tc-99	6.55																	
Th-228														2.40E+01				
Th-230														5.25				
Th-232														2.10E+01				
Th-234																		
U-234	1.85E+01	1.90E+01	1.16E+02	3.00E+01	3.80				1.46E+01					1.10E+01				1.30E-02
U-235	1.06	6.90E-01	5.27	1.20	1.40E-01				1.04					1.00				7.50E-04
U-238	1.83E+01	1.80E+01	1.09E+02	2.80E+01					1.50E+01					1.25E+01				8.60E-03
Zr-95					1.90E-01													

Sourced from RIFE (Environment Agency et al., 2014). Rabbit measurements are internal activity concentration (Bq kg⁻¹). Activity concentrations for ³H, ¹⁴C, and ³⁵S have been converted to Bq m⁻³)

d) Another assumption was required for the atmospheric radionuclides: ^{3}H, ^{14}C, and ^{35}S. These are all reported in RIFE as soil activity concentrations and, because the ERICA tool only contains air to biota CRs for these radionuclides, need to first be converted to air activity concentrations. This was estimated by assuming a) equilibrium between the soil and air concentrations and b) the stable element to isotope ratios were the same for both soil and air. It was assumed there is approximately 35% carbon content in UK soil (European Environment Agency, 2017) and 0.2 g m^{-3} carbon content in air (IAEA, 2010a). This equates to approximately 350g of carbon per kg of soil and (assuming an air density of 1.225 kg m^{-3}) 0.163 g of carbon per kg of air. Therefore, if the ^{14}C content is in equilibrium for air and soil, the ratio of ^{14}C activity concentration from soil to air is estimated to be 4.6x10^{-4}. Sulphur-35 was assumed to have the same ratio as for ^{14}C. This was based on recommendations from Brown et al. (2008) and Copplestone et al. (2001). Tritium air concentrations was assumed from the transfer of tritiated water between air to soil. This is estimated from equation 4.1 (IAEA, 2010a), where C_{sw} is the soil water concentration in Bq L^{-1}, C_{air} is the air concentration in Bq m^{-3}, CR_{s-a} is an empirical constant set to 0.3 and H_a is the absolute humidity in L m^{-3}.

$$C_{sw} = \frac{CR_{s-a}C_{air}}{H_a} \qquad\qquad 4.1$$

A 10% water content was assumed for soil. An absolute humidity of 10 g m^{-3} was assumed based on data from https://www.metoffice.gov.uk. Using these values results in a ratio of 1.6x10^{-3} for soil to air activity concentrations.

e) Lastly, radiation weighting factors were kept as the default values within the ERICA Tool (i.e. alpha, beta, and gamma emitting radionuclides were given weightings of 10, 3, and 1 respectively).

4.2.2   Assessment of organism and radionuclide importance

The most at-risk organism groups were assessed by calculating the internal, (Equation 2.9), external (Equation 2.10) and total doses from each radionuclide present in each site (henceforth referred to as a site profile). Weight and geometry of each organism group, along with their associated DCC and CR$_{wo-media}$ values, were set as the ERICA 1.2 Tool default values. The doses estimated to be received by each reference organism (internal, external and total) were fractionally weighted between 0 and 1 (such that 1 is the reference organism with the

largest dose) across each site. Comparison of these fractional weightings, along with details on what type of radiation dominates the dose, assists in identifying the organism types that would be most suitable to target a new detection method towards.

The radionuclides of importance were determined by calculating the internal dose received from each radionuclide that was present within a site profile. The top three contributors to dose were listed (for each reference organism and each site) in descending order of dose. A limit was set such that only radionuclides that contributed at least 10% to the internal dose were included. This was repeated using the data for activity concentrations in rabbit (rather than small mammal concentrations estimated using CR values) to verify result are similar when only limited data is used.

4.2.3 Assessment of detectability and measurability

Radionuclides identified as contributing most to the dose were assessed to determine if the radiations they emit are likely to be detected externally from the target organisms. Three methods were used to assess the detectability: 1) calculating maximum radiative range in soft tissue; 2) identifying potentially interfering radionuclides; and 3) determining the activity concentration of each radionuclide that would likely be present in the event of a screening dose rate level being reached.

4.2.3.1 Detectability of selected radionuclides

Radionuclides, once they are absorbed into an organism, will often accumulate in specific locations within the organism's body. They can distribute across soft tissues (e.g. ^{137}Cs), or within certain organs (e.g. ^{90}Sr in bone or ^{131}I in the thyroid). Therefore, a knowledge of where in the organism these radionuclides will be found, coupled with how far the emitted radiation can travel through body structures, highlighted which radionuclides could be potentially detected by an external detector.

Each radionuclide was categorised as either being accumulated largely in a specific tissue(s) or as having a relatively homogenous distribution throughout the organism based on) ICRP (1979). For each category, the primary alpha, beta, and gamma emissions were identified and their range through soft tissue was calculated (see table in Appendix 10.1). The (50% intensity) range, $R\gamma$, of gamma photons in soft tissue was estimated using Equation 2.4. As the mass attenuation coefficient (μ/ρ) values are energy dependant, soft tissue values were estimated from Hubbell and Seltzer (1996). Because all the beta decay energies of interest were below

2.5 MeV, the maximum range, $R_{\beta max}$, of beta particles in soft tissue was estimated using Equation (2.1). The range of alpha particles in soft tissue was determined to be negligible (Podgorsak, 2010). Variances in densities and attenuation of different soft tissue types and bone was ignored (deemed sufficient for the purposes of this chapter) and instead a single tissue type, assuming a density of 1 g cm^{-3} (assumed in many wildlife assessment models e.g. Vives i Batlle et al., 2007), was used for the calculation.

4.2.3.2 Radionuclides likely to interfere with detection

For each radionuclide determined to be of importance, the primary decay energy was looked at to determine what other radionuclides could interfere with their detection. For the gamma emitters, a search of readily available portable gamma detectors revealed a standard FWHM of around 8% of the decay energy for ^{137}Cs (see section 3.5.5). Therefore, the approach taken was to consider radionuclides within a $^+/_-$ 8% window of the primary decay energy as being potentially interfering. Because there are many potentially interfering radionuclides, the list of radionuclides was limited by considering only those that were likely to be present within all of the measurement locations. The naturally occurring radionuclides that were considered as potentially interfering were ^{40}K, ^{234}Th*sec*, ^{238}U*sec* originating from rock, and ^{3}H and ^{7}Be, ^{14}C, and ^{22}Na from cosmic sources. The anthropogenic radionuclides (see section 4.2.1) that are required to be monitored were also considered along with any progeny. For the beta emitting radionuclides, because they exhibit a range of energies (see section 2.1), their detection could be obscured by the decay of any other radionuclides within detection range. Because a thin detector is likely to be used (see section 3.5.5) it is assumed interfering radionuclides for the target radionuclides that are beta emitters would be other beta emitting radionuclides present within the monitoring locations.

4.2.3.3 Radionuclide activity concentration required to reach a screening dose rate

The activity concentration (for each radionuclide) that is required to be measured is that which would result in an undesirable dose to an organism; i.e. it would reach a screening dose rate (ERICA uses a default of 10 µGy h^{-1}). The screening dose rate can be reached by either a single or a combination of radionuclides.

The ERICA Tool has three tiers of assessment, the first two of which use a screening dose rate to determine the outcome of the assessment. Tier 1 compares input media radionuclide activity concentrations to a set of environmental media concentration limits (EMCL) (Larsson, 2008). The EMCL is defined as the "*activity concentration in the selected media that would*

result in a dose rate to the most exposed reference organism equal to the screening dose rate"
(Brown et al., 2008). Each reference organism and radionuclide combination has an EMCL that
is derived by back-calculation from the screening dose rate. In this tier, however, only the
most exposed reference organism is identified. The reason for this is that a site can be quickly
screened out if it is deemed to have radionuclide activity concentrations that are of negligible
risk to the reference organism of most concern. If the assessment fails, then the assessment
should continue into Tier 2. Tier 2 also uses a screening level to determine the outcome of the
assessment. The whole-body dose to individual reference organisms are calculated and are
directly compared to the screening dose rate (Larsson, 2008). Unlike Tier 1, Tier 2 assesses the
risk for multiple reference organisms (that have been selected by the assessor). A Tier 3
assessment is more complex and requires the assessor to define parameters such as
probability distributions for the input data and to include their own dispersion models
(Oughton et al., 2008). A Tier 3 assessment does not assess against a screening dose rate and
is therefore not considered for this thesis.

This chapter required a set of internal radionuclide activity concentrations, that would result
in a screening dose rate to be reached, to be derived for each reference organism of interest
(section 4.2.1). A Tier 1 assessment does not allow for this calculation and therefore estimates
on internal activity were made on a Tier 2 level. This tier further allowed each set of
radionuclide activity concentrations to be verified as resulting in a dose that would reach the
screening level.

The soil radionuclide activity concentration levels from the previous section were used to
estimate what activity concentrations for each radionuclide (within each site) would be
required for an organism to receiving a total dose of 10 μGy h^{-1}. For each radionuclide i,
present in a single site profile, the estimated activity concentration $C_{wo\text{-}biota}$ (Bq kg^{-1}) within a
reference organism b was calculated (Equation 4.2. The fractional contribution of each
radionuclide to total dose was first determined by dividing the soil activity concentration $C_{soil,i}$
for each radionuclide by the total dose received $D_{Total,I,b}$ (Equation 2.8) from all radionuclides
present within the site. This was then scaled to the desired screening dose rate, S (μGy h^{-1}),
and converted to an internal organism activity concentration using the appropriate
concentration ratio $CR_{i,b}$.

$$C_{wo-biota,i,b} = \left[\frac{C_{soil,i}}{\sum_i\left(D_{Total,\,i,b}\right)}\right] \cdot S \cdot CR_{i,b} \qquad\qquad 4.2$$

Equation 4.2 was used to determine the predicted activity concentration in each reference organism for each radionuclide present in each of the sites in Table 4.1. All activity concentrations were scaled to the ERICA default of 10 µGy h^{-1} for the purposes of this chapter. This calculation was repeated using the rabbit data (combined with the soil data; Table 4.1) to verify this resulted in activity concentrations consistent with the soil only data. Finally, assuming a single radiation detector would be used for analysis, the results for all reference organisms were amalgamated to generate maximum, minimum, and average radionuclide activity concentrations for each radionuclide. This provided a basis for estimating if the quantity of emitted radiation for each radionuclide would be sufficient for measurement.

4.3 Results

4.3.1 Assessment of importance

Reference organism weighted doses for internal, external, and total dose are shown in Table 4.2 (e.g. internal dose for all reference organisms in Capenhurst are scaled between 0 and 1 where 1 indicates the largest dose). The table indicates the most affected groups vary depending on the radionuclides that were present in a location. Generally (assuming ERICA defaults), large organisms receive a higher internal dose for sites where a gamma emitter dominates (see Table 4.3) and small organisms (annelid and mollusc) when an alpha emitter dominates. Small organisms that are close to the ground receive the largest external dose. Total dose shows the same patterns for internal dose.

Of the radionuclides that where present in each of the monitored locations, the main contributors to internal dose across all soil profiles were found to be ^{14}C, ^{90}Sr, ^{131}I, ^{137}Cs, ^{228}Th, ^{234}U, ^{238}U, $^{239+240}$Pu, and ^{241}Am (Table 4.3). Due to their low contribution to dose and low frequency on the table both ^{131}I and $^{239+240}$Pu will not be considered further. Of the remaining radionuclides, ^{137}Cs and ^{241}Am have gamma emissions; ^{14}C and ^{90}Sr only have beta emissions, and ^{234}U and ^{238}U only have alpha emissions. Thorium-228 is primarily an alpha emitter, though it has a small gamma emission that will be discussed. For completeness, the radionuclides contributing most to external dose were ^{60}Co, ^{137}Cs, ^{228}Th, and ^{235}U.

Table 4.2: Organism group weighted dose comparison.

	Organism	Capenhurst	Sellafield	Springfields	Dounreay	Culham	Chapelcross	Hunterston	Torness	Aldermaston	Auchengaich	Lochan Ghlas Laoigh	Amersham	Cardiff	East Northants
Internal	Amphibian	0.17	0.41	0.16	0.21	0.31	0.32	0.19	0.36	0.18	0.12	0.12	0.06	0.06	0.09
	Bird	0.04	0.16	0.04	0.09	0.28	0.23	0.17	0.26	0.08	0.11	0.11	0.10	0.09	0.04
	Large Mammal	0.17	1.00	0.16	0.53	1.00	1.00	1.00	1.00	0.61	1.00	1.00	1.00	1.00	0.12
	Small Mammal	0.17	0.55	0.16	0.36	0.66	0.58	0.55	0.59	0.38	0.51	0.50	0.50	0.50	0.09
	Reptile	0.16	0.27	0.15	0.19	0.20	0.20	0.15	0.23	0.18	0.11	0.11	0.09	0.08	0.19
	Annelid	1.00	0.78	1.00	0.98	0.46	0.24	0.11	0.26	0.89	0.10	0.09	0.01	0.01	0.87
	Arthropod	0.31	0.34	0.31	0.32	0.18	0.15	0.08	0.17	0.30	0.06	0.05	0.01	0.01	0.43
	Flying Insect	0.31	0.35	0.31	0.32	0.19	0.16	0.08	0.17	0.30	0.06	0.06	0.01	0.01	0.43
	Mollusc	1.00	0.70	1.00	1.00	0.46	0.20	0.09	0.22	1.00	0.08	0.07	0.01	0.00	1.00
External	Amphibian	0.98	0.97	0.98	0.97	0.97	0.97	0.97	0.97	0.97	0.97	0.97	0.97	0.97	0.99
	Bird	0.43	0.36	0.43	0.36	0.36	0.36	0.36	0.36	0.36	0.36	0.36	0.36	0.35	0.37
	Large Mammal	0.19	0.18	0.18	0.18	0.18	0.18	0.18	0.18	0.18	0.18	0.18	0.18	0.18	0.20
	Small Mammal	0.93	0.91	0.93	0.91	0.90	0.90	0.90	0.91	0.90	0.90	0.90	0.90	0.90	0.94
	Reptile	0.88	0.88	0.88	0.87	0.87	0.87	0.87	0.87	0.87	0.87	0.87	0.87	0.87	0.91
	Annelid	1.00	0.97	0.99	0.97	0.97	0.97	0.97	0.97	0.97	0.97	0.97	0.97	0.97	1.00
	Arthropod	1.00	1.00	1.00	1.00	1.00	1.00	1.00	1.00	1.00	1.00	1.00	1.00	1.00	1.00
	Flying Insect	0.44	0.39	0.44	0.39	0.39	0.39	0.39	0.39	0.39	0.39	0.39	0.39	0.39	0.37
	Mollusc	1.00	0.97	1.00	0.97	0.97	0.97	0.97	0.97	0.97	0.97	0.97	0.97	0.97	1.00
Total	Amphibian	0.17	0.65	0.16	0.28	0.47	0.53	0.42	0.57	0.27	0.36	0.36	0.31	0.30	0.26
	Bird	0.04	0.25	0.04	0.12	0.33	0.30	0.25	0.33	0.11	0.19	0.19	0.18	0.18	0.10
	Large Mammal	0.17	0.99	0.16	0.50	1.00	1.00	1.00	1.00	0.57	1.00	1.00	1.00	1.00	0.13
	Small Mammal	0.17	0.77	0.16	0.41	0.80	0.76	0.74	0.78	0.44	0.71	0.71	0.71	0.71	0.26
	Reptile	0.16	0.50	0.16	0.26	0.34	0.39	0.35	0.43	0.26	0.33	0.33	0.31	0.30	0.33
	Annelid	1.00	1.00	1.00	0.98	0.61	0.45	0.34	0.48	0.90	0.34	0.33	0.26	0.26	0.89
	Arthropod	0.31	0.60	0.31	0.38	0.34	0.37	0.31	0.40	0.38	0.31	0.31	0.27	0.27	0.54
	Flying Insect	0.31	0.43	0.31	0.33	0.25	0.24	0.17	0.26	0.31	0.16	0.15	0.12	0.11	0.42
	Mollusc	1.00	0.93	1.00	1.00	0.61	0.40	0.32	0.43	1.00	0.32	0.31	0.26	0.25	1.00

Comparison of doses received by each organism group for the selected radionuclide soil activity concentrations. Numbers are coloured such that solid red indicates the most affected group for each site profile and white is not affected. The smaller reference organisms that likely requiring multiple samples accumulated to achieve measurement are separated from the others using the dashed line. Weighted doses were calculated using data from RIFE (Environment Agency et al., 2014).

Table 4.3: Radionuclides that contribute most to internal dose.

Profile	Capenhurst	Sellafield	Springfields	Dounreay	Culham	Chapelcross	Hunterston	Torness	Aldermaston	Auchengaich	Lochan Ghlas Laoigh	Amersham	Cardiff	East Northants
Amphibian	^{234}U	^{241}Am	^{234}U	^{234}U	^{90}Sr	^{241}Am	^{241}Am	^{241}Am	^{234}U	^{241}Am	^{241}Am	^{137}Cs	^{137}Cs	^{228}Th
	^{238}U	^{137}Cs	^{238}U	^{238}U	^{234}U	^{90}Sr	^{137}Cs	^{90}Sr	^{238}U	^{137}Cs	^{137}Cs			^{234}U
			^{90}Sr		^{137}Cs	^{137}Cs	^{137}Cs	^{90}Sr	^{14}C	^{137}Cs				^{238}U
Bird	^{234}U	^{137}Cs	^{234}U	^{137}Cs	^{90}Sr	^{90}Sr	^{137}Cs	^{90}Sr	^{137}Cs	^{137}Cs	^{137}Cs	^{137}Cs	^{137}Cs	^{228}Th
	^{238}U	^{241}Am	^{238}U	^{90}Sr	^{137}Cs	^{137}Cs	^{90}Sr	^{137}Cs	^{234}U	^{241}Am	^{241}Am			^{234}U
			^{234}U			^{241}Am	^{14}C	^{14}C	^{238}U					^{238}U
Large Mammal	^{234}U	^{137}Cs	^{234}U	^{137}Cs	^{137}Cs	^{137}Cs	^{137}Cs	^{137}Cs	^{137}Cs	^{137}Cs	^{137}Cs	^{137}Cs	^{137}Cs	^{137}Cs
	^{238}U		^{238}U	^{234}U	^{90}Sr	^{90}Sr		^{90}Sr	^{234}U					^{234}U
			^{238}U						^{238}U					^{238}U
Small Mammal	^{234}U	^{137}Cs	^{234}U	^{137}Cs	^{137}Cs	^{137}Cs	^{137}Cs	^{137}Cs	^{137}Cs	^{137}Cs	^{137}Cs	^{137}Cs	^{137}Cs	^{137}Cs
	^{238}U		^{238}U	^{234}U	^{90}Sr	^{90}Sr	^{90}Sr	^{90}Sr	^{234}U					^{234}U
			^{238}U	^{234}U					^{238}U					^{238}U
Reptile	^{234}U	^{241}Am	^{234}U	^{234}U	^{234}U	^{241}Am	^{137}Cs	^{241}Am	^{234}U	^{137}Cs	^{137}Cs	^{137}Cs	^{137}Cs	^{228}Th
	^{238}U	^{137}Cs	^{238}U	^{238}U	^{90}Sr	^{137}Cs	^{241}Am	^{137}Cs	^{238}U	^{241}Am	^{241}Am			^{234}U
		^{234}U		^{137}Cs	^{137}Cs	^{14}C	^{14}C	^{14}C	^{137}Cs					^{238}U
Annelid	^{234}U	^{241}Am	^{234}U	^{234}U	^{234}U	^{241}Am	^{241}Am	^{241}Am	^{234}U	^{241}Am	^{241}Am	^{137}Cs	^{137}Cs	^{228}Th
	^{238}U	^{234}U	^{238}U	^{238}U					^{238}U		^{137}Cs			^{234}U
		^{238}U												^{238}U
Arthropod	^{234}U	^{241}Am	^{234}U	^{234}U	^{90}Sr	^{241}Am	^{241}Am	^{241}Am	^{234}U	^{241}Am	^{241}Am	^{137}Cs	^{137}Cs	^{228}Th
	^{238}U	^{234}U	^{238}U	^{238}U	^{234}U		^{137}Cs	^{14}C	^{238}U	^{137}Cs	^{137}Cs	^{131}I		^{234}U
		^{238}U												^{238}U
Flying Insect	^{234}U	^{241}Am	^{234}U	^{234}U	^{90}Sr	^{241}Am	^{241}Am	^{241}Am	^{234}U	^{241}Am	^{241}Am	^{137}Cs	^{137}Cs	^{228}Th
	^{238}U	^{234}U	^{238}U	^{238}U	^{234}U		^{137}Cs	^{14}C	^{238}U	^{137}Cs	^{137}Cs			
		^{238}U					^{90}Sr							
Mollusc	^{234}U	^{241}Am	^{234}U	^{234}U	^{234}U	^{241}Am	^{241}Am	^{241}Am	^{234}U	^{241}Am	^{241}Am	^{137}Cs	^{137}Cs	^{228}Th
	^{238}U	^{234}U	^{238}U	^{238}U					^{238}U			^{131}I		^{234}U
		^{238}U							^{240}Pu					^{238}U

Radionuclides (listed in descending order) for each reference organism at each site. Radionuclides were determined using data from RIFE (Environment Agency et al., 2014)

When incorporating internal radionuclide activity concentration measurements from rabbits (and limiting the measurement locations to where these are available) then ^{241}Am dominates the internal doses, with ^{14}C a close second. The only exception is for Aldermaston where ^{234}U and ^{238}U contribute the most to dose. As no further radionuclides were identified using the rabbit data then the list of important radionuclides as in Table 4.3 remains unaltered.

4.3.2 Assessment of detectability

4.3.2.1 Radionuclide emission range and organ accumulation location

The range of radiation (calculated using the properties included in Appendix 10.1) from each of the target radionuclides (beta and gamma) is shown in Figure 4.1. Alpha radionuclides are not included due to their previously discussed short range.

4.3.2.2 Potentially interfering secondary radionuclides

Radionuclides that may interfere (Figure 4.2) with the detection of the gamma emitting radionuclides of importance are as follows (percent decay probability is displayed in brackets): for ^{137}Cs, with a primary decay energy of 661.66 keV, the interfering radionuclides are ^{125}Sb (*11.3*), ^{131}I (*7.2*), ^{210}Bi (*3.8*), ^{90}Y (0.3), and ^{110m}Ag (*94.0*). For ^{228}Th, with a primary decay energy of 84.37 keV (*1.2*), the interfering radionuclides are ^{144}Ce (*1.36*), ^{131}I (*2.62*), ^{231}Th (*6.6*), ^{237}Np (*12.4*), ^{155}Eu (*30.7*), and ^{231}Th (*0.9*). For ^{241}Am, with a primary decay energy of 59.54 keV (*35.9*), the interfering radionuclides are ^{155}Eu (*1.1*), ^{234}Th (*4.8*), and ^{232}Th (*0.3*).
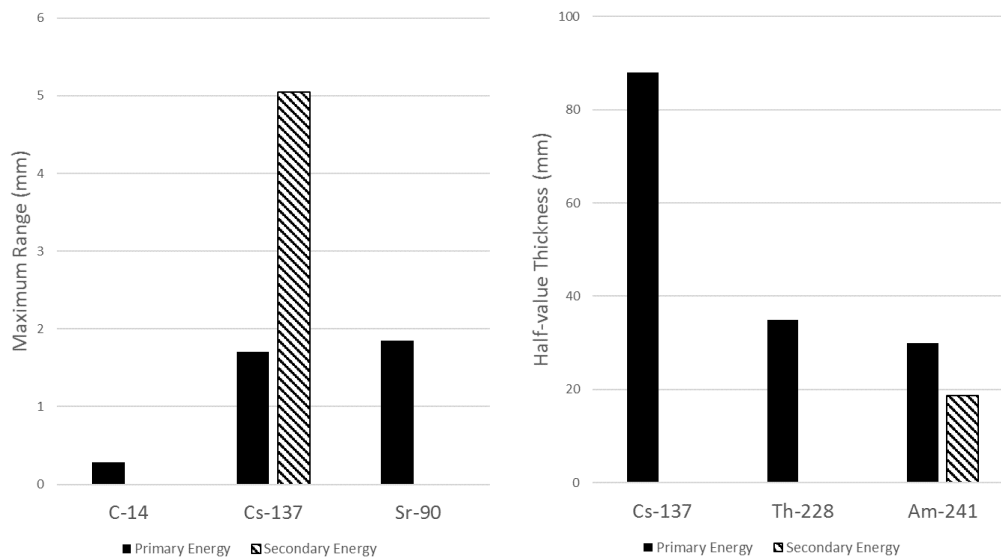
Figure 4.1: Range of radiation in soft tissue. Maximum range for beta particles (left). Half-value thickness for gamma photons (right). Calculated using information from Appendix 10.1. Carbon-14 and ^{137}Cs are relatively homogenously distributed throughout the whole-body; ^{90}Sr in bone; ^{228}Th mainly on the bone surface; and ^{241}Am on the bone surface and in the liver (ICRP, 1979).
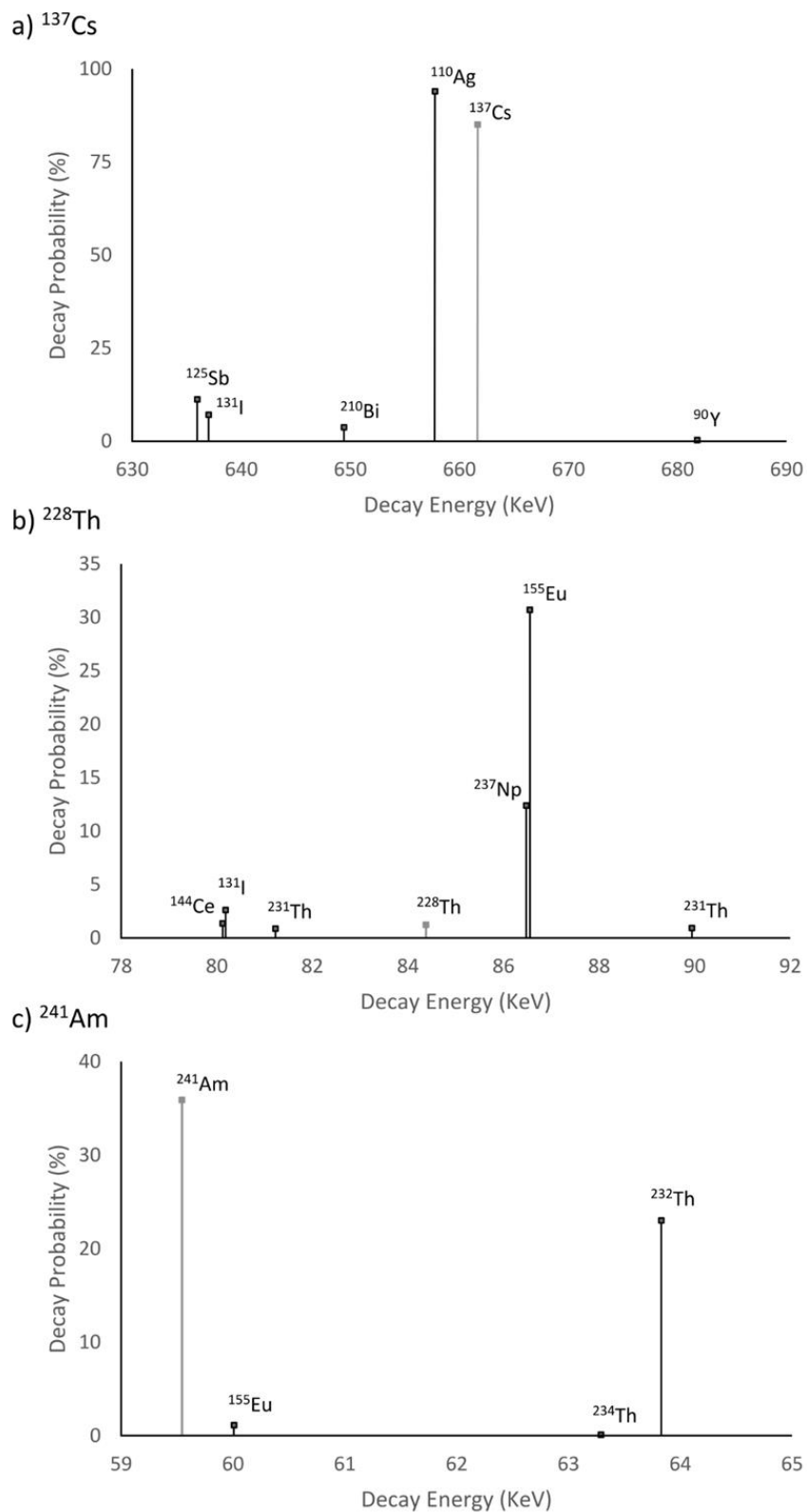
Figure 4.2: Interfering radionuclides. Interfering energies for a) ¹³⁷Cs, b) ²²⁸Th, and c) ²⁴¹Am.

4.3.2.3 Activity concentration within an organism required to reach a screening dose rate

The activity concentrations required to equal 10 μGy h^{-1} for the radionuclides deemed to be of importance are given in Figure 4.3 for the soil only measurements (averaged across all sites). A comparison between the soil only and the combined rabbit and soil measurements (averaged for the four locations where this data was available) is given in Figure 4.4. Individual tables, containing maximum, minimum, average and standard deviations for each organism group are provided in Appendix 10.2. The graph displays the combined results for all targeted organism groups. Each set of activity concentrations were checked in the ERICA 1.2 Tool to ensure they result in a 10 μGy h^{-1} dose at Tier 2. Activity concentrations can be scaled to different screening levels if required. For example, the activity concentrations given in the two graphs would be multiplied by 4 if a 40 μGy h^{-1} screening dose rate is required. Similar manipulations would correct for other screening dose rates, e.g. those detailed in Howard et al. (2010).
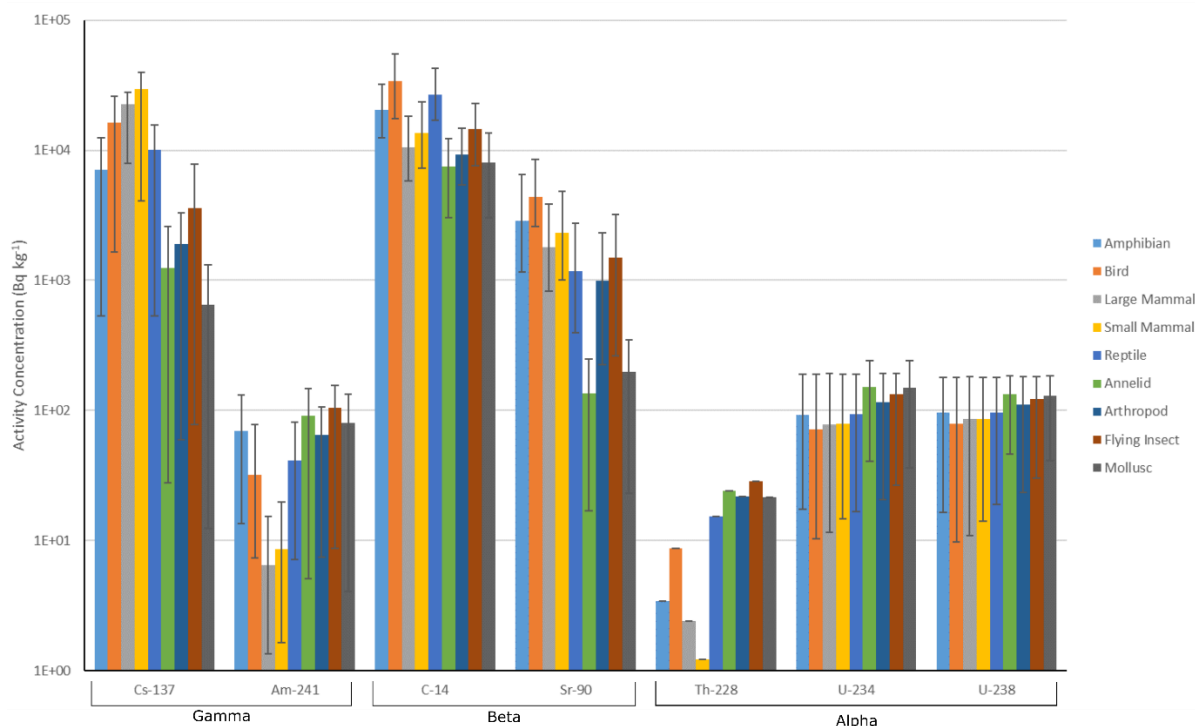
Figure 4.3: Average radionuclide activity concentrations required to reach a 10 μGy h^{-1} screening dose rate. Calculated for each reference organism. Activities are averaged across all measurement sites. Error bars denotes the maximum and minimum activity calculated from the measurement sites where the radionuclide appears. Activity concentrations calculated using data from RIFE (Environment Agency et al., 2014).
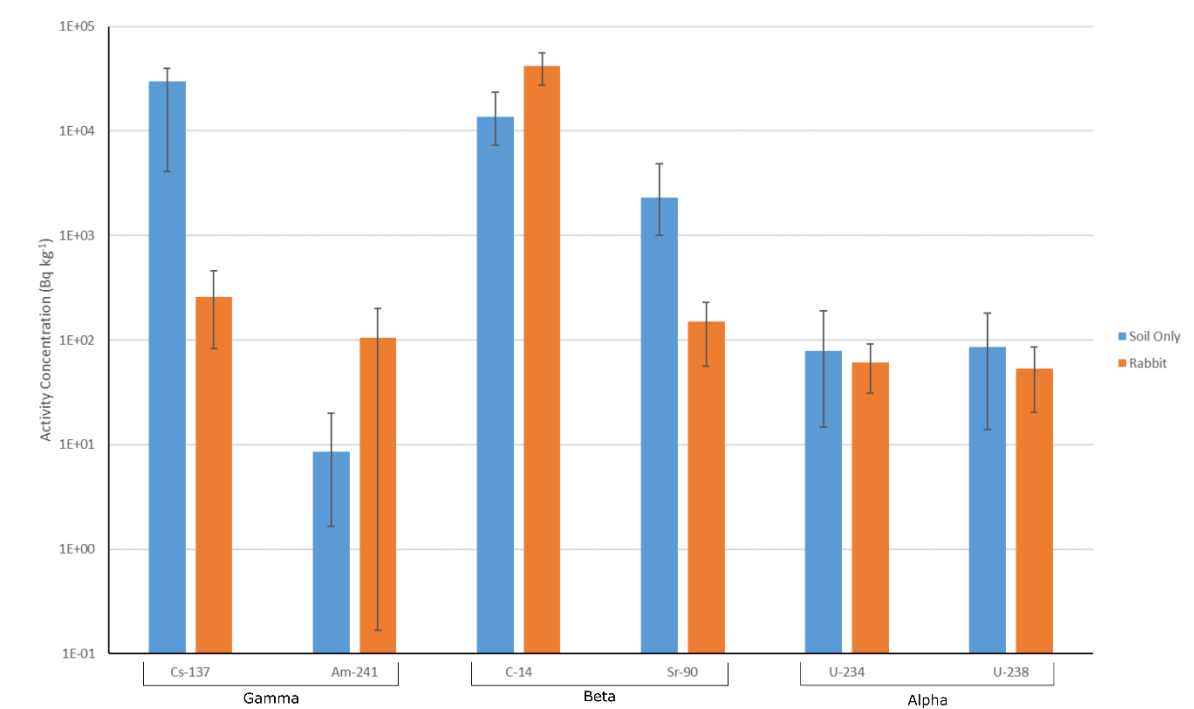
Figure 4.4: Small mammal activity concentrations required to reach a 10 µGy h⁻¹ screening dose rate. Compared for concentrations derived from rabbit only data and for rabbit and soil data. No ²²⁸Th activity concentrations are included because this radionuclide was not present/reported in RIFE for both rabbit and soil in the selected locations. Activity concentrations were calculated using data collected from RIFE (Environment Agency et al., 2014).

4.4 Discussion

4.4.1 Organisms and radionuclides of importance

Examination of the estimated doses to organisms (Table 4.2) in the 14 locations recorded in RIFE showed that, generally, small organisms close to the ground receive a high external dose whereas larger ground based organisms receive a larger internal dose (as shown by Vives i Batlle et al. (2007)). For the smaller organisms, this is likely because their body mass is assumed within soil and therefore in closer proximity to the radionuclides that are present there whereas for larger organisms, their larger volume means more energy is deposited inside the organism from the decay of internally present radionuclides. The exceptions in Table 4.2 are for Capenhurst, East Northants and Springfields, where measured radionuclides are predominately alpha emitters. It should be noted that these results rely heavily on the occupancy factor for each organism. For example, small mammals are generally assumed to be 'in soil' instead of 'on soil' which is not true for all cases (but is used in screening

assessments). Therefore, the range of doses calculated in this chapter is likely to be greater than what is shown and there is likely to be more overlap between the reference organism groups.

There were seven radionuclides in total that contributed most to dose in all of the targeted organism groups. This was a mixture of gamma (^{137}Cs and ^{241}Am), beta (^{14}C and ^{90}Sr), and alpha (^{228}Th, ^{234}U and ^{238}U) emitters. Most of these radionuclides are commonly investigated in the literature (see chapter 3.2). It is noted that ^{228}Th is only important at a single location (East Northants) and is so only because it has a relatively high soil concentration when compared to the other radionuclides that are present. Comparison of the activity concentrations (to reach a screening level) measured in rabbits to those estimated from the soil only data shows, whilst there is no difference in the outcome of the top dose contributing radionuclides (listed above), there is a discrepancy in the activity concentrations that were derived. In Figure 4.4 it is shown that there is an increase in ^{241}Am and ^{14}C activity concentrations in rabbit whereas the remaining radionuclides all decrease in activity concentration. This is caused by a difference between the measured and estimated (using ERICA CRs) internal activity concentration some of the radionuclides (e.g. the ^{137}Cs CR is up to 400 times smaller in the rabbit data). This comparison highlights the importance of ascertaining activity concentrations in both the media and within the targeted organism for detailed assessments instead of relying solely on the predictive models. The CRs in the ERICA tool are often derived from a limited set of highly variable data (e.g. Howard et al., 2013a) and this is the reason why site-specific data is preferred for more detailed assessments.

4.4.2   Live-monitoring potential of target radionuclides

According to this study, the gamma emitting radionuclides of importance (in a UK regulatory context) were ^{137}Cs and ^{241}Am. Accumulation of ^{137}Cs occurs within the soft tissues across the whole organism body (ICRP, 1979) and has sufficient penetration through tissue to be detected by a radiation detector placed externally to the target organism (e.g. Howard et al., 1987, Eldridge, 1989, Brynildsen and Strand, 1994, Moss and Horrill, 1996). Interference to measurement of ^{137}Cs would likely only come from ^{110m}Ag and ^{210}Bi. Bi-210 would only be present because it is a product in the ^{238}U decay chain and has a short half-life. It would, therefore, be highly unlikely to be in sufficient quantities to interfere with the measurement of ^{137}Cs. For ^{110m}Ag, even if this were to be present in greater quantities, there are seven characteristic gamma peaks that have a >10% decay probability and therefore ^{110m}Ag could

easily be identified if an MCA is used. Because the screening level activity concentrations that were derived (Figure 4.3) indicate there is likely to be sufficient radiation exiting the body of an organism to be measurable, even at the lower estimate indicated in Figure 4.4 (or if a lower screening level were to be applied: e.g. 5 uGy h[-1] (Copplestone et al., 2005)), this means ^{137}Cs is a suitable radionuclide for live-monitoring for compliance monitoring.

Despite accumulating mainly on the bone surface (45%) and in the liver (45%), the second gamma emitting radionuclide, ^{241}Am, has sufficient penetration of soft tissue (greater than 3 cm) to be externally detected by a suitably placed detector (e.g. in range of the liver). Further, the main interfering radionuclide, ^{232}Th, would unlikely be a problem for detection; with an estimated average concentration in UK soil of 32 Bq kg^{-1}(Beresford et al., 2008b) it is unlikely to accumulate in an organism (its CR is on the order of 10^{-3}) such that it would not interfere with measurement of ^{241}Am. The main problem with ^{241}Am, however, is it only has one low emission energy of 59.54 keV (Appendix 10.1), meaning a very low background is required for a measurement to be made. Because ^{241}Am has no daughter products that would be viable as an alternative measurement method, detection of this low emission energy is the only option. Detection of this low energy can be accomplished using a specially built detector (Clark et al., 2011) named "Field Instrument for the Detection of Low Energy Radiation" (F.I.D.L.E.R.). This is a rugged field instrument that uses a thin scintillation crystal to reduce background (including interactions caused by higher energy gamma decays) to a level where ^{241}Am can be quantified. Measurement of ^{241}Am could, therefore, be possible. The low screening level activity concentrations (Figure 4.3), however, mean the detection and measurement of ^{241}Am would be unlikely in a live-monitoring context (especially if a lower screening level were to be applied).

The beta emitting radionuclides determined to be of importance were ^{14}C and ^{90}Sr. Although the ^{14}C radionuclide accumulates across the whole body and has screening level concentrations that would be suitable for measurement, it does not have sufficient penetration ability (<0.3 mm; Figure 4.1) to detectable through fur or feathers on an organism. As it also decays to a stable daughter product, direct internal measurement of ^{14}C was deemed not possible.

The second beta emitter, on the other hand, presents a better prospect for measurement. The beta emission from ^{90}Sr has the potential for penetration through a soft tissue thickness of up to 1.9 mm (Figure 4.1) though, as this radionuclide accumulates mainly in bone (Appendix

10.1), measurement would be restricted to within organisms where the surrounding soft tissue and any fur/feathers are sufficiently thin for the beta emission to pass through. Another barrier to measurement is the interfering radionuclides. Of the other radionuclides likely to be present within a measurement location, ^{137}Cs would cause the greatest interference because it has a beta emission with a similar decay energy (Figure 4.1) and is often of higher abundance in soils (Table 4.1). To assist with the determination of ^{90}Sr content (Bondarkov et al., 2011), the daughter product of ^{90}Sr, ^{90}Y, can be used. The decay energy of ^{90}Y is 2.2 MeV (Appendix 10.1) translates to a soft tissue penetration of approximately 11 mm and, because it has a short half-life (64 hours), will be in equilibrium with ^{90}Sr. Measurement via ^{90}Y has already proved possible for small organisms (Bondarkov et al., 2011) and, because the derived activity concentrations to reach a 10 µGy h^{-1} screening dose rate (Figure 4.3) are relatively high, would therefore make ^{90}Sr a suitable radionuclide for live-monitoring.

The alpha emitting radionuclides determined to be of importance were ^{228}Th, ^{234}U, and ^{238}U. These radionuclides mostly accumulate within the bone or an internal organ (See Appendix 10.1). None of the alpha emissions from these radionuclides would have the penetrative ability to be detected externally from the body of an organism and only one of these radionuclides; ^{228}Th, has a gamma emission. This emission is, however, of low energy and low decay probability and, considering the derived screening level activity concentration is relatively low (Figure 4.3), means live-monitoring of this emission would be unlikely. Of the daughter products for these alpha emitters, only ^{228}Th and ^{238}U decay to radionuclides that have a detectable emission. For ^{228}Th, this is ^{212}Pb, which has a 238.63 keV (43.3%) gamma emission, and ^{208}Tl which has a 583.19 KeV (84.5%) gamma emission (though only 35% of the parent radionuclide decays to ^{208}Tl). The already low derived screening level activity concentrations (Figure 4.3) mean there would be insufficient quantities of these daughter products to live-monitor the concentration of ^{228}Th in the body of an organism. Similarly, whilst ^{238}U has a daughter product, ^{234m}Pa, that has a detectable 2290 keV (98%). emission, the initial derived screening level activity concentrations (Figure 4.3) would likely be too low for live-monitoring (and would be obscured by ^{90}Y if this was also present in the target organism. None of these three alpha emitters would, therefore, be suitable for live-monitoring.

4.4.3 Live-monitoring potential for organisms in the UK

Applying the likelihood of detection and measurement (discussed in the previous section) of the target radionuclides to the target organisms within each measurement site (Table 4.3) results in the following general categorisations for the reference organisms. The radionuclides likely to contribute most to internal dose in birds, large mammals and small mammals at the sites specified in Table 4.3 is ^{137}Cs and ^{90}Sr. These two radionuclides were the only two deemed viable for live-monitoring and large and small mammals are generally the highest (total) dose receivers in areas where these radionuclides appear (Table 4.2). There are already examples of these two radionuclides being live-monitored: ^{137}Cs has been (and in some cases still is) routinely monitored in (larger) livestock and there is one detector in Ukraine capable (though not fully portable) of ^{137}Cs and ^{90}Sr monitoring in small mammals and birds (see Chapter 3.4). For reptiles and amphibians (and to a lesser extent annelids and flying insects) the ^{137}Cs and ^{90}Sr radionuclides are a contributor to internal dose at some of the sites. The primary contributor to internal dose, however, is most often ^{241}Am which was deemed unlikely to be live-monitored. Therefore, live-monitoring of these organisms is limited (by site) but possible. For the remaining reference organisms: arthropods and molluscs, there are few sites where ^{137}Cs or ^{90}Sr are a main contributor to internal dose. In most instances, however, the radionuclides of interest are usually ^{241}Am or the uranium radionuclides. Live-monitoring is therefore deemed unlikely for these two organisms. Here, new alternative monitoring approaches would need to be found (the type of reference organism means the ones described in Chapter 3.3 would not be feasible).

A word of caution is applied to these results. They are derived from a limited set of data and it is assumed the monitored radionuclides are the only radionuclides present at the site. A look at the tables in RIFE (Environment Agency et al., 2014) shows this is unlikely (e.g. soil measurements from Capenhurst are limited to ^{99}Tc, ^{234}U, ^{235}U and ^{238}U whereas measurements from rabbit give a much wider list of radionuclides). Further, the use of generic ERICA CRs in these calculations means there is likely a high degree of error included in the derived screening level activity concentrations for each site. The radionuclides that contribute most to internal dose (Section 4.3.1) as well as for the screening level activity concentrations (Figure 4.4) does not, however, differ largely between the results for the soil only data and those derived using combined rabbit and soil data (Figure 4.4) though is not known how this would propagate across the other reference organisms.

4.5 Conclusion

It was determined in this study that small ground dwelling organisms are likely to be more susceptible to external doses for at least gamma-emitting radionuclides whereas larger ground based organisms were more susceptible to internal doses (as has been reported by other authors, e.g. Vives i Batlle et al. (2007)). Of the radionuclides (present at UK regulated sites) identified as contributing the most to internal dose for these organisms the only two viable for live-monitored would be ^{137}Cs and ^{90}Sr. Monitoring of ^{241}Am may be possible but is unlikely. The remaining radionuclides ^{14}C, ^{228}Th, ^{234}U, and ^{238}U all have properties unfavourable to live-monitoring. Quantification of these radionuclides would therefore have to rely on taking samples from the organism (see alternative methods in Chapter 3.3).

Based on the likelihood of live-monitoring (section 4.4.3), the results indicated that the focus of method development would be best placed on the measurement of ^{137}Cs and ^{90}Sr and the most suitable organism targets would be birds and small mammals (^{137}Cs content in large mammals is already possible with existing portable detectors though the determination of ^{90}Sr in large mammals should also be explored). The development of a capable portable live-monitor would, therefore, be a beneficial advancement of the currently available methods.

In deriving these conclusions, it was noted that results were reached from a limited data set and using a number of broad assumptions. Therefore, there is likely a large degree of error to the activity concentrations (required to reach a 10 µGy h^{-1} screening dose rate) that were derived. The conclusions drawn were, however, compared to measurements taken from rabbit and this did not appear to affect the outcome.

5 Configuration of detection materials

5.1 Introduction

The previous chapter concluded that the portable live-monitoring detector should focus on detection of ^{137}Cs and ^{90}Sr in small mammals and birds. Detection of ^{137}Cs can be achieved through measurement of a 0.662 MeV gamma emission (Figure 5.1). The most suitable detection material for this type of radionuclide was identified in Chapter 3.5.5 as a caesium iodide (CsI) scintillator. Detection of ^{90}Sr can be achieved through measurement of a 0.546 MeV beta emission. This energy is, however, very similar to a 0.514 MeV beta emission that emanates from ^{137}Cs. As a higher energy beta emitter, ^{90}Y (assumed to be in equilibrium with ^{90}Sr) can be used to assist in the determination of the ^{90}Sr content from a beta measurement containing a contribution from ^{137}Cs. The most suitable detection material for beta emitting radionuclides was identified in Chapter 3.5.5 as a thin plastic scintillator. A dual detector system is therefore required to accommodate the detection of the two target radionuclides.

The design of the detection materials has two further factors to consider: the size of the detection material and where it is placed in relation to the target organism. These two factors depend on the properties of both the target organism and each radionuclide and the background radiation contribution to count rate. It is the aim of this chapter to determine the optimal detector sizes and orientation for the detection of ^{137}Cs, ^{90}Sr and ^{90}Y.
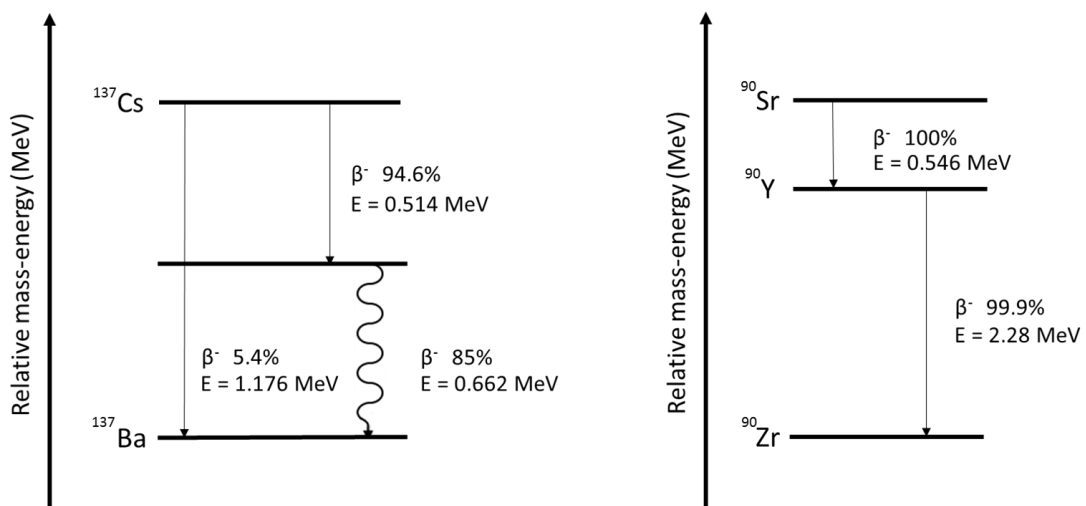
Figure 5.1: Decay schemes for a) ^{137}Cs and b) ^{90}Sr. Beta emissions are shown as straight lines, gamma by wavy line. Maximum energies are displayed for beta emissions.

5.2 Methods:

The detector size and orientation are discussed separately (sections 5.2.2 and 5.2.3 respectively). Preceding this is an outline of the wildlife properties and the radionuclide activity concentrations used in the calculations for this chapter.

5.2.1 Wildlife and radionuclide properties:

Five animals were selected to represent the target reference organisms (Table 5.1). Yellow-necked mouse (*Apodemus sylvaticus*) and bank vole (*Myodes glareolus*) were selected to represent part of the small mammal group. These species were selected because they are of radioecological interest (Baryakhtar et al., 2003) and have a large difference in their respective CRs. Two bat species were also selected as part of the small mammal group because of their protection status in the UK; the common pipistrelle (*Pipistrellus pipistrellus*) as a representative of the most abundant bat species in the UK and the serotine bat (*Eptesicus serotinus*) as the largest of the UK bat species (Battersby, 2005). The Great tit (*Parus major*) was chosen to represent the bird group as it is a likely focus species for radioecological research (e.g. Beresford et al., 2016).

A soil activity concentration was used, in combination with organism whole-body activity concentrations, to estimate internal and external doses to the organisms listed above. The soil radionuclide activity concentration was set at 10 kBq kg^{-1} for ^{137}Cs. This was the soil ^{137}Cs activity concentration required (in combination with organism internal activity) to reach a screening dose rate of 10 µGy h^{-1} in a small mammal (chapter 4). Calculations involving the bird reference organism were set at the same concentration so as to allow comparison of the measurability of each organism type under a single assumed activity concentration. Sections requiring activity concentrations for ^{90}Sr assumed an internal activity concentration of 2.3 kBq kg^{-1} (also based on the results from Chapter 4).

Table 5.1: Properties of target organism's

Animal	Scientific name	Weight (kg)	Dimensions (cm)			CR for ^{137}Cs
			L	W	H	
Yellow necked mouse	*Apodemus flavicollis*	0.035	7	3	3	1.9
Bank vole	*Myodes glareolus*	0.04	8	4	4	0.78
Common bat	*Pipistrellus pipistrellus*	0.008	4.5	3	3	0.005
Serotine bat	*Eptesicus serotinus*	0.034	7	4	4	0.005
Great tit	*Parus major*	0.018	8	4	4	0.096

Weights and geometries assumed from (Macdonald, 2010) for the rodents, (Bat Conservation Trust, 2016) for bats, and (British Trust for Ornithology, 2016) for the bird. The CRs were those presented in Beresford et al. (2016).

5.2.2   Detector size

For an activity measurement from the animal to be made with confidence, the radiation emitted from the animal must be of sufficient size such that it is distinguishable from the background radiation, i.e. it satisfies the criteria set out by Currie (described in chapter 2). It is assumed here the majority of external radiation will come from ^{137}Cs in the ground (See chapter 4 for interfering radionuclides) and that the skyshine contribution (radiation emitted from radionuclides in the ground that is reflected or scattered back down to the ground surface due to interactions in the atmosphere) will be minimal (Mitchell et al., 2009). Therefore, for the determination of ^{137}Cs in the body of an organism, the size of the CsI(Tl) scintillator must be optimised so as to maximise the measurement of the internal ^{137}Cs radiation emitted from the target organism whilst minimising the measurement of background ^{137}Cs gamma radiation present in the surrounding environment. In contrast, the low penetrative energy of ^{90}Sr means only a thin plastic scintillator is required and, therefore, the background gamma contribution can be considered to be minimal (when compared to the CsI scintillator). Due to the low penetrative energy of the ^{90}Sr, however, the detection material should cover as much of the organism's surface areas as possible.

To determine the optimal CsI scintillator size a model was created to estimate the radiation emitted from a) the ground (Section 5.2.2.1) and b) the organism (Section 5.2.2.2). The organism was assumed to be sitting on the surface of the detector (Figure 5.2) with the shielding positioned between the detector and the ground surface[3].
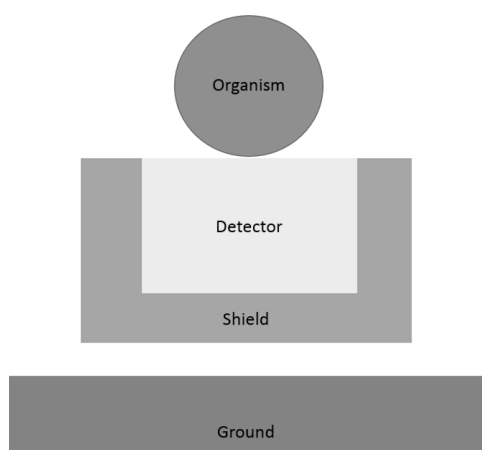
Figure 5.2: Assumed configuration for gamma detector. The detector is placed between the ground and organism and is surrounded by a shield on surfaces visible to the ground.

---

[3] This arrangement may not always be true for a portable detector but would be the ideal placement due to the animal located centrally on the surface of the detector. Where possible, the effect of different detector placements is considered

5.2.2.1 External radiation from the surrounding environment

For a given activity concentration in the ground, C_{soil} (Bq g^{-1}), the number of photons ϕ_{soil} (Equation 2.15) estimated to be detected in the detection material due to radiation emitted from the ground needs to take into consideration the fraction of emitted photons that are attenuated in the soil (defined in this chapter as a **soil coefficient**, μ_{soil}, specific to a radionuclide), the attenuation caused by any **shielding** that is present (μ_{shield}), the **surface area** of the detector ($A_{detector}$), and the **intrinsic efficiency** (ϵ_{int}) and **photopeak** (ϵ_P) of the scintillator. The assumptions made for each of these components are described in the rest of this subsection.

$$\phi_{soil} = C_{soil}\, \mu_{soil}\, \mu_{shield}\, A_{detector}\, \epsilon_{int}\, \epsilon_P \qquad\qquad 5.1$$

The fraction of gamma photons per radioactive disintegration that can reach the ground surface (the **soil coefficient, μ_{soil}**) was estimated by modelling the ground surrounding a detector (assumed to be positioned on the ground surface) as a series of hemispheres (of radius r cm) from which the radiation is emitted from the inner surface of each one (Figure 5.3). The quantity of gamma photons reaching the surface from each hemisphere, $\delta\mu_{soil}$, can therefore be estimated (Equation 5.2) by multiplying the equation for radiation attenuation within a spherical volume (Equation 2.3) by the visible volume ($2\pi r^2. \delta r$) of the hemisphere.

$$\delta\mu_{soil} = \frac{2\pi r^2}{4\pi r^2}\, e^{-(\mu/\rho)\rho r} \cdot \delta r \qquad\qquad 5.2$$
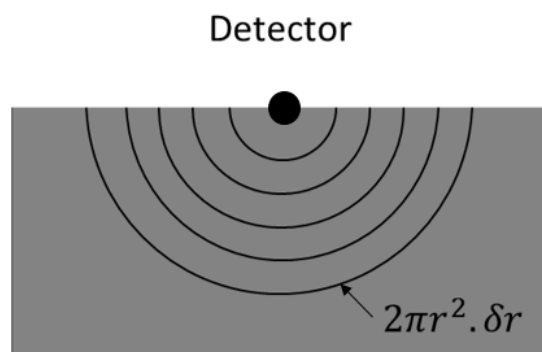
Figure 5.3: Model for radiation emitted from ground. Each hemisphere (volume V g cm^{-2}) is a radius r cm from central detector. The volume is defined as half the derivative of the equation for a spherical volume.

The radii of the hemispheres will range between zero and some maximum distance defined as R_{max}. Integration of Equation 5.2 between these two radii therefore results in Equation 5.3. By assuming R_{max} is large then the fraction of gamma photons that can reach the surface of the ground simplifies to the approximation shown in Equation 5.4.

$$\mu_{soil} = \frac{1}{2(\mu/\rho)\rho}\left[1 - e^{-(\mu/\rho)\rho R_{max}}\right] \qquad\qquad 5.3$$

$$\mu_{soil} \approx \frac{1}{2(\mu/\rho)\rho} \qquad\qquad 5.4$$

The emission rate from the soil depends on the activity concentration, C_{soil} (Bq g^{-1}), of the radionuclide, the density of the ground, ρ (g cm^{-2}), and the decay probability (branching ratio), BR (expressed as a decimal fraction). Therefore, per radioactive disintegration (Bq g^{-1}), the fraction of photons that reach the ground surface is given by equation 5.5 (note the densities in the equation cancel and therefore only the soil attenuation coefficient and branching ratio for the radionuclide are important).

$$\mu_{soil} \approx \frac{1}{2(\mu/\rho)} BR \qquad\qquad 5.5$$

The **shielding attenuation (μ_{shield})** depends on the thickness and mass attenuation coefficient of the shielding material (Chapter 2.2). The shielding was assumed to be lead (Chapter 3.5.5) and, therefore, has an attenuation coefficient of 0.1115 cm^2 g^{-1} (Hubbell and Seltzer, 1996). The shield thickness, however, is limited by the size of the scintillator and a maximum allowable weight for keeping the detection system portable. A maximum shield weight of 20 kg was assumed. Based on the scenario shown in Figure 5.2, along with the assumption the majority of interfering background radiation is emitted from the ground, it was decided half of this shield weight should be allocated to surround the scintillator such that a wall, of thickness x cm, surrounds the sides and bottom of the detection material but remains open at the top. The remainder of the shielding weight is allocated to the walls of any restraint. If a different orientation is used, or more detectors are included, then these allocations would need to be altered appropriately.

A set shield weight means the shield thickness will vary depending on the size of the internal scintillator. The total volume of the detector comprises of the volume of the shield and the volume of the detector scintillator (Equation 5.6). Therefore, for a weight of 10.0 kg and density of 11.34 g cm^{-1}, the maximum allowable lead shielding volume is 881.8 cm^3. If this surrounds a detector of length L, width W, and depth D, then equation 5.6 can be rewritten to that shown in equation 5.7 (where x is the shield thickness in cm).

$$V_{Total} = V_{shield} + V_{Detector} \qquad \text{5.6}$$

$$(L + 2x)(W + 2x)(D + x) = 881.8 + LWD \qquad \text{5.7}$$

Shield thicknesses were calculated (using equation 5.7) for a range of detector dimensions; lengths from 2 to 15 cm in increments of 1 cm, widths from 1.5 to 5.5 cm in increments of 0.5 cm and depth from 1.5 to 3.5 cm in increments of 0.5 cm (resulting in a total of 630 geometries). These allowable thicknesses where used in combination with Equation 2.3 to determine the attenuation (μ_{shield}) introduced by a lead shield (Equation 5.8).

$$\mu_{shield} = e^{-(\mu/\rho)\rho x} \qquad \text{5.8}$$

The detector was assumed as a single plane, parallel to the ground, passing through the centre of the detector crystal. This simplification was deemed sufficient for the purposes of this chapter due to the generalisations already made for calculated surface activities. Under this assumption, the detector **surface area ($A_{detector}$)** that is visible to the ground was therefore assumed to only be the area (in cm^2) covering the bottom surface of the detector material.

The **intrinsic efficiency** (ϵ_{int}) and **photopeak** (ϵ_P) depend on the choice of detection material. The detection material chosen for gamma detection was CsI(Tl) (see Chapter 3.5.5). The efficiency of this scintillator, for the range of volumes, was determined directly from Knoll (2010). The photopeak was determined using equation 5.9 from Cesana and Terrani (1989), where the variables a(E) and b(E) are photon energy dependent coefficients that are defined from tables reported in Cesana and Terrani (1989) and the volume to surface area ratio (V/A) was calculated for the targeted range of detector dimensions.

$$\epsilon_P = 1 - a(E)\, e^{\left[-b(E)\cdot\frac{V}{A}\right]} \qquad \text{5.9}$$

5.2.2.2   Internal radiation from the organism

For a given internal activity concentration in the organism, C_{org} (Bq g^{-1}), the number of photons ϕ_{org} (equation 5.10) that are estimated to be detected in the scintillating material needs to take into consideration the fraction of photons that will be attenuated in the organism (defined in this chapter as an **animal coefficient**, μ_{org}), the **surface area** (A_{org}) of the animal visible to the detector, and the **intrinsic efficiency** (ϵ_{int}) and **photopeak** (ϵ_P) of the scintillator. The assumptions made for each of these components are described in the rest of this subsection.

$$\phi_{org} = C_{org}\, \mu_{org}\, A_{org}\, \epsilon_{int}\, \epsilon_P \qquad\qquad 5.10$$

The **intrinsic efficiency** (ϵ_{int}) and **photopeak** (ϵ_P) values remain the same as for section 5.2.2.1. The **animal coefficient** (μ_{org}) was determined by modelling each organism as a cylinder with dimensions and weight as described in Table 5.1. The body was sectioned into cuboids such that the model was 11 cuboids long by 11 in diameter. The dimensions of each cuboid were determined by the length and diameter of each organism. The number of photons emitted from each cuboid ϕ_i (where i identifies a specific cuboid) was calculated using Equation 5.11, where C_{org} is the activity concentration (Bq g^{-1}), BR is the branching ratio for ^{137}Cs, m is the mass (g) of the organism, and n_T is the total number of cuboids in the model (set at 1869 in this model).

$$\phi_i = \frac{C_{org}\, BR\, m}{n_T} \qquad\qquad 5.11$$

The detector was assumed to be one cuboid in size and positioned centrally and underneath the organism, touching the skin surface (shown in Figure 5.4). The distance, r cm, between each cuboid and the detector was determined using Pythagoras theorem (calculated with three dimensions due to the 3D view of the model). The number of photons directed towards the detector, from a single cuboid, is attenuated along this distance according to Equation 2.3. The sum of the remaining photons from all cuboids (Equation 5.12) is therefore the total number of photons estimated to reach the detector (g cm^{-2} s^{-1}).
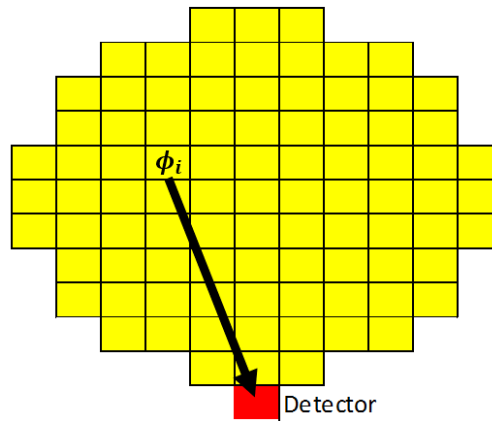
Figure 5.4: Cross section of organism model. Cross section 'slice' through central view of organism model. Ten further slices make up the length of the organism. Each cuboid is represented by the yellow squares. The detector is shown as the red square to the bottom of the model.

$$\mu_{org} = \sum_{i=1}^{n_T} \frac{\phi_i}{4\pi r_i^2} \, e^{-(\mu/\rho)\rho r_i} \qquad\qquad 5.12$$

By assuming an initial body activity concentration C_{org} of 1 Bq g^{-1}, μ_{org} becomes a coefficient for the fraction of photons, per radioactive disintegration (Bq g^{-1}), that reach the surface of the respective organism (g cm^{-2} s^{-1}). For the purposes of this chapter, the organism tissue density was assumed to be 1 g cm^2 (this does cause a discrepancy between the organism volume and mass but is accepted here because the model ignores internal cavities and bones). Mass attenuation for soft tissue was assumed to be 7.87x10^{-2} cm^2 g^{-1} (Hubbell and Seltzer, 1996).

The **surface area** (A_{org}) was assumed to be the area of contact between the animal and the detector i.e. a detector that is much larger than the organism will be limited by the surface area of the organism and a detector that is much smaller than the organism will be limited by the surface area of the detector. It could be expected there will be some degree of detection in the sides of the detector material due to the parts of the organism overlapping the edges of the detector. It was assumed for the purposes of this model, however, that this influence was negligible due to the already simplified shape used for the organism model. There are four scenarios (Figure 5.5) for how the animal can vary in size in relation to each of the scintillator sizes defined in section 5.2.2.1. The surface area in contact was therefore determined by multiplying the minimum width by the minimum length (detector vs animal dimensions).
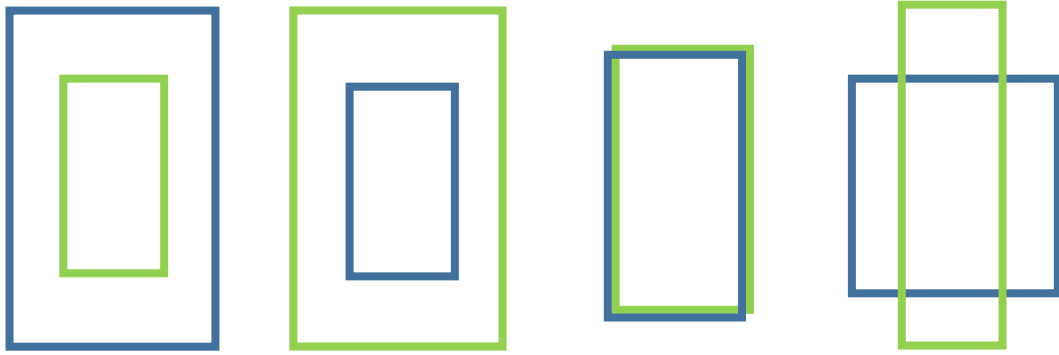
Figure 5.5: Arrangement of animal over detector. Arrangements of animal (green) and detector (blue) showing a) detector > animal, b) detector < animal, c) detector = animal and d) detector crosses under animal.

5.2.2.3 Determination of optimal detector size for gamma detection

Optimal detector dimensions were determined by calculating the ratio (ϕ_{ratio}; dimensionless) for the estimated detected photon emission from the organism (ϕ_{org}; Equation 5.10) against the limit of detection, L_D (Equation 2.16), for the estimated detected photon emission from the ground (ϕ_{soil}; Equation 2.15). In this form, this ratio (Equation 5.13) defines how far above the background L_D the estimated emission from the organism is (i.e. if ϕ_{ratio} is less than one then the source measurement cannot be statistically separated from background). ϕ_{ratio} was calculated for each detector size and each organism. The maximum ϕ_{ratio} for each organism would indicate the optimal detector dimensions.

$$\phi_{ratio} = \frac{\phi_{org}t}{(2.71 + 4.65\sqrt{\phi_{soil}\,t})} \qquad\qquad 5.13$$

A counting time was set based on the desire for a short restraint time. Bondarkov et al. (2011) found in the use of their live-monitor that small mammals could reasonably withstand (though would be unethical to restrain for) several hours in the sampling box but are likely to destroy the restrain if held for a long period of time. For birds, on the other hand, Bondarkov et al. (2011) found they can only survive for up to 600 seconds when held in the restraint. It was therefore decided to set a count time of 600 s as an absolute maximum for each organism, though the use of shorter count times, especially for birds, will also be discussed. The background counting time was also set at 600 s as a conservative measure though in practice it is expected that longer background readings would be made whilst in the field.

5.2.3 Detector orientation

The penetrative ability of gamma radiation from ^{137}Cs, coupled with the accumulation across the soft tissues, means the location of the CsI scintillator should not impact greatly on measurement, provided the detector is aligned centrally and lengthways on the organism body. In contrast to this, the accumulation of ^{90}Sr in bone, coupled with its short penetration in tissue, means the measurement of this beta radiation from an organism requires the plastic scintillator to be orientated in such a way that the maximum emission from the organism can be measured. The detector could be designed in such a way that it surrounds the entire animal. This design, however, limits the possibility of adapting a detector to multiple animal sizes and could hinder the measurement of ^{137}Cs from the organism (especially if any supporting backing material and covering is sufficiently thick enough). Placement for the ^{90}Sr detector was therefore considered in one of the following orientations; above, below, or to the side of the organism. The direction of maximum detection of ^{90}Sr from an organism was estimated by modelling the fractional radiation emitted from bone and its subsequent attenuation through the surrounding soft tissues before reaching the plastic scintillator. This estimation was repeated for ^{90}Y since it will be used to assist the determination of ^{90}Sr content.

For a given bone surface emission, N_{bone} (Bq), emitted from an infinitely small surface area on the bone, δa (cm^2), the quantity of radiation, N_{surf} (Bq), that passes through a distance, R (cm), of surrounding tissues can be estimated using equation 5.14. Integration of this equation over the whole surface area, A_{bone} (cm^2), of a single bone results in equation 5.15.

$$N_{surf} = \int^{A_{bone}} \frac{N_{bone}}{4\pi R^2} e^{-(\mu/\rho)\rho R} . \delta a \qquad 5.14$$

$$N_{surf} = \frac{N_{bone} A_{bone}}{4\pi R^2} e^{-(\mu/\rho)\rho R} \qquad 5.15$$

If the radioactivity present on the bone is assumed to be distributed evenly across the bone surface (see section 5.2.3.1), the emission rate per cm^2 is dependent (as shown in equation 5.16) simply on the radionuclide activity concentration, C_{org} (Bq kg^{-1}), the mass, m (kg), of the organism and the total surface area, A_{Total} (cm), of all bones within the organism.

$$N_{bone} = \frac{C_{org}\, m}{A_{Total}} \qquad 5.16$$

Radiation emitted from the surface of the bone traverses through a layer of muscle, skin, and fur before it reaches an externally located detector (Figure 5.6). The emission geometry in this model is only considered in a single direction (i.e. it ignores the standard 4π geometry) for the purpose of simplifying the calculation of attenuation within the tissues covering the bone. This was considered appropriate as the model is designed to only estimate the optimal orientation of a detector and not to provide an accurate estimation of measurement. The tissues (of R cm) surrounding the bone was simplified to be only a layer of soft tissue (thickness R_{tis} cm) and a layer of fur (thickness R_{fur} cm). Substituting this, along with equation 5.16, into equation 5.15 results in the total estimated externally measurable radiation from an organism's body (Equation 5.17), where ω_{Tis} and ω_{fur} are equal to the mass attenuation coefficient multiplied by the density, $(\mu/\rho)\rho$, for tissue and fur respectively. Density of tissue is again assumed as 1 g cm^{-3} and the density of fur was assumed 1.32 g cm^{-3} (Robbins, 2012).

$$N_{surf} = \frac{1}{4\pi(R_{tis} + R_{fur})^2}\frac{C_{org}\, m\, A_{Bone}}{A_{Total}}e^{-(\omega_{tis}\, R_{tis}+\omega_{fur}\, R_{fur})} \qquad 5.17$$

Animal masses and radionuclide content are given in section 5.2.1. To use equation 5.17 to set up a model for the estimation of the quantity of detectable ^{90}Sr and ^{90}Y emerging an organism, the following information was required: surface area of each bone and the total bone surface area, tissue and fur thicknesses, and tissue and fur attenuation coefficients. These are detailed in the following subsections.
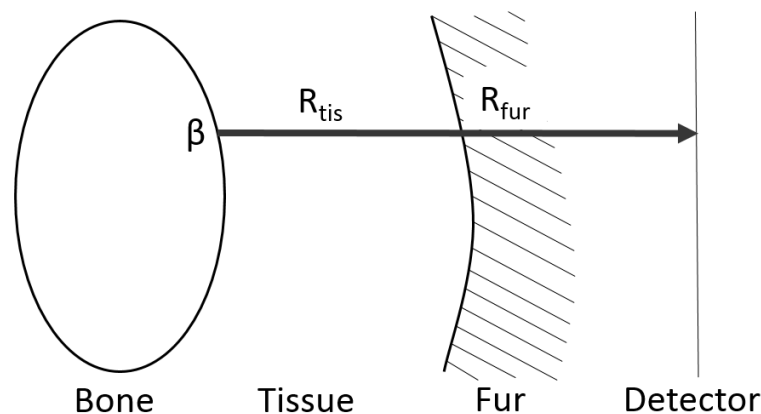
Figure 5.6: Emission of ^{90}Sr beta radiation from within an organism. Diagram showing radiation path for bone surface to animal surface.

5.2.3.1 Model data

Beta emissions from the organism body were modelled based on properties of a mouse (as a likely main sampling organism) though the effect the different anatomical structures, such as wings in birds and bats, would have on the model are discussed in section 5.4.2. Anatomical properties of a mouse were defined from CT images by Dogdas et al. (2007). This was a CT scan of a 28 g nude normal male mouse saved as a matrix of 380 x 992 x 208 pixels (0.1 mm per pixel). Dogdas et al. (2007) have used the CT data to define an atlas model of the mouse that shows details of the skeletal structure as well as various internal organs. Conversion of the CT images into the atlas model has, however, introduced some differences in object placement as can be seen in Figure 5.7 and Figure 5.8. These visual differences are present because Dogdas et al. (2007) have accounted for imaging artefacts such as those caused by scatter and beam hardening. Measurements from the atlas view (in Brainsuite version 16a1) for bone lengths (e.g. Figure 5.7) and bone surface to skin surface distances (e.g. Figure 5.8) are in close agreement to measurements taken from the CT images as shown in Table 5.2. As the atlas view has been corrected for the previously mentioned artefacts, it was decided to use this model view to define the bone surface areas and tissue thicknesses.
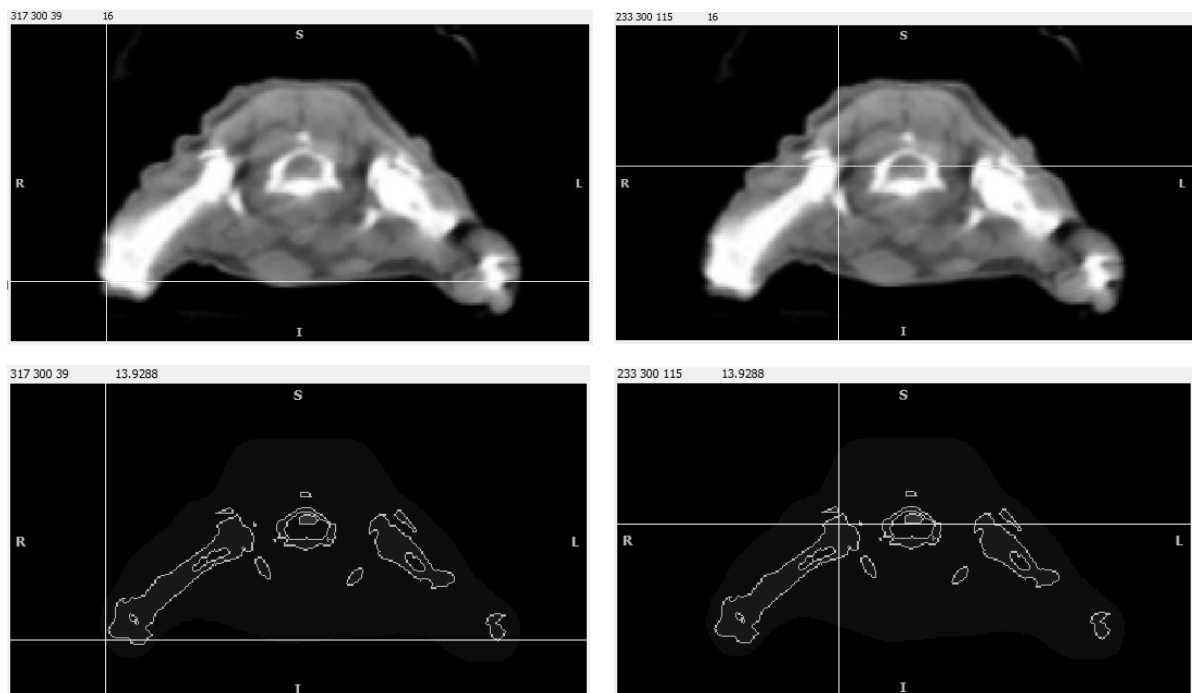
Figure 5.7: Axial cross section of forearms. Bone on the right side of the animal was measured. Coordinates for each view are given in the same position. CT Images from model by Dogdas et al. (2007).
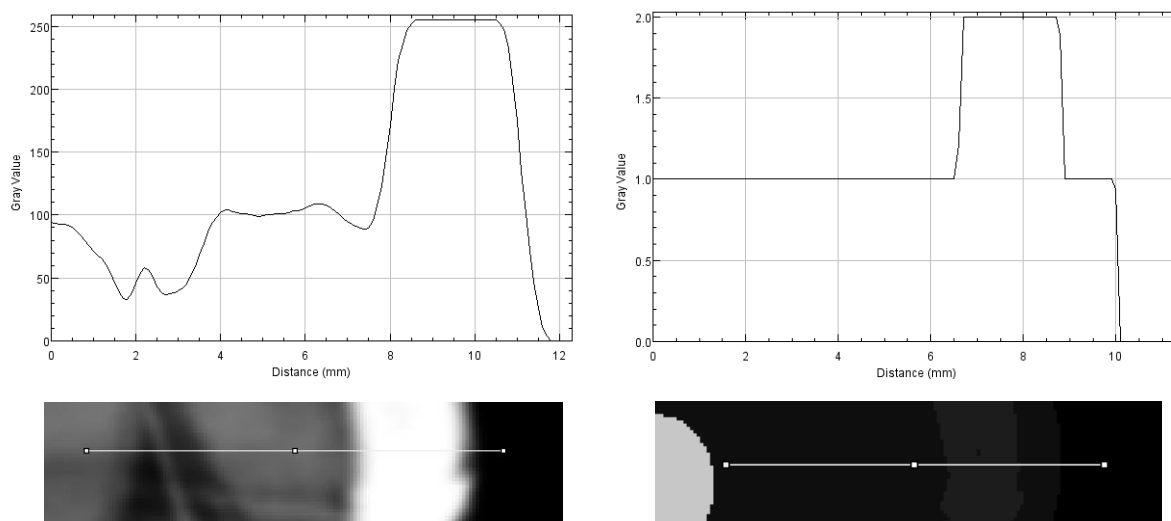
Figure 5.8: Intensity profile for coronal cross section of left mouse knee. Right shows the CT image, left shows the atlas view. Skin for knee in CT image could be 0.6 +/- 0.3 mm. Skin for knee on for atlas view could be 1.0 +/- 0.1 mm. CT Images from model by Dogdas et al. (2007).

Table 5.2: Comparison of CT and Atlas bone lengths.

	Coordinate 1 (pixel)			Coordinate 2 (pixel)			Length	
	x	y	z	x	y	z	Pixels	mm
CT	317	300	39	233	300	115	113	11.3
Atlas	313	300	42	223	300	114	115	11.5

CT coordinates are as described from Figure 5.7. Atlas coordinates are defined as positional coordinates in terms of pixels.

The position the mouse was placed in for the CT images was assumed to be close to the natural resting posture the organism would take if placed in a detector. Although deposition of ^{90}Sr occurs mainly within the bone (Cooper et al., 2012), due to the small bone sizes within the target organisms, it was assumed sufficient for this model that all the ^{90}Sr is distributed evenly over all bone surfaces. For the estimation of ^{90}Y emission rate, it was assumed ^{90}Y was in equilibrium with ^{90}Sr at the bone surface.

5.2.3.2 Bone surface area

The total surface area of bone was determined by analysing the atlas view images (208 slices) with ImageJ[4] (version 1.50i). The following instructions detail how a surface area was reached:

1. With all slices loaded into ImageJ, the scale was set using the *"set scale"* function (Analyze → Set Scale) to give a scale of 1 pixel per pixel[5].

---

[4] https://imagej.nih.gov/ij/
[5] Measurements in ImageJ are made from the middle of each pixel

2. The *"threshold"* function in ImageJ (Image → Adjust → Threshold) was then used to convert each slice into a black and white image. A "Default", "B&W" image was selected and the options for "Dark background" and "stack histogram" were set to true. The threshold range was set from 2 to 3. This setting gave an image for only the bones within the mouse being filled black and the area outside the bones filled white.

3. With the threshold option window left open, the *"analyse particles"* function (Analyse → Analyse Particles) was used to create an outline of the mouse (Figure 5.9) in each slice and measure its internal area the area. The pixel size was set to "0-Infinity" and "Outlines" was selected for the show option. "Display results", "Clear results" and "Summarize" were set to true.

4. Pressing "OK" then processed all 208 slices and output the perimeter of each bone in a table. The calculated perimeters were summed to produce a surface area in pixels and converted to mm^2 using the scale of 100 pixels per mm^2.

The surface area of each bone, or bone section, was calculated from the dimensions of the respective bone. Only bone surfaces that would be visible to an external detector were calculated (e.g. only the outer surface area of the ribs were calculated). Potential detection of radiation emitted from the inner surface of the bone is ignored under the assumption that the contribution from this 'hidden' surface will be minimal compared to the outer bone surface area. The body of the mouse was categorised into 5 regions for these calculations (Figure 5.10) and the nomenclature of bones and regions was defined from Bab et al. (2007). The bone or bone sections were modelled as follows:
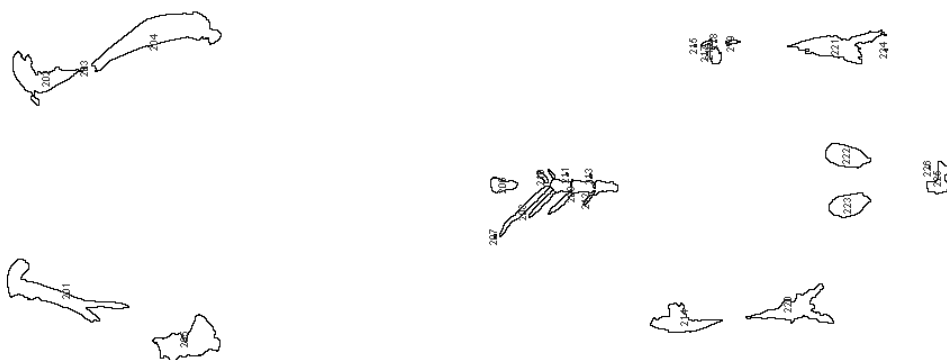
Figure 5.9: Outlines for bone perimeter in ImageJ. Slice 40. Each bone region is identified with a number (used for summing the bone surfaces). Image produced using data from Dogdas et al. (2007)
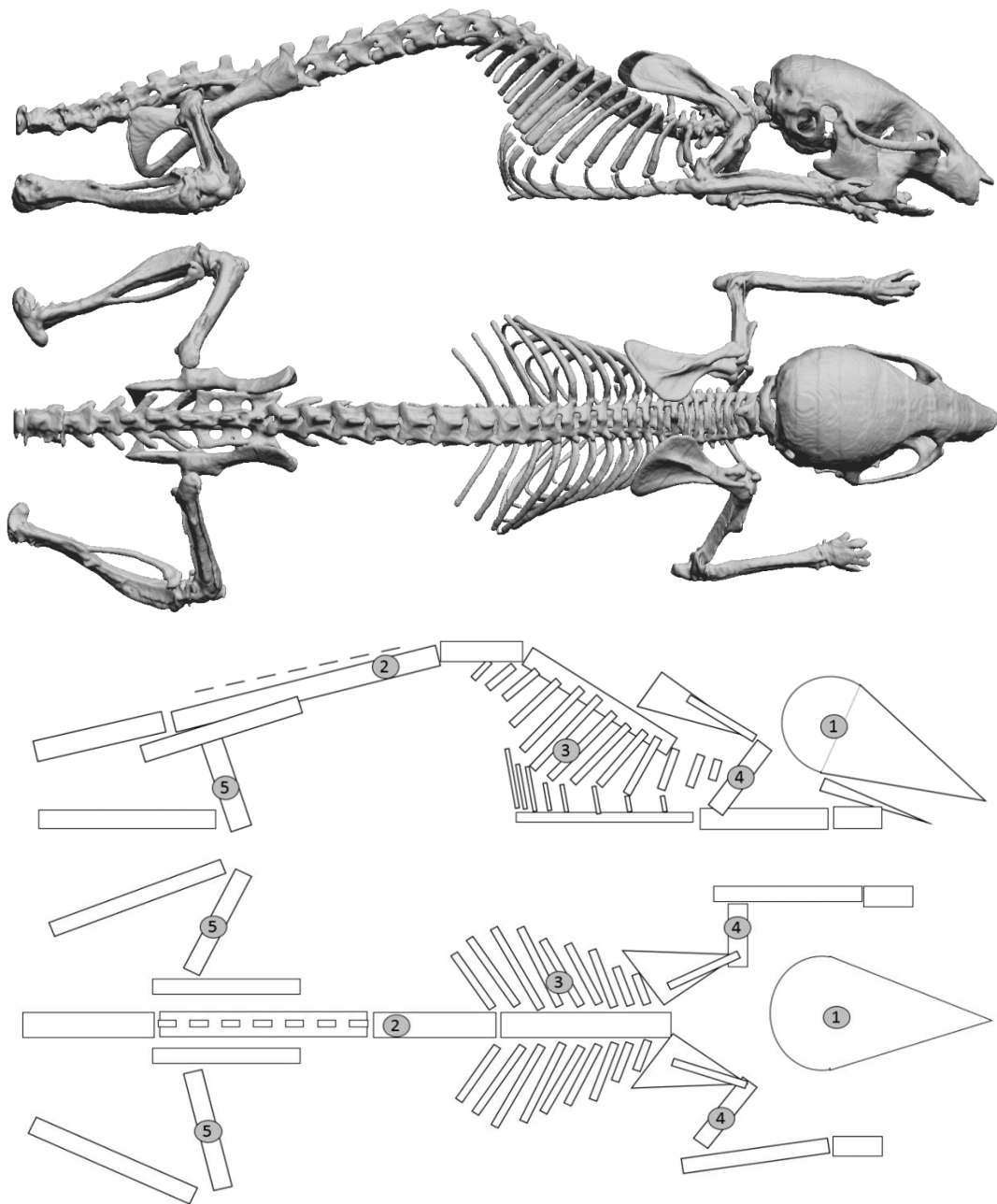
Figure 5.10: Partitioning of bone structures (above) for surface area modelling (below).1. Head: cranium and mandible, 2. Back: spinal column and caudal vertabrae, 3. Chest: ribs and sternum, 4. Arms: scapula, clavicle, humerus, forearm and manus. 5. Legs: pelvis, femur, tibio-fibular complex and hind foot. Skeletal model developed using data from Dogdas et al. (2007).
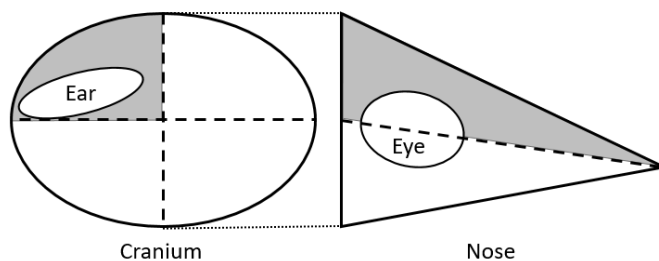
Figure 5.11: Model structure for skull. Grey regions are considered the only section of the skull where ^{90}Sr can penetrate to the skin surface.

Head: The skull was modelled in three sections; cranium, nose, and mandible (Figure 5.11). The cranium was modelled as a quarter sphere with flat circular holes removed to represent the ears (ignored for the ^{90}Y calculations). The nose section joins the cranium at the mid-point of the cranium sphere and was modelled as a half cone, without the base, and two holes removed to account for eyes. For ^{90}Sr, the mandible (jaw) is partially hidden behind the cheek muscles and so the bottom surface is the only part of the jaw likely to be visible to the outer surface of the organism. The mandible was therefore modelled for ^{90}Sr as two flat triangular surfaces (to represent each side of the bottom of the jaw) that connect at the central point of the mouth. For ^{90}Y, the mandible was assumed triangular (with right angle connected to skull) as for ^{90}Sr except wider at the base to account for the sides covered by the cheek muscle.

Back: The spinal cord was separated into 6 sections each containing a number of vertebra (V) with V1 at the base of the skull and V35 at the base of the tail. Section one (V01-V08) was deemed not visible to the skin surface due to the surrounding tissue. Sections 2 (V08-V17), Section 3 (V17-20), Section 4 (V20-V23) and Section 6 (V31-V35) were modelled as a cylinder with the top half curved surface being visible to the skin surface (the ends of the cylinder were not included); section 2 was deemed visible for only ^{90}Y. The vertebrae in Section 5 (V23-V31) had a prominent ridge that was the only part visible to the skin surface for ^{90}Sr. This section was therefore modelled as a half cylinder (without the ends) and a raised flat strip of individual rectangles to represent the ridge; the surface area of the ridge was assumed to be half the area of the flat strip and was subtracted from the cylinder surface area. It was assumed the ridge was only visible to ^{90}Sr and the ridge plus the cylinder was visible to ^{90}Y. No caudal vertebrae (tail) was present on the atlas view (nor the CT data). The bone surface area for this region was therefore estimated by using images recorded by Bab et al. (2007). This was deemed acceptable because the mouse skeleton described by Bab et al. (2007) had similar dimensions to those that were measured from the mouse atlas view. The diagram for the caudal vertebrae was copied into ImageJ and the "set scale" function was used to define the measurement scale (as indicated on the scale in the image). The caudal vertebrae volume was assumed to be solid and was modelled as an elongated cone with the base (surface of the base was not included) attached at the end of the spine (V35).

Chest: There are 13 pairs of ribs in total with each rib comprising of a dorsal bone (attached to spine) and a ventral bone (of which most are attached to the sternum). Each rib pair was labelled from R1 (closest to skull) to R13 (closest to tail). The dorsal and ventral bones in R1

were modelled as a single thin cylinder. R2-R8 were modelled as two thin cylinders to account for the curvature of the rib; one for the dorsal bone and another for the ventral bone. The ventral bones for R9 to R12 showed little to no presence and therefore only the dorsal bones were modelled as a single cylinder extruding from the spinal column. Only the outer surface (i.e. the outer half of the curved cylinder) for each rib was used to calculate the total surface area (the ends of the cylinder were not included). The shape of the sternum was assumed to be the lower half of a flattened cylinder.

Arms: The scapula was divided into two structures due to the prominent ridge that is present on the upper surface. A flat rectangle represented the ridge. A triangle, minus the area for the ridge, represented the larger scapula surface. The collar bone was deemed invisible to the skin surface due to the surrounding tissue. The humerus and forearm were each modelled as a cylinder. The ends of the cylinder were not included for the humerus and for the end of the forearm that attaches to the manus (the other end represents the elbow). Only the outer half of the humerus was deemed visible to the skin surface whereas the whole of the forearm was included in the visible surface area. The manus was simplified to a rectangular box with the surface that attaches to the forearm not included in the surface area.

Legs: The pelvis is a large bony structure that is largely central and to the rear end of the organism. Most of the pelvis lays at a greater tissue depth than for the proximal spinal column and was therefore deemed largely invisible for ^{90}Sr. Each side of the pelvis, however, has a ridge that runs parallel to the vertebrae V26 to V27 and is close to the back surface of the organism. This region was therefore modelled as a rectangular strip for ^{90}Sr. For ^{90}Y, the pelvis was modelled as a half cylinder with ends laying parallel to the spine. The femur and tibio-fibular complex was modelled in the same way as the humerus and forearm with the knee modelled as the flat end of the cylinder. The hind foot was not present on the CT images. As for the tail, the hind foot dimensions were determined from Bab et al. (2007) and the geometry was assumed to be similar to the manus; a rectangular box with the surface attaching to the tibio-fibular complex not included.

5.2.3.3   Tissue and fur thickness

Each bone was assigned a tissue thickness. These were measured from the Atlas view using Brainsuite[6] (version 16a1). Three measurements, positioned approximately evenly across the

---

[6] http://brainsuite.org/

bone, were made for each bone because the thickness can vary across the bone surface. This variance was assumed to be normally distributed and therefore the 95th percentile confidence intervals were calculated to provide an average, upper and lower estimates for the thickness of tissue covering each bone. The caudal vertebra, though absent, was estimated from the tissue surrounding the edge of the vertebrae stump shown in the atlas view. The hindfoot and manus were estimated separately because the former was not present and the latter was difficult to distinguish on the atlas view. These were assumed to only be covered in skin; the underlying muscle was considered negligible. The additional sole thickness was considered balanced with the layer of fur on the top of the hands/feet and therefore included in the fur thicknesses (see below). The hindfoot and manus skin thicknesses were estimated from Sundberg et al. (2012) at between 15 - 400 µm.

The mouse in the CT images was a nude mouse and therefore no information was directly present in these images about fur thickness. Dawson and Webster (1967) estimated a fur thickness of 1.3 mm for a house mouse. From the description of their experiment it was assumed this is the thickness of fur including the insulative air gaps. A compact fur layer was instead assumed to have an average thickness of 0.65 mm. To allow for variation in depth, and for an allowable error in differences between species, a range of ± 50% was assumed. Images of mice show fur present on the caudal vertebrae, hindfeet and manus is much shorter than for the main body. Therefore, the fur covering these locations was assumed to be half the main body fur thickness. These assumed thicknesses were combined with the tissue thickness range such that an absolute minimum and absolute maximum range could be determined.

5.2.3.4 Tissue and fur attenuation coefficients

The mass attenuations for fur and tissue were calculated using equation 5.18 from Gürler and Yalçın (2005) and Mahajan (2012), where E_m is the maximum beta energy and Z_{eff} is the effective atomic number of the absorber material. In this form, the mass attenuation is given in $cm^2 g^{-1}$.

$$\frac{\mu}{\rho} = 8 \, Z_{eff}^{0.28} E_m^{-1.57 \left[\frac{Z_{eff}}{160}\right]} \qquad\qquad 5.18$$

For tissue, a Z_{eff} of 7.6 was assumed based on Hendee and Ritenour (2003) and (Spiers, 1946). Taylor et al. (2012) does suggest a lower Z_{eff} due to overestimations made in the typical power-law approach used to calculating these effective numbers. It was decided, however, to

take a more conservative approach and use the higher estimate. No Z_{eff} was readily available for mouse fur and therefore one was derived using equation 5.19 (Spiers, 1946, Taylor et al., 2012); where Z_n is the atomic number for a constituent element and a_n is its fractional contribution. It was assumed the composition of fur was primarily keratin (Robbins, 2012, Wang et al., 2016) and is composed of carbon (45%), oxygen (28%), hydrogen (7%), nitrogen (15%), and sulphur (5%). The Z_{eff} of fur was therefore estimated to be 9.39.

$$Z_{eff} = \sqrt[2.94]{\sum_0^n a_n Z_n^{2.94}} \qquad\qquad 5.19$$

Inserting these values into equation 5.18 gave a ^{90}Sr mass attenuation of 35.47 cm^2 g^{-1} in tissue and 37.39 cm^2 g^{-1} in fur. For ^{90}Y, the mass attenuation was determined to be 4.02 cm^2 g^{-1} in tissue and 4.31 cm^2 g^{-1} in fur.

5.2.3.5 Determination of optimal detector orientation for beta detection

The placement for the detector was assumed to be either above, below, or to the side of the organism. Each bone was assigned a fractional visibility (between 0 and 1) for each view, based on visual observations of the CT images. The position of the mouse legs in the CT images was considered to be different from a live mouse. Images of mice show a more natural sitting position where the arms and legs are directly below the main body. They would therefore not be visible to the top detector as would be assumed by looking at the CT images only. The visibility of the arm and leg bones to the detector was therefore assumed based on a more natural sitting position. The calculated emission rate at the tissue surface for each bone was scaled according to the fractional visibility and totalled for each detector placement. These totals were compared to determine the most suitable detector position in relation to the body of the organism.

5.3 Results

5.3.1 Gamma detector size

The following factors were calculated for use in Equation 2.15 (number of photons, ϕ_{soil}, from the ground). The **soil coefficient (μ_{soil})** was defined for ^{137}Cs because this was assumed to be the most abundant type of interfering radiation that would be present in the soil (see trigger levels in Chapter 4.3.2). Setting a branching ratio of 0.85 for ^{137}Cs and a mass attenuation of 0.077 cm^2 g^{-1} for soil (Al-Masri et al., 2013) means μ_{soil} equals 5.5 g cm^{-2} s^{-1} and therefore the photons per cm^2 incident on the surface of the detector is 5.5 times the soil activity

concentration (in Bq g^{-1}). The shield thicknesses used to determine the **shielding attenuation** (μ_{shield}) are detailed in Appendix 10.3 The resulting values used for the **intrinsic efficiency** (ϵ_{int}) and **photopeak (ϵ_P)** are displayed in Table 5.3. The **animal coefficients (μ_{org})** for use in Equation 5.10 (number of photons, ϕ_{org}, emitted from the organisms) are defined in Table 5.4 for the five organisms listed in Table 5.1.

The ratios (ϕ_{ratio}) for the estimated detected photon emission from the organism, ϕ_{org}, against the limit of detection, L_D, for the estimated detected photon emission from the ground, ϕ_{soil}, are displayed in Table 5.5 for a mouse and Appendix 10.4 for the remaining four organisms. Each table is presented as a heat map with red indicating the highest ϕ_{ratio} for each organism (i.e. the largest measurement above the limit of detection) and white indicating the lowest. A comparison between each organism is made in Table 5.6 for a 2.5 cm thick detector.

The largest ϕ_{ratio} in these tables indicates the optimal detector dimensions for each organism. The effect of depth on measurement is displayed in Figure 5.12. Visual inspection the tables showed no difference between each organism for the order of most to least optimal detector depth. This figure therefore shows the maximum ϕ_{ratio} for each detector depth, normalised to the largest ϕ_{ratio} for the respective organism, and averaged across all organisms. The optimal length and widths for each detector depth and each organism are displayed in Table 5.7. There was little difference for optimal detector dimensions at each detector depth except for the depth of 2.5 cm.

Table 5.3: Derived detection efficiencies and photopeaks for CsI

	Depth (V/A)				
	1.5	2	2.5	3	3.5
ϵ_{int}	0.47	0.53	0.58	0.64	0.69
ϵ_P	0.67	0.79	0.85	0.89	0.92

Units for the depth are in cm.

Table 5.4: Animal coefficients (μ_{org}) for target organisms.

Organism	Animal Coefficient
Yellow necked mouse	5.94E-01
Bank vole	4.13E-01
Common bat	1.88E-01
Serotine bat	3.88E-01
Great tit	1.65E-01

Units for the animal coefficient are in g cm^{-2} s^{-1}.

Table 5.5: Table of ϕ_{ratio} for yellow necked mouse.

Depth (cm)	Width (cm)	length (cm)													
		2	3	4	5	6	7	8	9	10	11	12	13	14	15
1.5	1.5	171.47	193.33	205.32	211.71	214.79	214.62	186.71	164.63	146.01	130.92	117.85	107.10	97.60	89.73
	2.0	190.57	214.21	227.06	232.39	235.55	235.18	204.47	180.21	159.77	143.21	128.88	117.09	106.69	98.06
	2.5	204.33	229.17	241.11	248.06	251.26	250.74	217.91	190.81	170.17	151.55	137.21	123.87	113.56	103.71
	3.0	214.21	239.84	252.08	259.16	**262.38**	261.73	227.39	199.06	176.39	158.05	143.08	129.15	118.39	108.11
	3.5	189.52	211.92	223.93	228.68	231.43	230.78	200.46	175.45	156.42	139.26	126.05	113.77	104.28	95.23
	4.0	170.30	189.06	199.64	205.05	206.16	205.53	178.50	157.18	139.24	124.73	112.19	101.89	92.80	85.27
	4.5	153.19	170.96	180.43	184.11	186.21	185.61	161.17	141.01	125.69	111.88	101.26	91.96	83.75	76.95
	5.0	139.44	155.50	164.04	167.33	169.21	168.63	146.40	128.08	113.44	101.61	91.95	83.50	76.05	69.87
	5.5	128.30	142.11	149.86	152.82	154.50	153.95	133.65	116.91	104.19	92.73	83.92	76.20	69.40	63.76
2.0	1.5	178.18	200.22	212.20	218.50	220.09	219.73	191.03	168.36	149.25	133.78	120.39	109.38	99.66	91.03
	2.0	197.59	221.47	232.92	239.56	242.61	242.06	210.35	184.17	163.21	146.26	131.59	119.53	108.89	100.07
	2.5	211.52	235.20	248.60	255.51	257.02	256.33	222.67	196.12	173.77	155.69	140.05	127.20	115.87	106.47
	3.0	221.47	245.92	259.72	266.78	**268.24**	267.44	232.27	204.53	181.20	162.32	146.00	132.59	120.77	110.97
	3.5	195.76	218.48	229.16	235.29	236.50	237.21	204.69	180.22	159.64	143.00	128.60	116.79	107.04	97.73
	4.0	174.69	194.79	205.48	209.59	211.93	211.20	183.36	160.42	142.97	128.06	115.16	104.58	95.24	87.50
	4.5	158.00	176.06	184.49	189.30	190.18	190.68	165.53	144.80	129.04	114.85	103.93	94.37	85.94	78.96
	5.0	143.74	160.07	167.67	172.00	172.77	173.21	150.34	131.50	117.19	104.29	94.37	85.69	78.03	71.69
	5.5	131.38	146.23	153.13	157.05	157.73	158.11	137.22	120.02	106.95	95.77	86.12	78.19	71.65	65.82
2.5	1.5	178.87	200.54	212.24	216.98	218.40	219.28	189.38	166.85	147.87	132.51	119.22	108.30	98.66	90.11
	2.0	198.05	220.20	232.73	239.19	240.59	239.94	208.43	182.43	161.64	144.82	130.27	118.32	107.77	99.04
	2.5	210.49	235.10	248.25	253.39	256.35	255.56	221.94	194.21	172.05	154.12	138.62	125.89	115.38	105.35
	3.0	220.20	245.66	259.22	264.46	**267.45**	266.56	231.45	202.50	179.36	160.65	145.39	131.20	120.25	110.48
	3.5	195.71	216.80	228.64	233.17	235.74	234.91	203.93	179.52	158.99	142.40	128.06	116.28	105.90	97.29
	4.0	174.55	194.42	203.67	208.94	209.89	210.43	182.65	159.77	142.38	126.71	114.66	104.11	94.81	87.10
	4.5	157.81	174.57	183.96	188.68	189.50	188.77	163.83	144.20	127.69	114.35	103.47	93.94	86.09	79.09
	5.0	143.51	158.68	167.16	171.41	172.12	171.44	148.78	130.94	116.68	104.48	93.94	85.29	78.16	71.80
	5.5	131.13	144.93	152.63	156.48	157.12	157.47	136.64	120.25	106.47	95.34	86.26	78.32	71.77	65.93
3.0	1.5	178.77	200.06	210.21	214.74	217.37	216.80	187.17	164.86	146.08	130.88	117.73	106.27	97.41	88.95
	2.0	196.49	219.48	231.76	236.57	237.84	237.11	205.92	180.19	160.63	142.99	129.42	116.80	107.05	97.75
	2.5	209.93	234.18	245.56	252.07	253.33	252.47	219.21	191.78	170.94	152.15	137.70	125.04	113.88	104.63
	3.0	219.48	244.58	256.31	263.00	**264.23**	263.28	228.55	201.19	178.18	159.58	143.50	130.30	119.42	109.02
	3.5	193.77	215.76	226.00	231.82	232.85	231.97	201.35	177.22	156.94	140.55	127.18	115.47	105.15	96.61
	4.0	173.82	192.23	202.53	206.40	208.58	207.77	180.32	158.70	140.52	125.84	113.86	103.38	94.74	87.03
	4.5	156.13	173.65	181.75	186.35	188.29	187.53	162.74	143.22	126.81	113.55	102.74	93.28	85.48	78.52
	5.0	141.94	157.80	165.12	169.27	171.01	170.31	147.78	130.04	115.87	103.75	93.87	85.22	78.09	71.74
	5.5	129.66	144.10	150.75	154.51	156.09	155.43	135.71	119.42	105.73	94.67	85.65	78.25	71.25	65.87
3.5	1.5	175.93	195.43	205.17	210.77	211.95	211.33	182.40	160.63	142.30	126.69	114.67	103.49	94.85	86.61
	2.0	193.21	214.24	226.08	230.66	231.82	231.05	200.62	175.52	156.45	139.25	126.03	113.73	104.23	95.77
	2.5	205.03	228.48	239.44	245.70	246.85	245.97	213.52	187.96	166.46	149.09	134.07	121.74	110.86	101.86
	3.0	214.24	238.55	249.86	256.29	**257.43**	256.45	222.59	195.92	173.49	155.37	140.59	127.65	116.25	106.80
	3.5	189.08	210.38	221.64	225.87	226.82	227.35	197.31	172.56	153.76	137.69	123.80	113.12	103.00	94.63
	4.0	169.56	187.39	197.35	202.33	203.15	202.33	176.68	154.51	137.67	123.28	111.54	101.27	92.79	85.25
	4.5	152.26	169.24	178.19	181.51	183.37	182.61	159.45	139.43	124.23	111.23	100.64	91.37	83.72	76.91
	5.0	138.40	153.78	161.87	164.86	166.53	166.87	144.78	127.40	113.50	101.63	91.95	83.47	76.49	70.26
	5.5	126.40	140.40	147.76	151.42	151.98	152.28	132.12	116.25	103.57	93.31	84.42	76.64	70.23	64.92

Table shows ϕ_{ratio} calculated for each detector length, width and depth. Results are grouped by depth.

Table 5.6: Table showing ϕ_{ratio} of all organisms for 2.5cm detector depth.

Depth (cm)	Width (cm)	length (cm) 2	3	4	5	6	7	8	9	10	11	12	13	14	15
Mouse	1.5	178.87	200.54	212.24	216.98	218.40	219.28	189.38	166.85	147.87	132.51	119.22	108.30	98.66	90.11
	2.0	198.05	220.20	232.73	239.19	240.59	239.94	208.43	182.43	161.64	144.82	130.27	118.32	107.77	99.04
	2.5	210.49	235.10	248.25	253.39	256.35	255.56	221.94	194.21	172.05	154.12	138.62	125.89	115.38	105.35
	3.0	220.20	245.66	259.22	264.46	**267.45**	266.56	231.45	202.50	179.36	160.65	145.39	131.20	120.25	110.48
	3.5	195.71	216.80	228.64	233.17	235.74	234.91	203.93	179.52	158.99	142.40	128.06	116.28	105.90	97.29
	4.0	174.55	194.42	203.67	208.94	209.89	210.43	182.65	159.77	142.38	126.71	114.66	104.11	94.81	87.10
	4.5	157.81	174.57	183.96	188.68	189.50	188.77	163.83	144.20	127.69	114.35	103.47	93.94	86.09	79.09
	5.0	143.51	158.68	167.16	171.41	172.12	171.44	148.78	130.94	116.68	104.48	93.94	85.29	78.16	71.80
	5.5	131.13	144.93	152.63	156.48	157.12	157.47	136.64	120.25	106.47	95.34	86.26	78.32	71.77	65.93
Vole	1.5	51.06	57.25	60.59	61.94	62.35	62.60	61.78	54.43	48.24	43.23	38.90	35.33	32.19	29.40
	2.0	56.54	62.86	66.44	68.28	68.68	68.50	68.00	59.52	52.73	47.25	42.50	38.60	35.16	32.31
	2.5	60.09	67.11	70.87	72.34	73.18	72.96	72.41	63.36	56.13	50.28	45.22	41.07	37.64	34.37
	3.0	62.86	70.13	74.00	75.50	76.35	76.10	75.51	66.07	58.52	52.41	47.43	42.81	39.23	36.05
	3.5	65.18	72.20	76.15	77.66	78.51	78.24	77.62	68.33	60.52	54.20	48.74	44.26	40.31	37.03
	4.0	66.44	74.00	77.52	79.53	79.89	**80.09**	79.45	69.50	61.94	55.12	49.88	45.29	41.24	37.89
	4.5	60.07	66.45	70.02	71.81	72.13	71.85	71.27	62.73	55.54	49.74	45.01	40.87	37.45	34.40
	5.0	54.62	60.40	63.62	65.24	65.51	65.26	64.72	56.96	50.75	45.45	40.87	37.10	34.00	31.23
	5.5	49.91	55.16	58.09	59.56	59.80	59.94	59.44	52.31	46.32	41.47	37.52	34.07	31.22	28.68
Small Bat	1.5	0.15	0.17	0.18	0.16	0.14	0.12	0.10	0.09	0.08	0.07	0.06	0.06	0.05	0.05
	2.0	0.16	0.18	0.19	0.18	0.15	0.13	0.11	0.10	0.09	0.08	0.07	0.06	0.06	0.05
	2.5	0.17	0.20	0.21	0.19	0.16	0.14	0.12	0.10	0.09	0.08	0.07	0.07	0.06	0.06
	3.0	0.18	0.20	**0.22**	0.20	0.17	0.14	0.12	0.11	0.10	0.09	0.08	0.07	0.06	0.06
	3.5	0.16	0.18	0.19	0.17	0.15	0.13	0.11	0.10	0.08	0.08	0.07	0.06	0.06	0.05
	4.0	0.14	0.16	0.17	0.16	0.13	0.11	0.10	0.09	0.08	0.07	0.06	0.06	0.05	0.05
	4.5	0.13	0.15	0.15	0.14	0.12	0.10	0.09	0.08	0.07	0.06	0.06	0.05	0.05	0.04
	5.0	0.12	0.13	0.14	0.13	0.11	0.09	0.08	0.07	0.06	0.06	0.05	0.05	0.04	0.04
	5.5	0.11	0.12	0.13	0.12	0.10	0.08	0.07	0.06	0.06	0.05	0.05	0.04	0.04	0.04
Large Bat	1.5	0.31	0.34	0.36	0.37	0.38	0.38	0.33	0.29	0.25	0.23	0.20	0.19	0.17	0.15
	2.0	0.34	0.38	0.40	0.41	0.41	0.41	0.36	0.31	0.28	0.25	0.22	0.20	0.19	0.17
	2.5	0.36	0.40	0.43	0.44	0.44	0.44	0.38	0.33	0.30	0.26	0.24	0.22	0.20	0.18
	3.0	0.38	0.42	0.45	0.45	0.46	0.46	0.40	0.35	0.31	0.28	0.25	0.23	0.21	0.19
	3.5	0.39	0.43	0.46	0.47	0.47	0.47	0.41	0.36	0.32	0.29	0.26	0.23	0.21	0.19
	4.0	0.40	0.45	0.47	0.48	0.48	**0.48**	0.42	0.37	0.33	0.29	0.26	0.24	0.22	0.20
	4.5	0.36	0.40	0.42	0.43	0.43	0.43	0.38	0.33	0.29	0.26	0.24	0.22	0.20	0.18
	5.0	0.33	0.36	0.38	0.39	0.39	0.39	0.34	0.30	0.27	0.24	0.22	0.20	0.18	0.16
	5.5	0.30	0.33	0.35	0.36	0.36	0.36	0.31	0.28	0.24	0.22	0.20	0.18	0.16	0.15
Bird	1.5	2.51	2.82	2.98	3.05	3.07	3.08	3.04	2.68	2.38	2.13	1.91	1.74	1.58	1.45
	2.0	2.78	3.09	3.27	3.36	3.38	3.37	3.35	2.93	2.60	2.33	2.09	1.90	1.73	1.59
	2.5	2.96	3.30	3.49	3.56	3.60	3.59	3.56	3.12	2.76	2.48	2.23	2.02	1.85	1.69
	3.0	3.09	3.45	3.64	3.72	3.76	3.75	3.72	3.25	2.88	2.58	2.34	2.11	1.93	1.77
	3.5	3.21	3.55	3.75	3.82	3.87	3.85	3.82	3.36	2.98	2.67	2.40	2.18	1.98	1.82
	4.0	3.27	3.64	3.82	3.92	3.93	**3.94**	3.91	3.42	3.05	2.71	2.46	2.23	2.03	1.87
	4.5	2.96	3.27	3.45	3.54	3.55	3.54	3.51	3.09	2.73	2.45	2.22	2.01	1.84	1.69
	5.0	2.69	2.97	3.13	3.21	3.23	3.21	3.19	2.80	2.50	2.24	2.01	1.83	1.67	1.54
	5.5	2.46	2.72	2.86	2.93	2.94	2.95	2.93	2.58	2.28	2.04	1.85	1.68	1.54	1.41

Table shows ϕ_{ratio} calculated for each detector length, width and depth. Results are grouped by depth.

Table 5.7: Optimal detector surface area.

Depth	Mouse		Vole		Small Bat		Large Bat		Bird	
	Length	Width	Length	Width	Length	Width	Length	Width	Length	Width
1.5	6	3	6	4	4	3	6	4	6	4
2.0	6	3	6	4	4	3	6	4	6	4
2.5	6	3	7	4	4	3	7	4	7	4
3.0	6	3	6	4	4	3	6	4	6	4
3.5	6	3	6	4	4	3	6	4	6	4

All dimensions are in cm.
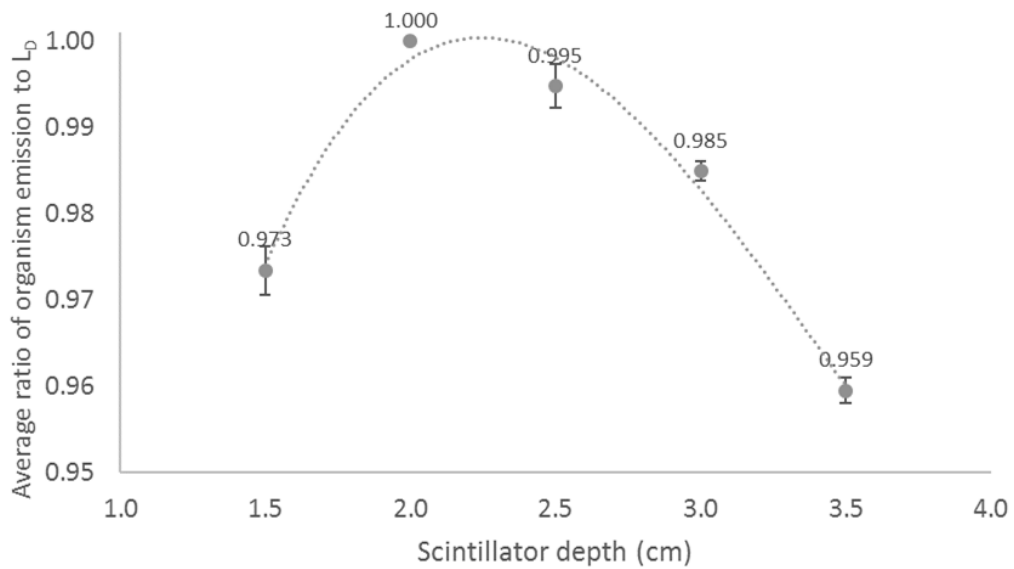
Figure 5.12: Optimal detector depth. ϕ_{ratio} normalised to a fraction of one and averaged over each organism. The error bars show the standard deviation between organism averages.

5.3.2 Beta detector orientation

Bone surface areas, tissue depth and the fractional view to each detector orientation are detailed in Table 5.8. Tissue depth is reported with an upper and lower 95th percentile estimate. The total emission from each bone (ignoring detector orientation) is shown in Figure 5.13 for ^{90}Sr and Figure 5.14 for ^{90}Y. The graphs show the largest emissions for both radionuclides are likely to occur in the caudal vertebrae (tail), the manus, hindfoot, and head (cranium and nose). The optimal orientation, based in the information in Table 5.8 and the two figures, for a detector is shown in Figure 5.15. This figure suggests a detector would be best placed under the organism.

Table 5.8: Bone and tissue properties for mouse model

Region	Bone	Surface Area (mm^2)	Tissue Depth (mm) Average	Up95	Low95	Fractional View Top	Bottom	Side
1. Skull	Cranium (^{90}Sr)	61.87	0.41	0.59	0.23	1		0.25
	Cranium (^{90}Y)	71.77	0.41	0.59	0.23	1		0.25
	Nose	69.48	0.84	1.12	0.56	1		0.25
	Mandible (^{90}Sr)	13.92	1.50	1.57	1.42		1	
	Mandible (^{90}Y)	89.09	1.79	2.56	1.03		0.25	0.75
2. Spine	V01-08	37.04	5.78	6.34	5.22	1		
	V08-V17	56.17	4.56	6.36	2.76	1		
	V17-V20	29.94	1.70	2.36	1.04	1		
	V20-V23	41.30	1.52	1.90	1.14	1		
	V23-V31	5.65	1.62	2.02	1.22	1		
	V23-V31 (^{90}Y)	78.35	3.10	3.70	2.50	1		
	V31-V35	32.31	0.88	1.14	0.63	1		
	Caudal Vertabrae	282.80	0.40	0.51	0.29	0.5	0.5	0.5
3. Ribs	R1 D	13.83	3.90	6.20	1.60	1		0.5
	R2 D	9.46	3.12	4.79	1.45	1		0.5
	R2 V	3.75	1.57	1.77	1.37		1	0.5
	R3 D	13.36	2.84	4.17	1.51	1		0.5
	R3 V	4.98	1.31	1.51	1.11		1	0.5
	R4 D	13.46	2.62	3.45	1.79	1		0.5
	R4 V	5.15	1.31	1.63	0.98		1	0.5
	R5 D	13.42	2.42	2.85	1.99	1		0.5
	R5 V	6.82	1.41	1.79	1.02		1	0.5
	R6 D	18.12	2.10	2.66	1.54	1		0.5
	R6 V	13.14	1.40	2.01	0.79		1	0.5
	R7 D	29.17	1.90	2.63	1.17	1		0.5
	R7 V	21.13	1.52	2.21	0.83		1	0.5
	R8 D	24.68	1.78	2.12	1.44	1		0.5
	R8 V	12.11	1.41	2.27	0.56		1	0.5
	R9 D	23.39	1.57	1.99	1.15	1		0.5
	R10 D	23.83	1.29	1.61	0.97	1		0.5
	R11 D	18.68	1.31	1.79	0.83	1		0.5
	R12 D	15.84	1.22	1.60	0.84	1		0.5
	R13 D	8.95	1.21	1.57	0.84	1		0.5
	Sternum	29.46	1.40	1.92	0.88		1	
4. Arm	Scapula Plate	42.06	1.82	2.45	1.19	1		0.5
	Scapula Ridge	10.49	1.30	1.62	0.98	1		0.5
	Clavicle	16.35	3.83	4.81	2.85		1	
	Humerus	47.49	2.46	2.92	2.01	1		0.5
	Forearm + Elbow	134.62	0.70	1.23	0.17	0.25	0.5	0.25
	Manus	49.15	0.28	0.40	0.15		0.5	
5. Leg	Pelvis (^{90}Sr)	10.04	2.73	3.10	2.36	1		
	Pelvis (^{90}Y)	70.67	3.61	4.48	2.73	1		
	Femur	59.44	2.17	2.53	1.82	1		0.5
	TFC + Knee	239.34	0.84	0.91	0.76	0.25	0.5	0.25
	Hindfoot	187.00	0.28	0.40	0.15		0.5	

The ear and eye surface areas were measured at 36.79 and 9.90 mm² respectively. The nose and cranium surface areas are adjusted to reflect the loss from these two areas. Measurements taken from model produced by Dogdas et al. (2007).
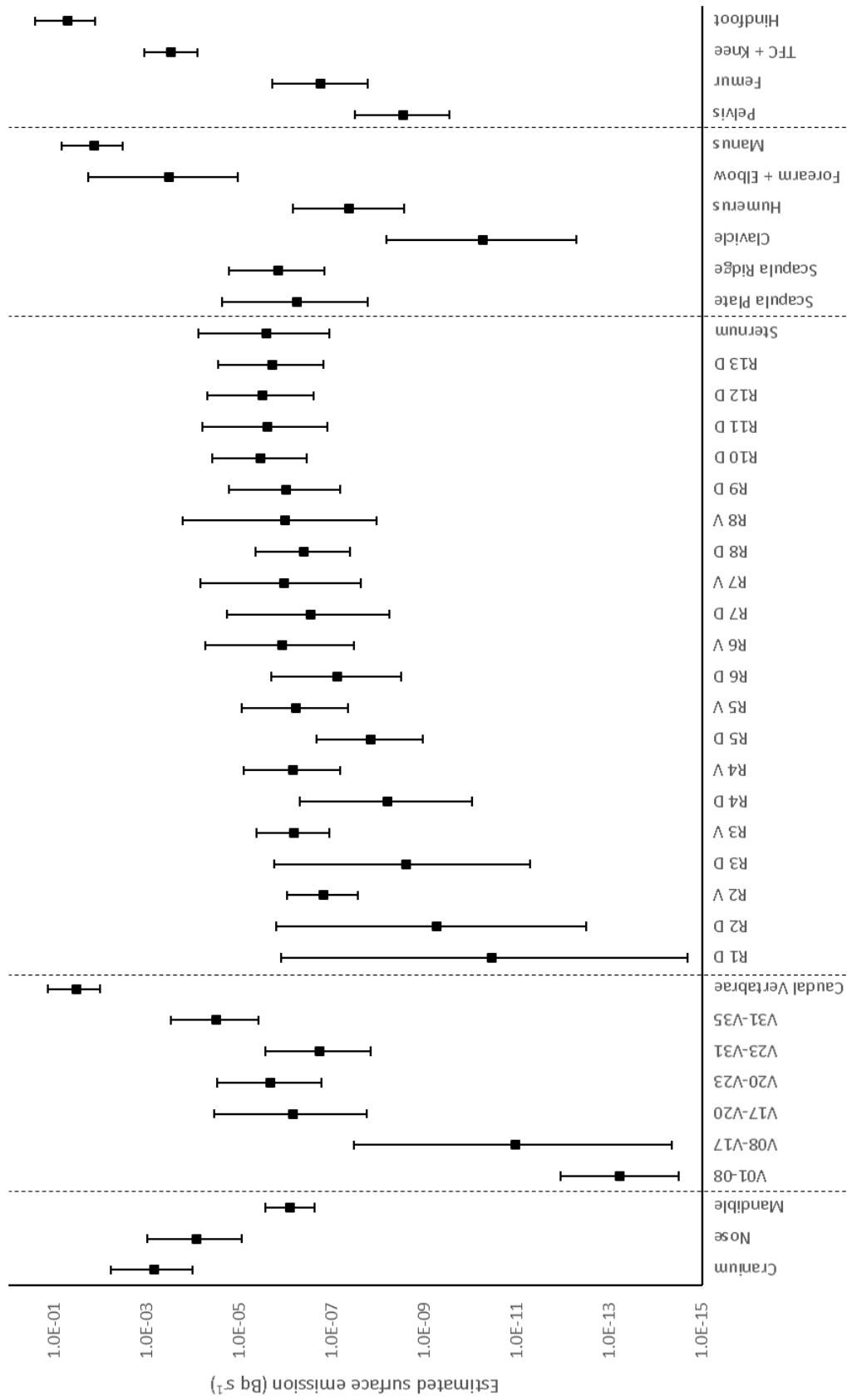
Figure 5.13:Total estimated ⁹⁰Sr emission rate at skin surface for a mouse. Mouse model based on Dogdas et al. (2007).
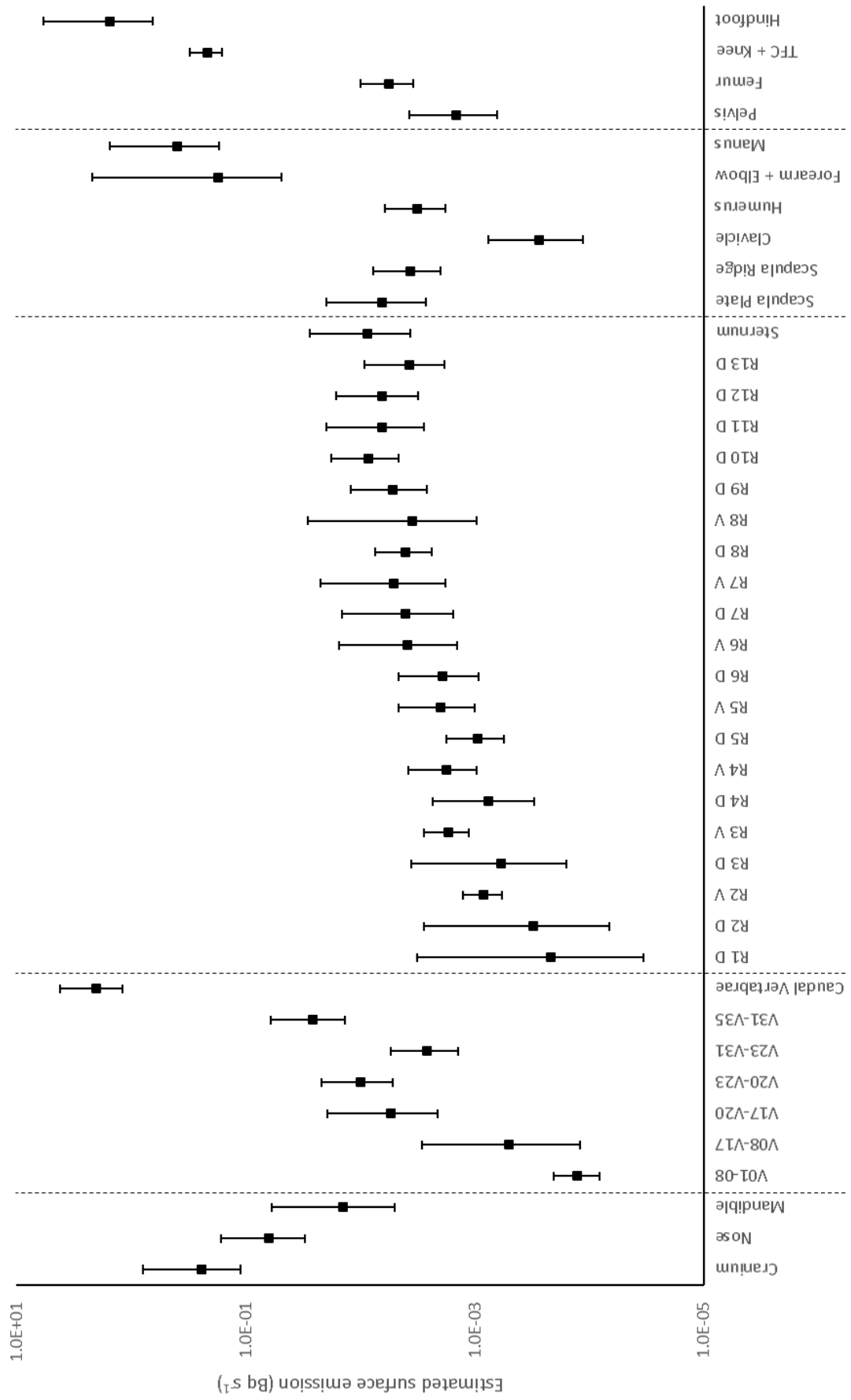
Figure 5.14: Total estimated ^{90}Y emission rate at skin surface for a mouse. Mouse model based on Dogdas et al. (2007)
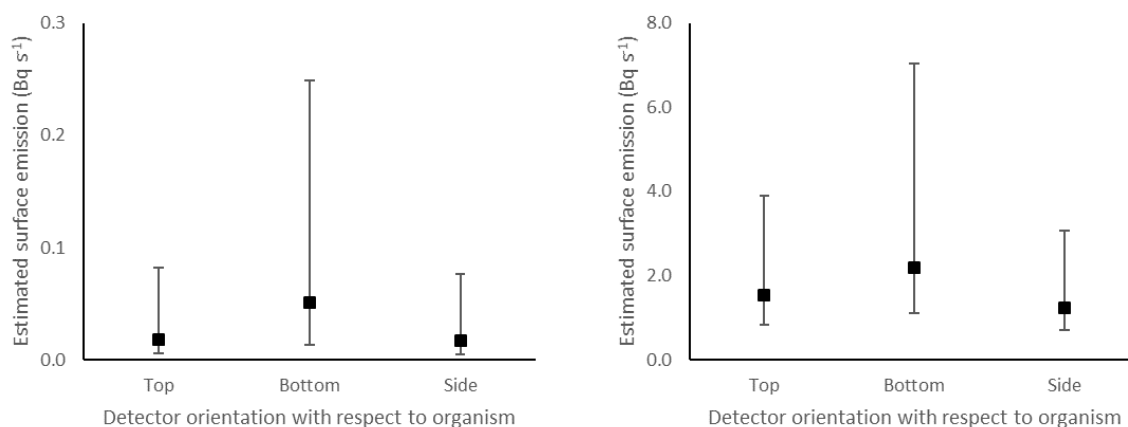
Figure 5.15: Estimated emission rate (Bq s⁻¹) at mouse skin surface for three different detector orientations. Left: ^{90}Sr, Right: ^{90}Y. Mouse model based on Dogdas et al. (2007)

5.4 Discussion

5.4.1 Detector size

The optimal length and width of the ^{137}Cs detector varied for each organism (Table 5.6). In general, a detector size slightly smaller than the size of the organism provided the best ratio (ϕ_{ratio}) against the limit of detection. For the mouse, vole, large bat, and bird, a detector length of 6 cm was deemed optimal (though the detector depth of 2.5 cm resulted in a 7 cm length having the largest ϕ_{ratio}). The model for the small bat indicated a 4 cm length would provide the optimal count rate. For most of these organisms there was little difference in count rate (<1%) for detectors ±1 cm from the identified optimal detector lengths. A detector width of 4 cm was deemed optimal for the vole, large bat, and bird whereas it was 3 cm for the mouse and small bat.

For all organisms, the most suitable detector depth was between 2 to 2.5 cm (Figure 5.12). The difference in ϕ_{ratio} between these two depths was >1% so choosing between them should not influence measurements greatly. The thicker (2.5 cm) depth may be preferable though as it is typically the smallest size of detector commercially available (approx. 1 inch; see chapter 3.5.5). For depths outside this range, however, ϕ_{ratio} falls rapidly (the largest difference between the ratios calculated for each depth was 4%).

Besides the optimal detector sizes, ϕ_{ratio} shown in Table 5.5 and Appendix 10.4 indicate the likelihood of attaining measurement that can be statistically distinguished from background (anything above one indicates a measurement that is above the MDA). From these results, the mouse and vole indicate a count rate far above the limit of detection and the bird

116

approximately three to four times above. A shorter count time would therefore be possible for birds, placing it within more acceptable restrain times (Bondarkov et al., 2011). The ϕ_{ratio} for the two bats, however, indicate their count rate would be below this limit of detection. These two organisms would require a longer counting time (approximately 43 minutes for the large bat) or for a much lower background to be present. An optimal detector for the organisms, from which a good detection is likely, would therefore be between 6 and 7 cm, 3 to 4 cm for the width, and 2 to 2.5 cm for the depth.

The model created to derive these dimensions included a number of simplifications that could impact the conclusions drawn above. The small sizes of the organisms included in this chapter means the use of a cylinder to represent the organism, along with the exclusion of structures that are denser than tissue (e.g. bone) and the assumption of an evenly distributed internal contamination, was considered to be sufficient due to the high penetrability of the target radionuclide, ^{137}Cs. For larger organisms, a more accurate representation of the anatomical structure would be required to account for the distribution of the target radionuclide and additional absorption caused by internal structures. The range of animal dimensions provided for the model was limited but was also deemed sufficient to reach conclusions for the average dimensions of each respective species. The CR applied to each organism, whilst not having an influence the optimal detector size, does have a large impact on the size of ϕ_{ratio} provided in Table 5.5 and Appendix 10.4; a mouse, with the largest CR, had a very high ϕ_{ratio} whereas the two bats, with the smallest CR, were estimated to have a ϕ_{ratio} below the minimum (statistically significant) detection levels. These CRs were considered sufficient for this model (as an example of an environment where the detector will be used) but may not be fully representative of species in other locations. A final limitation of the model is the position of the organism with respect to the detector. It was assumed the animal is located centrally directly on the top of the detector crystal. If the animal is capable of moving off the edge of the detector then the emission rate from the organism will be reduced. Whilst a live animal is unlikely to be restrained to the extent where it cannot move (unless it is anaesthetised e.g. Barnett and Dutton (1995)) it is still expected it can be restrained to an extent where the contact surface area will not be reduced significantly. A larger impact to detection would be if the detector was moved away from the organism, e.g. if the detector is positioned to the side of a large restraint. This would reduce the count rate according to the inverse square law (Knoll, 2010). This is, however, unlikely to be a concern for the organisms that are already

listed (above) as being above the background limit of detection due to how large their estimated emission rate already is. For the requirements of this chapter, therefore, it is still expected that the range given for the dimensions provide a suitable basis on which to design a detector. Any large deviation (e.g. using a large restraint where the animal has more mobility) should, however, be considered before finalising a design for a detector.

5.4.2   Detector orientation

A detector placed below the organism was found to be the optimal position for both ^{90}Sr and ^{90}Y (Figure 5.15). By placing the detector above or to the side of the organism, it was estimated the count rate of ^{90}Sr would reduce by 65% and 67% respectively. For ^{90}Y, this reduction in count rate was estimated to be 31% and 44% for the top and side orientations respectively. The data presented in the results are, however, an idealised position for the mouse; assumed to be sat with arms and legs under the body and tail visible to the bottom detector. Because the estimated emission is largest from the feet and tail (e.g. Figure 5.13 for ^{90}Sr) this means movement of the organism, such that any of these parts are no longer visible to the detector (the tail is the most likely to do this), would result in a reduced count rate from the organism. Whilst the estimates show a detection will still be made there are other compounding factors that affect this estimated count rate. Contamination in the fur is not estimated in this model but is likely to be present. Physical removal of this contamination is difficult to accomplish (Ishida et al., 2015). Separating the ^{90}Sr and ^{90}Y components of the beta detection (i.e. using a different detector for each, along with an appropriately thick attenuation layer) could provide a way to estimate surface contamination from an organism. This would, however, use ^{90}Y as the internal contamination indicator and would rely on the assumption it is in equilibrium with the ^{90}Sr present in the organism. This model also only looks at one organism type out of those listed in Table 5.1. The other two types, bats and birds have anatomical features, different from the mouse, that need to be considered. The largest physical difference is the presence of wings. Whilst unlikely to be so for the bird, this feature could be beneficial for detection of ^{90}Sr + ^{90}Y in bats because they have a large proportion of bone in their wings (as compared to the whole body) that is covered by only a thin membrane (Barlow, 1999). For the bird, the presence of feathers on the wings would hinder detection. The locations for the highest emissions from a bird would likely be in the legs. For both bats and birds, the optimal location for the ^{90}Sr + ^{90}Y beta detector would therefore potentially differ from that shown in Figure 5.15, depending on how the organism is positioned in any restraint.

5.5 Conclusion

Models were constructed to estimate suitable detector sizes and orientations for the measurement of ^{137}Cs, ^{90}Sr, and ^{90}Y. Both models were considered to be sufficient to draw the following conclusions. The recommended dimensions of the CsI scintillator (for detection of ^{137}Cs) were between 6 to 7 cm in length, 3 to 4 cm width and 2 to 2.5 cm depth. Appropriate adjustments should, however, be made based on the ability for the organism to move within the restraint. The recommendation for the plastic scintillator (for detection of ^{90}Sr and ^{90}Y) was to have a surface area that covers as much of the organism as possible and to have a thin depth to reduce the detection of ^{137}Cs in this detector. This coverage should not, however, be to the extent that it hinders detection of ^{137}Cs in for the CsI detector. The orientation of these two detectors was dictated by the beta detector. The constructed model indicated the best orientation for the plastic scintillator was underneath the organism. This was, however, based on the anatomical structure of a mouse only. For other species, such as bats and birds, their properties may mean a different orientation may be optimal. Because the plastic scintillator is likely best placed under the organism, the housing of the beta detector may dictate the orientation of the CsI scintillator so as to maximise its detection (i.e. a thick housing for the beta detector would mean a side placement for the CsI detector would be better).

6 Design and construction

6.1 Introduction

The previous three chapters have served to identify the main design requirements for the construction of a portable radiation detector. The requirements for this detector are to live-monitor the ^{137}Cs and ^{90}Sr (incl. ^{90}Y) radionuclide content within small mammals (incl. bats) and small birds (chapter 4.5). Suitable detection materials were identified (chapter 3.5.5) as a CsI scintillator for gamma detection and a general plastic scintillator for beta detection. Suitable sizes and positioning of these materials, in relation to the target organism, were suggested in chapter 5.5. This chapter takes these requirements, outlines the design specifications of a small animal radiation detector and details the construction and calibration of a fully working unit.

6.2 Methods:

The general description of the radiation detector from chapter 3.5 was categorised (Figure 6.1) into five sections: 1) restraint, 2) scintillators (detection materials), 3) processing electronics, 4) shield, and 5) supports and inserts (for holding the items in place within the shield). The designs for each of these are detailed in the following subsections.
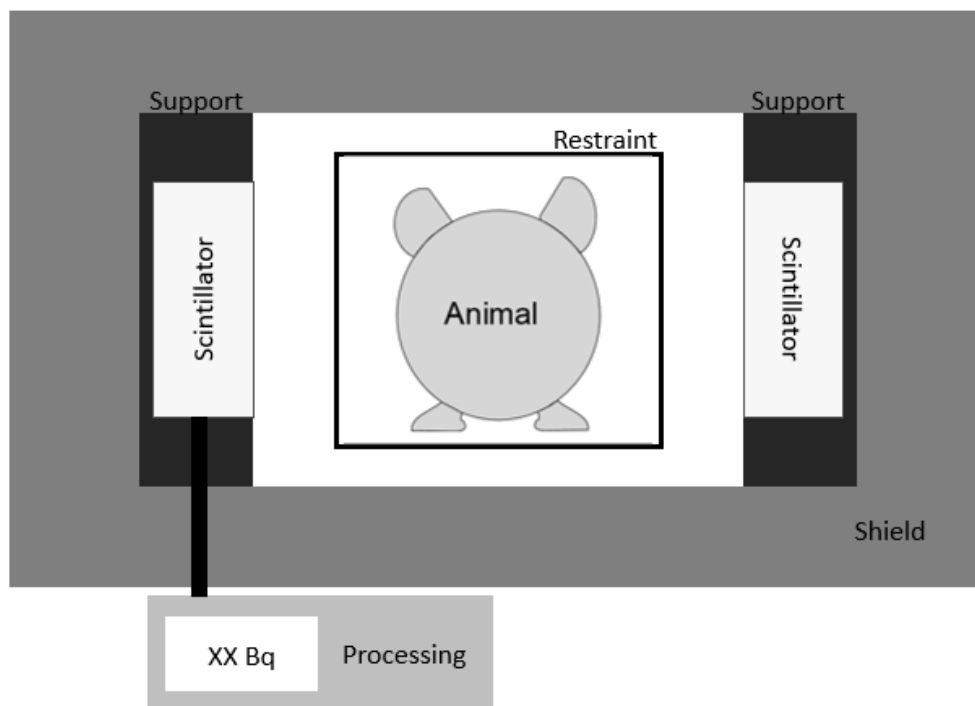
Figure 6.1: Components of the small animal radiation detector.

6.2.1   Restraint

A flatpack restraint box was designed in Inkscape[7] (version 0.92) and laser cut on 160 gsm card. This material was chosen because it was relatively cheap to acquire (so easily replaceable if damaged by the restrained animal) and provided a good balance between being thin enough for the detection of ^{90}Sr but also thick enough to provide a sturdy box for restraint of a moving animal. The manufacturing method was chosen because it provided a rapid means of creating many boxes to the same specification. The laser cutter used was a GRAVOGRAPH (IS900) and required a line thickness on the templates to be 0.009 mm (or 0.026 pt). The internal dimensions of the detector were set according to the maximum animal size expected to be monitored, i.e. appropriate for small rodents (mice / voles), bats, and birds. The current radiation detector used to live-monitor these animal groups in the Chernobyl Exclusion Zone (Bondarkov et al., 2011) uses restraint boxes (three in total) that are similar to the animal geometries used in the models from Chapter 5.2.1. Therefore, for the new detector described within this thesis, the same box dimensions were adopted: 170 x 60 x 50 mm (LxWxH) for a large box, 100 x 50 x 35 mm for a medium, and 70 x 40 x 35 mm for a small box.

6.2.2   Detector

The final designs of the detectors were reached based on the conclusions of chapters 4 and 5. Materials for the individual scintillators were sourced from and assembled (from the design in this chapter) by John Caunt Scientific (JCS) and Scionix.

6.2.2.1   Materials and positioning

A CsI(Tl) scintillator was chosen for the detection of ^{137}Cs and a plastic scintillator (BC-400) for the detection of ^{90}Sr + ^{90}Y (see chapter 5.5). Dimensions were set at 70 x 40 x 25 mm and 100 x 60 x 0.5[8] mm respectively based on the outcomes of the models in chapter 5. To account for movement of the animal within the restraint box, two of each scintillator were used. A plastic scintillator was positioned above and below the animal and the CsI scintillators were rotated through 90 degrees so that they could be placed either side of the animal (the rotation was decided upon to reduce attenuation that would have been present if it were placed behind the plastic scintillator). Each scintillator was covered using reflective Teflon tape except for the detection surface for the plastic scintillators, which was covered using 6 μm Mylar.

---

[7] https://inkscape.org/en/
[8] Mounted on a 9.5 mm plastic backing for support of the thin scintillator. The upper scintillator had a reduced width of 50 mm to allow space for a protective case

6.2.2.2 Light collection

Each scintillator was connected to a type 5611A 26 mm PMT (with single MHV connectors) sourced from Scionix. Whilst SiPMs had been considered, it was decided to use the specified PMTs due to the availability of materials and a suitable SCA/MCA. To avoid compromising the integrity of the side shielding (see section 6.2.4 for shielding design) the PMTs were mounted on the scintillators such that they were directed upwards out the top of the detector. For the CsI scintillators, the optimal placement of the PMT was determined to be towards one of the short edges on the top face because this is where the maximum amount of scintillation light can be collected (Menge et al., 2016).

The design of the plastic scintillator presented a unique problem for mounting the PMTs in an upwards direction. Information for the optimal position for this design was not readily available in the literature and was therefore determined by means of the following experiment. A 0.5 mm thick plastic scintillator from a DP6 series alpha-beta probe was reconfigured to allow a PMT from a Nuclear Enterprises BP4 to be mounted (using coupling gel) on the lightguide surface in various positions (centre, normal, end; Figure 6.2). The PMT was connected to an Electra rate meter (beta channel set to 0.1 -0.3 V, alpha channel 0.3+ V) for measurement of a 16 mm diameter ^{90}Sr + ^{90}Y source with an activity (all source activities are decayed to measurement date) of 2.48 kBq (therefore a 100% efficiency should be 1240 cps). Measurements were taken for a range of high voltages (HV) with the source in the a) far, b), centre, and c) near position (Figure 6.2). All results for these measurements were scaled to a fraction of 1 such that 1 represented 100% efficiency to allow for comparison. This experiment was repeated for a scintillator coating of aluminium foil and Teflon tape. A further experiment was undertaken with the PMT positioned in the Normal position but with the corners of the light guide chamfered as shown in Figure 6.3. This final experiment used a 0.25 mm scintillator from a Ludlum 44-142 detector instead of the one from the DP6 due to accidental damage caused to the previous scintillator material.

6.2.3 Processing

A RMS30 unit was sourced from JCS for the processing and display of the signal from the scintillators. Two interface boxes were designed and constructed by JCS to allow for all four of the PMTs to be connected to the two inputs of the RMS30.
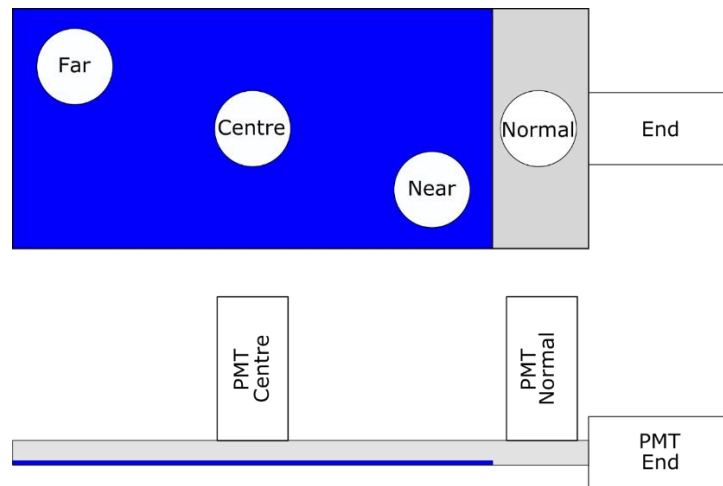
Figure 6.2: Experimental setup for testing the positioning of the beta scintillator PMT. Above, top view, below, side view. The scintillator is coloured blue and the light guide is coloured grey. The source is placed in the Far, Centre, or Near positions with the PMT in either the Centre, Normal or End position.
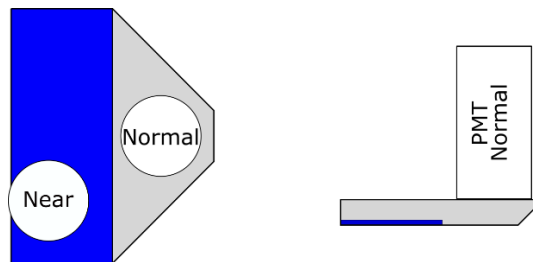
Figure 6.3: Modification of the light guide for PMT placement. Left, top view, right, side view. The scintillator is coloured blue and the light guide is coloured grey.

6.2.4 Shielding

A shield for the detector was designed in LibreCAD[9] (version 2.1.3). It was designed to enclose the restraint box and scintillators but allowed gaps for the PMTs to be orientated upwards out of the detector. The thickness of lead was set to be a maximum of 22 kg as an upper level to being portable; this limit also allows for transportation on most airlines if transport overseas is required. It was assumed (chapter 5.2.2.1) that the majority of the background count would come from ^{137}Cs in the ground and therefore the walls of the shield were set to be half the thickness of the base. The design of the shield was optimised such that the scintillators were shielded with the maximum amount of lead allowable for the weight of lead specified. The lid thickness was set at a thickness of 10 mm to ensure a minimum level of shielding on the upper surface. The lid was further designed to be removable to allow for insertion and future replacement of the scintillators. This design was cast from lead by Perry Products Ltd.

---

[9] http://librecad.org/cms/home.html

6.2.5 Supports and inserts

Two main support structures were required: one to position and support the walls of the restraint box when placed in the cavity and the other to position and hold the scintillators within the shielding. The supports for the restraint boxes were designed in Inkscape (version 0.92) and laser cut from 3 mm Perspex. The parts were assembled using plastic weld. Similar to the reasons for the production choice of the restraint boxes, this allowed for cheaply manufactured parts that could be quickly replaced if damaged. The main body of the support structure for positioning the detectors was also designed in Inkscape and laser cut from 3 mm Perspex. A protective case for the upper ^{90}Sr detector and separate housings to protect the part of the PMT tubes extruding from the shielding were designed in Autodesk Fusion360[10] (version 2.0.3706) and 3D printed from PLA (Polylactic Acid) material on an Ultimaker 2+ 3D printer. 3D printing was initially considered for all components, both as a means to fully automate their manufacture and to have fewer breakage points, but laser cutting from Perspex was opted instead for the simpler structures because it allowed for faster prototyping.

6.2.6 Assembly

The detector was assembled at the University of Salford. All dimensions were checked against design blueprints prior to assembly. Two toughened cases were acquired to hold the disassembled detector; one for the scintillators and electronics and the other for the shielding.

6.2.7 Preliminary system testing

6.2.7.1 Energy calibration

The two gamma scintillators were calibrated using a 9 kBq ^{137}Cs source that was contained within a circular tin. The lower and upper level discriminator window on the two scintillators was set to 800-1100 mV. The two beta scintillators were calibrated using a 1.6 kBq ^{36}Cl source. The window was set to disabled. The optimal HV bias for each PMT was determined by taking 10 second counts for a range of voltages and identifying the peak voltage (when compared to background radiation levels). All sources were positioned centrally and in contact with the detection surfaces.

6.2.7.2 Response to sources

Detection of ^{137}Cs in the two gamma scintillators and ^{36}Cl in the two beta scintillators was confirmed during the energy calibration stages in section 6.2.7.1. Three further radioactive

---

[10] https://www.autodesk.com/products/fusion-360/overview

sources: 3.02 kBq ^{14}C, 3.06 kBq ^{90}Sr, and 2.57 kBq ^{60}Co, each having a surface area of 10x15 cm and a calibration date of 31/07/2014, were placed onto the two beta scintillators to test their responses to different energy beta emitters (sources fully covered the detection surface). The response to the gamma emission from the ^{137}Cs source was also measured with the source being placed 65 mm away from the detector.

6.2.7.3   Attenuators for beta detectors

To assist with determining the ^{90}Sr content of targeted animals, and to provide protection to the lower beta scintillator (from the animal), the two beta scintillators were configured as follows:

- the upper scintillator had no filtering between the source and the scintillator so was able to measure ^{90}Sr, ^{90}Y and the beta from ^{137}Cs.
- the lower scintillator used a layer of aluminium to filter lower energy betas so measured ^{90}Y only

It is expected the ^{90}Sr and ^{137}Cs contribution will be low compared to the ^{90}Y measurement due to the lower penetrative ability of these radionuclide emissions. Determination of ^{90}Sr is therefore to be made via measurement of ^{90}Y. The ^{90}Sr source was used to estimate this thickness of aluminium that was required to be placed on the lower beta scintillator. Counts lasting 100 seconds were taken for aluminium thickness between 0 to 0.4 mm in increments of 0.1 mm. These were graphed to identify the point at which ^{90}Sr is removed from detection.

6.3   Results

6.3.1   Restraint

Three templates were designed for the restraint boxes: small (Figure 6.4a), medium (Figure 6.4b), and large (Figure 6.4c). The design of each restraint box means they have a single layer of card on the top and bottom to ensure a consistent thickness on these surfaces for the beta scintillators. A side hole is present to ensure there is an air supply for the contained animal. The dashed lines allow the box to be easily folded into shape and the tabbed design means no further materials are required to hold the box together once it is assembled. The perimeter of the box is coloured red. This is so the laser cutter can be set to cut the black lines first and then the red lines. Cutting in this order means there is no chance of the box shape moving within the laser cutter (due to the attached smoke extraction fan) before the entire shape is cut.

Five sheets of card could be stacked and cut at the same time. Therefore, batches of 10 small boxes, 5 medium boxes, or 5 large boxes could be cut (Figure 6.5). Using setting of 30% power and 15% speed meant cutting times (batched) for each box was approximately 188 seconds for the small box, 114 seconds for the medium box and 158 seconds for the large (timing may change for other laser cutters). The final assembled boxes are displayed in Figure 6.6.
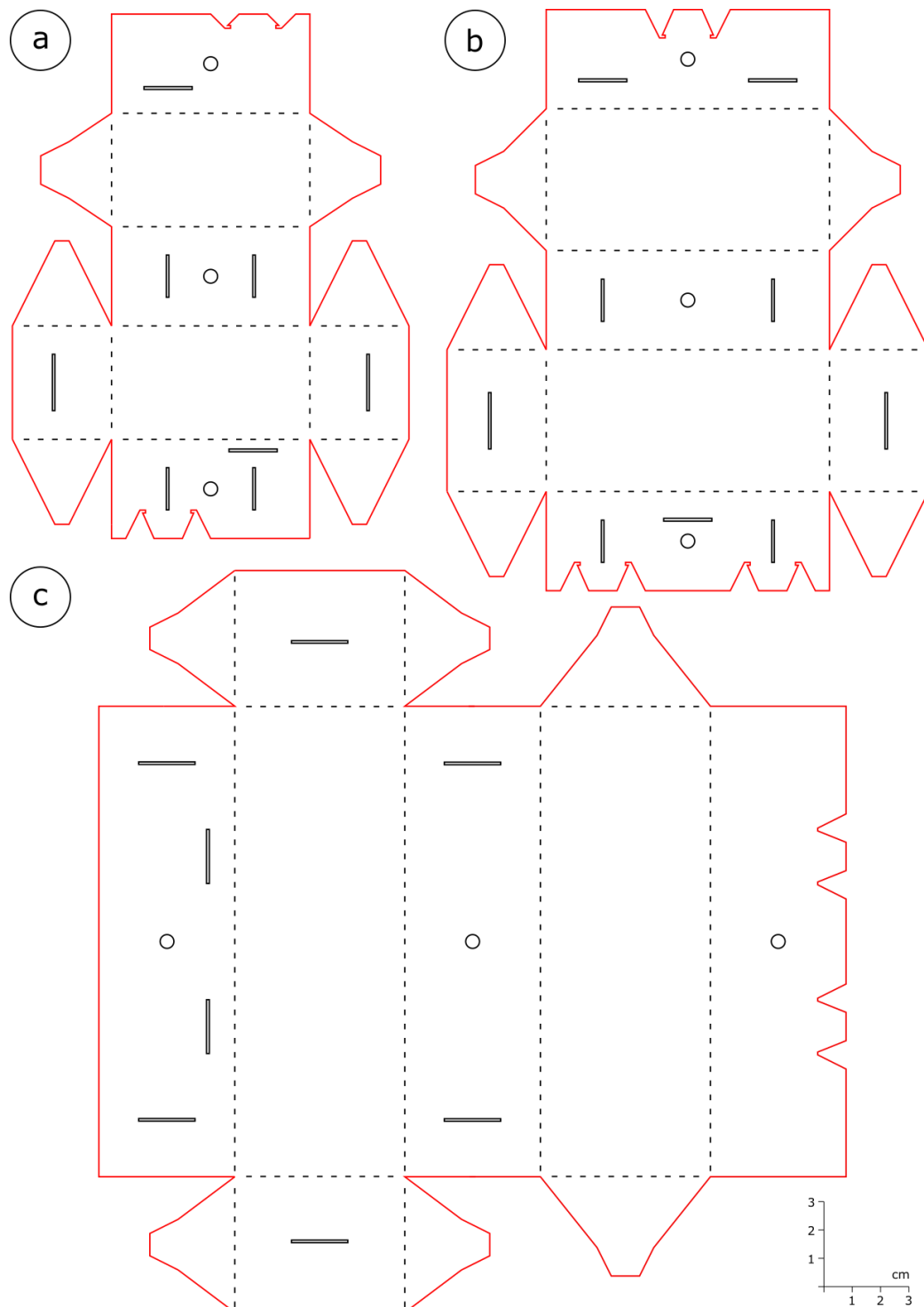
Figure 6.4: Template for the a) small, b) medium and c) large restraint boxes. Scale is shown in the lower right-hand corner of the figure (units are in cm)
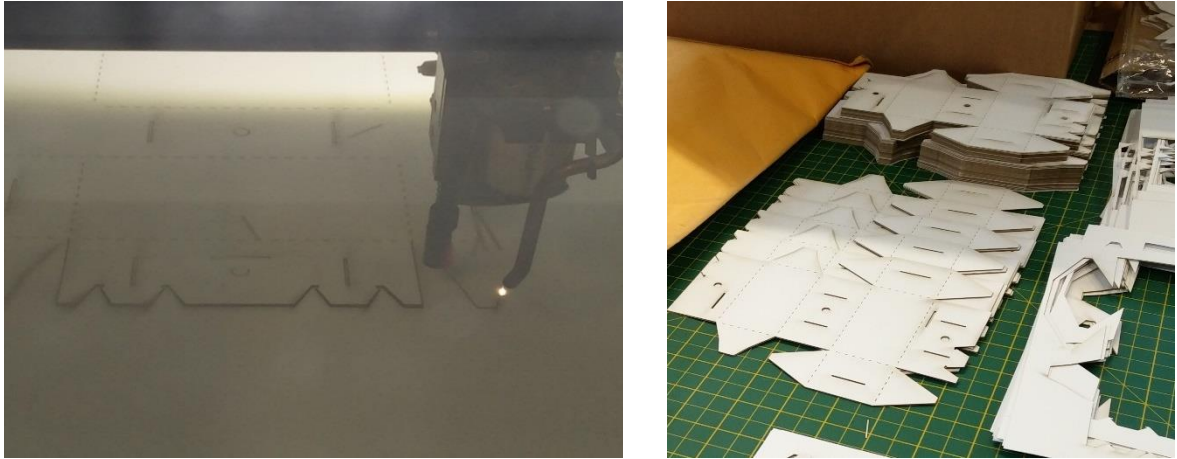
Figure 6.5: Left: laser cutting of one of the large restraint boxes. Right: batches of boxes ready for testing following cutting.
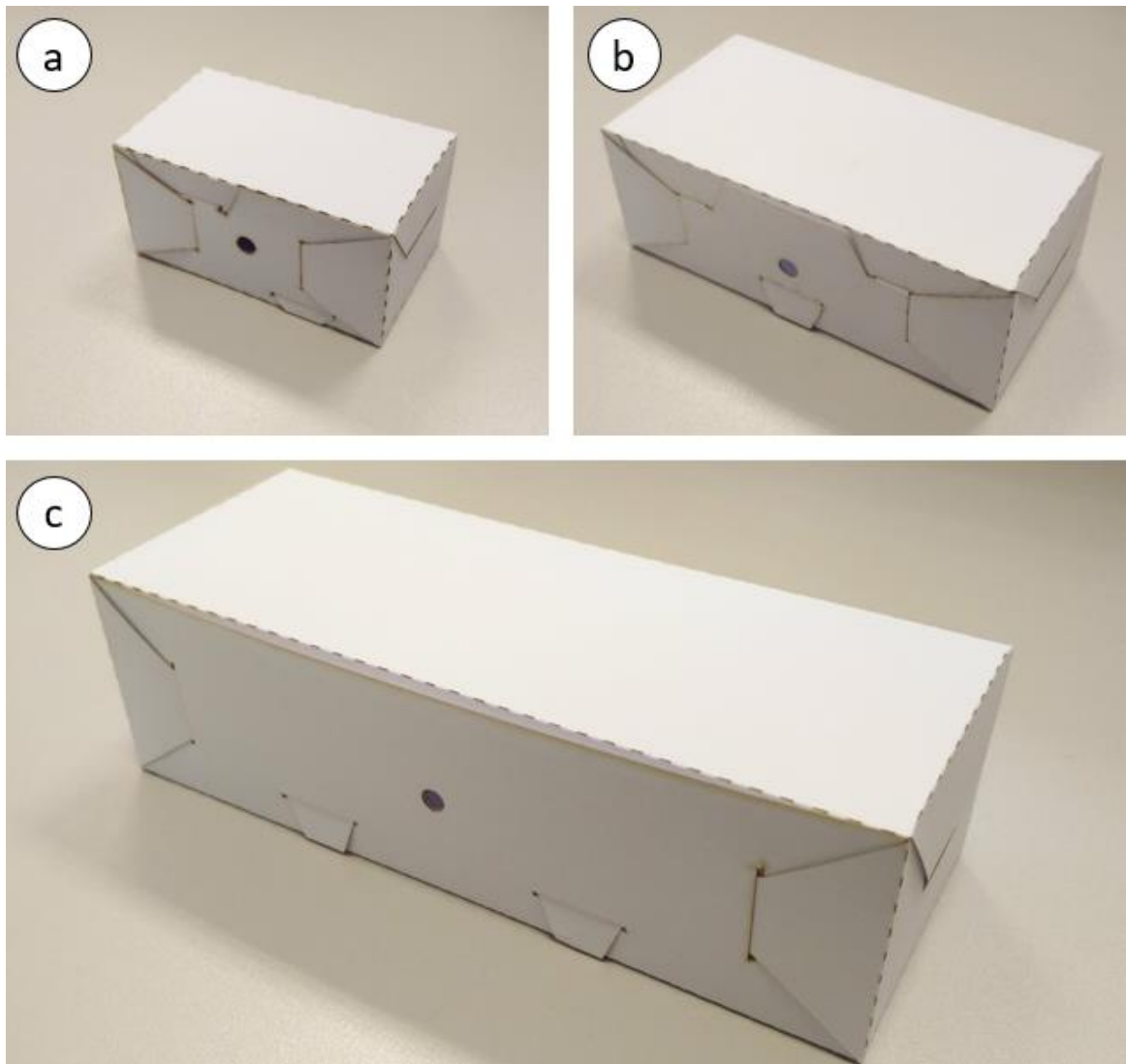
Figure 6.6: Final assembly for each of the restrain boxes. a) small restraint box, b) medium restraint box, and c) large restraint box.

6.3.2 Scintillators

6.3.2.1 PMT positioning

Mounting the PMT centrally on the scintillator allows for the best count rate when the source is positioned centrally (Figure 6.7). Moving the source away from the PMT, however, give a large reduction in the count rate and therefore makes this a poor PMT mounting position for the purposes of this application. The use of Teflon tape instead of aluminium foil helps to alleviate this but still shows a lot of variation as the HV is changed. Mounting the PMT at the end of the lightguide (as often seen for these types of detectors though not viable for the scintillator placement in this project) resulted in the best overall consistency between counts, especially with the aluminium foil (Figure 6.8). Count measurements with the aluminium foil in place showed little deviation of the signal when the source was moved across the surface of the scintillator or as the HV is changed. Using Teflon tape gives an increase in the detected signal (though the furthest position gives a greater count rate over the closer two positions). At higher voltages, however, this relationship broke down for the Teflon tape wrapping. Rotating the PMT so it was mounted normal to the surface but at the end of the scintillator (Figure 6.9) allowed for a better count rate close to the PMT but overall poorer count rate at any distance away from the PMT. Angling the edges of the lightguide, however, assists in directing the light up into the PMT and therefore there is a marked decrease in variation of count rates across the surface and between HV increments (Figure 6.10). Whilst not as good as the count rates in Figure 6.8 it does show that this is a usable position to have the PMT mounted onto the scintillator.
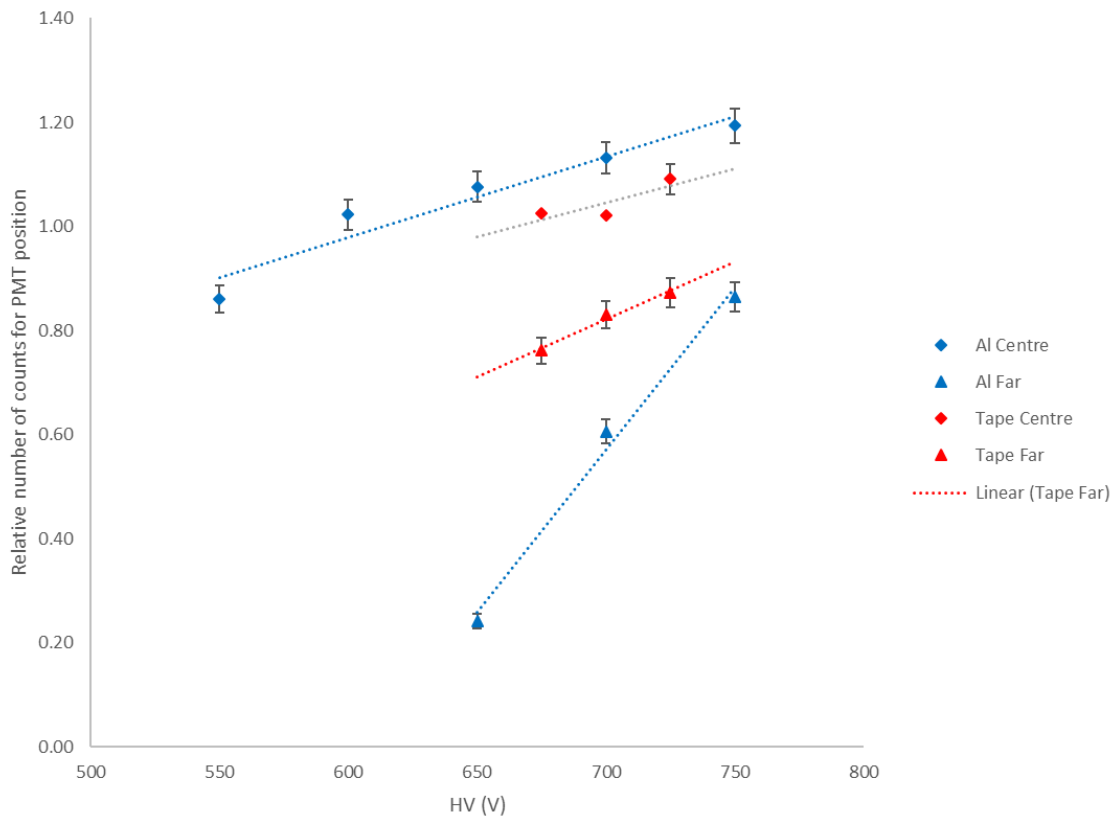
Figure 6.7: Count rate for PMT mounted centrally on scintillator. Blue – aluminium wrapping, red – reflective tape wrapping.
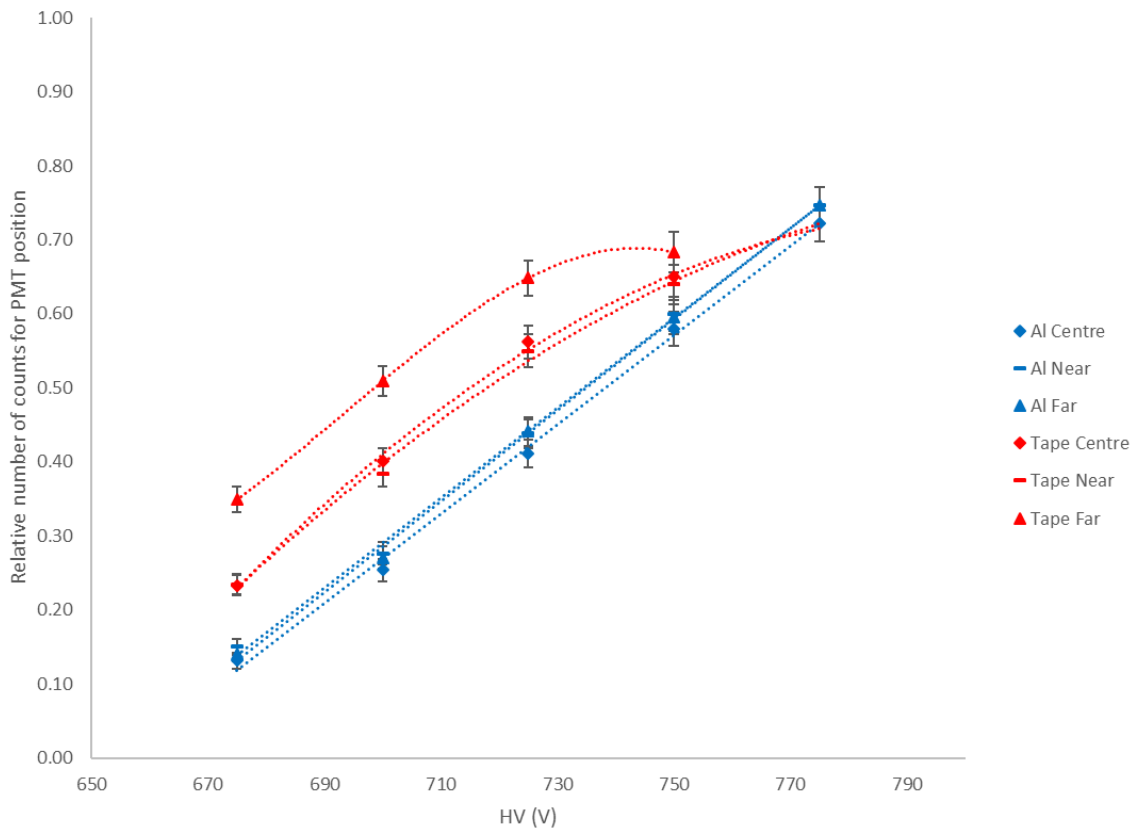
Figure 6.8: Count rate for PMT mounted end on to the scintillator.
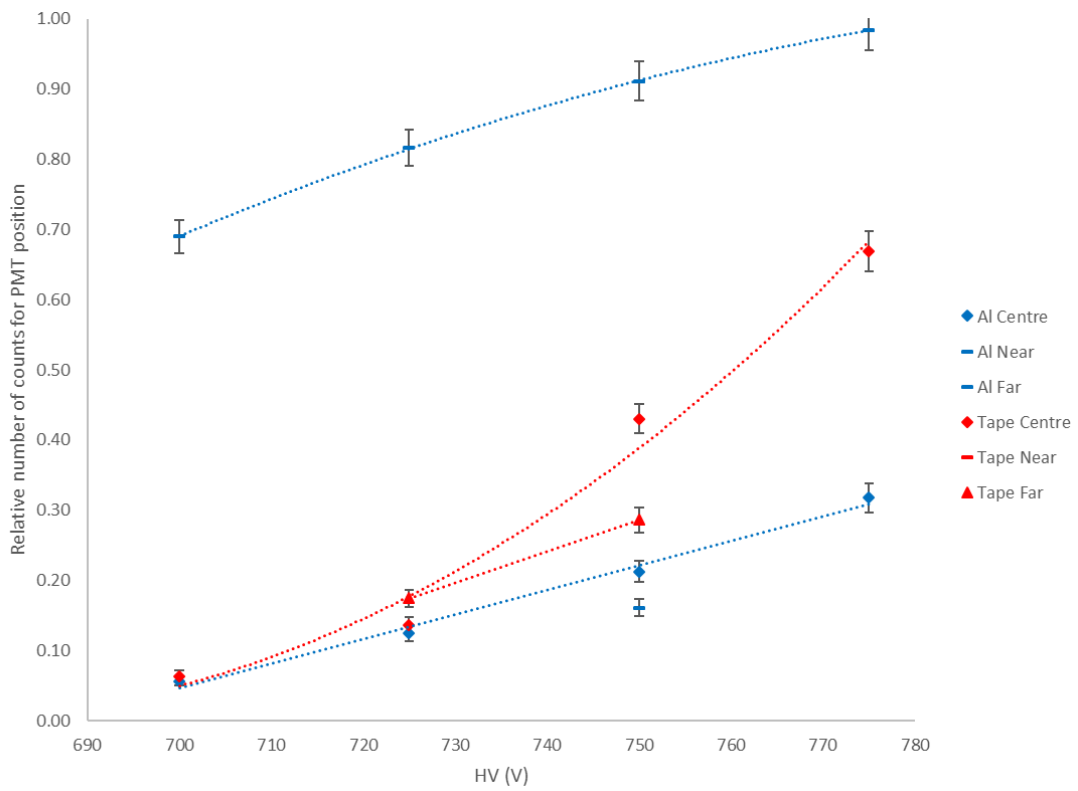
Figure 6.9: Count rate for PMT mounted normal to scintillator surface.
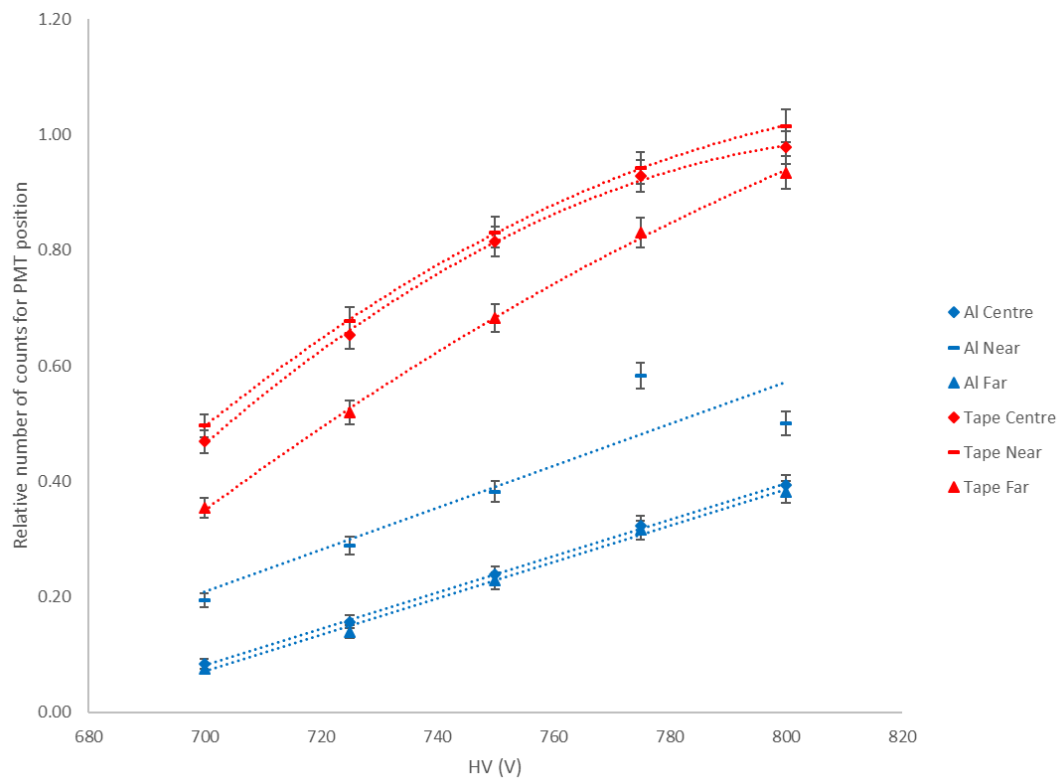
Figure 6.10: Count rate for PMT mounted normal to scintillator surface and edges of light guide chamfered to assist in directing light into PMT.

6.3.2.2 Detector design

The requirements of the scintillators outlined in sections 6.2.2 and 6.3.2.1 were developed into the schematics displayed in Figures 6.11 to 6.13 (final drawings provided by Scionix). Construction of each scintillator shown was completed by Scionix (delivered via JCS)

Figure 6.11: Schematic diagram for one of the gamma scintillators. Above: top view, below: side view. The other gamma scintillator is a mirror image of this design. All units are in mm.

Figure 6.12: Schematic diagram for the lower beta scintillator. Above: top view, below: side view. All units are in mm.

The figure shows engineering drawings with the following labels and dimensions:

Top view dimensions: 50, 53, 100

Side view (Doorsnede: A-A):
- Ø 26
- MHV Connector
- Built-in voltage divider
- Magnetic shield
- 5611 PMT
- PMMA Lightguide
- Reflector + Cover
- EJ-212 Scintillator 100x50x0.5 mm
- AL. mylar foil entrance window
- Dimensions: 94, 81, 45°, 10, 13, 120, 130

Title block:
CHECKED: RodH	⊕⊏	DIMENSIONS: MM	revisie	omschrijving
SCALE: 1:1	DRAWN: 13-07-2017		R4	
			R3	
SCIONIX	P.O. Box 143 3980 CC Bunnik The Netherlands		R2	
	Tel. 31 (0)30 657 0312 Fax. 31 (0)30 656 7563		R1	
SCIONIX HOLLAND BV Radiation Detectors & Crystals			TYPE:	R50*0.5BM100/1.1M-E1-P-X
TITLE: ASSEMBLY			DWG. No. VS-1515-30	A3

Figure 6.13: Schematic diagram for the upper beta scintillator. Above: top view, below: side view. All units are in mm.

The arrangement of all four scintillators is modelled in Figure 6.14. These scintillators were constructed at a cost of £2775.40 for the two gamma scintillators, £1758.15 for the lower beta scintillator, and £1734.60 for the upper beta scintillator (these values do not include VAT). The final constructed scintillators are shown in Figures 6.15 and 6.16.
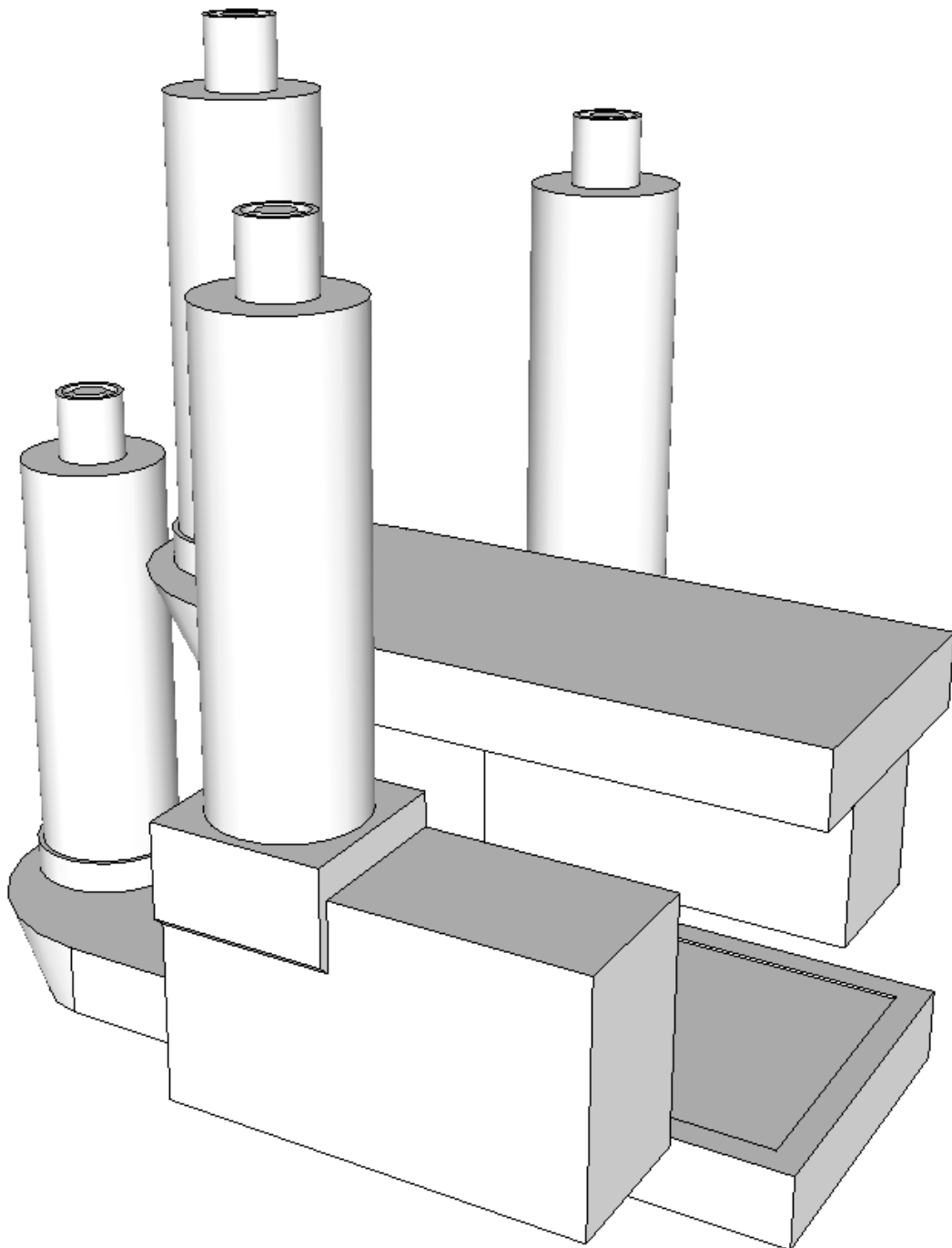
Figure 6.14: 3D model created in Sketchup 2017. The cavity where the animal is to be placed is visible in the centre with a gamma scintillator to each side and a beta scintillator above and below. The PMTs are directed upwards from the detection materials.

Figure 6.15: The two CsI gamma scintillators. The detection material is wrapped within the black tape.

Figure 6.16: The two beta scintillators. Top: the upper beta scintillator with the detection surface visible as the silver rectangle on the lower surface. Bottom: the lower beta scintillator with the detection surface visible as the silver rectangle on the upper surface.

6.3.3 Processing unit

The RMS30 processing unit (Figure 6.17) was reconfigured by JCS to simultaneously display counts from all four scintillators described in the previous subsection. The four outputs from the scintillators are transferred to the two inputs of the RMS30 via two interface boxes (Figure 6.18) that have been custom designed for this project. Operating instructions for this unit are available in Appendix 10.5.

Figure 6.17: The RMS30 unit from JCS. Left, visible are the two scintillator inputs to the left side of the unit. Power and computer connections are available (not shown) on the right side. Right, display on the RMS30 showing all four inputs active. The top two rows display the counts for the gamma scintillators and the bottom row for the beta scintillators.
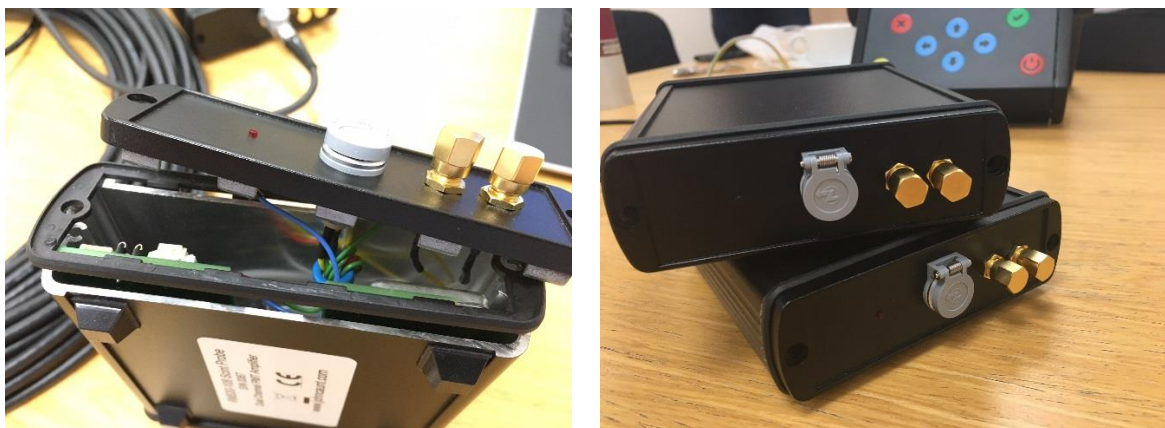
Figure 6.18: The two interface boxes for the scintillators. One for the beta scintillators and the other for the gamma scintillators. One side has two inputs for the two of the scintillators and the other side has a single output (shown) to the RMS30. The brass connectors shown above are outputs to an oscilloscope to allow for a more detailed calibration if required.

6.3.4 Shielding

The design shown in Figure 6.19 was determined to be optimal (in maximising the shield thickness) for the specification of the internal scintillators and for the requirements set out in the methods. An access door was built into the lid and the upper beta scintillator was fully removable to allow access to the cavity.
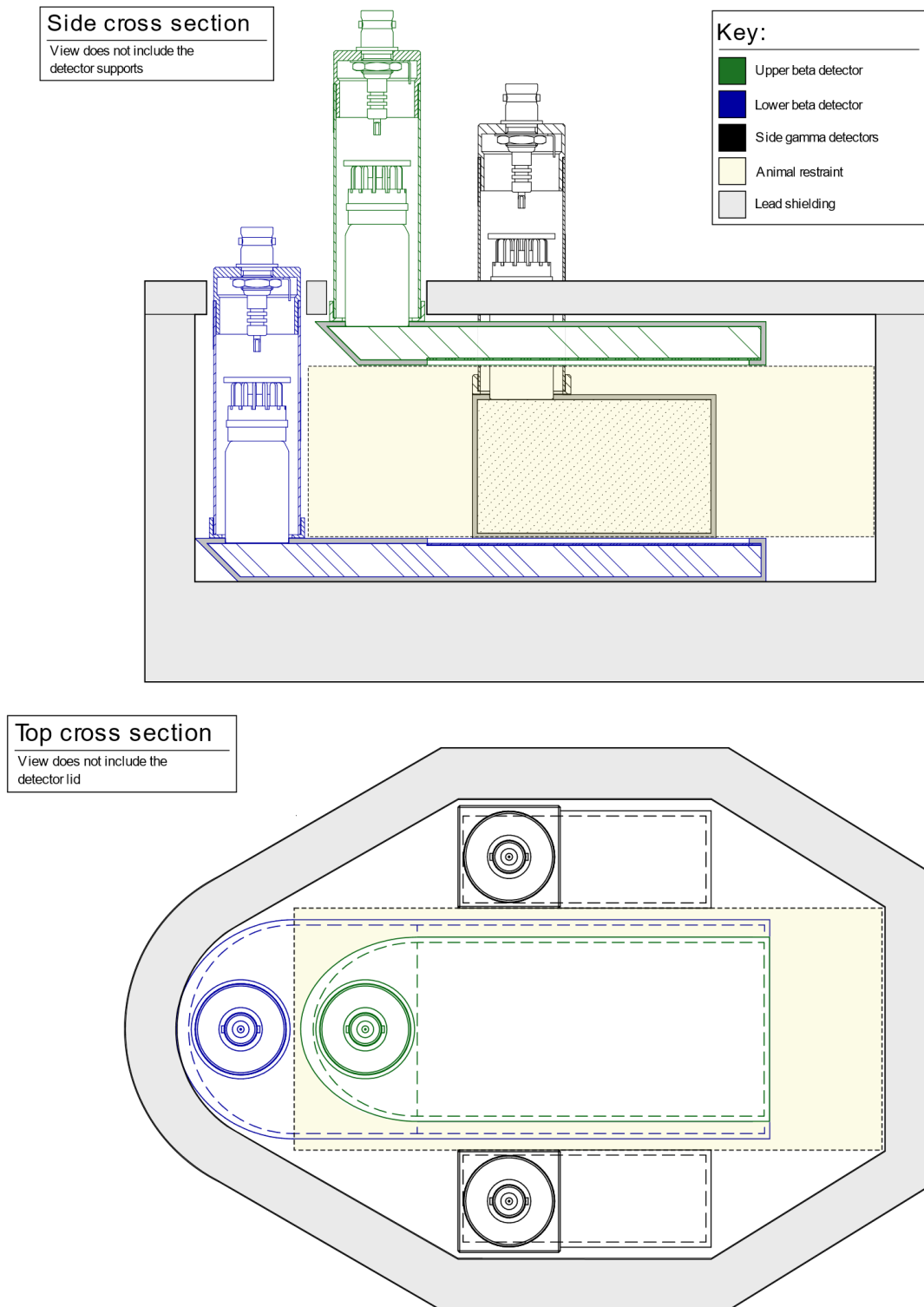
Figure 6.19: Shield design for optimal balance between lead thickness and weight.

The design in Figure 6.19 allowed for a base lead thickness of 30 mm and wall thicknesses of 15 mm (Figure 6.20). The lid and door were 10 mm with the lid attaching to the base section of the shield by use of four screws. The door rested in place by use of ridges cast into it and the lid. A 3D model of this plan, generated in Sketchup 2017 (Figure 6.21), shows how the overall design should appear once constructed. The final cast shield is shown in Figure 6.22.
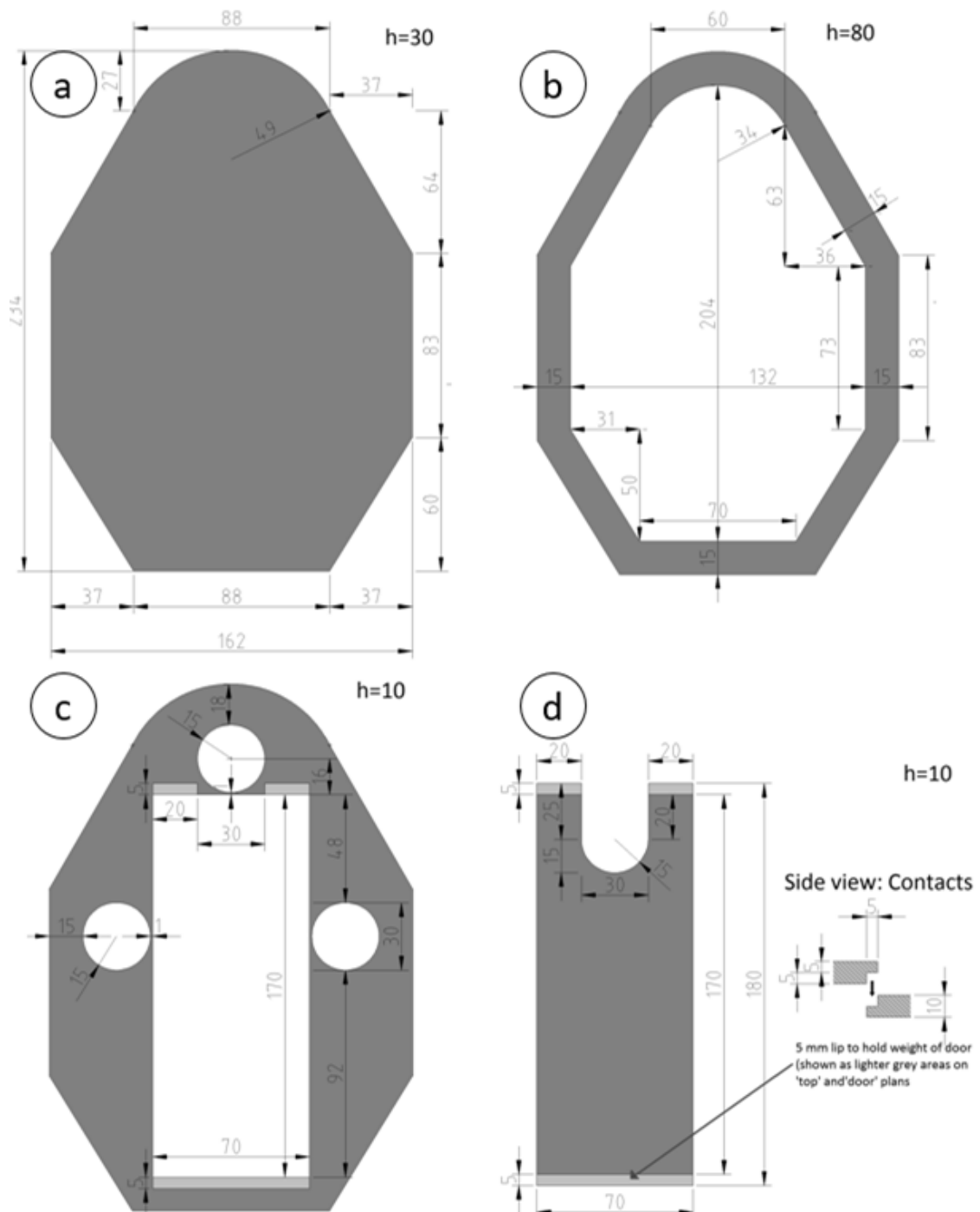
Figure 6.20: Schematic of shielding. a) the base unit, b) the walls, c) the lid with spaces left for the PMTs and access to the cavity, and d) the door to allow access to the cavity. All units are in mm. h is the height (in mm) of each section.
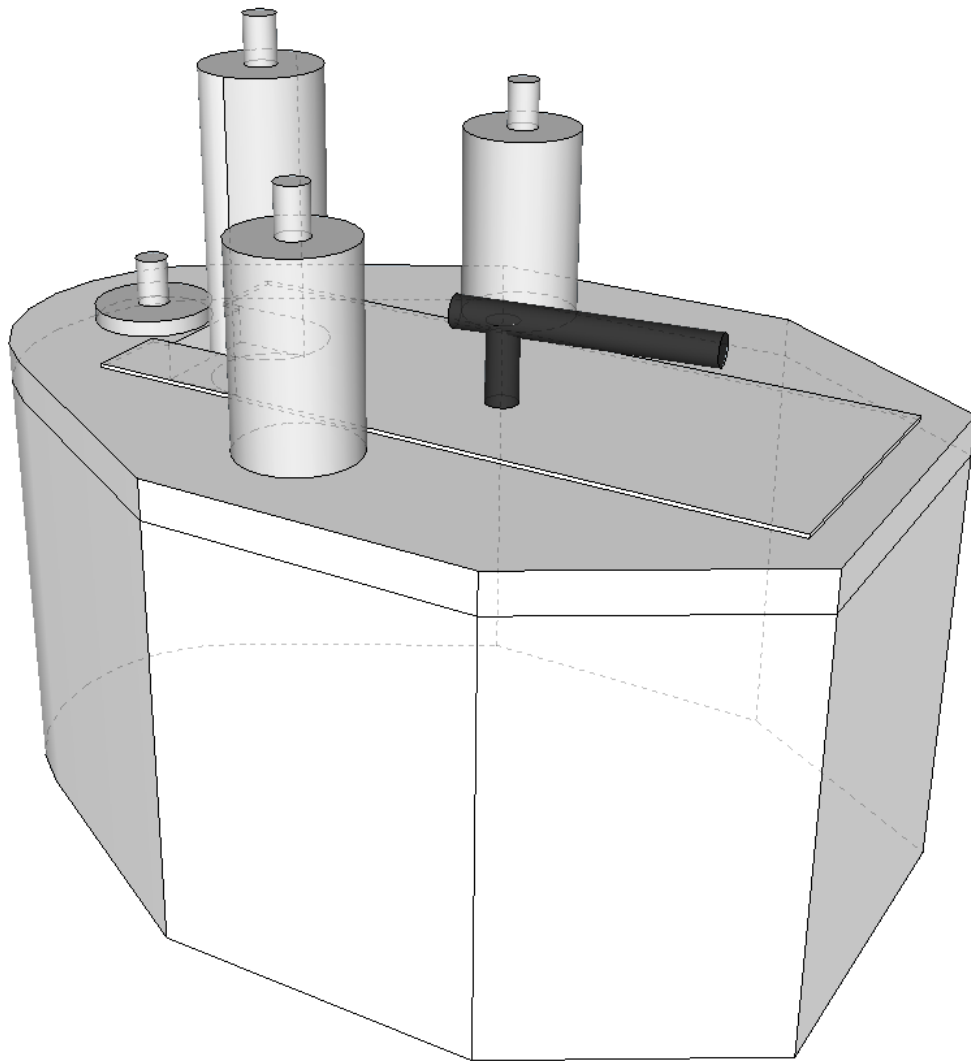
Figure 6.21: 3D generated model of the shielding. On the upper surface is the location and expected protrusion of the four PMTs. The access door will be opened using a handle.
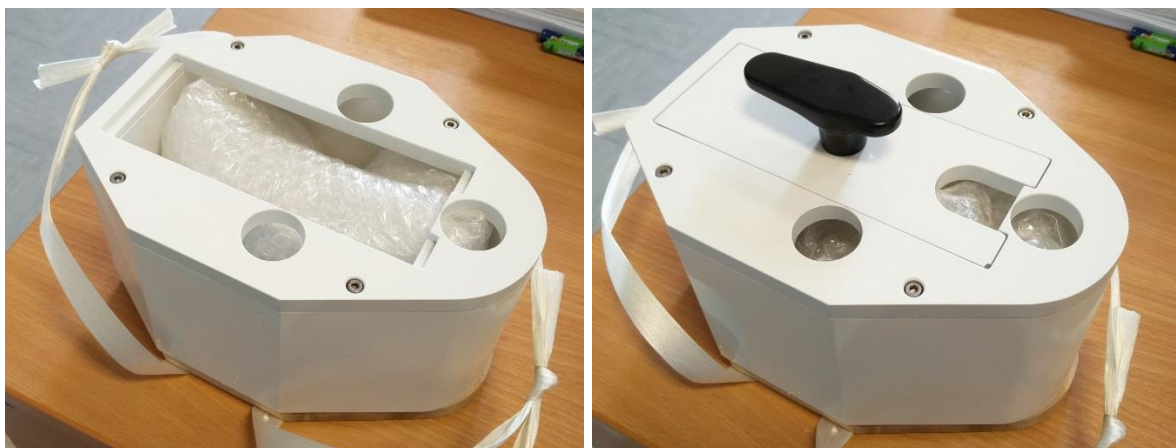
Figure 6.22: Cast lead shield. Left, door not in place, Right, door in place.

6.3.5   Supports and inserts

The three sets of supports for the restraint boxes were designed (Figure 6.23) to pack together into the cavity of the detector during storage or transportation; the small restraint support fits inside the medium restraint support which fits in between the two parts of the large restraint supports. During use of the detector, the small restraint support must sit inside the medium restraint support if a small restraint box will be used. The other two restraint supports are used by themselves if either a medium or large restraint box is to be used. The gaps visible in the structures were included as a weight saving measure only. The round holes visible in the side of the two smaller restraint supports match up to the positions of the air holes present in the restraint boxes. The design was drawn as a 2D image of parts (Figure 6.24) and laser cut and glued to form the final product shown in Figure 6.25. The laser cutter used power setting of 100% and speed 7%, taking 605 seconds to cut a set of restraint supports.
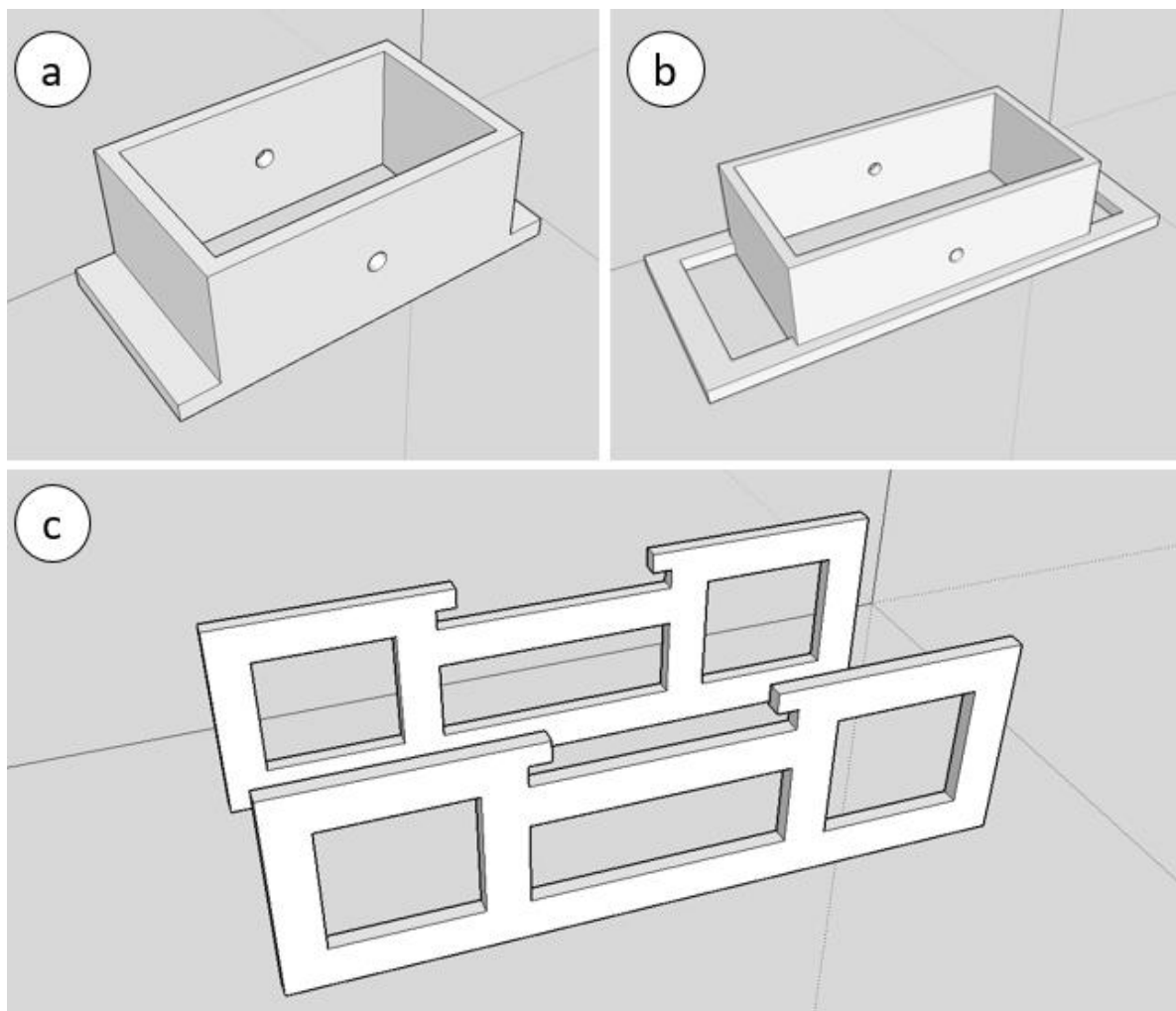
Figure 6.23: 3D generated model of the supports for the three restraint boxes. a) the small restraint support, b) the medium restraint support, and c) the large restraint support.
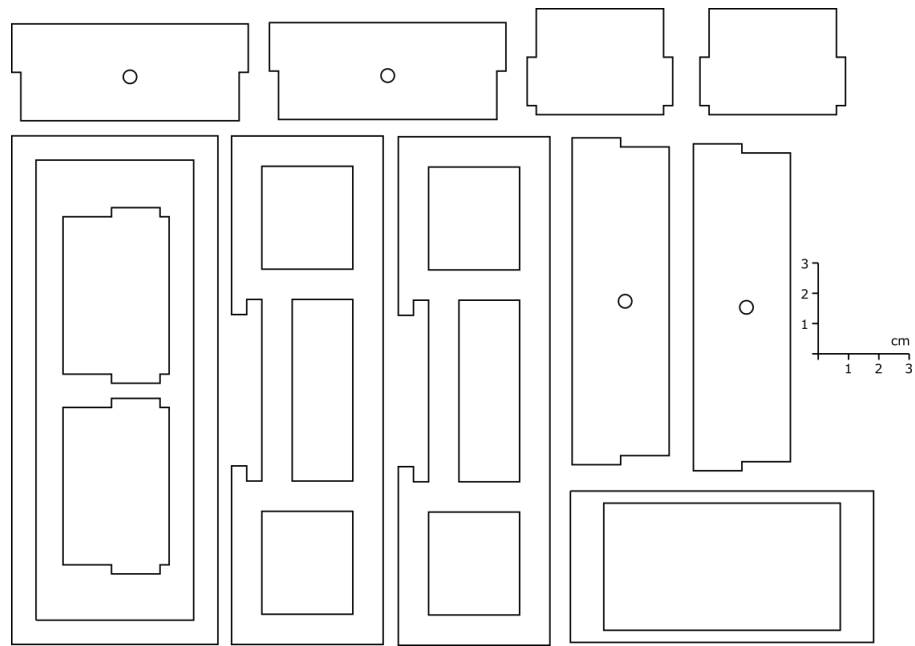
Figure 6.24: 2D template for the three restraint supports. This image is laser cut onto 3 mm Perspex and assembles using plastic weld glue. Scale is shown to the right-hand side of the figure (units are in cm).
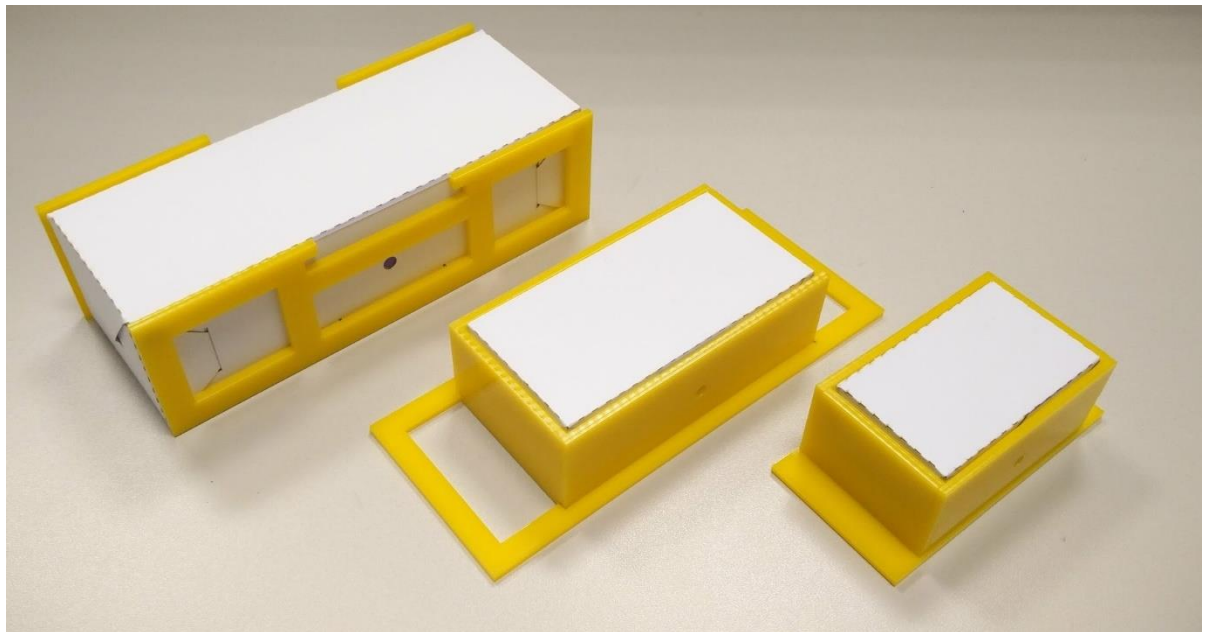
Figure 6.25: Restraints with boxes inserted. From left to right: large, medium, and small restraints.

The insert for positioning the three scintillators within the shield was a more complicated design (Figure 6.26). The design created for the insert allowed for easy removal of each scintillators whilst maintaining enough support to hold all the parts (three of the scintillators and the restraints) in place (Figure 6.27). A 0.1 mm aluminium sleeve for the cavity was constructed to protect these three scintillators from any animal or animal waste that may escape from the restraint boxes.
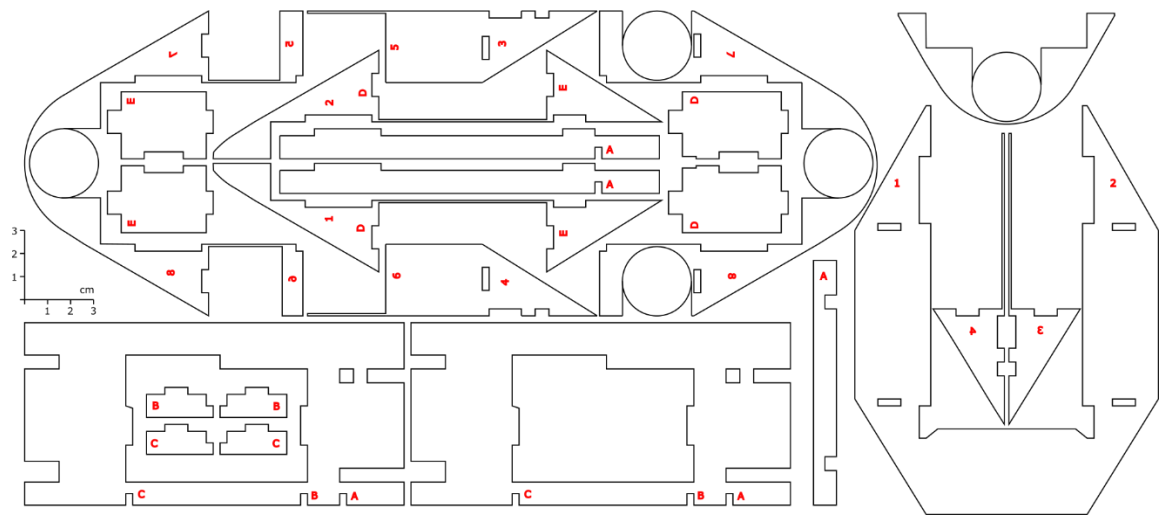
Figure 6.26: 2D template for the scintillator positioning insert. The numbers and letters (in red) were etched (settings: power 100%, speed 100%) into the surface of the parts by the laser cutter as a visual marker for what parts connect. Scale is shown to the left hand side of the figure (units are in cm).
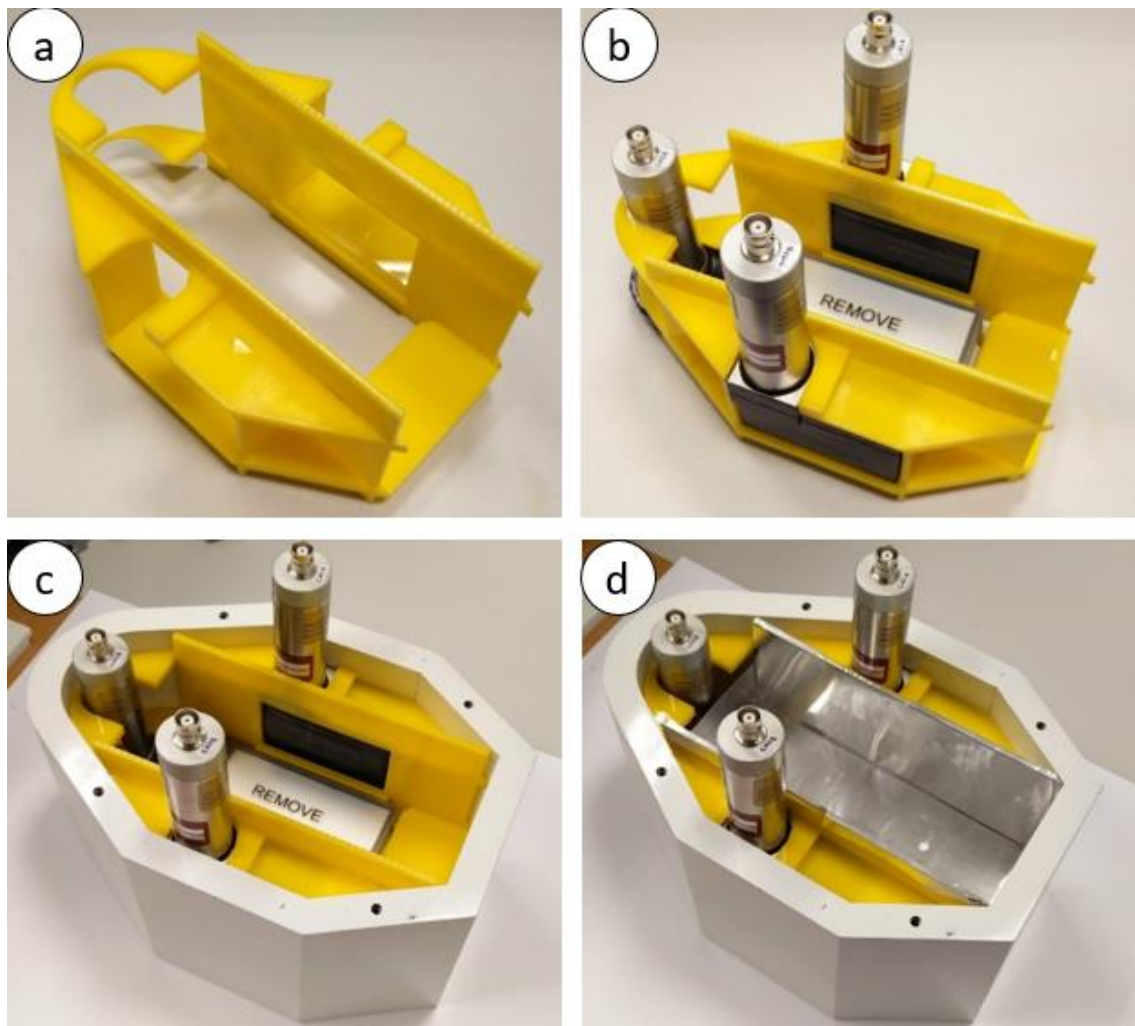
Figure 6.27: Insert for positioning the scintillators within the shield. a) The fully constructed insert, b) The three scintillators placed into the insert, c) the insert and scintillators placed within the shield, and d) an aluminium box placed into the cavity to protect the scintillators.

The case for the upper beta scintillator was designed (Figure 6.28) as two parts; an upper and lower section. The two sections are secured together using screws. A ridge along the top of the case (level with the bottom of the shield door) is included for both structural support and a means to keep the scintillator level whilst inside the detector (this rests directly under the lid when the largest box is used). The assembly of this case is detailed in Figure 6.29.
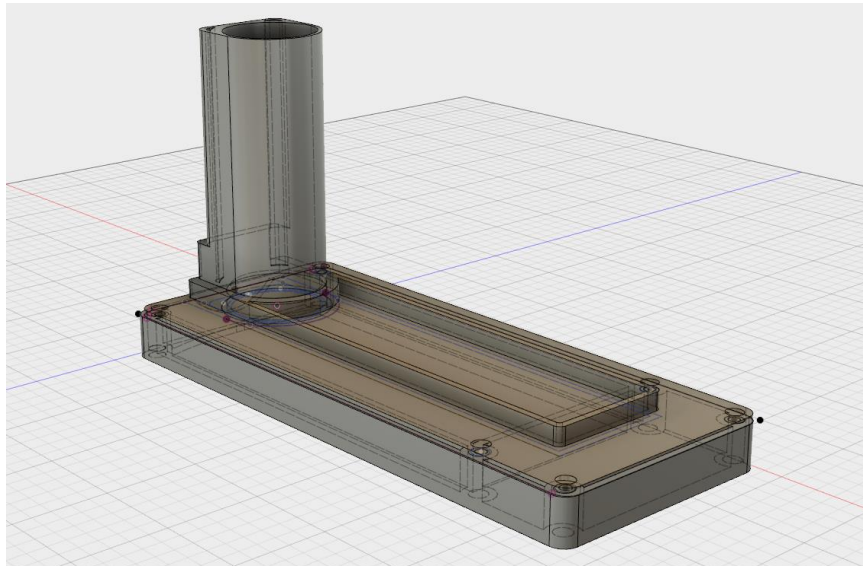
Figure 6.28: 3D design of the case for the upper beta scintillator.
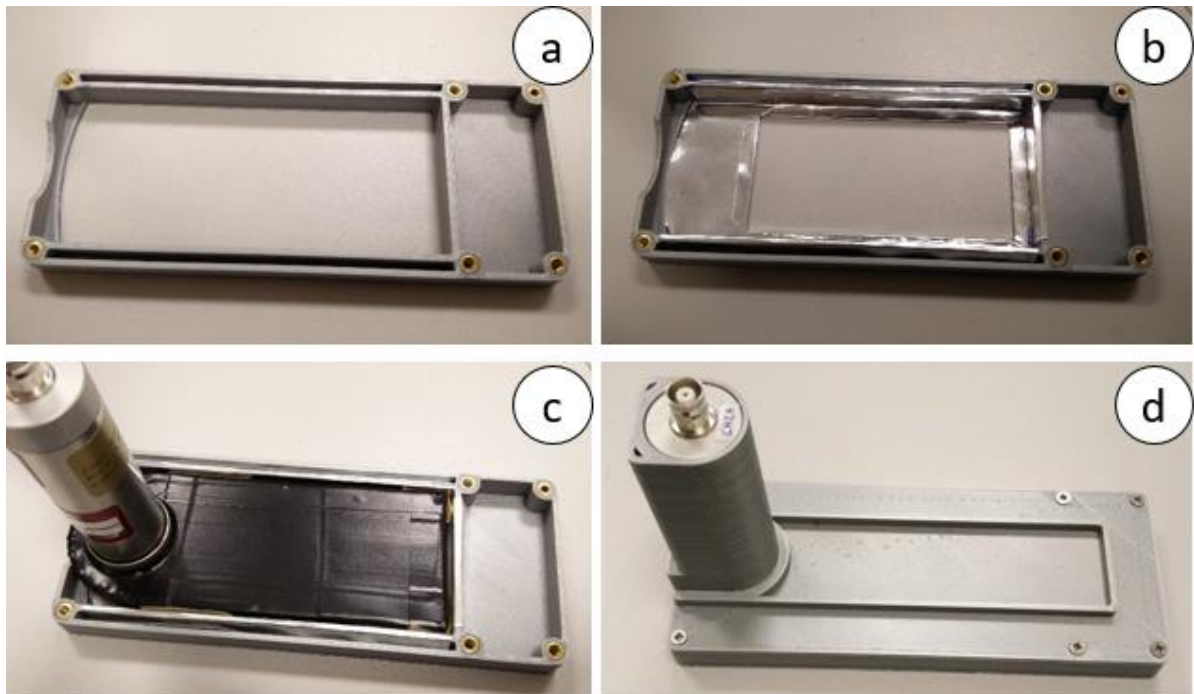
Figure 6.29: Construction of the upper scintillator case. a) tap screws inserted into base section, b) an aluminium insert creates a window for the detection surface, c) scintillator positioned in base section, and d) the upper section of the case is screwed into place.

The supports for the remainder of the scintillators took the form shown in Figure 6.30. Only the PMT section that penetrated through the shield was required to be protected (from accidental knocking). The design included two small protrusions on the bottom to secure the support between the detector insert (Figure 6.27) and the shield lid. A small gap is included due to the proximity of the PMT to the internal wall of the cavity. It is arched because of limitations in the 3D printing process. These supports are placed onto the PMTs as shown in Figure 6.31.
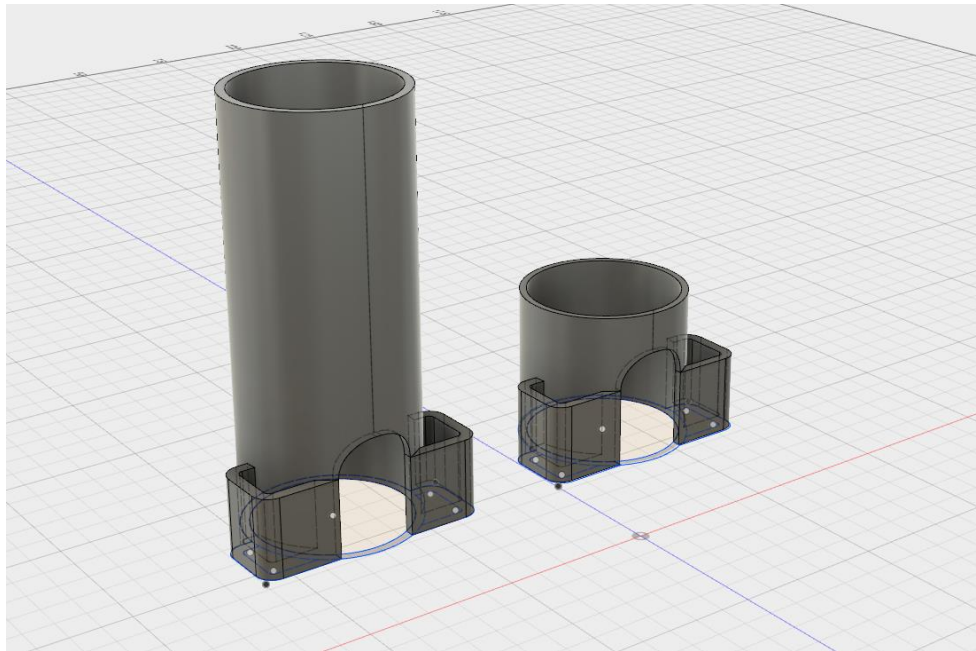
Figure 6.30: 3D design of the protective support for the PMTs. Two of the left support were printed for the gamma scintillators. The small support of the right was designed for the lower beta scintillator.
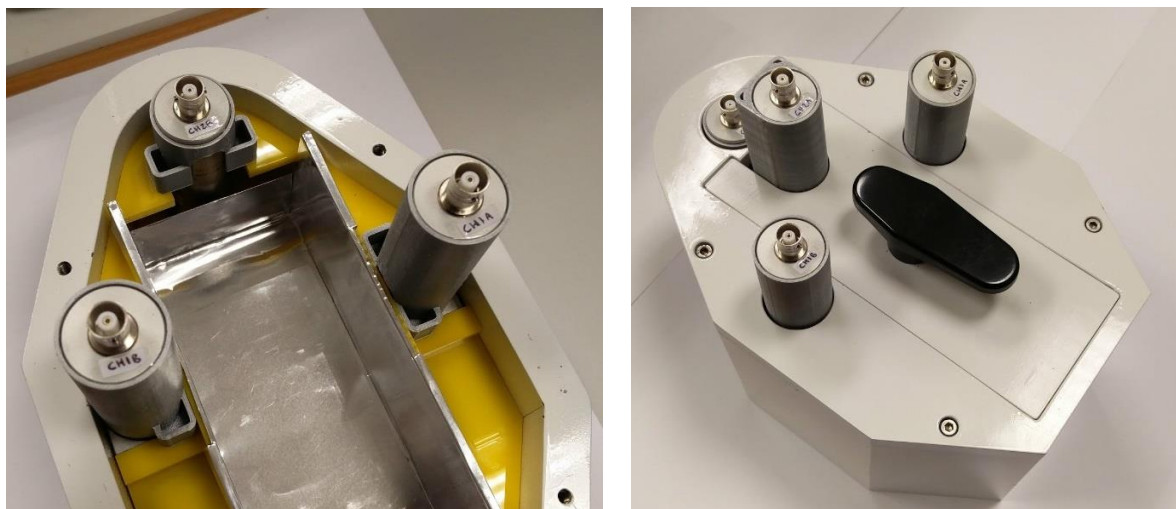
Figure 6.31: Protective supports placed onto the PMTs. Left, lid off, right, lid on.

6.3.6 Assembly

The detection system (electronics and scintillators) were initially assembled (Figure 6.32) to check its operation and was confirmed to be working. The final assembly of the full detection system is shown in Figure 6.33 and individual component properties are available in Table 6.1. To assist with assembly, the scintillators, cabling and ports were labelled. The Gamma scintillators to the right and left sides were labelled CH1A and CH1B respectively. The upper and lower beta scintillators were labelled CH2A and CH2B respectively.

Figure 6.32: Partial assembly of the detection system. The four scintillators connected to the RMS30 via the interface boxes.
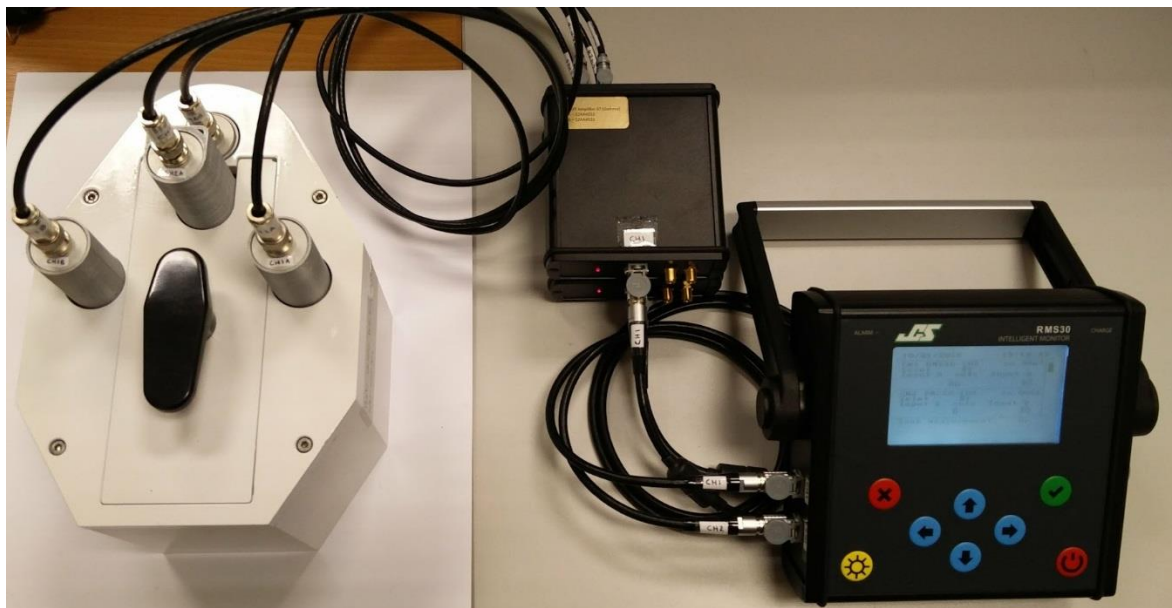
Figure 6.33: Full assembly of the detector. The shielded scintillators are to the left and the RMS30 and interface boxes are to the right.

Table 6.1: Properties of the detector components

Unit	Part	Identification code	Serial Number	Quantity	Cost (£)	L (mm)	W (mm)	H (mm)	Weight (g)
Detectors	Gamma scintillator	CH1A	S2AA4532	1	1387.70	75	30	135	404.8±0.1
Detectors	Gamma scintillator	CH1B	S2AA4531	1	1387.70	75	30	135	404.6±0.1
Detectors	Beta upper scintillator	CH2A	S2AA4533	1	1734.60	170	110	70	230.3±0.1
Detectors	Beta lower scintillator	CH2B	S2AA4534	1	1758.15	170	110	65	200.6±0.1
Processing	RMS30	RMS30	0007	1	5995.00	210	220	60	1500±100
Processing	Interface Box (Gamma)	Gamma	0067	1	1695.00	130	110	40	276.6±0.1
Processing	Interface Box (Beta)	Beta	0066	1	1695.00	130	110	40	274.4±0.1
Cables	Cables RMS30	-	-	2	-	1070	-	-	217.1±0.1
Cables	Cables Detectors	-	-	4	-	880	-	-	188.5±0.1
Cables	RMS30 power cable	-	45120	1	-	3300	-	-	502.5±0.1
Cables	Laptop USB cable	-	-	1	-	197	-	-	68.5±0.1
Inserts	Restraint support (all)	-	-	1	4.70	170	60	35	110.4±0.1
Inserts	Detector support	-	-	1	4.70	210	135	80	165.3±0.1
Inserts	Aluminium insert	-	-	1	<2.80	168	75	65	13.0±0.1
Restraints	Large (flat)	-	-	1	-	263	261	-	8.5±0.1
Restraints	Large (assembled)	-	-	1	-	166	60	48	-
Restraints	Medium (flat)	-	-	1	-	205	170	-	4.9±0.1
Restraints	Medium (assembled)	-	-	1	-	100	50	35	-
Restraints	Small (flat)	-	-	1	-	185	140	-	3.5±0.1
Restraints	Small (assembled)	-	-	1	-	70	40	35	-
Shield	Door	-	-	1	-	180	70	40	1300±100
Shield	Lid	-	-	1	-	240	165	10	1900±100
Shield	Base	-	-	1	-	240	165	125	18300±100
Shield	All	-	000001	1	918.00	240	165	165	21400±100

The detectors weights included the 3D printed supports. The weight of the plastic insert did not include the 3D printed supports or the aluminium insert. The aluminium insert was 0.1 mm in thickness. Error for dimensions is ±1 mm.

6.3.7 System testing

6.3.7.1 Energy calibration

Energy calibration of the detection system resulted in the following high voltage (HV) setting for each scintillator: CH1A was set to 1075 V (Figure 6.34), CH1B was set to 975 V (there was a lower than expected reading for 960 V (Figure 6.35). It was assumed that this was caused due to a discrepancy in the positioning of the gamma source between readings. This calibration was redone for 950 to 1000 V (Figure 6.36) with the source left in position between readings). CH2A was set to 975 V (Figure 6.37) and CH2B was set to 1000 V (Figure 6.38). Because there is no distinctive peak for these latter two, the voltage is set at the point where the source counts per second squared divided by the background counts per second (S^2/B) is largest (Knoll, 2010).
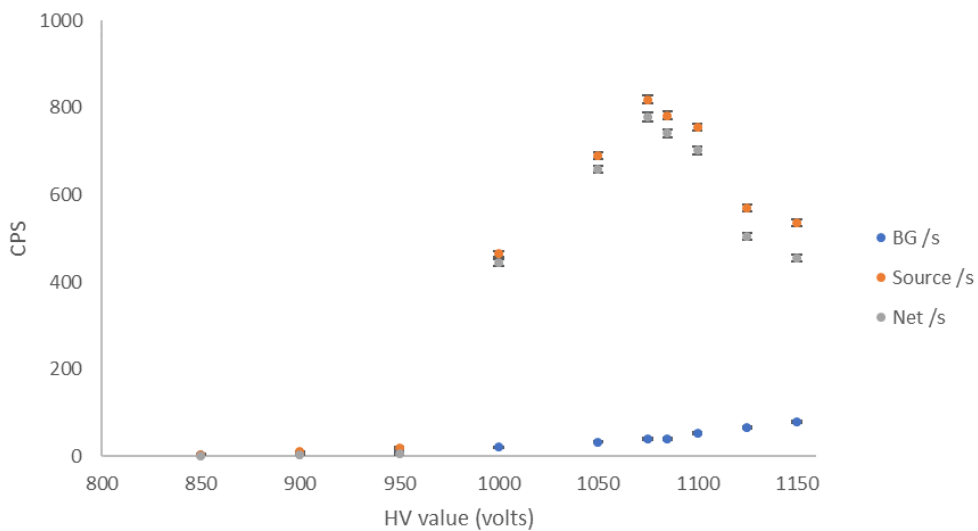
Figure 6.34: Energy calibration curve for CH1A. 9 kBq ^{137}Cs source (in circular tin) placed on top of scintillator (detection side facing up). LL = 800 mV, UL = 1100 mV. Not in shield.
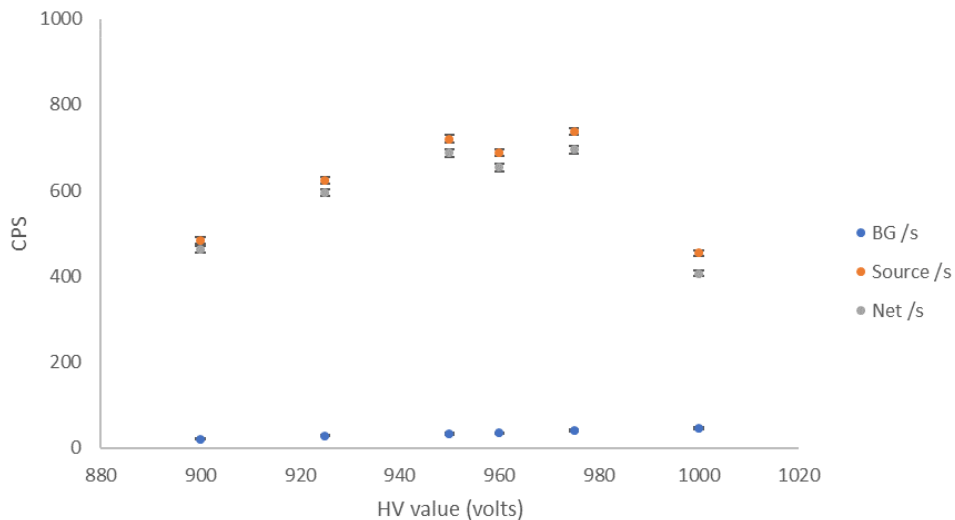
Figure 6.35: Energy calibration curve for CH1B. 9 kBq ^{137}Cs source (in circular tin) placed on top of scintillator (detection side facing up). LL = 800 mV, UL = 1100 mV. Not in shield.
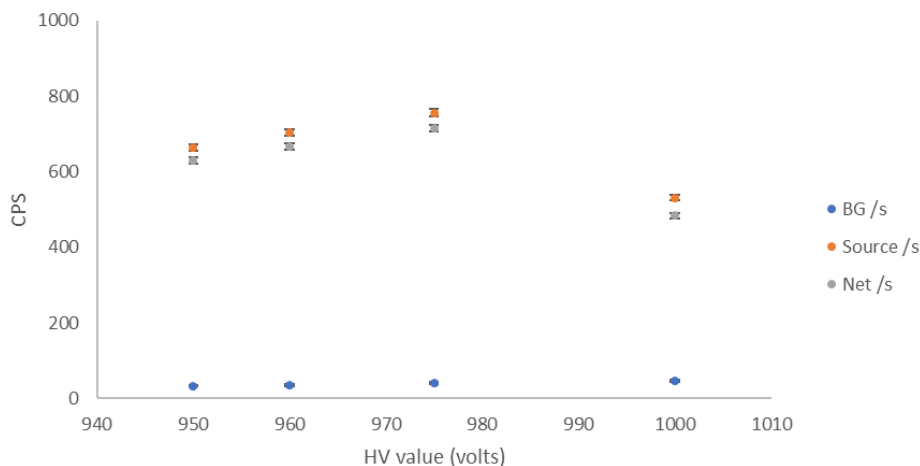
Figure 6.36: Energy calibration curve check for CH1B. Repeat of 950 to 1000V for CH1B Gamma. 9 kBq ^{137}Cs source (in circular tin) placed on top of scintillator (detection side facing up). LL = 800 mV, UL = 1100 mV. Detector not in shield.
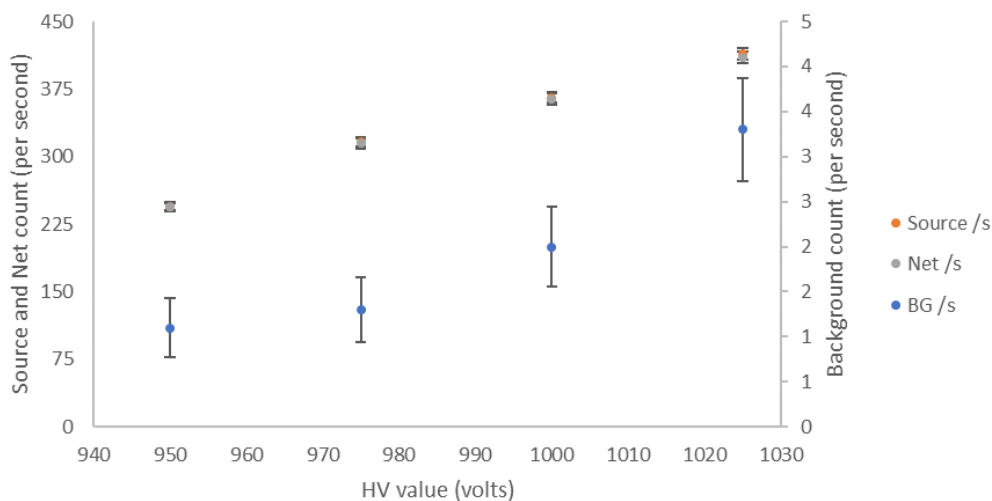
Figure 6.37: Energy calibration curve for CH2A. 1.6 kBq ^{36}Cl source placed in the centre and on top of scintillator. Scintillator was placed upside down with detection side facing up. Window is left open (disabled). Scintillator not in shield.
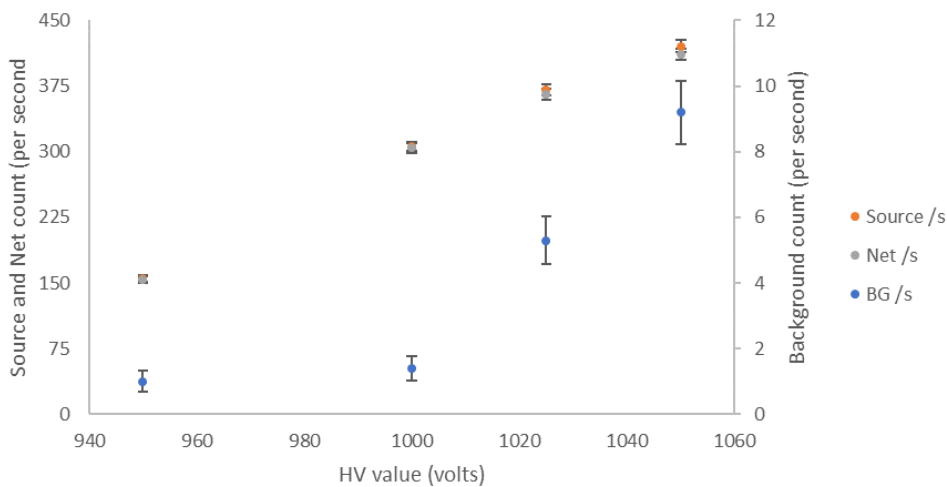
Figure 6.38: Energy calibration curve for CH2B. 1.6 kBq ^{36}Cl source placed in the centre and on top of scintillator. Scintillator side facing up. Window is left open (disabled). Scintillator not in shield.

6.3.7.2 Response to sources

The response of the beta scintillators to different radioactive sources is shown in Figure 6.39. Out of the three beta emitters tested, ^{60}Co and ^{90}Sr are measurable at a 100 second count. The third, ^{14}C, is measurable on CH2A but is below the limit of detection for CH2B. The gamma from ^{137}Cs is picked up on both scintillators but is below the limit of detection for the 10 seconds it was counted for. This is likely to be a significant detection on a longer count and therefore will need to be accounted for during sample monitoring.

6.3.7.3 Attenuators for beta scintillators

Filtering of the ^{90}Sr beta emissions showed a sharp drop in recorded count rate between 0 and 0.1 mm levels out across 0.2 to 0.4 mm (Figure 6.40). This indicates that a thickness of between 0.1 to 0.2 mm of aluminium is required to remove the majority of the lower energies. Therefore, the lower beta scintillator should be covered with 0.2 mm of aluminium to ensure there is only a signal detected from the ^{90}Y emission.
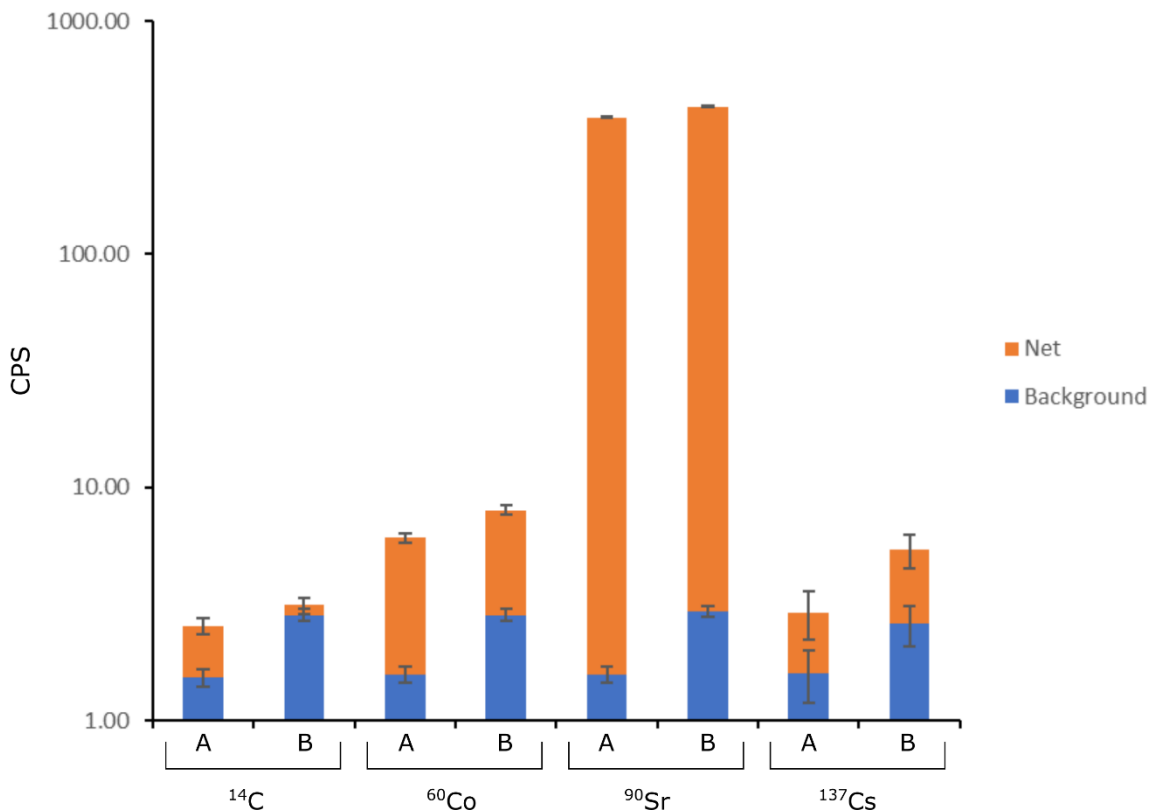
Figure 6.39: Beta scintillator response to difference sources. A and B identify the upper and lower beta scintillator respectively. Each source was counted for 100 seconds except ^{137}Cs, which was counted for 10 seconds.
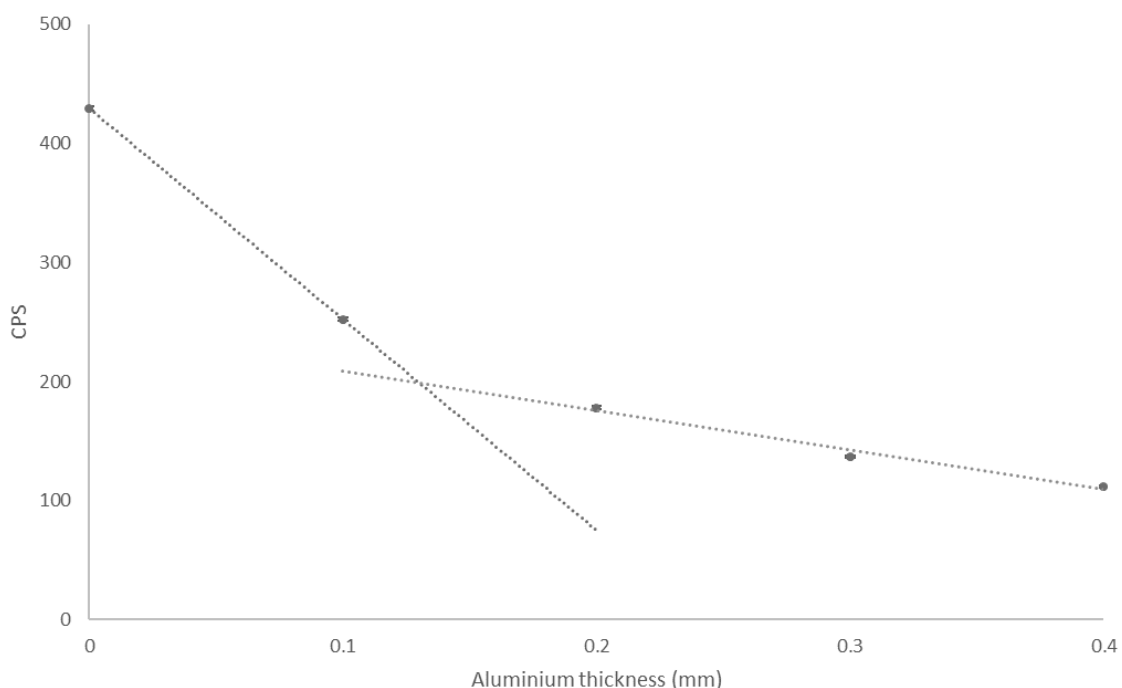
Figure 6.40: Effect on count rate for different thicknesses of aluminium placed between scintillator and source. CH2B used with the ⁹⁰Sr source placed centrally to the detection surface.

6.4   Discussion

The overall design created in this project allows for a modular and portable detector. Further, some parts are designed to be easily replaced or adjusted if the task requires it. The restraint boxes are designed as consumables and can be easily adjusted if a different size is required (within the constraints of the cavity size). With practice, they can be quickly assembled and the flatpack design means many restraint boxes can be transported easily. A limitation, however, is that these restraint boxes are designed to be discarded after each measurement and therefore a sufficient quantity of boxes must be laser cut in advance of any field work. A further consequence in the manufacture method is the current requirement to laser cut in batches of 5 (or 10 for the smaller restraint box). This means a person is required to be physically present at the laser cutter to insert new card and activate the next batch. If a few hundred of each box is required then a number of hours of access to a laser cutter must be available. A more suitable alternative could therefore be to outsource this work to an online box making service (e.g. http://www.tinyboxcompany.co.uk).

The design of the scintillators has been reached through both a review of relevant literature and from experimentation (e.g. Section 6.2.2.2). Each of the scintillators were designed to be

housed as a separate unit with the supports inside the shielding designed (Figure 6.27) to both hold the scintillators in the correct position but also allow for their removal. The user can therefore opt to use all or a combination of the four scintillators (within the current scintillator support structure) depending on the radionuclides targeted for measurement. This means transportation and assembly requirements can be reduced in the event of only part of the detector being required. The scintillators should be operated in pairs, however, as the design attempts to account for movement of the animal within the restraint box. Another design choice for the scintillators was in positioning all of the PMTs such that they are directed upwards out of the shield (Figure 6.19). This was mainly to ensure the PMTs do not compromise the sides of the shielding but this arrangement has created a simple structure to the overall design whereby the entire detection unit can be broken down to facilitate ease of transportation. Initial results for the two beta scintillators (Figure 6.10), however, shows there is a decline in detected counts the further away a source is placed from the PMT. This is investigated further in the next chapter.

The overall weight of the shield is balanced between having a low weight and having a reasonable level of shielding against background radiation. The modularity of the shield assists with portability: the heaviest item is 18.3 kg (Table 6.1) and the remainder of the components are at a weight carriable by a second person. A concern of the PMT placement, however, lies in the shape of the two beta scintillators (Figure 6.16) and also the strength of the PMTs protruding from the shield. The shape of the two beta scintillators means there is a potential for these to snap at the interface between the PMT and the scintillator. This is negated in the upper beta scintillator due to the 3D printed case it is inserted in (Figure 6.29). Whilst the scintillators could remain in the shielding during transportation, if the mode of transportation means the case containing the shielding cannot be guaranteed to stay in an upright direction, the scintillators must be removed or risk damage to the PMTs. In this case, care should be taken when handling or transporting the lower beta scintillator as excessive stress or strain on the PMT connection could cause it to snap. The unique design of the overall system means placement of the scintillators is restricted by the dimensions of the shielding (Figure 6.20), though there is scope to raise or lower the two gamma scintillators. If a large alteration to the position of the scintillators is required then a new shield will need to be cast.

Processing of the detected signal for this project is performed by an RMS30 unit from JCS (section 6.2.3). Despite costing half of the total unit (when including the interface boxes; Table

6.1), this processing unit was chosen due to its field readiness (rugged and waterproof construction), simplicity of use, and its ability to accept and display the signal from all four scintillators at the same time. The non-removable power supply, whilst not an ideal solution, is accepted here as it can be operated for at least a day and is fast at recharging (if extended fieldwork keeps the user away from mains power then a suitable portable power bank or car adapter can be used to recharge the unit). For operation, the unit is a single channel analyser and therefore outputs a reading for a pre-set window of energies. The unit is currently configured (section 6.3.7.1) for ^{137}Cs detection on the two gamma scintillators and the window is left open on the beta scintillators for the measurement of beta emitting radionuclides. The settings can, however, be easily changed to allow for detection of other radionuclides. The devices ability to detect ^{137}Cs was confirmed through the energy calibration of the two gamma scintillators. Initial testing of the two beta scintillators showed it was responsive to ^{90}Sr though further testing is required to determine how much this detection is altered by moving the source over the surface of the scintillator (Section 6.3.2.1). Further, any detection made from the beta scintillators will need to consider the proportion of the count that is from ^{137}Cs gamma (Figure 6.39). The insertion of an aluminium attenuator over the lower beta scintillator (Section 6.3.7.3) will assist with identifying the components of the detected signal.

A current drawback of the current detection system is the use of the two interface boxes. This adds extra components and cabling and therefore increases set up time and the space required for operation and transportation. The modular design of the detector, however, means these could eventually be built into the RMS30 unit for an additional cost, or swapped out for a different processing unit if desired (useful for any end users who already have their own SCA or MCA).

6.5   Conclusion

A design of a portable beta / gamma detector for monitoring radionuclides in small animals was identified and has been constructed to specifications outlined in the methods and results of this chapter. All components of the detection system have been confirmed to operate and are capable of detecting the required energy emissions of the target radionuclides. Variation in the count rate, however, was seen when repositioning the detection source. The extent of this change, as well as the performance of the detector with animal targets, is explored in the next chapter.

7 Laboratory and field testing

7.1 Introduction

The design, construction, and energy calibration of a portable detector was detailed in the previous chapter. The ability to detect the target radionuclides with this detector was also confirmed during calibration and preliminary laboratory testing. This chapter aims to establish the performance of the detector in monitoring target animals. Investigated are: the performance of the restraint boxes, the positional (horizontal and rotational) effect, and the extent to which measurements obtained with the developed detector compare to animal internal activity concentrations measured by other approaches.

7.2 Methods:

The following methods used the full detection system (as detailed in chapter 6) and a supply of each restraint box. The RMS30 settings were set to those defined in chapter 6.3.7.1. Determination of ^{90}Sr is determined via measurement of ^{90}Y. Each of the four scintillators are subsequently identified using the codes shown in Figure 7.1.
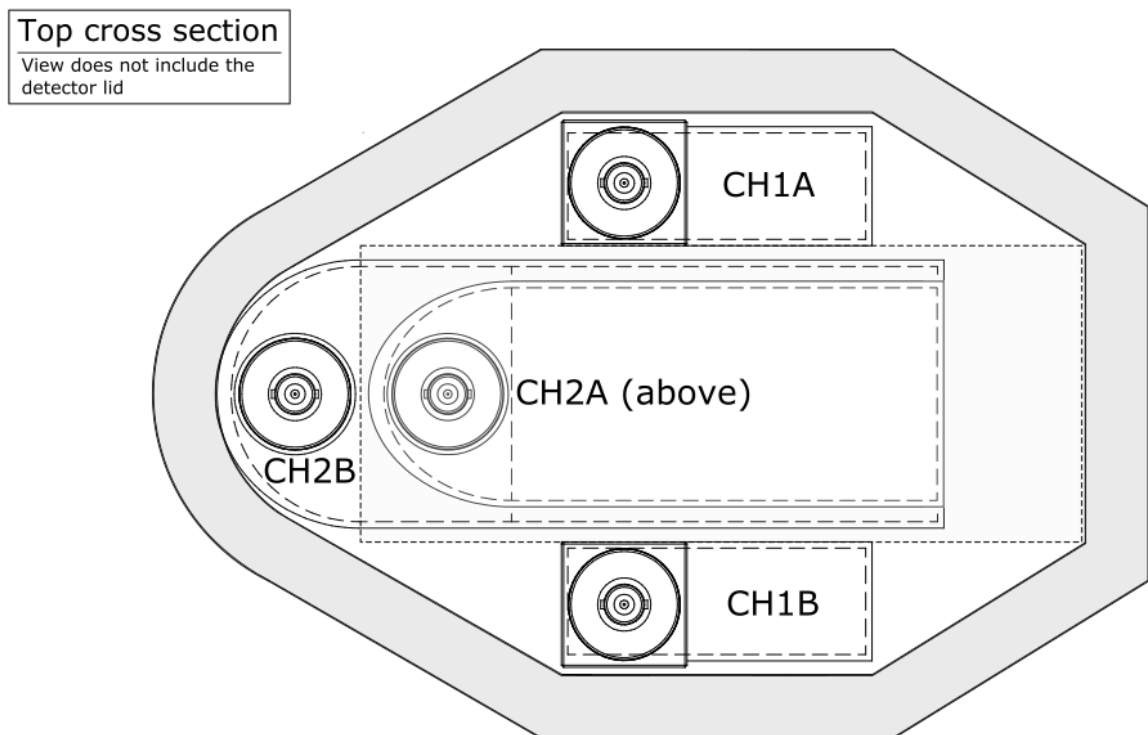
Figure 7.1: Codes used to identify each scintillator. The two gamma scintillators are identified as CH1A and CH1B. The upper beta scintillator is identified as CH2A and the lower scintillator as CH2B. This corresponds with the display output on the RMS30.

7.2.1   Restraint testing

Initial testing of the restraint boxes was conducted with rescued bats in Silverdale, UK, and with mice in the CEZ. All testing was conducted in line with research ethics requirements (Appendix 10.6). Testing in Silverdale made use of four live bats, each of a different species: Brandt's, (*Myotis brandtii*), brown long eared (*Plecotus auritus*), natterer's (*Myotis nattereri*), and pipistrelle (*Pipistrellus pipistrellus*), that had been rescued from the wild. All bats had been held in captivity for a period of time such that they were used to being handled. The aim of this experiment was to a) check the difficulty of placing a live animal into the box and b) check how the bats reacted to being held in the restraint box for a period of at least 120 seconds. A dead Greater horseshoe bat (*Rhinolophus ferrumequinum*) was further used, as an example for one of the largest bat sizes found in the UK, to check sizing of the restraint boxes. A box for each bat was assembled and a trained handler inserted a bat into each box. Observations were made on the ease of inserting and removing the bat as well as how the bat reacted to being in the box. Testing in the Chernobyl Exclusion Zone (CEZ) was undertaken as part of a separate study to live-monitor ^{137}Cs in small rodents caught within the exclusion zone (this study did not use the live-monitor developed in this thesis and instead only focuses on gamma detection). Testing for these small rodents was similar to that of the bats in which observations were made as to the insertion and subsequent restraint of the animal within the restraint boxes. Count time for each rodent was 180 seconds with some held in boxes for >10 minutes during processing.

7.2.2   Laboratory testing

7.2.2.1   Response to phantoms

Three phantoms (produced for and used by the Chornobyl Center, Slavutych, Ukraine. Phantoms are checked periodically by the Center) were placed individually into the cavity to determine the response rate per Bq of each scintillator. This 'response rate' is used in place of absolute efficiency (see section 2.5.4) as a direct comparison between the detected count rate and the radionuclide activity concentration within the sample is instead desired. Each phantom was a semi-cylinder with base dimensions of 6 cm by 3 cm and a height (i.e. radius) of 1.5 cm. The weight of each phantom was approximately 20 g and had a density of 1 g cm^{-3}. The first phantom contained 552 Bq of ^{137}Cs, the second contained 540 Bq of ^{90}Sr, and the third phantom contained 5480 Bq of ^{137}Cs and 53.7 Bq of ^{90}Sr (all activities decayed to date of experiment). Radionuclide content was distributed evenly throughout the phantom. The
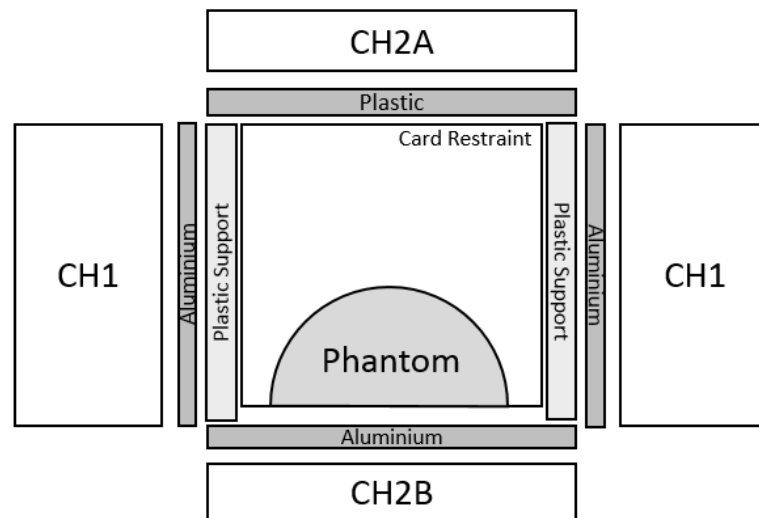
Figure 7.2: Cross-section of cavity and scintillators. CH1 are the gamma scintillators, CH2A is the upper beta scintillator, and CH2B is the lower beta scintillator. Shown are the attenuators between the phantom and each scintillator (thicknesses described in text). Between 0.18 and 0.53 mm of 1.22 g cm^{-3} tape surrounds CH1 scintillators. .

phantoms were placed centrally within the medium restraint box and positioned in the cavity using the plastic support (Figure 7.2). The thickness of the plastic restraint support was 3 mm and the aluminium covering each gamma scintillator (CH1) had a thickness of 0.1 mm (as described in chapter 6). The aluminium covering on the lower beta scintillator (CH2B) was varied between 0.1 and 0.3 mm. A 0.1 mm plastic sheet was added to the upper beta scintillator (CH2A) due to concerns of damaging the Mylar covering when in the field. A 120 second count was taken of each phantom for the CH2B aluminium thicknesses described above. An additional 120 second count was taken of each phantom with the plastic covering of CH2A removed (aluminium on CH2B set to 0.1 mm). Background counts (120 seconds each) were recorded at intervals throughout the experiment.

The response rate of each scintillator to ^{137}Cs and ^{90}Sr (via ^{90}Y) was determined in the following way. All readings were converted to counts per second. The background component was subtracted from each scintillator reading. The net counts recorded on each scintillator for the ^{137}Cs and ^{90}Sr phantoms were divided by the phantom activity to provide a detection response rate for each scintillator (counts s^{-1} Bq^{-1}). This was repeated for the sum of counts on CH1A and CH1B and for the sum of CH2A and CH2B (summing was found to reduce the positional influence. See section 7.3.2.3). These response values were tested by estimating the ^{137}Cs + ^{90}Sr phantom count and comparing to the counts recorded by the scintillator for that phantom. Repeated measurements, for the testing described in this chapter, was not possible

due to restricted sampling time. There is no possibility, therefore, to account for the dead (or decay) times described in chapter 2.5.4.

7.2.2.2 Effect of source position on count rate

Two radioactive sources, one ^{137}Cs (circular tin, 38 mm diameter) and the other ^{90}Sr (flat, 50 x 30 mm), were used to investigate the response of the scintillators to a source placed at different points within the detector cavity. The positional effect of the ^{137}Cs source on the gamma scintillators was determined by measuring the count rate with the ^{137}Cs source in the positions identified in Figure 7.3. The two measurements taken outside of the shield were to check the shield was attenuating the external count rate by the desired amount. Each count was for 100 seconds. A 100 second background count was taken before and after this set of measurements. The upper beta scintillator and lid was not used for this test, nor was the source placed in the restraint box, due to the size of the ^{137}Cs source. The positional effect of the ^{90}Sr source on the beta scintillators was determined by measuring the count rate with the ^{90}Sr source placed at intervals across the surface of the scintillators as described in Figure 7.4. The beta scintillators were not placed in the shielding for this determination and were both positioned such that the detection surface was facing upwards. Each count was taken for 10 seconds. For both experiments, background count was subtracted from the results before scaling to a fraction of 1; for ^{137}Cs, 1 was defined as the result for position c (Figure 7.3) and for ^{90}Sr 1 was defined as the largest count on each beta scintillator surface.
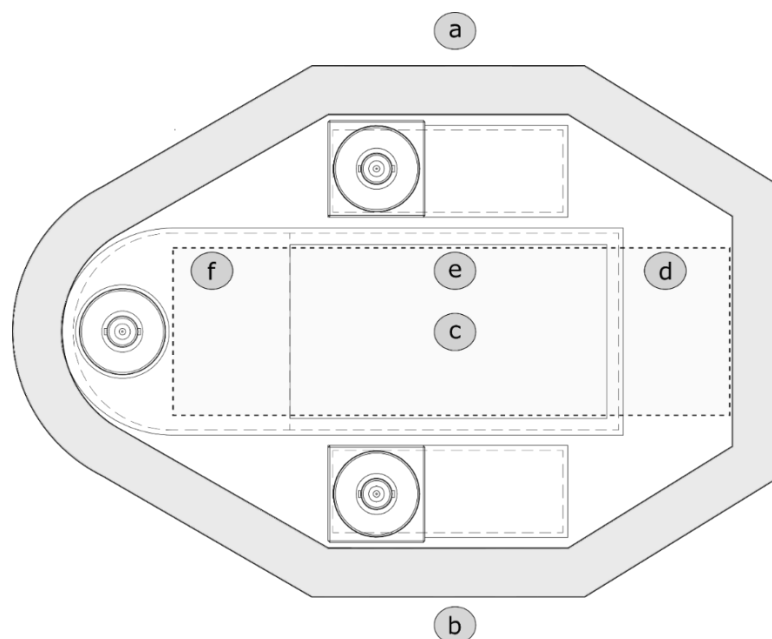
Figure 7.3: Gamma scintillator response to ^{137}Cs source. Markers (a) to (f) indicate source positions. (e) is midsection of cavity, (f) and (d) are placed 38 mm from ends of cavity
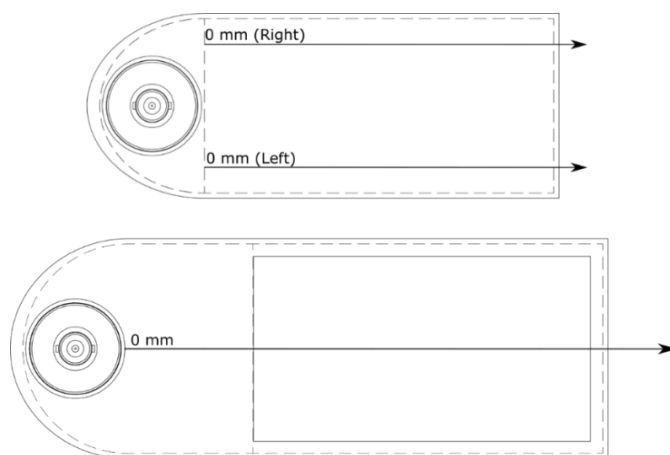
Figure 7.4: Beta scintillator response to ^{90}Sr source. Above, upper scintillator (CH2A), below, lower scintillator (CH2B). Source was moved along black line in direction of arrow.

7.2.2.3   Effect of animal placement on count rate

Testing with animal sources took place in Ukraine. Small rodent and bird samples (caught in the CEZ during August 2017 and May 2017 respectively and were frozen for later analysis) were analysed in a laboratory in Slavutych (for small rodents) and in a laboratory in the CEZ (for birds). Details of samples are given in section 7.2.3 (only a subset is used for this section).

Testing the effect of movement of the animal for radiation detection was conducted in two main parts for both rodent and bird species, with a further positional test performed on the rodents due to the presence of the tail (and potential impact on ^{90}Sr estimation). The first positional test (as an extension to the experiment detailed in section 7.2.2.2) measured count rates from each scintillator with the animal placed in each of the positions shown in Figure 7.5. This was conducted for one rodent moved horizontally within the medium restraint box with the box fixed centrally in the cavity using the plastic restraint support. A further test was conducted using one bird placed in the medium restraint box (without the plastic support) but with the restraint box moved to each of the far corners. This was to simulate the potential maximum change in count rate due to too small an animal being placed into too large a restraint box. These two animals were placed with their head facing towards the beta PMT and limbs facing the gamma scintillator CH1A (position R_B in Figure 7.6). Three of each organism type were then selected to test the effect of rotating the animal within the cavity (Figure 7.6) and one mouse was further used to test the effect of the tail position on count rate (Figure 7.7). Example placements for each species is shown in Figure 7.8. The top of the card restraint box was removed to allow easier access to the inside of the restraint. Count times for each position detailed in this section was 120 seconds with background readings

being taken periodically throughout the experiment. Results were scaled to a fraction of 1 for comparison, where 1 is defined as placement in the middle of the cavity with feet directed to the bottom CH2B beta scintillator (position H_A in Figure 7.5, orientation R_A in Figure 7.6 and tail position T_A in Figure 7.7).
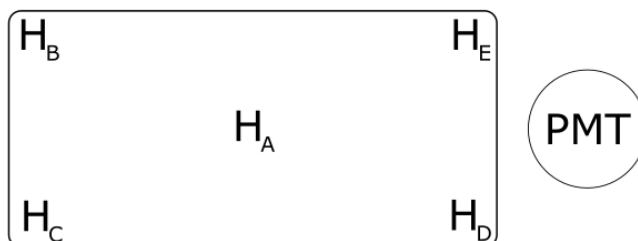
Figure 7.5: Response of scintillators to moving organism inside cavity. Shown is top view of cavity. H denotes this is the horizontal movement test, the subscript identifies position.
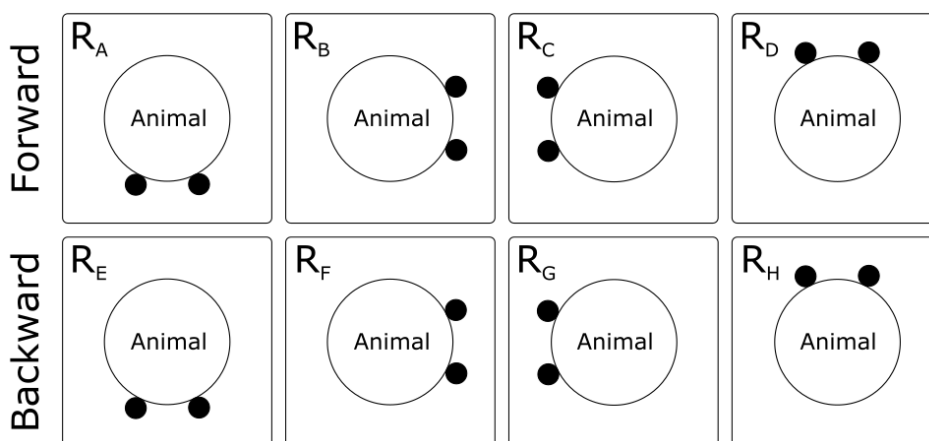
Figure 7.6: Orientation of animal samples in detector cavity. The two black circles on the animal indicates the direction of the feet within the restraint box. CH1A is to the right of each box, CH1B is to the left. Forward position has head directed towards the beta PMT, backwards is away from the PMT. R denotes this is the rotational movement test, the subscript identifies the position.
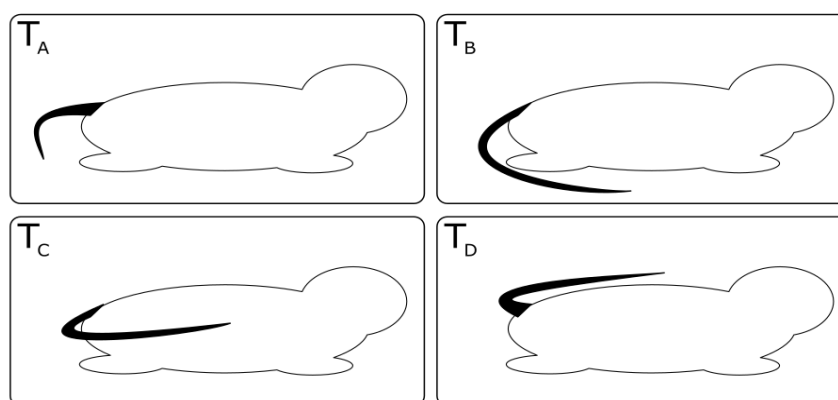
Figure 7.7: Tail position for mouse. T_A – behind, T_B – under, T_C – side, T_D – above. Beta PMT is to the right of each box. CH1A is in front of box, CH1B is behind, CH2A is above and CH2B is under.
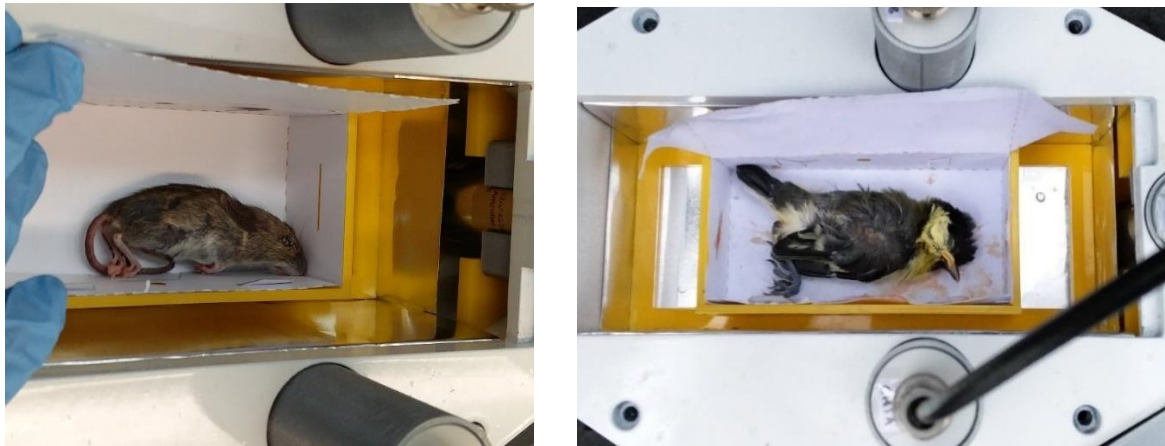
Figure 7.8: Animal samples placed in detector. Left, mouse placed in corner of restraint box, Right, bird placed in central position. The restraint box lid was removed to give easier access for positioning of animal samples.

7.2.3 Field testing

The portable detector was field tested in the CEZ in Ukraine. Testing comprised of monitoring 10 small rodents and 10 birds (caught in the CEZ and frozen for storage in the Slavutych laboratory) in the presence of different levels of background radiation. Animals were entire with pelt, feathers and gastrointestinal tracts. Results of this testing were compared to values (Table 7.1) that were determined using a calibrated radiation detector based at the Slavutych laboratory. Methodology is similar to that used in Bondarkov et al. (2011).

Three test sites in the CEZ were selected for radiation measurements of the animal samples with a further set of measurements taken at the laboratory in Slavutych (a low background site). These were all located within or close to the Red Forest (Figure 7.9) and were designated as the 'car park' (Figure 7.10 and Figure 7.11), 'vehicle inspection ramp' (Figure 7.12), and 'roadside' (Figure 7.13). Background dose rates at these sites were 5.7, 4.5 and 1.8 µSv h^{-1} respectively. The temperature at the time of measurement was approximately 0˚C (laboratory site was at room temperature 22˚C) with weather conditions consisting of rain and snow with a light (patchy) covering of snow on the ground. It was not desirable at the time to test if the detection system was waterproof and therefore it was deemed necessary to place the detector under shelter at each site (detailed in the figures).

Table 7.1: Properties of small rodents and great tits.

Sample #	Species	Weight (g)	Total count (Bq)			
			^{137}Cs	± Bq	^{90}Sr	± Bq
G025113	*Myodes glareolus*	22.8	31433	4650	981	109
G025115	*Sylvaemus flavicollis*	32.1	2133	319	5012	507
G025118	*Myodes glareolus*	22.5	36378	5381	138	501
G025119	*Apodemus agrarius*	21	2678	400	251	27
G025120	*Myodes glareolus*	16.5	6931	1031	1440	147
G025121	*Sylvaemus flavicollis*	27.4	14241	2110	1180	123
G025123	*Sylvaemus sylvaticus*	23.3	5560	825	1372	139
G025125	*Sylvaemus sylvaticus*	10.3	1623	243	811	82
G025126	*Myodes glareolus*	16.9	19092	2828	517	56
G025127	*Sylvaemus sylvaticus*	12.6	1354	203	987	99
G025040	*Parus major*	16.9	1298	197	5480	556
G025041	*Parus major*	16.5	1623	246	5011	513
G025042	*Parus major*	15.2	840	129	3753	388
G025043	*Parus major*	16.1	965	147	3883	396
G025044	*Parus major*	17.5	328	51	1529	158
G025045	*Parus major*	17.0	272	42	1233	126
G025046	*Parus major*	17.6	175	32	715	74
G025047	*Parus major*	16.9	91	14	690	70
G025048	*Parus major*	17.3	77	12	403	42
G025050	*Parus major*	15.8	170	26	242	25

Uncertainty for G025118 is larger than the count rate because of the large ^{137}Cs activity and the methods used to estimate ^{90}Sr (Bondarkov et al., 2011)
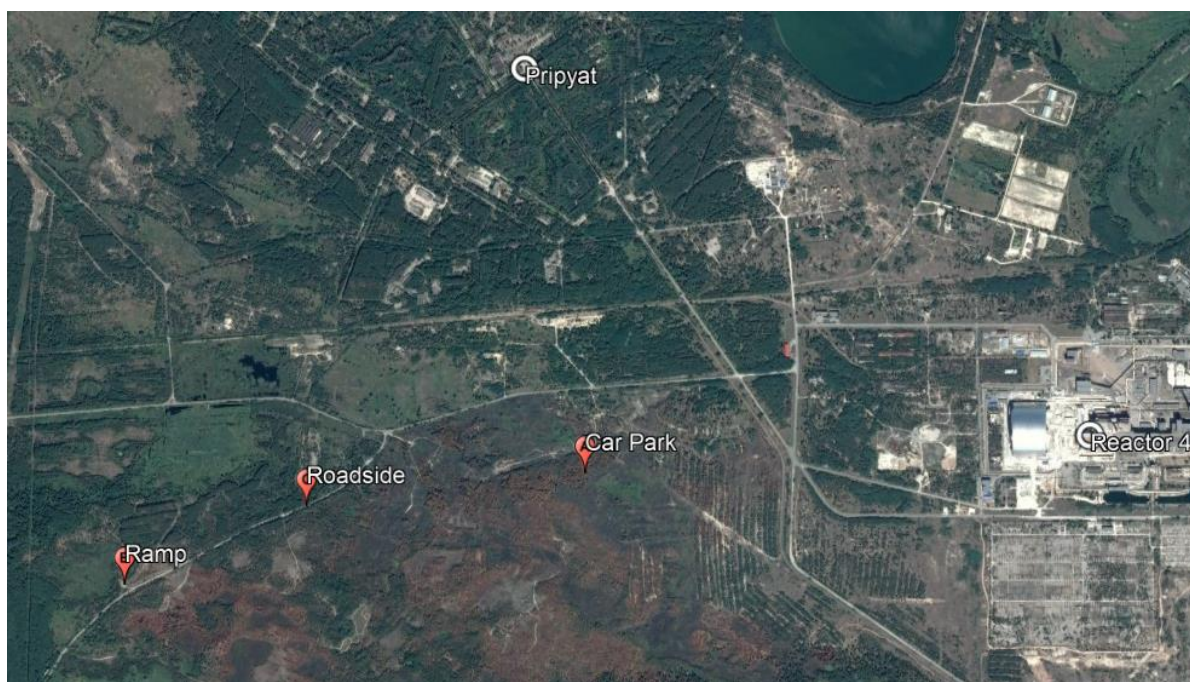
Figure 7.9: Map of test site locations in the CEZ. Test locations are labelled A to C. Their positions are shown in relation to Pripyat and the nuclear power plant.

Figure 7.10: Car park test site.

Figure 7.11: Car park test site. The detector shield was located under the tailgate of the transport vehicle due to adverse weather.

Figure 7.12: Vehicle inspection ramp test site. The detector was positioned under a folding table next to the tailgate of the transport vehicle. An emergency tent was used to cover the table.

Figure 7.13:Roadside test site. The detector was positioned inside the transport vehicle with access provided through the tailgate.

Each animal was placed (in orientation R_B; Figure 7.6) in the medium restraint box and positioned centrally in the cavity (position H_A; Figure 7.5) using the plastic restraint support. The small rodents had tails in approximately position T_A (Figure 7.7). All animals were monitored for 120 seconds each with periodic background counts (each 120 seconds). Based

on preliminary measurements during the position response experiment (Section 7.2.2.3), it was decided to monitor mice at all sites described above but only to measure the bird samples at the control (lab) site and at the roadside site. This decision was made after observing that the count rate from the rodents with low ^{137}Cs activity concentration were at or below the MDA (for the high background site) and therefore the birds (with a ^{137}Cs activity concentration lower than the rodents) would definitely be below the MDA at those sites.

Results were interpreted in the following way. Background count was subtracted from each scintillator reading. The count rates on CH1A and CH1B were summed to provide the measured ^{137}Cs count rate. The count rates on CH2A and CH2B were summed and the ^{137}Cs contribution subtracted (fractional contribution determined from analysis of phantoms in section 7.2.2.1) to provide the measured ^{90}Sr count rate. A correction factor (k) is required to account for self-absorption of the ^{90}Y beta emission within the body of the organism. This factor varies depending on the mass (m) of the animal. Bondarkov et al. (2011) derived Equation 7.1 to correct for this self-absorption in their detector. It was assumed this factor would be similar for the newly developed live-monitor.

$$k = 0.949 + 1.24e^{-\frac{m}{6.28}}$$

7.1

The similarity of the results across the measurement sites was determined by first determining if the data was normally distributed. This was tested in SPSS (v24) and the output assessed against the Shapiro Wilk test because the sample size was 10 animals. A one-way repeated measurement ANOVA was applied to results determined as having a normal distribution. A non-parametric repeated measurement ANOVA (Friedmans test) was applied to the results that were determined as not being normally distributed. If the outcome had P<0.05 then a pairwise comparison was applied to check if the significant difference that was found applied between all sites or between specific sites.

To ascertain the correlation between measured count rate and internal activity, the site measurements for each organism were plotted against verified internal activities (results attained from the separate study the samples were acquired from) shown in Table 7.1 for ^{137}Cs and ^{90}Sr respectively. These graphs therefore provide a conversion coefficient between measured count rate and actual internal activity. The strength of the correlation was tested by applying a bivariate correlation (Pearson) test using SPSS.

7.3   Results

7.3.1   Restraint

Out of the four bats placed into the restraint box, only one (*Plecotus auritus*) repeatedly attempted to exit the restraint. This meant two persons were required: one to handle the bat and the other to hold / close the restraint box. This bat, along with two of the other bats did, however, settle rapidly once in the box. The *Myotis nattereri* settled after a few minutes but if the restraint box was moved then it would start moving around / making noise again. Upon closing the restraint box, care was needed as some bats pushed their feet back out before the flaps could be fully closed. Placing the restraint box into the plastic restraint support also required observation of the breathing holes as the bats would protrude their thumbs through these. All the live bats fitted into the small restraint (Figure 6.1a). The largest bat (*Rhinolophus ferrumequinum* – dead) would only fit into the medium restraint box. All bats had to be enticed out of the box upon reopening. They were either dropped directly into a waiting bag by means of a gentle shake of the box or, in the case of the *Plecotus auritus*, both ends of the restraint box were opened and it was pushed out of the box. There was no visible damage to the boxes after use although one of the bats did defecate into the box (Figure 6.1b). The trained handlers were confident the bats were not under any excessive stress during handling or placement in the restraint boxes. They advised a darker colour card may be more appropriate for use due to the reflection on the card from head torches at night. This reflection could deter the bats from entering the box whereas a darker, less reflective, card may entice the bats into the darker space.

Mice placed into the medium restraint box were more problematic overall. It was noted that, similar to the bats, care needs to be taken to ensure the tail and limbs are fully inside the restraint box (Figure 7.15a). The mice were overall more active than the bats. This increased activity meant it was difficult to close the restraint box without deforming (crushing) the box. The mice also caused damage to the restraint box (Figure 7.15b and c) and could easily escape from the restraint box if it was left unattended (i.e. not handled but watched) for more prolonged periods (Figure 7.15d). The handlers also noted that assembly of the box was sometimes problematic and would benefit from stapling or taping the two long ends of each box together before starting fieldwork (for more rapid in-field assembly).
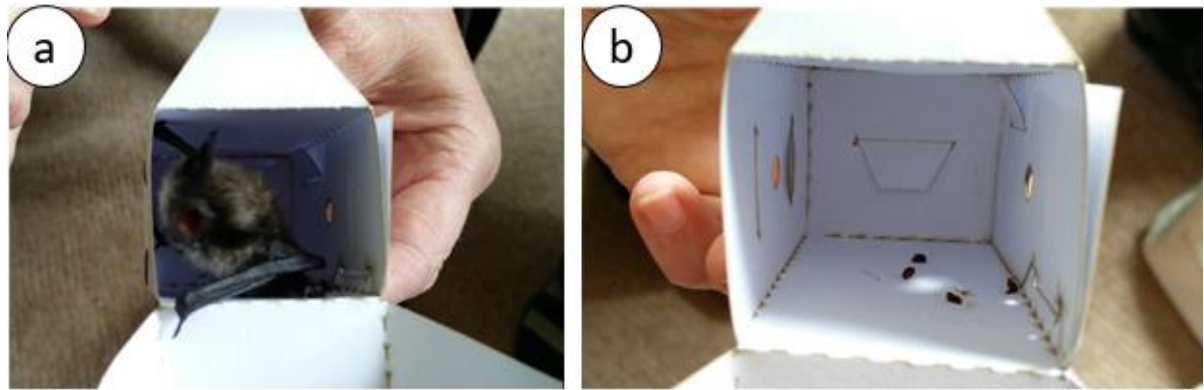
Figure 7.14: Bat placed in small restraint box. a) bat remains in restraint despite open end, b) faeces left in box after bat held for 120 seconds.
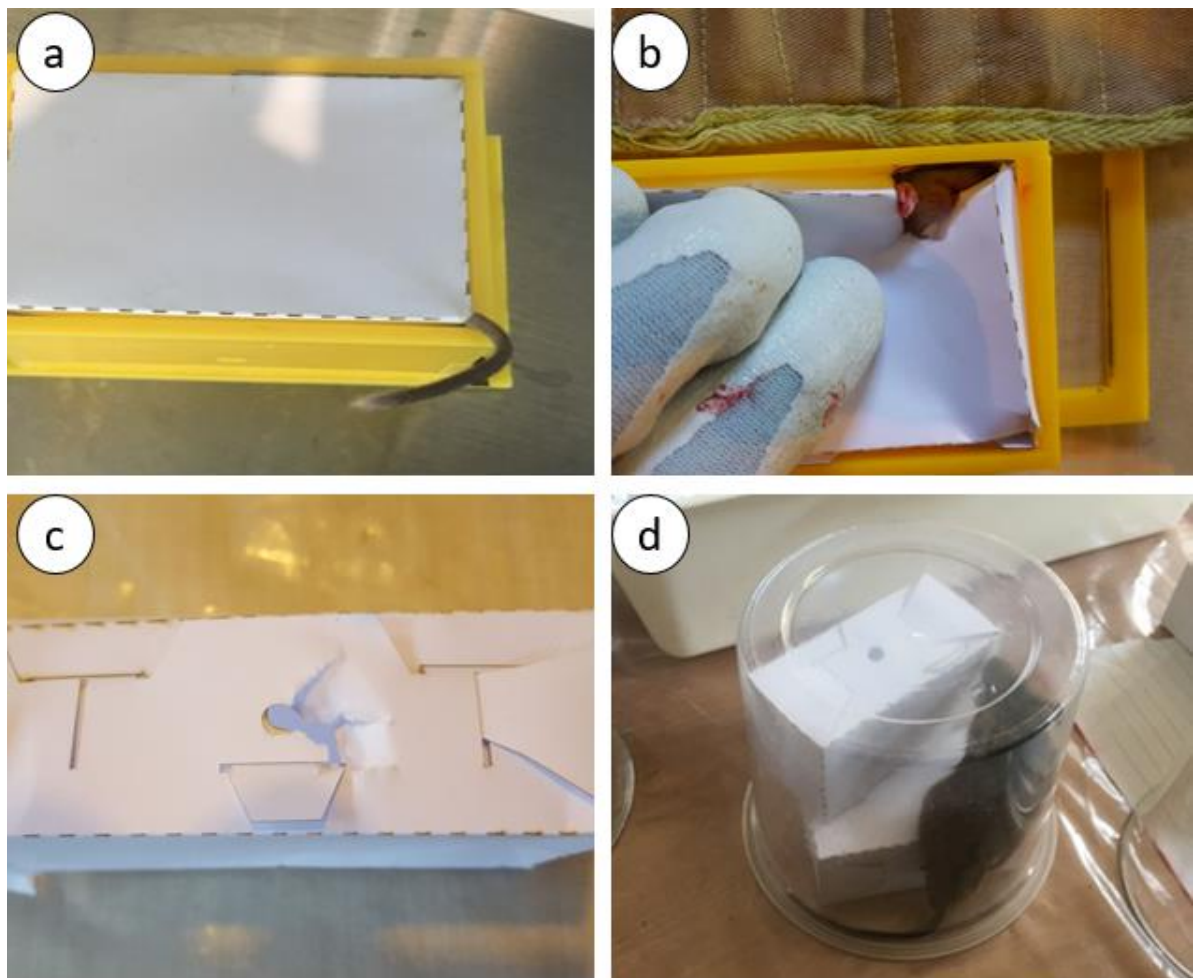
Figure 7.15: Mouse placed in medium restraint box. a) tail extruding from corner of restraint box, b) mouse clawing through upper surface of restraint box, c) damage caused to restraint box, and d) mouse having escaped from restraint box left unattended.

7.3.2 Laboratory testing

7.3.2.1 Response to phantoms

The response rates (counts s^{-1} Bq^{-1}) of the scintillators to the ^{137}Cs and ^{90}Sr phantoms are shown in Figure 7.16 and Figure 7.17 respectively. The following was determined from these response rates. The gamma scintillators (CH1A and CH1B) have a response to the ^{90}Y from the ^{90}Sr phantom but is negligible compared to the ^{137}Cs response (as long as the beta activity is not much larger than the gamma activity). The two beta scintillators (CH2A and CH2B) have a response to the ^{137}Cs gamma. The gamma component from the net signal on the beta scintillators therefore needs to be removed to determine the ^{90}Sr count rate. A small change in the source position has an effect on the count rates from each gamma scintillator. Summing the counts for these two scintillators helps reduce this positional effect. The 0.1 mm plastic added to the upper beta scintillator (CH2A) appears to have little effect on detection of ^{90}Y from the ^{90}Sr source. All measurements in the subsequent sections therefore have this layer of plastic present on CH2A. The change in aluminium thickness on the lower beta scintillator (CH2B) shows a clear attenuation affect to the ^{90}Sr source. Additional measurements (not shown) suggested the beta from ^{90}Sr was removed (and subsequently so will the ^{137}Cs beta) from the measurements when using an aluminium thickness of 0.2 mm on CH2B (as also shown in chapter 6.3.7.3). All measurements in the subsequent sections therefore use 0.2 mm aluminium on CH2B. Response rates on CH1A+B are therefore defined as 0.0346 ± 0.0015 and 0.0007 ± 0.0004 counts s^{-1} Bq^{-1} for ^{137}Cs and ^{90}Y respectively. Response rates on CH2A+B are defined as 0.0048 ± 0.0013 and 0.0250 ± 0.0007 counts s^{-1} Bq^{-1} for ^{137}Cs and ^{90}Y respectively. The quantity of ^{90}Sr (via ^{90}Y) beta radiation on CH2 is therefore found by multiplying the total CH1A+B count rate by 0.140 ± 0.012 and subtracting this from the total CH2A+B count rate.

The measured count rate for the ^{137}Cs + ^{90}Sr phantom is shown in Figure 7.18. Included on this figure is the expected ^{137}Cs + ^{90}Sr phantom count rates as was estimated from the individual ^{137}Cs and ^{90}Sr phantom response rates and reported activity concentrations. As shown, the estimation was different to what was measured. The measured values were 26%, 24%, and 29% greater than the estimated values for CH1A+B, CH2A, and CH2B respectively.
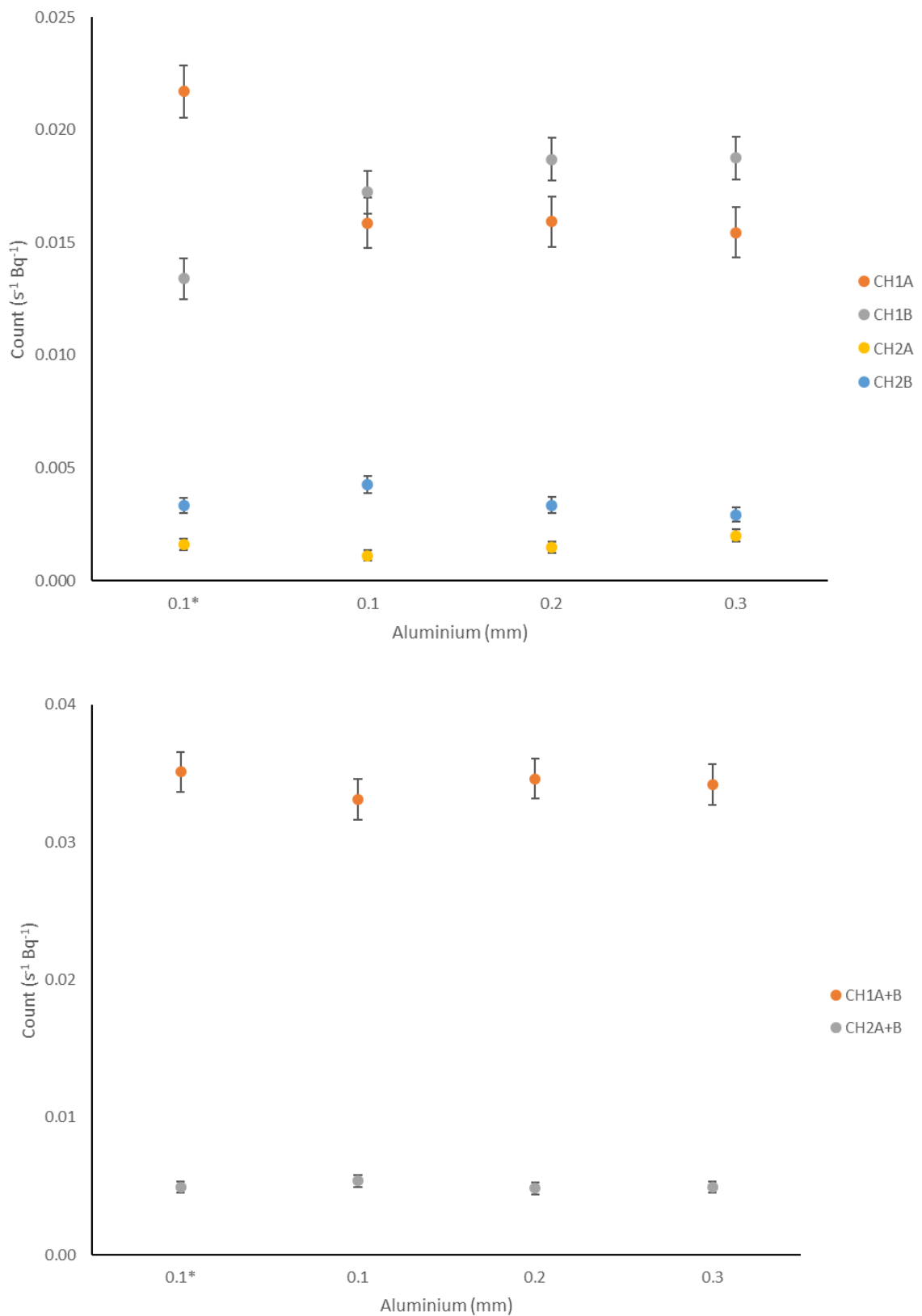
Figure 7.16: Response of scintillators to ^{137}Cs phantom. Individual channels are above, combined channels are below. Uncertainties shown are one standard deviation of the measurement (Currie, 1968). * - 0.1 mm plastic not included on CH2A scintillator.
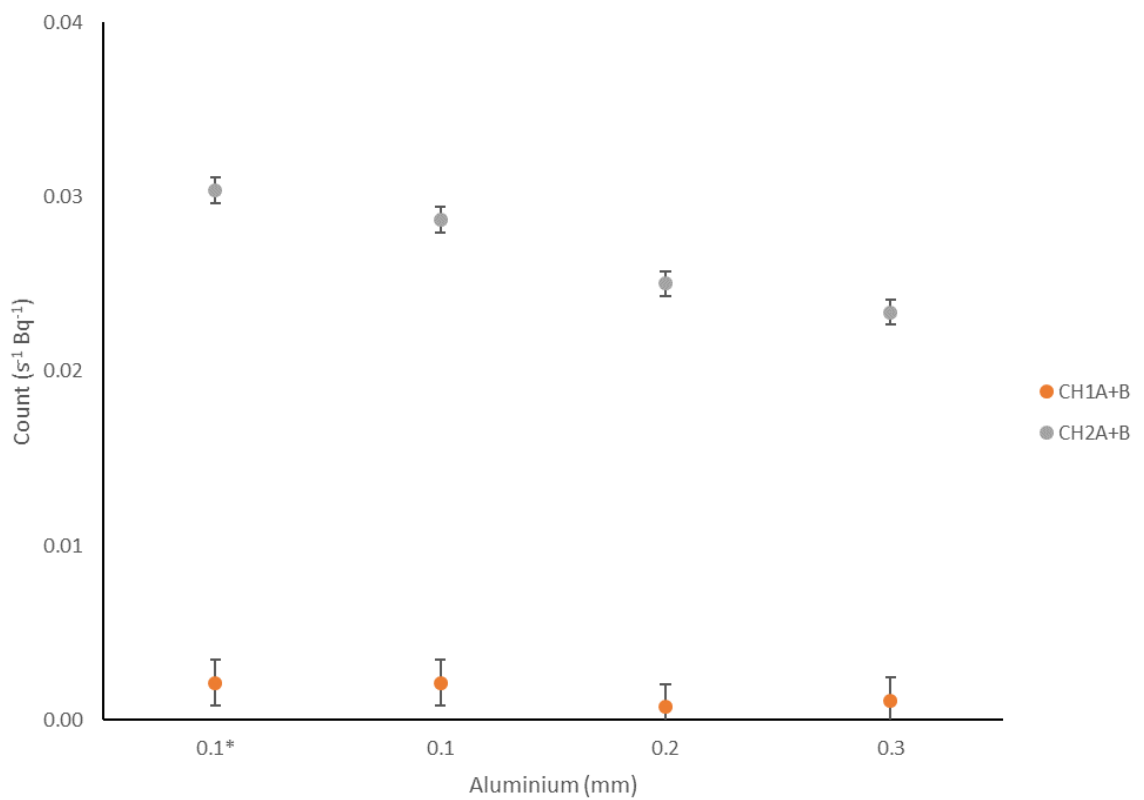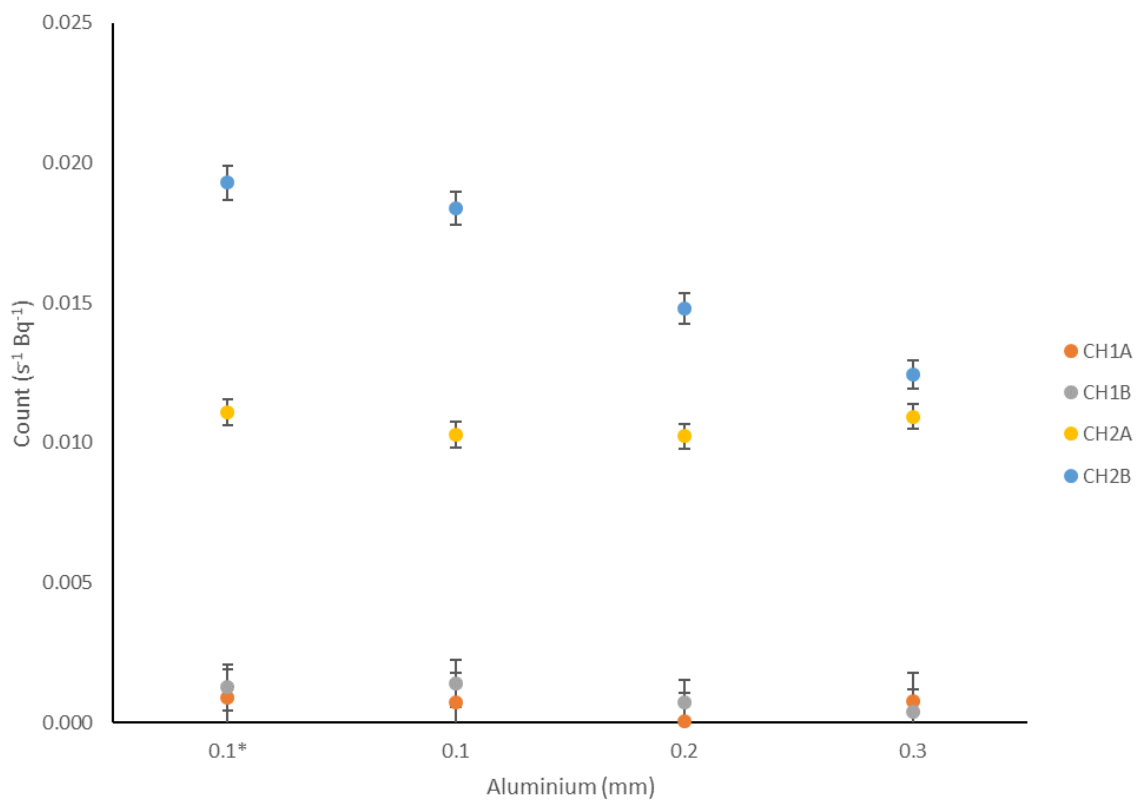
Figure 7.17: Response of scintillators to ^{90}Sr phantom. Individual channels are above, combined channels are below. Uncertainties shown are one standard deviation of the measurement. * - 0.1 mm plastic not included on CH2A scintillator.
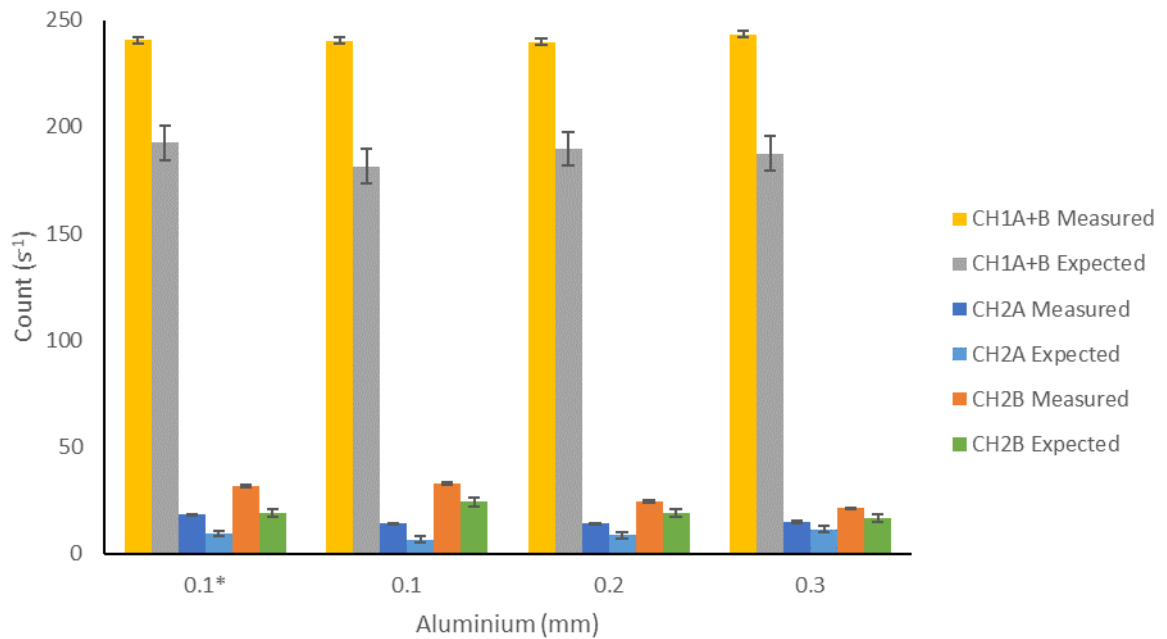
Figure 7.18: Count rate of ^{137}Cs +^{90}Sr phantom on each scintillator. Uncertainties shown are one standard deviation of the measurement. * - 0.1 mm plastic not included on CH2A scintillator.

7.3.2.2 Effect of source position on count rate

Results for source positioning are shown in Figure 7.19 for the two gamma scintillators (CH1A and CH1B), Figure 7.20 for the upper beta scintillator (CH2A), and Figure 7.21 for the lower beta scintillator (CH2B). Results were normalised (as a fraction of 1) to the middle of the cavity placement (C - Figure 7.3) for the gamma results and to the largest measurement for each of the beta scintillators. CH1 (Figure 7.19) shows a low count rate for a ^{137}Cs source placed outside of the shielding. For a ^{137}Cs source placed inside the cavity, there is a 370% increase in count rate when the source is placed to the right side of the cavity and against the gamma scintillator. Moving the source to the corners of the cavity resulted in a 65 to 80% increase in count rate. CH2A (Figure 7.20) shows up to a 20% decrease in counts as the source moves away from the PMT. Counts recorded on the left and right side of the detector were similar. CH2B (Figure 7.21) shows a similar decrease in count rate as for CH2A. There is negligible detection for a source placed off the edge of this scintillator.
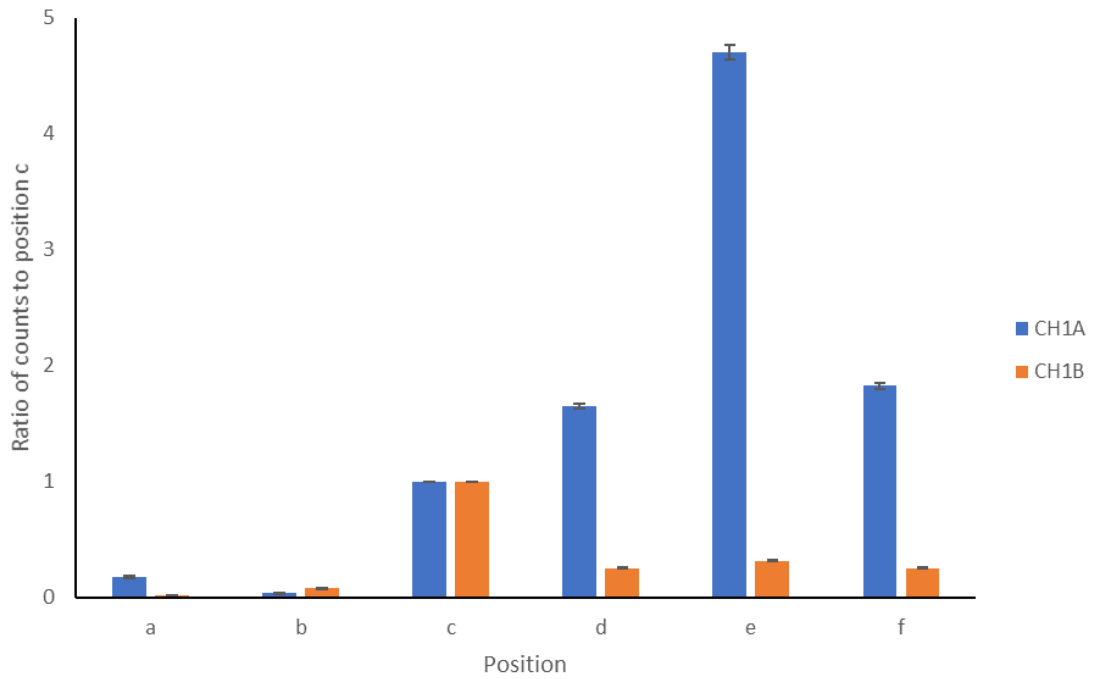
Figure 7.19: Positional change to detected counts for CH1A and CH1B. Uncertainties shown are one standard deviation of the respective measurement scaled to position c.
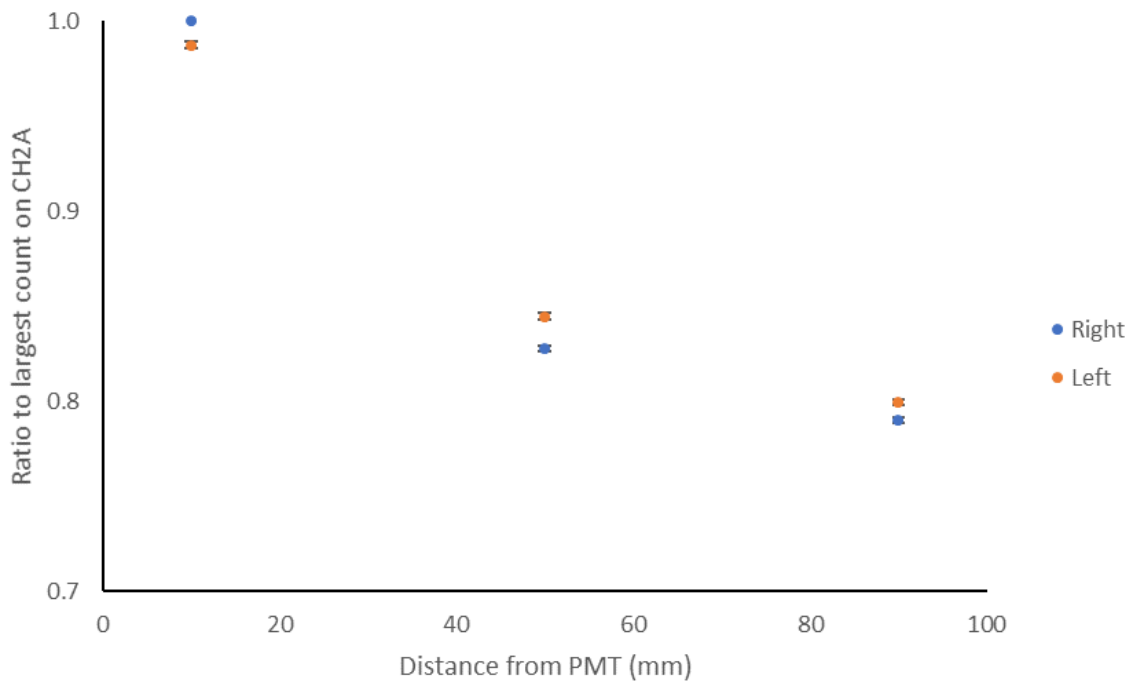
Figure 7.20: Positional change to detected counts for CH2A. Edges of detection surface are at 0 and 100 mm (0 mm is also the edge of the PMT). Uncertainties shown are one standard deviation of the respective measurement scaled to the highest count.
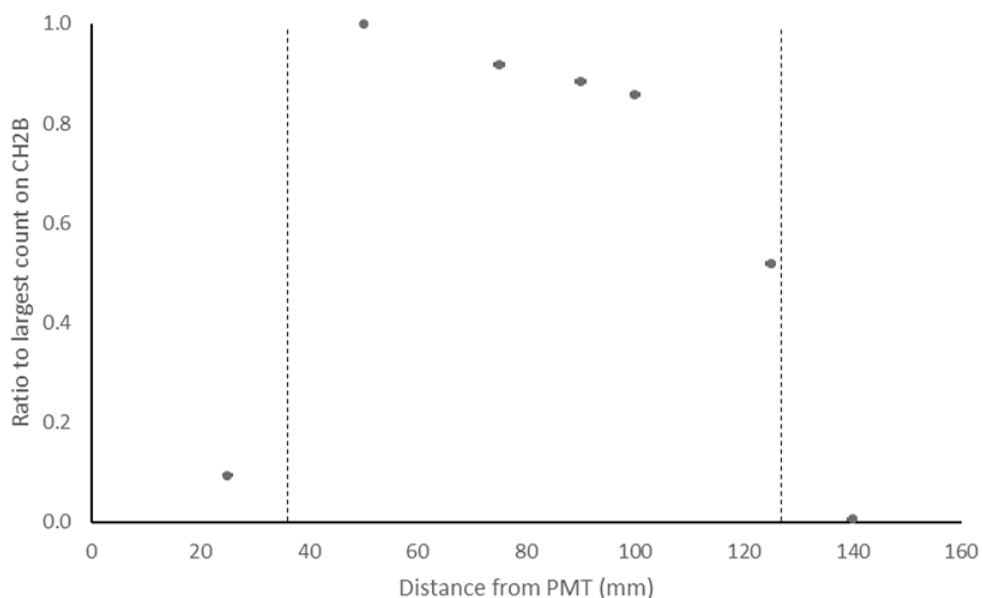
Figure 7.21: Positional change to detected counts for CH2B. PMT is at 0 mm. Dashed vertical lines indicate start and end of the active detection surface. Uncertainties shown are one standard deviation of the respective measurement scaled to the highest count.

7.3.2.3 Effect of animal placement on count rate

Repeated measures (3 times) of one rodent in the same position gave a percentage uncertainty (one SD) in the total count of 0.4, 0.2, 0.7 and 0.9% for CH1A, CH1B, CH2A, and CH2B respectively. Movement of the mouse in the medium restraint box showed a large deviation (compared to the measurement uncertainty above) in the count rate for CH1A and CH1B (Figure 7.22). Summing these two channels, however, meant there was a more consistent measurement with little deviation (SD =1% between the count rates for each position). This was similar for the bird (Figure 7.23) though there was a larger reduction in the combined count rate if the animal is placed in the extreme corners of the cavity (SD = 4%). Count rates on the two beta channels (CH2A and CH2B) for both the mouse and bird showed there was a poorer detection of counts when the animal is placed either to the corners of the beta scintillator or further away from the PMT. SD was 9% for the mouse restricted in the medium box and 25% for the bird in the extreme corners of the cavity.

Count rates for each rotational view (N = 3) are shown in Figure 7.24 and Figure 7.25 for the mouse and Figure 7.26 and Figure 7.27 for the bird. The individual gamma channels (CH1A and CH1B) for the mouse indicated the gamma detection was not consistent for different rotational orientations of the animal (SD = 21% and 19% respectively). This was a little more consistent for the bird (SD = 12% and 14% respectively). Summing of CH1A and CH1B, for both the mouse and bird, meant there was little deviation of count rate for all rotational

orientations of the animal (SD = 2% and 4% for bird and mouse respectively). The mouse showed the greatest count rate for when the legs were directed towards the respective beta scintillator. The bird showed the greatest count rate in CH2B when the animal was on its side and the wings were in full view of the of the two beta scintillators. This deviation was not as obvious in CH2A. Summing CH2A and CH2B for the mouse and mouse count rates balanced this deviation in a similar way (but not as well) to the two gamma scintillators (SD = 7% and 8% for mouse and bird respectively). Repositioning of the tail appeared to show (Figure 7.28) a small effect on count rate in the beta scintillators for one mouse but not for the other.
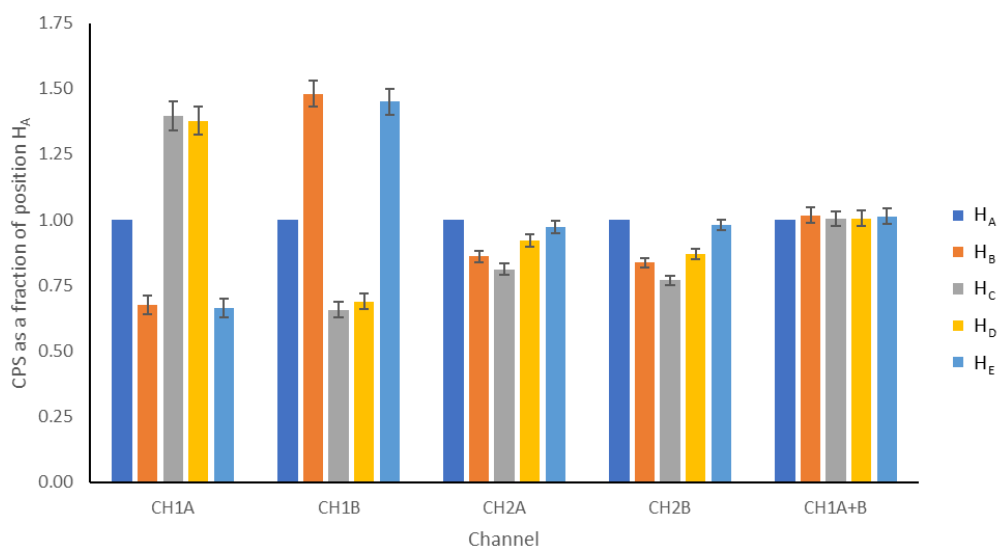
Figure 7.22: Effect on detected counts for horizontal mouse movement in detector cavity. H_A to H_E denotes horizontal position. Results scaled to a fraction of counts from position H_A. Uncertainties shown are one standard deviation of the respective measurement.
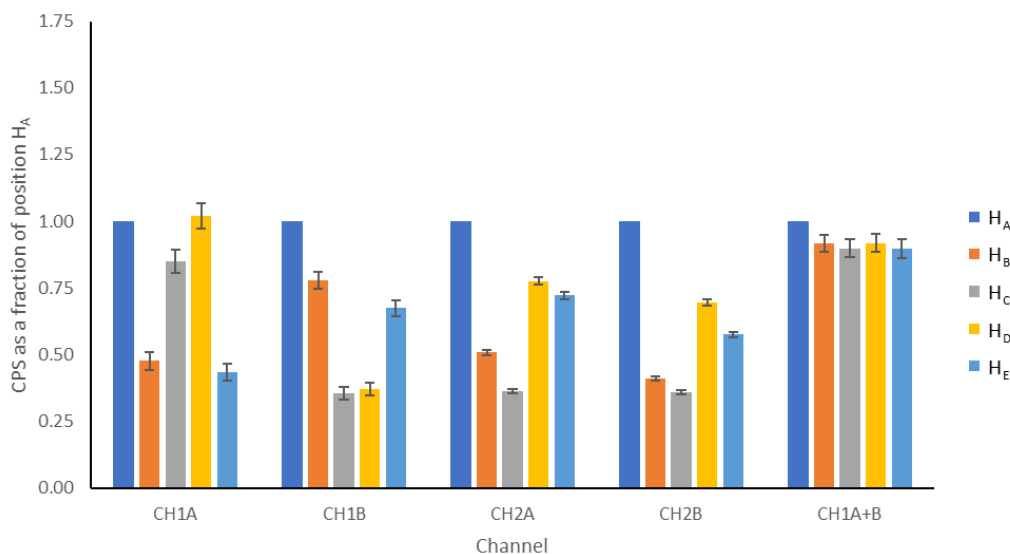
Figure 7.23: Effect on detected counts for horizontal bird movement in detector cavity. H_A to H_E denotes horizontal position. Results scaled to a fraction of counts from position H_A. Uncertainties shown are one standard deviation of the respective measurement

172
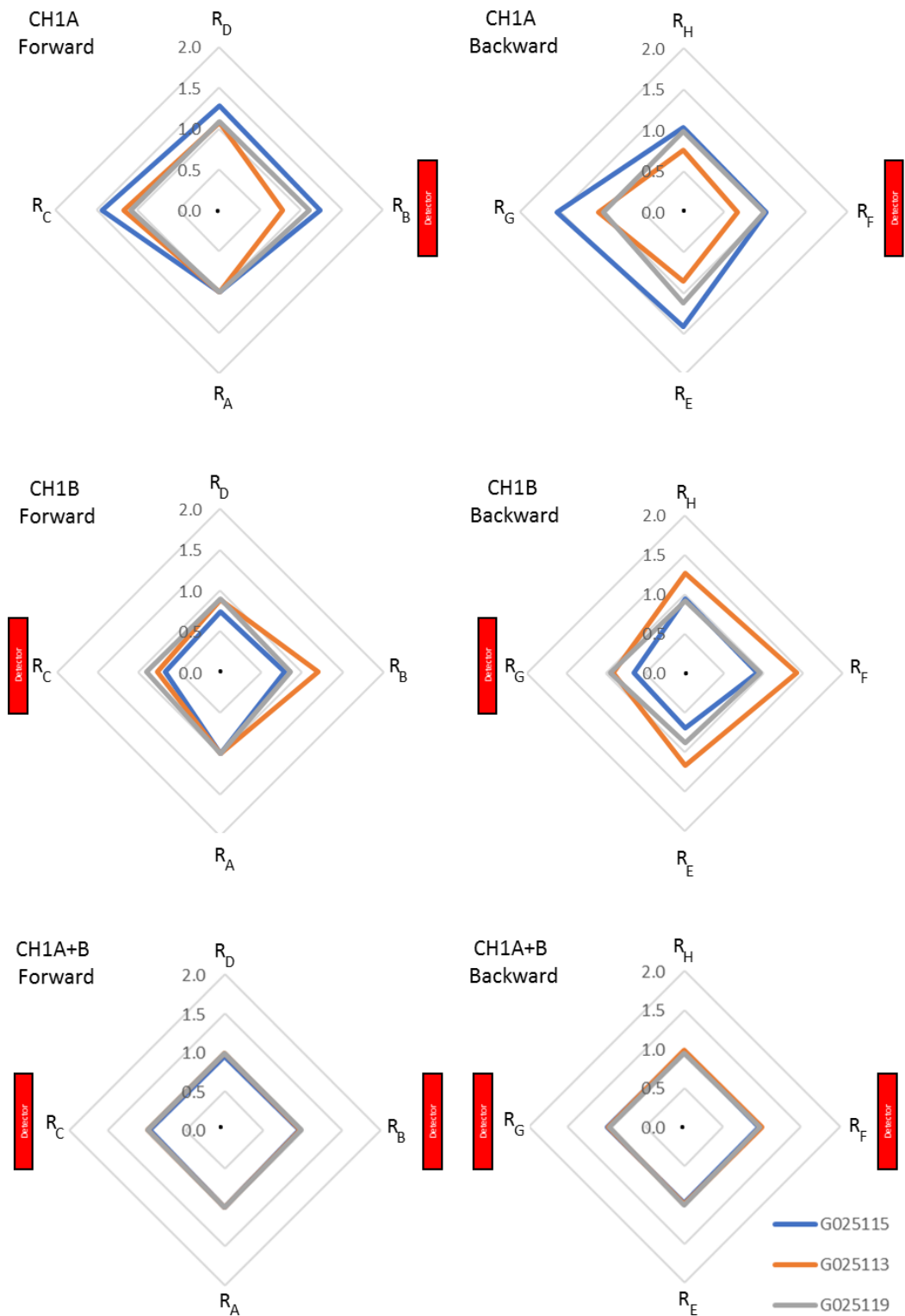
Figure 7.24: Effect on CH1 detected counts for rotational mouse movement in detector cavity. Scale shown is fraction of counts normalised to position R_A (with zero marking the centre of the radar and each ring indicates an increase of 0.5). R_A to R_G are the rotation of the animal. Results are organised such that the subscript letter is positioned in the direction the animal feet are facing e.g. position R_D has legs directed upwards towards CH2B.
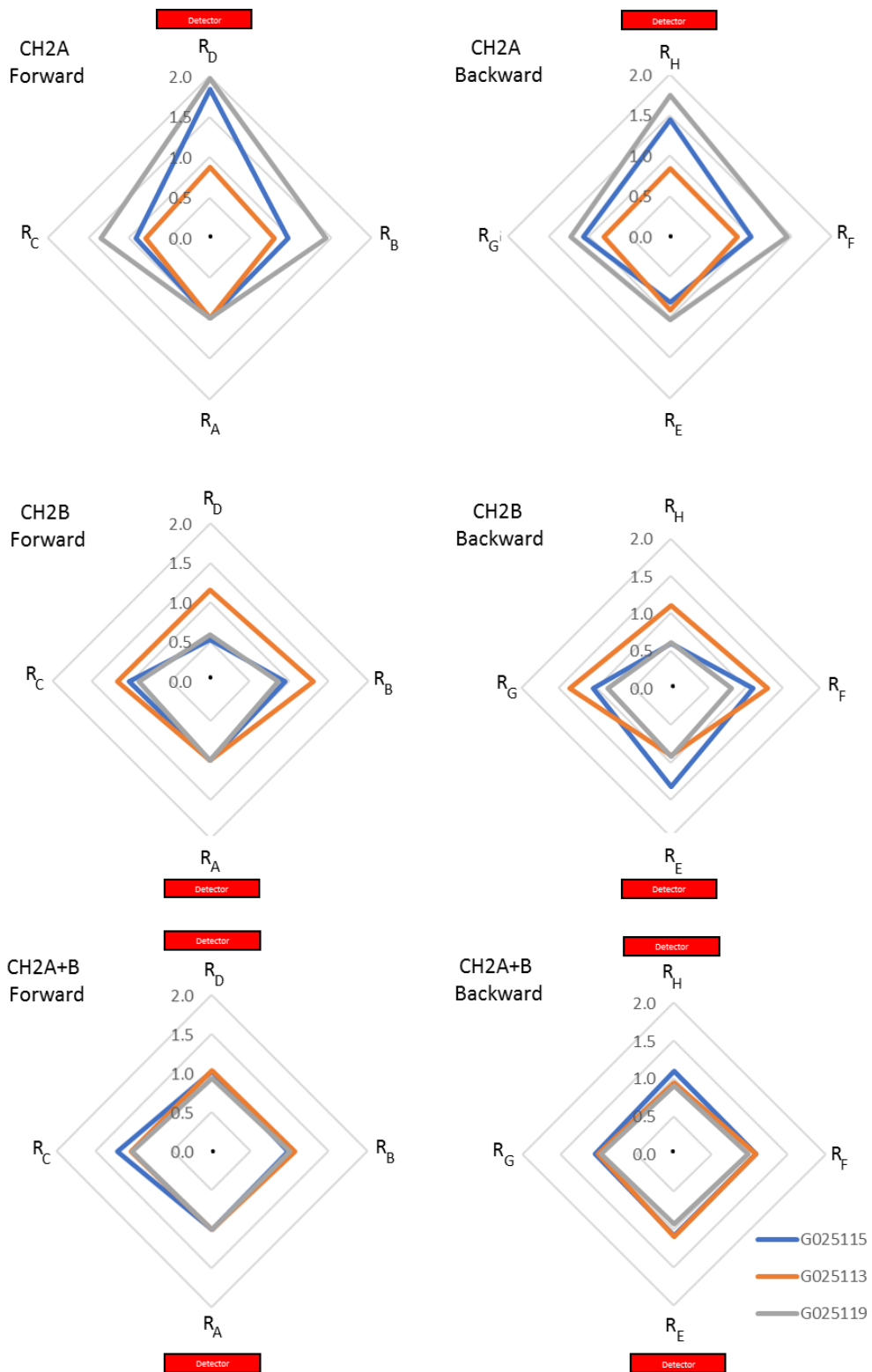
Figure 7.25: Effect on CH2 detected counts for rotational mouse movement in detector cavity. Scale shown is fraction of counts normalised to position R_A (with zero marking the centre of the radar and each ring indicates an increase of 0.5). R_A to R_G are the rotation of the animal. Results are organised such that the subscript letter is positioned in the direction the animal feet are facing e.g. position R_D has legs directed upwards towards CH2B.
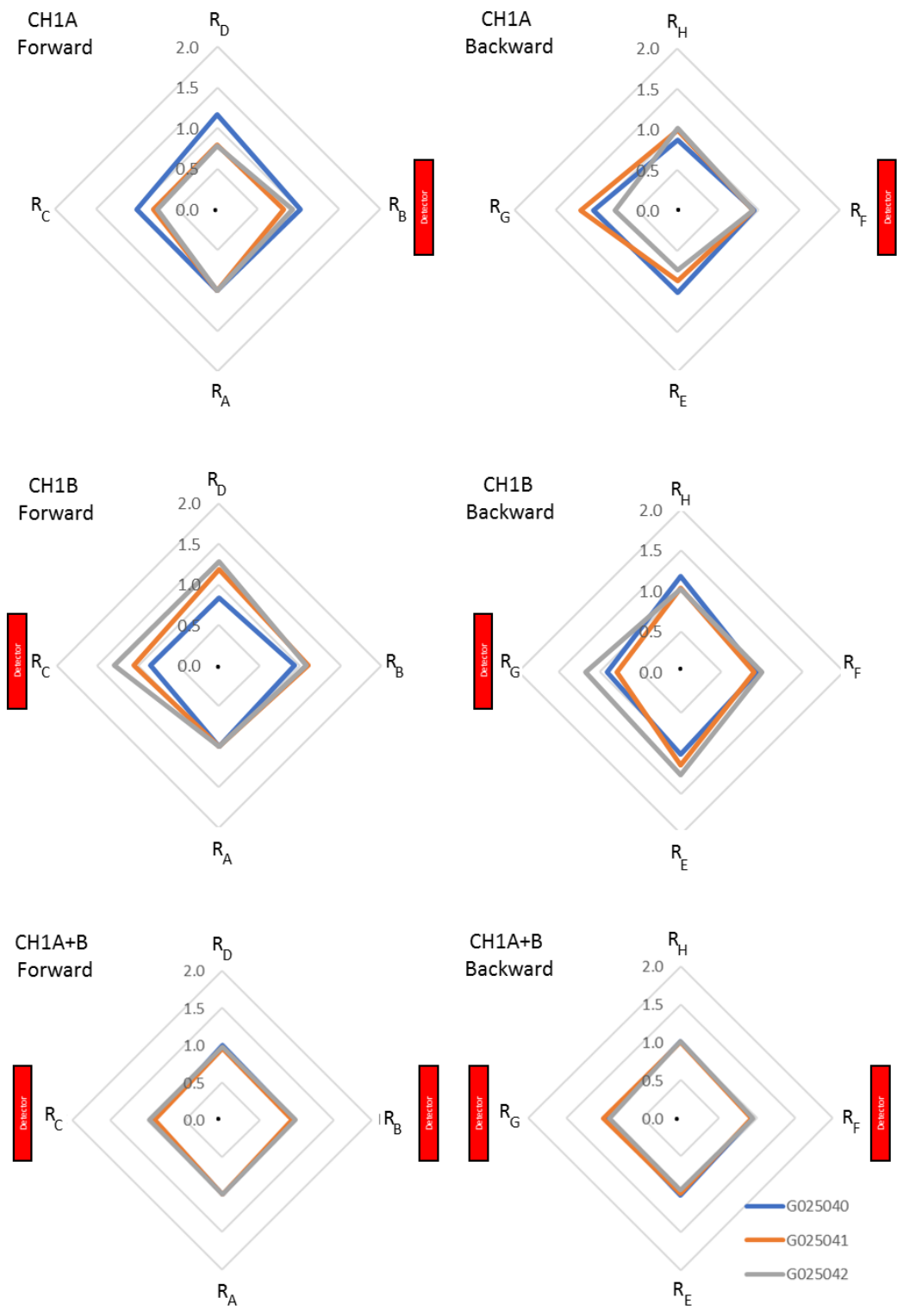
Figure 7.26: Effect on CH1 detected counts for rotational bird movement in detector cavity. Scale shown is fraction of counts normalised to position R_A (with zero marking the centre of the radar and each ring indicates an increase of 0.5). R_A to R_G are the rotation of the animal. Results are organised such that the subscript letter is positioned in the direction the animal feet are facing e.g. position R_D has legs directed upwards towards CH2B.
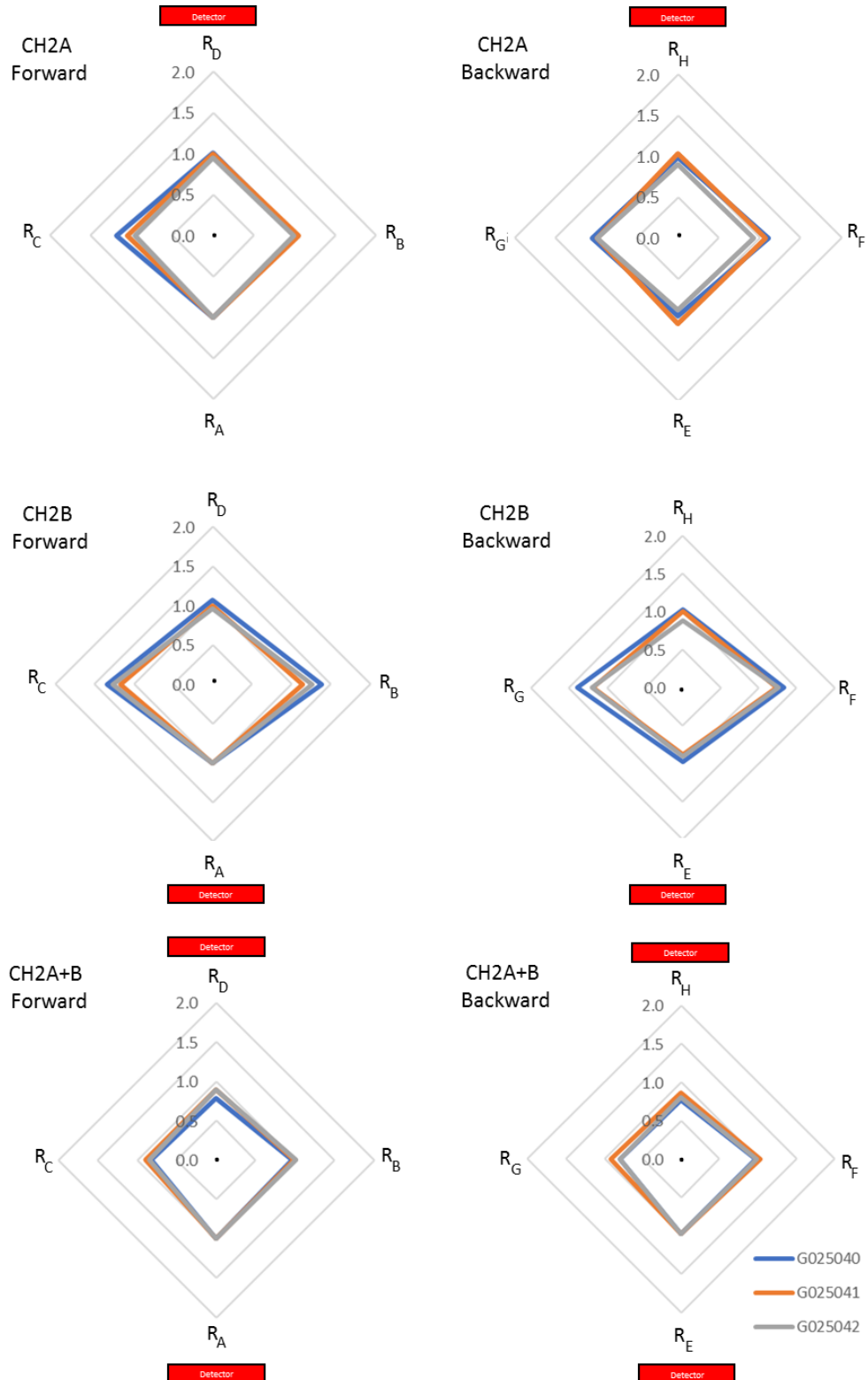
Figure 7.27: Effect on CH2 detected counts for rotational bird movement in detector cavity. Scale shown is fraction of counts normalised to position R_A (with zero marking the centre of the radar and each ring indicates an increase of 0.5). R_A to R_G are the rotation of the animal. Results are organised such that the subscript letter is positioned in the direction the animal feet are facing e.g. position R_D has legs directed upwards towards CH2B.

176

G025115

G025119
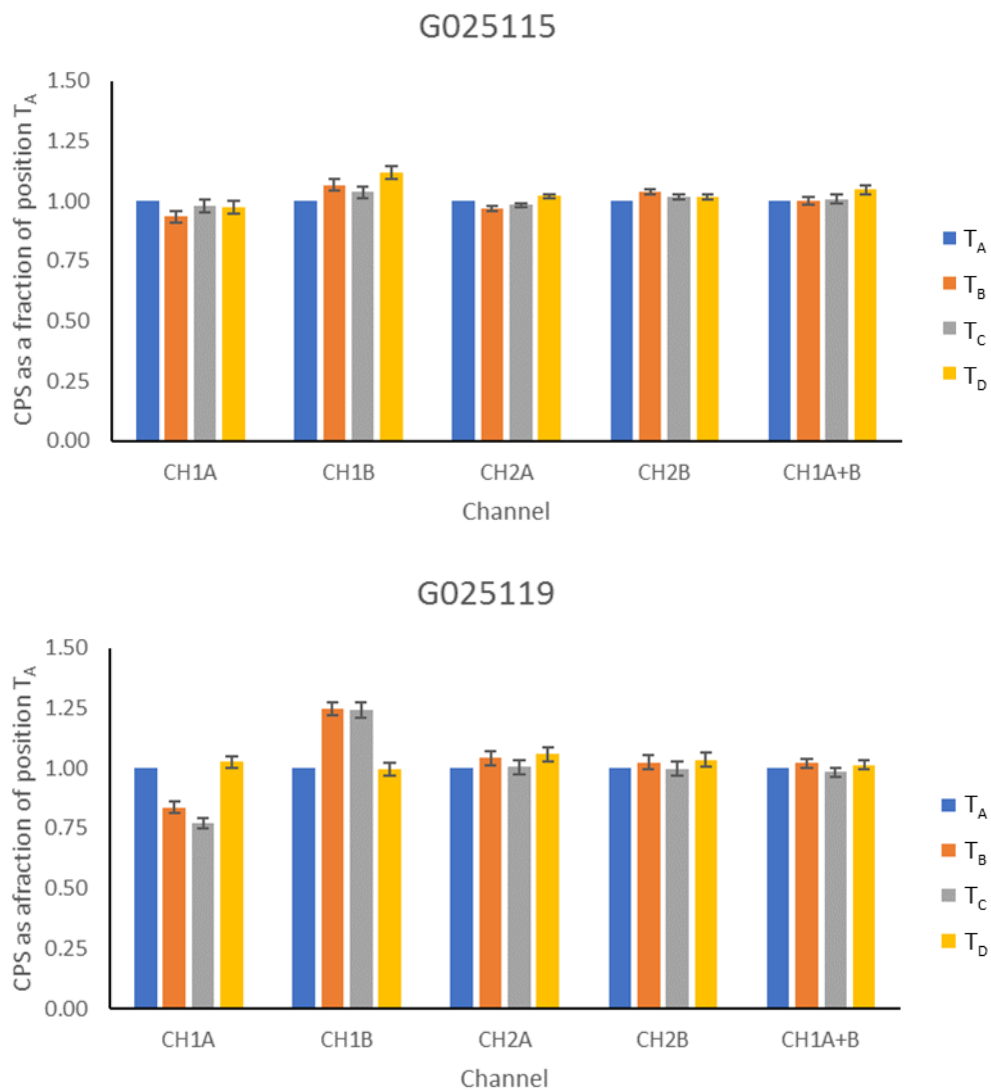
Figure 7.28: Effect on detected counts for mouse tail placement in detector cavity. T_A to T_D denote the tail position. Results scaled to a fraction of counts from position T_A. Uncertainties shown are one standard deviation of the respective measurement.

7.3.3   Field testing

Results for small rodents at each measurement site were found to be not normally distributed (Shapiro Wilk test P<0.05). Comparison of the net count rate for each small rodent between the four measurement sites (laboratory, car park, vehicle ramp, and roadside), using the Friedmans test on both the ^{137}Cs and ^{90}Sr results, showed there was a significant difference between the different sites (^{137}Cs: N = 10, χ^2 = 18.4, P < 0.05. ^{90}Sr: N = 10, χ^2 = 18.4, P < 0.05). Dunn-Bonferroni corrected pairwise comparisons (Table 7.2 for ^{137}Cs, Table 7.3 for ^{90}Sr) showed this difference was between the laboratory measurements and the field measurement sites (except laboratory and car park ^{137}Cs measurements).

Table 7.2: Friedmans pairwise comparison of sites for ^{137}Cs measurement.

Sample1-Sample2	Test Statistic	Std. Error	Std. Test Statistic	Sig.	Adj.Sig.
ramp-roadside	.000	.577	.000	1.000	1.000
ramp-carpark	1.100	.577	1.905	.057	.340
ramp-lab	2.100	.577	3.637	.000	.002
roadside-carpark	1.100	.577	1.905	.057	.340
roadside-lab	2.100	.577	3.637	.000	.002
carpark-lab	1.000	.577	1.732	.083	.500

Each row tests the null hypothesis that the sample 1 and sample 2 distributions for count rates are the same. Asymptotic significances (2-sided tests) are displayed. The significance level is .05. Significant values have been adjusted by the Bonferroni correction for multiple tests.

Table 7.3: Friedmans pairwise comparison of sites for ^{90}Sr measurement.

Sample1-Sample2	Test Statistic	Std. Error	Std. Test Statistic	Sig.	Adj.Sig.
lab-Carpark	-1.800	.577	-3.118	.002	.011
lab-Ramp	-1.900	.577	-3.291	.001	.006
lab-Roadside	-2.300	.577	-3.984	.000	.000
Carpark-Ramp	-.100	.577	-.173	.862	1.000
Carpark-Roadside	-.500	.577	-.866	.386	1.000
Ramp-Roadside	-.400	.577	-.693	.488	1.000

Each row tests the null hypothesis that the sample 1 and sample 2 distributions for the count rates are the same. Asymptotic significances (2-sided tests) are displayed. The significance level is .05. Significant values have been adjusted by the Bonferroni correction for multiple tests.

For comparison between measured count rate and known internal activity, the field measurements for the small rodents were averaged across the sites and plotted against the known internal activity. Laboratory measurements (as they were significantly different) were plotted separately (shown in Appendix 10.7). Bird results were similarly plotted. A correlation comparison (in SPSS) of the field results against the verified internal activities are shown in Figure 7.29 for ^{137}Cs in rodents (R = 0.982, P < 0.001), Figure 7.30 for ^{90}Sr in rodents (R = 0.975, P < 0.001), Figure 7.31 for ^{137}Cs in bird (R = 0.992, P < 0.001), and Figure 7.32 for ^{90}Sr in bird (R = 0.998, P < 0.001). The R^2 values shown on these figures are for a y = 0 intercept (this setting

was deemed acceptable as the true intercept did not differ greatly from zero and the calculated regressions for these non-zero intercepts were not significantly different from those shown for a zero intercept). Uncertainties displayed on each figure are expanded uncertainties (k = 2). Analysis of the laboratory measurements produced similar results. The rodent ^{90}Sr results shown in Figure 7.30 has a close grouping of results towards the lower end of the scale. The top most result was removed from the data set and the correlation test repeated to check it is not influencing the significance of the correlation. With this point removed, the correlation comparison produced R = 0.810, P < 0.001. The change in the gradient of the line was minimal from 0.072 to 0.076. A comparison of uncertainties between the portable detector and the alternative measurement method showed small rodent gamma uncertainties were 3 times lower whereas the beta uncertainties were much larger, and the bird gamma uncertainties were comparable to the alternative method whereas the beta uncertainties were approximately double.

The gradient of the lines in these graphs show (for the field results) the ratio of the portable detector to the known internal activity. The gradients are as follows: ^{137}Cs in rodent and bird is 0.027 and 0.028 respectively (0.029 and 0.030 for the laboratory results), ^{90}Sr in rodent and bird is 0.072 and 0.036 respectively (0.064 and 0.034 for the laboratory results).
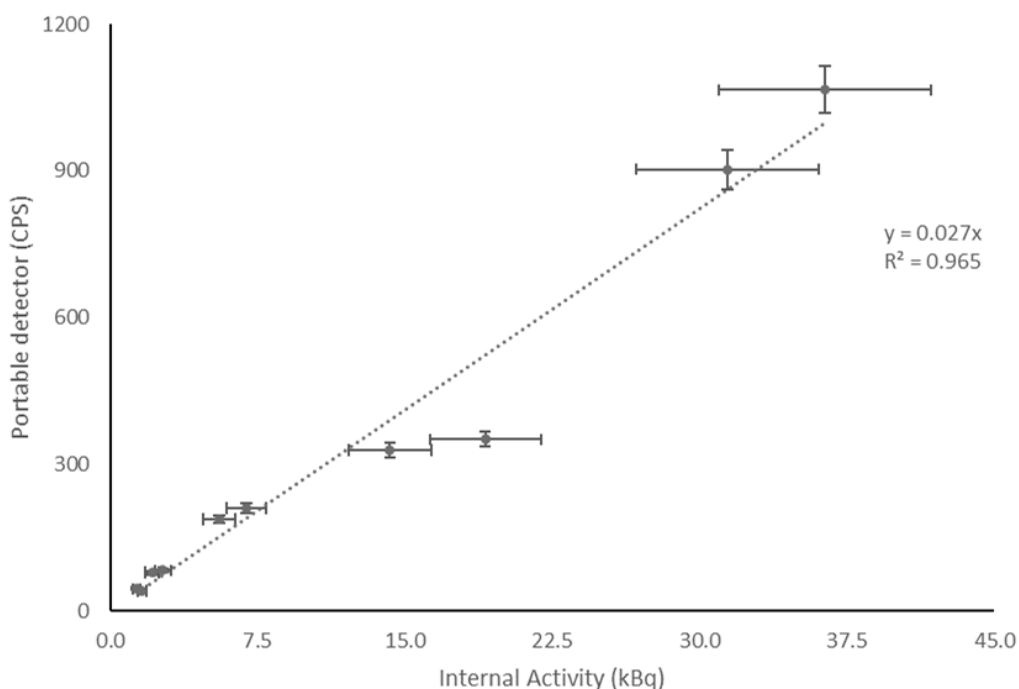
Figure 7.29: Mouse measured ^{137}Cs count rate (field site average) compared to internal activity. Uncertainties shown are the expanded uncertainties. For the portable detector this includes the uncertainty in the measurement (Currie, 1968) and the horizontal and rotational movement.
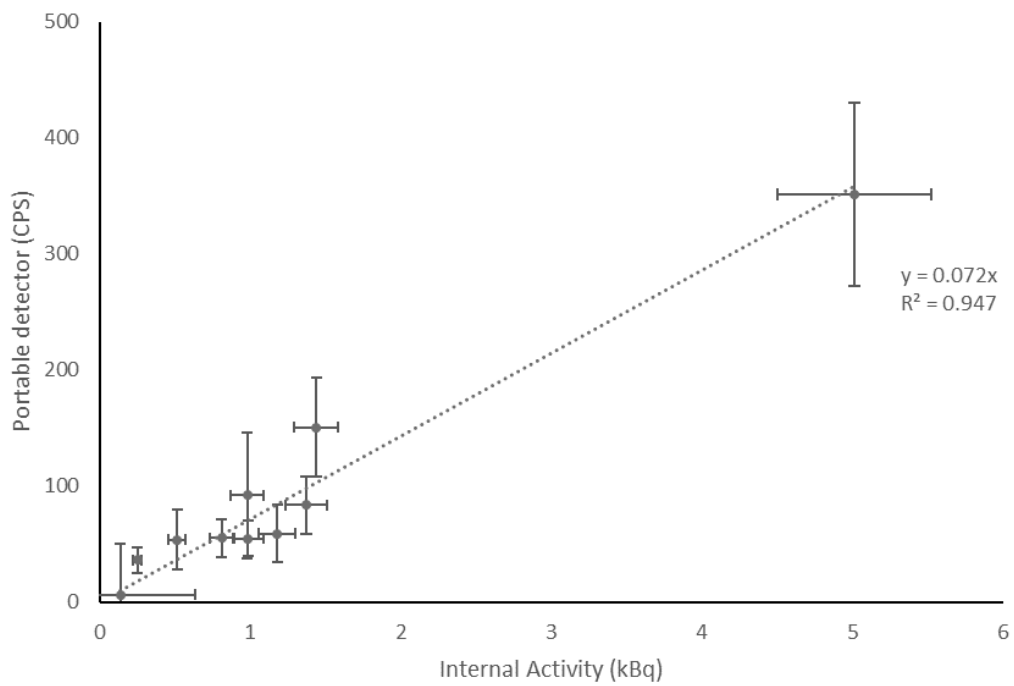
Figure 7.30: Mouse measured ^{90}Sr count rate (field site average) compared to internal activity. Uncertainties shown are the expanded uncertainties. For the portable detector this includes the uncertainty in the measurement (Currie, 1968), the horizontal and rotational movement, and the detector response rate.
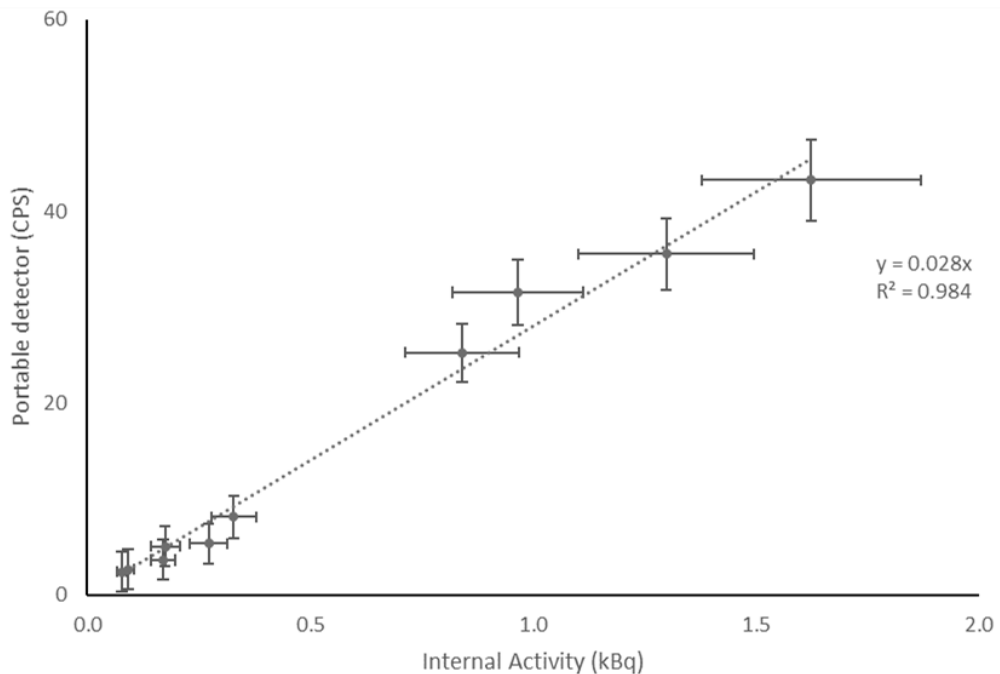
Figure 7.31: Bird measured ^{137}Cs count rate (field site) compared to internal activity. Uncertainties shown are the expanded uncertainties. For the portable detector this includes the uncertainty in the measurement (Currie, 1968) and the horizontal and rotational movement.
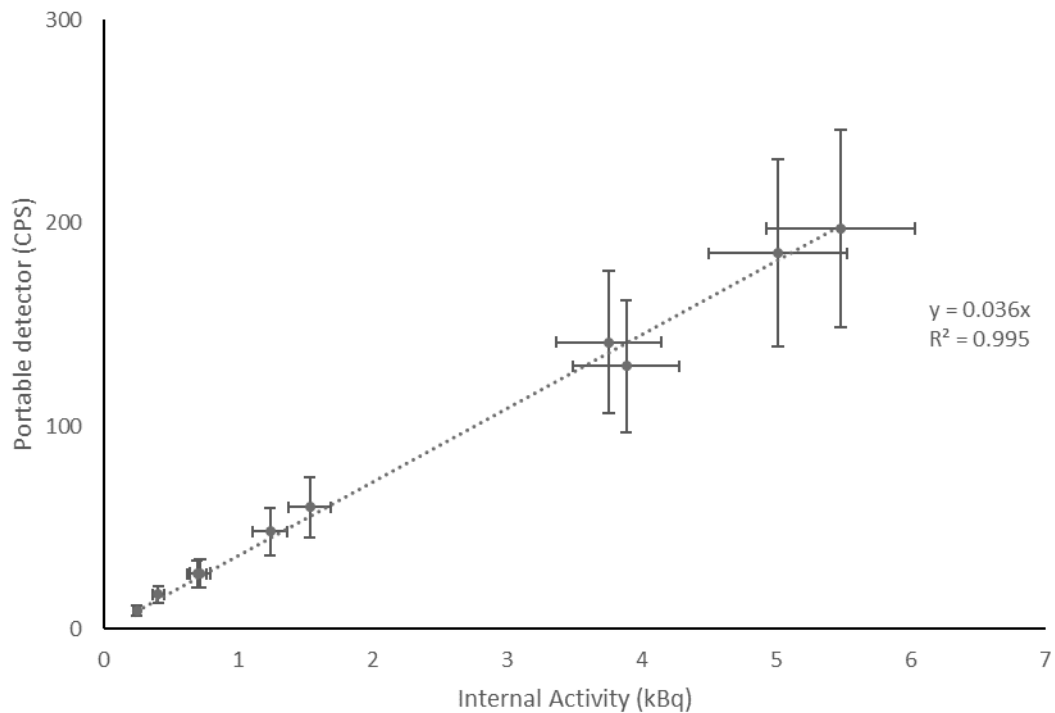
Figure 7.32: Bird measured ^{90}Sr count rate (field site) compared to internal activity. Uncertainties shown are the expanded uncertainties. For the portable detector this includes the uncertainty in the measurement (Currie, 1968), the horizontal and rotational movement, and the detector response rate .

These results were analysed further because of the discrepancy seen in the results for the measurement of the ^{137}Cs + ^{90}Sr phantom (Section 7.3.2.1). Figure 7.33 and Figure 7.34 show graphs for the measured counts per second from the small rodents at each individual site as compared to the expected counts per second (estimated from the phantom response rate). Whilst there is a strong grouping for measurements at each field site (as found in the statistical analysis for Table 7.2), there is a visible deviation of these count rates from the expected counts per second. This is not unexpected considering the discrepancy seen for the phantom measurements (Section 7.3.2.1). Graphs of this deviation from the expected counts per second is given Figure 7.35 to Figure 7.38 for the ^{137}Cs and ^{90}Sr measurements in small rodents and birds. Uncertainties displayed in these figures are derived from the uncertainty in the phantom response rates. These figures show that ^{137}Cs measurement was generally lower than expected whereas ^{90}Sr is larger than expected. For the ^{90}Sr measurement, this likely due to the way this value is derived from the gamma measurement recoded from CH1A and CH1B. There appears to be no strong correlation between the expected count rate and the deviation from this seen in the measured count rates for all figures, except for birds where the beta estimation was generally 1.5 times greater than expected.
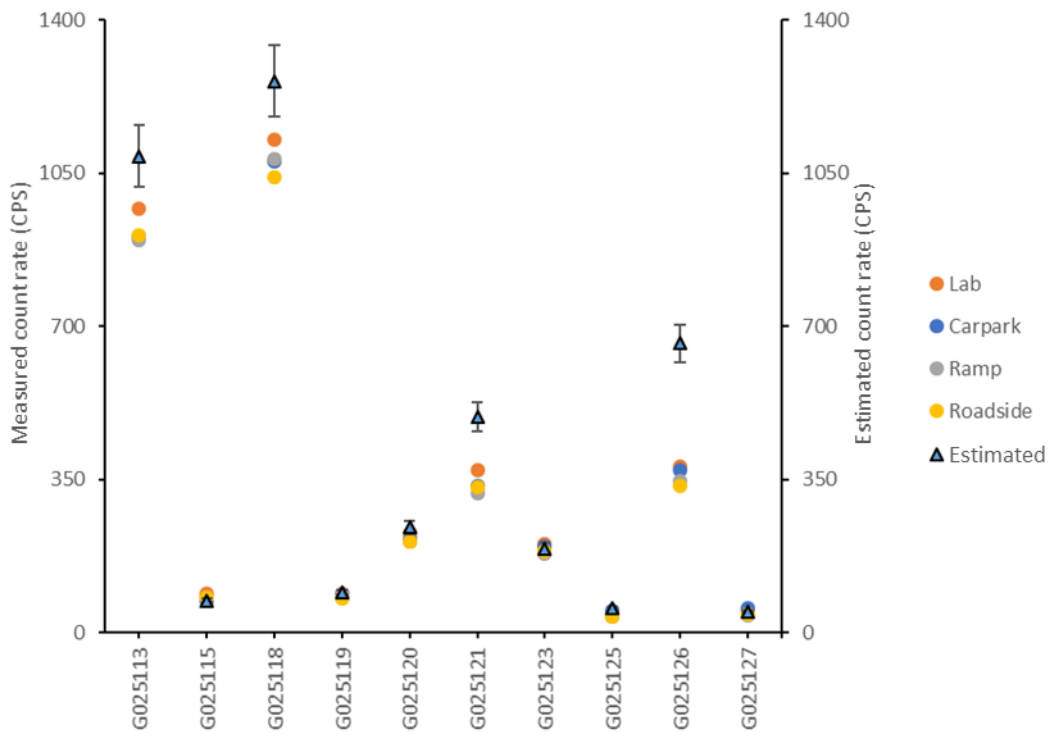
Figure 7.33: Mouse individual site measured ^{137}Cs count rate compared to estimated count rate (derived from phantom response rates and animal internal activity concentration). Uncertainties are only included for estimated count rate and represent the uncertainty in the measured scintillator response rates (one standard deviation).
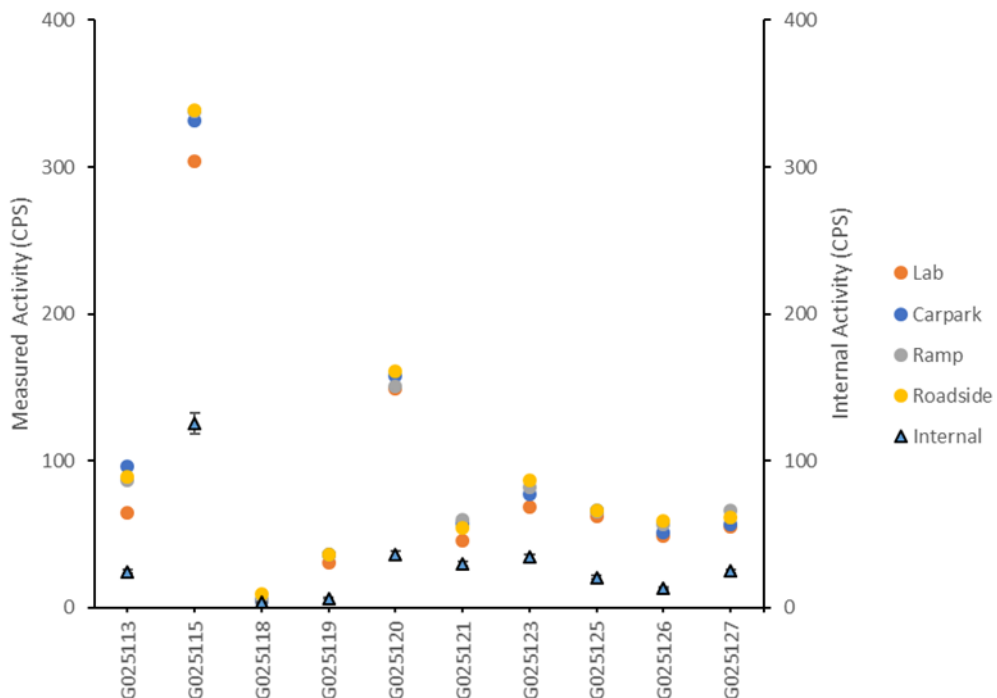
Figure 7.34: Mouse individual site measured ^{90}Sr count rate compared to estimated count rate (derived from phantom response rates and animal internal activity concentration). Uncertainties are only included for estimated count rate and represent the uncertainty in the measured scintillator response rates (one standard deviation)
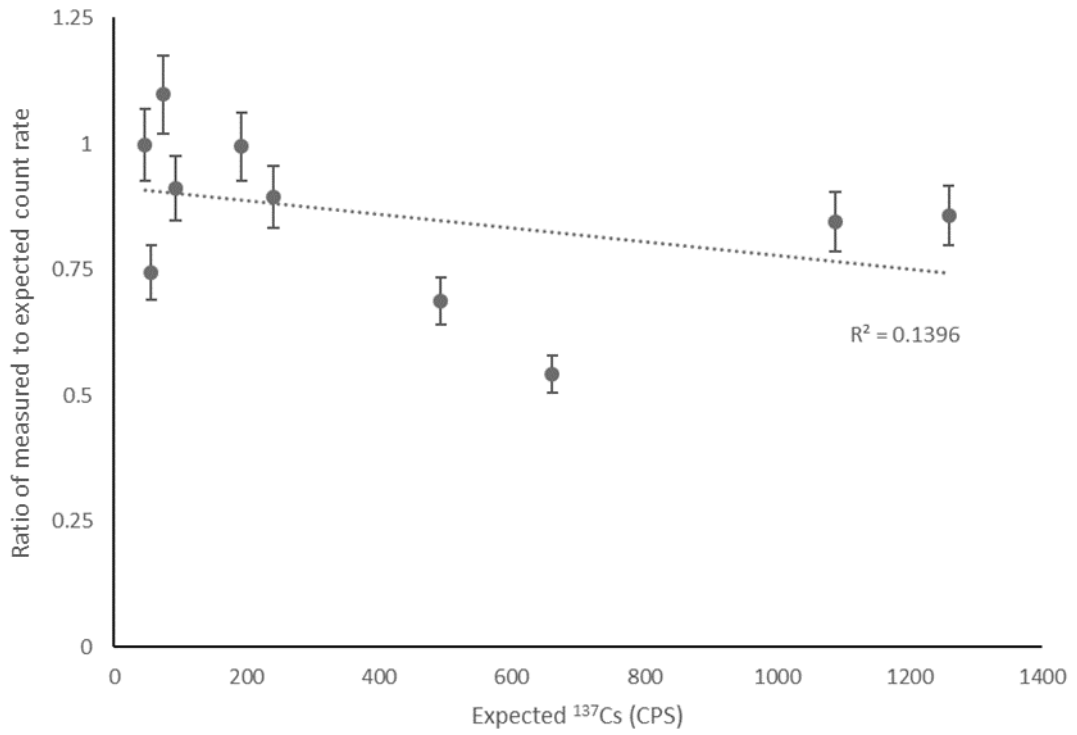
Figure 7.35: Mouse measured ^{137}Cs count rate deviation from expected count rate Uncertainties are derived from the standard deviation of each measurement.
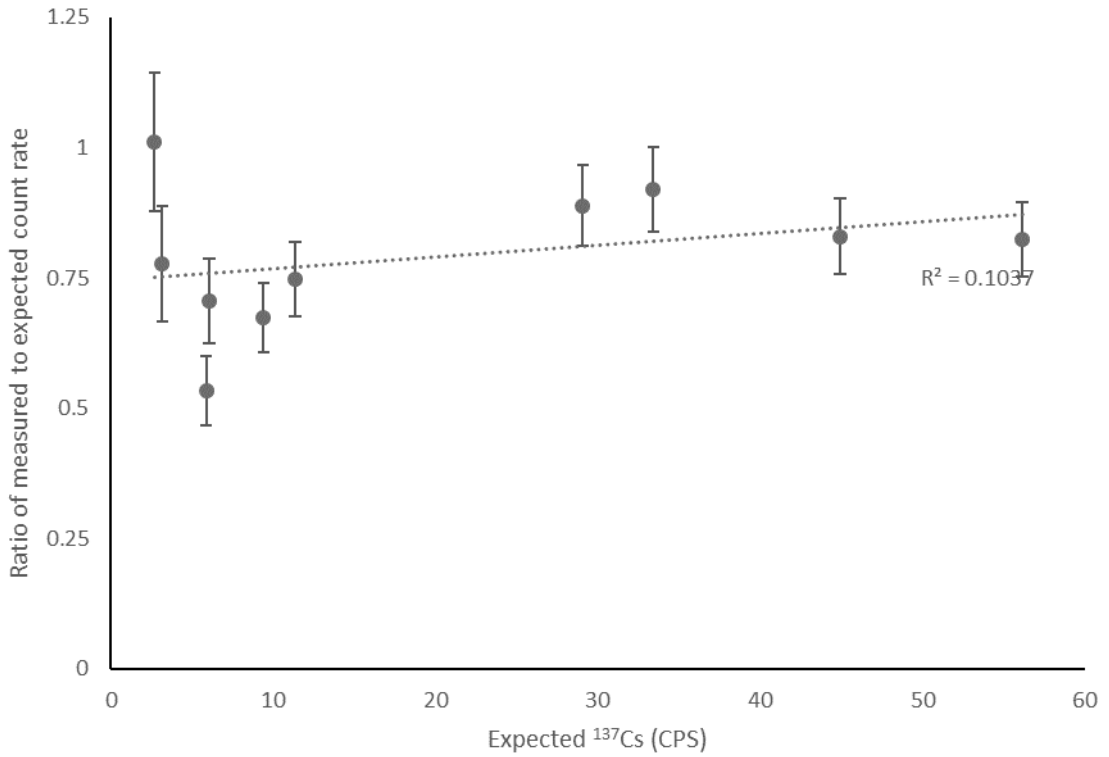
Figure 7.36: Bird measured ^{137}Cs count rate deviation from expected count rate. Uncertainties are derived from the standard deviation of each measurement.
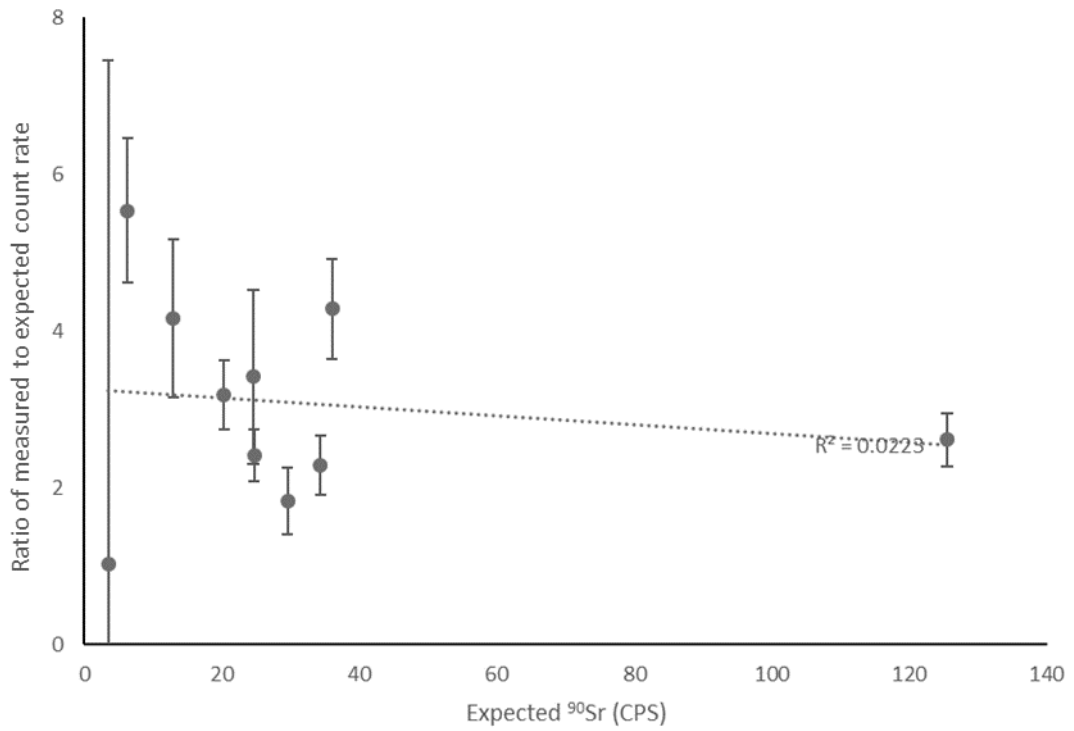
Figure 7.37: Mouse measured ^{90}Sr count rate deviation from expected count rate. Uncertainties are derived from the standard deviation of each measurement.
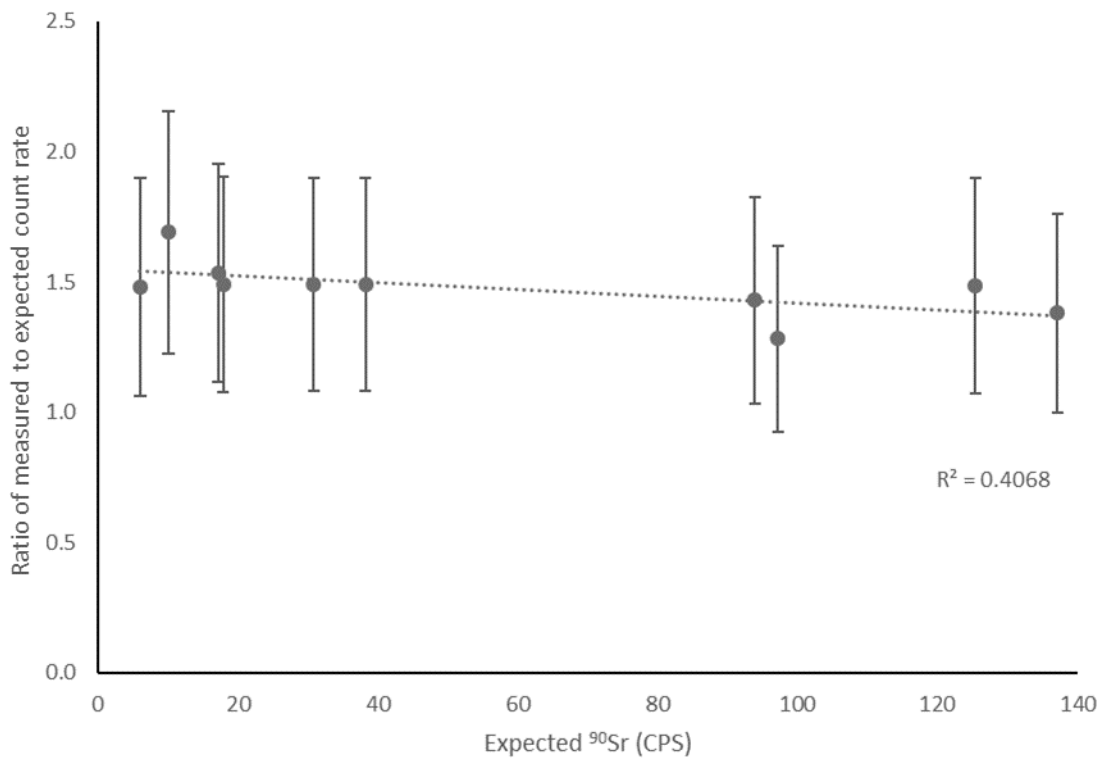
Figure 7.38: Bird measured ^{90}Sr count rate deviation from expected count rate. Uncertainties are derived from the standard deviation of each measurement.

7.4   Discussion

7.4.1   Animal restraint

The restraint boxes that were designed in chapter 6.3.1 worked well overall. During the insertion of the animals into the restraint box, however, it was often the case that part of the animal would protruded from the box. For bats, this was the placement of thumbs out of the two breathing holes and also feet out the end of the box where the flaps close. For mice, this was the tail (Figure 7.15). A smaller hole, or series of small holes, would prevent (or at least minimise) the animal from putting part of its body through the breathing hole. Preventing protrusion through the end of the box requires the flaps to be closed rapidly. This was tried with the mice but resulted in the box being deformed due to the non-rigid property of the walls. To solve this, two support structures (Figure 7.39) have been constructed to facilitate animal insertion into the restraint box.

The bats caused no visible damage to the boxes and settled quickly once enclosed inside the restraint box. The mice, on the other hand, did cause damage to the box by tearing at the card (Figure 7.15). This creates the concern that damage could occur to the scintillators. A short counting time, coupled with the protective coverings of the scintillators, means damage to the scintillators during normal operation should, however, be unlikely. Whilst the mice were observed escaping the box, this was only at times where the box containing the animal was not held securely (i.e. it was waiting to be placed into the plastic support) For normal operation, the animal would likely be placed into the box at the time it is ready to be inserted into the cavity and would be then surrounded on all sides by the walls of the detector.
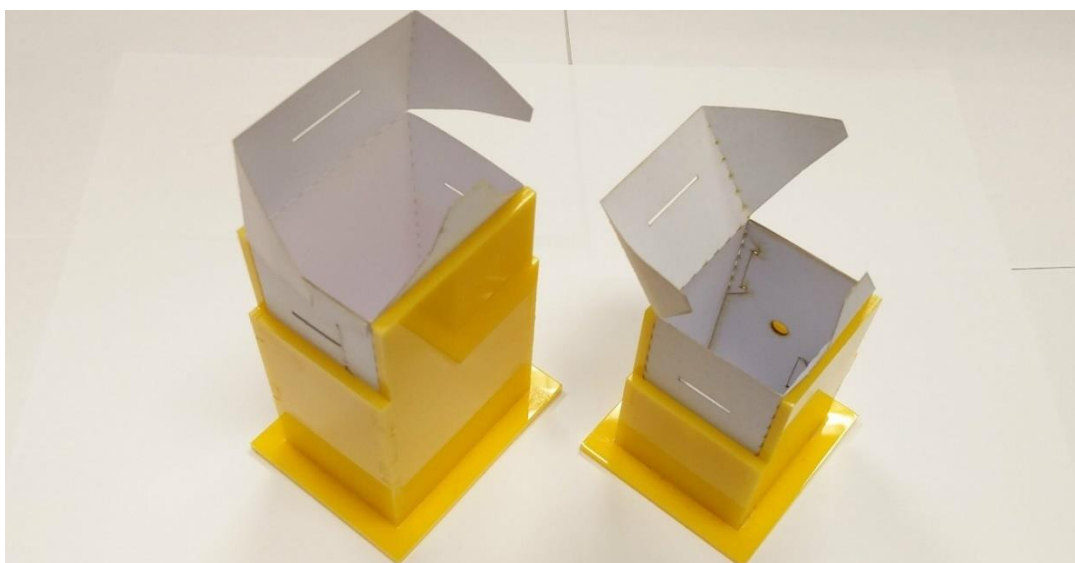
Figure 7.39: Supports for assisting animal insertion into restraint boxes.

7.4.2 Phantom response

A set of response rates were derived in section 7.3.2.1 from the ^{137}Cs and ^{90}Sr phantoms. These response rates, however, did not provide the correct estimated count rates for the measurement of the combined ^{137}Cs + ^{90}Sr phantom. The measurement of ^{137}Cs was up to 29% greater than what was estimated (conversely giving under predictions of a similar proportion for the counts on the beta scintillators). Multiple measurements were taken due to the investigation for count rate attenuation with different aluminium thicknesses on CH2B. All of these measurements show similar count rate discrepancies. This disagreement between results could be caused by the gamma scintillator as altering the known gamma activity in the ^{137}Cs + ^{90}Sr phantom (i.e. assuming the ^{137}Cs activity given for the phantom was wrong) realigns all separate scintillator channel estimates to the measured count rates, whereas altering the known beta activity does not. Testing with additional sources is therefore required to confirm the response rate estimations.

The response rates from each phantom showed that all four scintillators (the two gamma and two beta) are responsive to both beta and gamma radiation. Whilst this is unavoidable for the two beta scintillators, this was not desirable for the two gamma scintillators (the two gamma scintillators are used to estimate the gamma component on the two beta scintillators). This is not problematic (and can be effectively ignored) if the gamma radiation measurement is greater (e.g. 10 times) than beta radiation measurement because the response rate for beta radiation in the two gamma scintillators was low compared to the gamma response rate. If, instead, the beta radiation measurement is similar or greater than the gamma radiation measurement then the beta component of the measurement becomes more significant. It would therefore be desirable to remove this beta radiation measurement. 1.095 g cm^{-2} is the estimated maximum range of ^{90}Y (Equation 2.1). The total material between the source and the detection material, estimated from the material properties described in Figure 7.40, is between 0.423 g cm^{-2} to 0.466 g cm^{-2} (depending on the number of layers of tape surrounding the scintillator material) therefore 0.629 to 0.672 g cm^{-2} of additional material is required to eliminate measurement of ^{90}Y. This equates approximately to 5 to 6 mm of additional plastic.

7.4.3 Source positioning

The horizontal position of the animal in the detector cavity had a measurable effect on the count rate recorded by each scintillator (Section 7.3.2.3). The rotational position also had an effect on each scintillator (Section 7.3.2.3). The gamma count rate on CH1A and CH1B showed

up to 50% change when the animal was rotated. One of the three rodents rotated did not show much difference (nor the birds) but the other two rodents appeared to produce a larger count rate when the back of the animal was facing the respective scintillator. This is likely caused from the positioning of the animal as a similar difference is seen in the horizontal positioning of the rodents (Figure 7.22); the protrusion of the feet from the animal body (the rodents were frozen) can force the rodents centre of mass to one side of the restraint box. The beta count rate on CH2A and CH2B showed the count rate was largest when either the feet of the rodent (Figure 7.25) or wings of the bird (Figure 7.27) were directed towards the respective scintillator. This was expected based on the results of Chapter 5.4.2.

The effect the position of the tail had on count rate (for ^{90}Y detection in CH2A and CH2B) was inconclusive. It was estimated in chapter 5.3.2 that approximately 7% of the skeletal mass in a mouse was in the tail and there was up to 15% of the total emission detectable from this region. The small sample size (N=2) for this experiment is the reason the result is inconclusive. Further experimentation for this is likely unnecessary, however, because the results for source positioning in the cavity (above) showed movement of the animal has little effect on count rate when the two beta channels were summed (CH2A+B).

The variation in count rate on each scintillator means the results cannot be used separately. Summing the count rate on the respective channels (i.e. to give CH1A+B and CH2A+B) means a total count rate with a lower variance is given on each channel (e.g. Figure 7.24 and Figure 7.25). CH1A+B has a 1% SD for horizontal positioning and between 2 to 4% for rotational positioning. CH2A+B has a 9% SD for horizontal positioning and between 7 to 8% for rotational positioning. For measurement of ^{137}Cs gamma on CH1 this means movement of the animal in
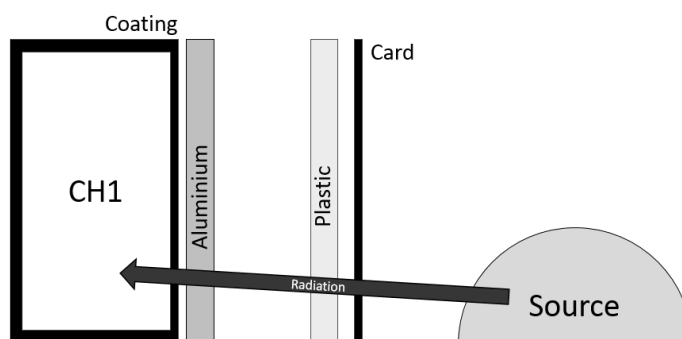
Figure 7.40: Attenuating materials between source and gamma scintillator. Material thickness: plastic = 3.00 mm, aluminium = 0.10 mm, scintillator coating = 0.18 to 0.54 mm (detailed on packaging). Material density: plastic = 1.19 g cm^{-3} (Hubbell and Seltzer, 1996), aluminium = 2.70 g cm^{-3} (Hubbell and Seltzer, 1996), scintillator coating = 1.22 g cm^{-3} (detailed on packaging). Card = 0.02 g cm^{-2} (160 gsm).

the restraint box has little effect on the measured count rate. This is provided the animal is positioned centrally in the cavity otherwise the solid angle of gamma scintillators makes detection less effective (as expected from the models in chapter 5). Whilst summing significantly reduces the effect of movement on ^{90}Sr beta measured count rate, as compared to the individual CH2 channels, it would still be desirable to restrict the available movement of the animal and therefore ensure the animal is placed in a similar size restraint box.

7.4.4   Field results

The net count rates measured for each animal were all found to have no significant difference (Friedmans pairwise comparison, P>0.34) between the field sites (Section7.3.3). The laboratory results were, however, significantly different from field measurements (Friedmans pairwise comparison, P<0.05), except for gamma (CH1A+B) measurements for rodents at the car park site (Friedmans pairwise comparison, P=0.5). The laboratory and car park sites were at the lowest and highest background activity sites respectively. The laboratory count rates were recorded on a different day to the field measurements and the only known differences between the laboratory and field sites was the temperature (approximately 22˚C difference) and that the laboratory site was indoors whereas the field sites were outdoors. It was also raining/snowing/sleeting during the measurement period and there was some snow cover on the ground (though not total cover). With a low number of measurement sites (N=4) it is unclear, from the data collected, as to the exact cause. Testing under different temperatures and increasing the number of sample sites in a second study is therefore required. A recommendation for this testing is to count the phantoms before and after (and, if possible, at regular intervals during) any set of animals that are monitored. This would allow for adjustment of the data if it has deviated from the initial calibration.

There was a good correlation between the portable detector count rates and the known internal activities (determined using and alternative method; section 7.2.3) despite the uncertainty surrounding the count rate difference between sites and the discrepancy with the phantom measurements. The results for both birds and small rodents showed correlations with R^2>0.9. The small rodent results did show one definite outlier in the gamma comparison and the beta comparison for small rodents does not look as visually good as the bird results. As with the number of sample sites, these correlations are derived from a low sample size (N=10 for each animal type). Increasing the number of samples monitored would therefore assist in better defining the gradients calculated from the comparison graphs.

Using the results from this chapter, the internal activity (Bq) for an animal monitored in the newly developed portable detector can be estimated using Equation 7.2 for ^{137}Cs and Equation 7.3 for ^{90}Sr. S_1 and S_2 are the count rates (count s^{-1}) on CH1A+B and CH2A+B respectively, f is the gradient of the comparison graphs (Section 7.3.3) for the specified animal (a = bird or rodent) and radionuclide (r = ^{137}Cs or ^{90}Sr), R is the response rate (counts s^{-1} Bq^{-1}) of the combined beta scintillators to ^{137}Cs (determined in this chapter as 0.140±0.012 counts s^{-1} Bq^{-1}), and k is the correction factor for self-absorption of ^{90}Y due to mass.

$$^{137}Cs = f_{a,r}\, S_1 \qquad\qquad 7.2$$

$$^{90}Sr = f_{a,r}\left(\frac{S_2 - RS_1}{k}\right) \qquad\qquad 7.3$$

7.5 Conclusion

The results of this chapter showed the newly developed portable detector met nearly all expectations. The animal restraints worked as expected and held the test animals for a time that was adequate for live-monitoring. Some minor refinements such as pre-stapling part of the card restraint box before conducting fieldwork would assist in decreasing assembly time whilst in the field. The design of a dual scintillator system for both beta and gamma detection, along with their positioning within the shielding, means that positioning (and therefore movement) of the animal within the restraint box has little effect on the count rate. The condition for this is the animal must be of similar size to the restraint box. The detector was confirmed to respond to both of the target radionuclides; ^{137}Cs and ^{90}Sr (via ^{90}Y) though the gamma scintillator gave a higher reading from ^{90}Y than was wanted (including additional material between the source and gamma scintillator will correct this) and there was a discrepancy recorded in the expected count rate for phantoms with a different radioactivity. This discrepancy is likely due to the phantom activity being recorded incorrectly and requires further testing to confirm this is the case. Count rates measured from sample animals using the newly developed portable detector did, however, match well with verified internal activities. Measurements for ^{137}Cs and ^{90}Sr in birds displayed a very good correlation (R^2>0.98). Mice also showed a good overall correlation though would benefit from a greater sample number. These results, like the phantoms, showed a discrepancy between measured count rates and count rates estimated (using the derived response rates) from the verified internal activities of the samples. Further testing is, therefore, still required (after refinement of the detector design) and would benefit from using a larger sample size and more test locations.

8 Conclusions and recommendations

8.1 Introduction

Monitoring of radionuclide content in wildlife is conducted for two main reasons: i) to demonstrate that (often protected) species and/or habitats are not significantly impacted by regulated releases of radioactivity (Copplestone et al., 2003, Copplestone et al., 2005); and ii) for the purposes of research to, for instance, establish transfer parameters for radionuclides or investigate the effect of radiation on wildlife. The current methods for determining internal activity concentrations, however, often require the use of destructive sampling (IAEA, 1989). Because there is a drive in science to reduce the number of animals euthanised for the purposes of research (Home Office, 2013), there is need to develop non-lethal monitoring techniques, such as live-monitoring (Wood et al., 2011, Bondarkov et al., 2011).

The aim of this research project was to develop a new detector for measuring gamma and beta radionuclide activity concentrations within wildlife (primarily small animals) without the need to destroy the target organism. This new detector would contribute to the development of non-invasive monitoring techniques (discussed in chapter 3.3), for gamma and beta emitting radionuclides, by using new technology to provide a fully portable detection system. The previous chapters within this thesis have outlined the development decisions for a live-monitor that meets this aim and to detail the construction and testing of a fully working device. This chapter draws together the conclusions made throughout this thesis and discusses them in relation to the wider aims and objectives outlined in chapter 1.

8.2 Outcomes

8.2.1 Design and construction

A portable detector was built according to the specifications outlined in chapter 6. This met objective 4 "*Development and construction of a detection device for the live-monitoring of radionuclides present within the targeted organism(s)*". This detector is custom designed to live-monitor gamma and beta radionuclide concentrations in small animals. It comprises of an animal restraint, a detection system, and a lead shield. It uses a replaceable card restraint box and a series of plastic supports (depending on the size of restraint box used) that are designed to hold and position the targeted animal within the detector cavity. There are two caesium iodide (CsI) scintillators for the detection of ^{137}Cs, situated to either side of the animal, and two plastic scintillators for the detection of ^{90}Sr, situated above and below the animal. Four

PMTs, for collection of the scintillation light, are attached to these detection materials and a single channel analyser (SCA) is used for processing the signal. Surrounding the detection materials is a lead shield with access to the sample cavity provided via a removable lid on the upper surface.

8.2.2   Detection targets

Determination of the organisms and radionuclides of monitoring interest under a UK regulatory context, as part of objective 2 "*Critical assessment of UK relevant radionuclides and wildlife to identify which radionuclides are most radiologically significant and what wildlife are likely to be most impacted (from a radiological assessment viewpoint) by these radionuclides*", determined smaller organisms such as small mammals and birds to be suitable targets for live-monitoring. Smaller organisms were chosen because gamma detection in larger organisms (such as sheep) has already been accomplished (e.g. Howard et al., 1987) and the smaller organisms present a greater potential for internal beta detection. Whilst field testing was limited to small rodents and birds (bats were only tried in the restraint box and were not monitored), the detector has the potential to be used for other organisms or media provided they fit within the cavity. This means live-monitoring of other small organisms such as amphibians and reptiles is feasible, as are amassed plant and invertebrate samples and soil samples. This is of particular benefit because it means the detector (once calibrated to the target) would be capable of live-monitoring a wide range of protected species.

It was also determined, as part of this objective, that the only radionuclides of monitoring interest (under a UK regulatory context) that could be live-monitored were ^{137}Cs and ^{90}Sr; ^{137}Cs has long been a target for live-monitoring in livestock (e.g. Howard et al., 1987, Mayes et al., 1994, Beresford et al., 1998). Whilst the detector is calibrated for the detection of these two radionuclides (a single channel analyser (SCA) is used for processing) the detector can still be recalibrated for other radionuclides.

8.2.3   Detection materials

The detection materials were selected based on the review conducted to meet objective 1 "*Critical review of current radiation detection methods and technologies to identify suitable detection solutions for a portable radiation live-monitor*". Here, it was concluded CsI and plastic scintillators were more suited to the requirements for this detector, over other materials, due to their low relative cost, robustness for fieldwork, and characteristic properties (e.g. resolution) for detecting the required radionuclides. Reviewing currently

available detection systems revealed that, whilst the currently used gamma detectors and methods were appropriate for large organisms (e.g. livestock), there were no detectors fully suitable to the live-monitoring of smaller organisms such as small mammals, bats, or small birds. This unsuitability was caused by a limitation for simultaneous gamma and beta detection, an absence of an appropriate restraining system (though this could be incorporated), and poor potential for shielding (i.e. the dimensions of the available detection systems means surrounding it, along with any restraint, with an appropriate thickness of shielding would be unlikely). On this basis, it was decided to construct an entirely new system.

8.2.4   Detection system

The size and anatomy target organisms were determining factors in deciding the detection material size and orientation. Optimal scintillator material size and orientation were calculated in chapter 5 as part of objective 3 "*Development of computer based models of radiation interaction, between radionuclides within the targeted organisms and an externally placed detector, to determine optimal radiation detector configuration(s) specific to the target organism(s)*".

The size of the CsI scintillator was determined to be optimal when the detection material volume was slightly smaller than the target organism. Optimal size was calculated in chapter 5 as the point at which the net count rate (from the organism) was maximised compared to the background. Because there was a range of organisms targeted for live-monitoring, it was decided to compromise between optimal size and overall weight and use a CsI scintillator size of 70 x 40 x 25 mm. For the plastic scintillator, the low penetration of the beta emissions meant the scintillator needed to be in close proximity to as much of the organism surface as possible. The size of this scintillator was set to 100 x 50 x 0.5 mm (based on the size of the medium animal restraint box).

The orientation of the scintillators around the target organism was decided by the optimal beta collection in the plastic scintillator. The models constructed in chapter 5 concluded this was for anatomical features, such as legs on a rodent or wings on a bird (i.e. a large bone volume with thin soft tissue covering), to be directed towards the beta scintillator. These conclusions were verified during testing in chapter 7 where animals were rotated in the cavity. One plastic scintillator (beta) was therefore positioned under the organism with another placed above These were positioned primarily for optimal detection from a small rodent. Position of a bird was assumed to have little effect if the two beta scintillator count rates were

summed. A CsI scintillator (gamma detector) was placed to either side of the target animal; positioned to not experience attenuation from the beta scintillator. Two of each scintillator material were used to minimise the effect of animal movement within the restraint box.

To keep the overall size of the detector low, silicon photomultipliers (SiPM) were initially considered for the light collection method. Availability and cost, however, meant small photomultiplier tubes (PMT) were instead opted for. These PMTs are smaller than those used in current live-monitors (Table 3.1) and therefore the overall size of the detection system can still be kept low. The scintillator sizes and their orientation around the cavity, however, created a unique problem for extracting the light signal. The size of the PMTs meant they would protrude from the detector shield (a larger shield was not possible as this would increase the weight passed what would be portable). It was desirable to direct the PMTs upwards, out the top of the shield, to remove any gaps where background gamma from the ground (Mitchell et al., 2009) could more readily penetrate the shielding. This was easily solved for the CsI scintillators because they were at either side of the cavity and had a top surface area comparable to the PMT surface (Chapter 6.3.2.1). The two plastic scintillators were more difficult due to their thinness and where they were to be positioned in the detector unit. PMT coupling for these two scintillators was solved by extending the plastic backing of each scintillator and angling the end such that the scintillation light was directed up into the PMT (Chapter 6.3.2.1). This solution does, however, mean there are four PMTs protruding out the top of the shield and as a result the entire detector unit needs to be disassembled for transportation (otherwise the PMTs could be damaged if the case is tipped). A future advancement of the detector may want to reconsider SiPMs instead of PMTs. Whilst the overall size of the detector would (likely) not change these would remove the disadvantage of requiring disassembly for transportation.

8.2.5   Restraints and support structures

The animal restraint was an important consideration throughout the design process. A good design of the restraint was important to reduce the stress of the animal (compared to bad design) (Russell et al., 1959). The restraint was designed to fully enclose the animal but to allow air for breathing to enter; holes were provided in the restraint system for air provision (see chapter 6.3.5).

The restraint boxes for the animal was also designed (Chapter 6.3.1) to be simple to produce, transport and assemble. Whilst a single permanent restraint would have been preferred, as

this would remove additional material costs, the replaceable card box allows for alternatives sizes to be rapidly produced (before fieldwork commences) and for the easy transportation of multiple restraint boxes because they can be flat-packed. A driving factor for making the restraint in this way was so it could be easily replaced if damaged by the animal or contaminated with animal waste. The restraint boxes were damaged by small rodents (Figure 7.15) during testing but not by bats. This damage may have been caused because of features inside the restraint where rodents could see a potential exit, i.e. the air hole or joints in the card box. The design was further found to be somewhat time consuming to assemble when in the field. A simpler design, that is partially assembled using staples or tape (but can still be flat packed) before fieldwork commences, was advised in the discussion for chapter 7. The restraint box was also easily deformed when inserting small rodents. Two supports were designed and constructed to assist with inserting animals into the restraints (Figure 7.39).

Both the animal restraint box and the detection materials were held in place using a series of plastic supports. Three laser cut plastic supports (for each restraint box size) were designed to hold the weight of the upper beta scintillator, reinforce the walls of the card restraint, and to position the restraint box centrally in the cavity. In a similar fashion to the card restraints, these were designed to be simple to produce and transport. This design worked well for these restraint support structures though the large restraint box has not yet been tested with radioactive samples.

Three of the detection scintillators were held in position around the cavity by use of a laser cut plastic support structure. This support structure slots into the shielding that was cast to surround the detection system. Although this support allows for redesigned if required, the positioning of the scintillators is limited by the design of the shield. Any repositioning of the detection materials would therefore require a redesign of the shield. Similarly, the 3D printed case of the upper beta scintillator is limited in any redesign due to the restriction of the shield. The design does however, allow for the entire detection system to be quickly disassembled for transport or storage. The advantage of this is in the modularity of the system, i.e. if only the gamma component of the detection system is required then the beta scintillators can be left out.

8.2.6 Testing

Initial testing of the entire detection system, as part of objective 5 "*Critical evaluation of the constructed detector, through a combination of laboratory and field tests using radioactive*

phantoms and (samples) target organisms, to assess the suitability for field deployment",
showed each detection material responded as required to the targeted radionuclides (Chapter
6.3.7.2). Testing also showed that the count rate on each scintillator was affected by the
positioning of the source within the cavity. The use of two beta and two gamma scintillators,
however, meant this positional effect could be minimised; summing the two gamma
scintillators (Figure 7.24) meant it did not matter how the sample was placed within the
restraint box whereas summing the two beta scintillators (Figure 7.25) resulted in a
significantly reduced effect. Any deviation still seen in the count rate for the two beta
scintillators is likely caused by degradation of detected signal when the source is placed away
from the end of the plastic scintillator where the PMT is attached (Chapter 7.3.2.2).

Two discrepancies arose during field work conducted to meet Objective 6 "*Development of
correlation ratios (between measured and verified activity concentrations) for the selected
organism(s) for the estimation of internal radionuclide concentration through external
measurement with the constructed scintillator*". Determination of detection response rates
(Chapter 7.3.2.1) using two phantoms resulted in an incorrect estimation of activity using a
third phantom. This requires further testing with other radioactive sources (separate ^{137}Cs and
^{90}Sr). A discrepancy was also seen in the difference between measurement locations. There
was a significant difference found between the net counts recorded in the laboratory as
compared to the three field sites (Chapter 7.3.3). There was, however, a 22°C temperature
difference between these site that could have been the cause of this difference. This could be
tested by counting a radioactive sample under different temperature regimes. Despite these
discrepancies, there was a still a good correlation (R>0.96) found between the ^{137}Cs count rate
measured using the portable detector and the activity determined using the alternative
method (laboratory detector). This was similar for the ^{90}Sr correlation; R=0.93 for the small
rodent correlation and the bird measurements showing a near perfect correlation at R=0.99.
The detector therefore partially meets objective 6 as it showed a good correlation ratio
between measured and actual internal activity for different organisms can be calculated.
Samples sizes were low, however, and the estimation of internal activity would benefit from
the measurement of more samples (i.e. Howard et al. (1987) required a larger number of
samples for determining a more accurate ratio).

8.3   Limitations of the portable detector

Although the detector worked well overall, there are still a few limitations in its use:

1) The current design of the detector means it can only accept sample sizes up to 170 x 60 x 50 mm. The combination of detection components means a larger cavity size would increase the overall weight such that it would no longer be portable. The allowed sample sizes did, however, still meet the aim of this research project.

2) The use of a SCA means only one detection peak can be counted. There was, however, only one gamma emitting radionuclide that was required to be monitored for this research project. The SCA could, however, be exchanged for an MCA if multiple peaks were required to be counted (at a cost of new equipment).

3) The detection system requires disassembly for storage and transportation. This increases the set-up time and increases the risk of a component being damaged. Robust packaging and careful handling will reduce this risk though checks should be made for damage before and after field work.

8.4   Recommendations and further work

The newly developed detector worked well. Based on this first version, a few points need to be addressed before it can be deployed for use in live-monitoring studies.

1) The attenuation material between sample and gamma scintillators needs to be increased to remove as much of the detected beta as possible. The discussion of chapter 7.4.2 recommended between 5 to 6 mm of extra plastic to be inserted (or a thinner amount of a higher density material).

2) The discrepancy between the estimated and measured count rates from the phantoms needs to be investigated. This can be accomplished by checking the phantom used or testing the detector with a greater range of phantom activities.

3) The significant difference between the laboratory and field measurement locations needs to be investigated. This could either be caused by the temperature difference between the laboratory and field sites or because of the low number of sampling sites. Both factors can be investigated; testing under different temperatures and increasing the number of sample sites in a second study.

4) The transport casing for the detector requires waterproofing to ensure it can operate in adverse weather. During the fieldwork conducted in the CEZ, it was possible to place the

detector system under cover. In future work, however, the availability of shelter may not always be present.

Completion of these changes and further testing will advance the new detector to a stage where it is expected to be deployable in live-monitoring field studies. Further testing should incorporate calibration against a range of additional targets (e.g. soil) to broaden the capabilities of the detector.

8.5   Overall conclusion

A fully working portable live-monitoring device was designed, constructed and tested as part of the research conducted for this thesis. The research described in the previous chapters detail a detector that can be deployed rapidly for various monitoring scenarios. It has been developed to be used for research involving the study of radionuclides (though currently calibrated to only two radionuclides; ^{137}Cs and ^{90}Sr) within living organisms and for use as a rapidly deployable monitor for use in emergency situations (e.g. in the event of an unplanned radioactive release).

The newly developed detector comprises of a unique arrangement of four detection materials, for gamma and beta detection in small animals (small rodents and birds were tested in this research), and a restraint system for humanely holding animal targets for the required counting time. Development of this detection system has provided a template for the creation of a broader range of detectors that could monitor different radionuclides or organism types and sizes. This template includes choices for the arrangement of detection materials around the target organism and how to efficiently extract the scintillation light from these uniquely designed material shapes.

Testing of the device showed it worked well for providing a consistent count rate for animal samples, no matter how they were positioned within the detector. It also gave good correlation for the estimation of internal activity concentrations of ^{137}Cs and ^{90}Sr in animal targets. Further work is, however, still required to ensure the device is ready to be deployed in further research studies. A change to be made in the design is the addition of extra material between the sample and the gamma scintillators to remove a beta response that is currently present from ^{90}Y decay. Further testing is also required to provide a better estimation of the response rates for each scintillator and to test how temperature may be affecting the measured count rates.

9   References

AL-MASRI, M. S., HASAN, M., AL-HAMWI, A., AMIN, Y. & DOUBAL, A. W. 2013. Mass attenuation coefficients of soil and sediment samples using gamma energies from 46.5 to 1332 keV. *Journal of Environmental Radioactivity,* 116**,** 28-33.

ASTM INTERNATIONAL 2014. ASTM D3648-14. *Standard Practices for the Measurement of Radioactivity.* West Conshohocken, PA.

BAB, I., HAJBI-YONISSI, C., GABET, Y. & MÜLLER, R. 2007. *Micro-tomographic atlas of the mouse skeleton,* New York, Springer.

BARLOW, K. 1999. *Expedition field techniques: bats,* London, Royal Geographical Society (with IBG).

BARNETT, A. & DUTTON, J. 1995. *Expedition field techniques: small mammals (excluding bats),* London, Royal Geographical Society (with IBG).

BARNETT, C. L., BERESFORD, N. A., WALKER, L. A., BAXTER, M., WELLS, C. & COPPLESTONE, D. 2014. Transfer parameters for ICRP reference animals and plants collected from a forest ecosystem. *Radiation and Environmental Biophysics,* 53**,** 125-49.

BARYAKHTAR, V. G., BONDARKOV, M. D., GASCHAK, S. P., GORYANAYA, J. A., MAXIMENKO, A. M., LIABIK, V. V., CHESSER, R. K. & BAKER, R. G. 2003. Problems in small mammal radioecology. *Environmental Science and Pollution Research***,** 95-106.

BAT CONSERVATION TRUST. 2016. *UK bats* [Online]. Available: http://www.bats.org.uk/pages/uk_bats.html [Accessed August 2016].

BATTERSBY, J. 2005. UK mammals: species status and population trends. first report by the tracking mammals partnership. *JNCC/Tracking Mammals Partnership.* Peterborough.

BERESFORD, N. A. 2010. The transfer of radionuclides to wildlife. *Radiation and Environmental Biophysics,* 49**,** 505-8.

BERESFORD, N. A., BARNETT, C. L., HOWARD, B. J., HOWARD, D. C., WELLS, C., TYLER, A. N., BRADLEY, S. & COPPLESTONE, D. 2012. Observations of Fukushima fallout in Great Britain. *Journal of Environmental Radioactivity,* 114**,** 48-53.

BERESFORD, N. A., BARNETT, C. L., HOWARD, B. J., SCOTT, W. A., BROWN, J. E. & COPPLESTONE, D. 2008a. Derivation of transfer parameters for use within the ERICA Tool and the default concentration ratios for terrestrial biota. *Journal of Environmental Radioactivity,* 99**,** 1393-407.

BERESFORD, N. A., BARNETT, C. L., JONES, D. G., WOOD, M. D., APPLETON, J. D., BREWARD, N. & COPPLESTONE, D. 2008b. Background exposure rates of terrestrial wildlife in England and Wales. *Journal of Environmental Radioactivity,* 99**,** 1430-9.

BERESFORD, N. A., GASCHAK, S., MAKSIMENKO, A. & WOOD, M. D. 2016. The transfer of Cs-137, Pu isotopes and Sr-90 to bird, bat and ground-dwelling small mammal species within the Chernobyl exclusion zone. *Journal of Environmental Radioactivity,* 153**,** 231-6.

BERESFORD, N. A., HOSSEINI, A., BROWN, J. E., CAILES, C., BEAUGELIN-SEILLER, K., BARNETT, C. L. & COPPLESTONE, D. 2010. Assessment of risk to wildlife from ionising radiation: can initial screening tiers be used with a high level of confidence? *Journal of Radiological Protection,* 30**,** 265-81.

BERESFORD, N. A., MAYES, R. W., BARNETT, C. L., LAMB, C. S., WILSON, P. J., HOWARD, B. J. & VOIGT, G. 1997. The effectiveness of oral administration of potassium iodide to lactating goats in reducing the transfer of radioiodine to milk. *Journal of Environmental Radioactivity,* 35**,** 115-28.

BERESFORD, N. A., MAYES, R. W., BARNETT, C. L., MACEACHERN, P. J. & CROUT, N. M. J. 1998. Variation in the metabolism of radiocaesium between individual sheep. *Radiation and Environmental Biophysics,* 37**,** 277-81.

BERGER, M. J., COURSEY, J. S., ZUCKER, M. A. & CHANG, J. 2005. *TESTAR, PSTAR, and ASTAR: computer programs for calculating stopping-power and range tables for electrons, protons, and helium ions (version 1.2.3).* [Online]. National Institute of Standards and Technology, Gaithersburg, MD. Available: h ttp://physics.nist.gov/Star [Accessed July 2015].

BOLOTNIKOV, A. E., ACKLEY, K., CAMARDA, G. S., CUI, Y., EGER, J. F., DE GERONIMO, G., FINFROCK, C., FRIED, J., HOSSAIN, A., LEE, W., PROKESCH, M., PETRYK, M., REIBER, J. L., ROY, U., VERNON, E., YANG, G. & JAMES, R. B. 2015. High-efficiency CdZnTe gamma-ray detectors. *IEEE Transactions on Nuclear Science,* 62**,** 3193-8.

BONDARKOV, M. D., GASCHAK, S. P., GORYANAYA, J. A., MAXIMENKO, A. M., RYABUSHKIN, A. N., SALYI, O. V., SHULGA, A. A., AWAN, S., CHESSER, R. K. & RODGERS, B. E. 2002. Parameters of bank vole decontamination from radiocesium and radiostrontium. *Radioprotection,* 37**,** C1-385-90.

BONDARKOV, M. D., MAKSIMENKO, A. M., GASCHAK, S. P., ZHELTONOZHSKY, V. A., JANNIK, G. T. & FARFAN, E. B. 2011. Method for simultaneous Sr-90 and Cs-137 in-vivo measurements of small animals and other environmental media developed for the conditions of the Chernobyl exclusion zone. *Health Physics,* 101**,** 383-92.

BONISOLI-ALQUATI, A., KOYAMA, K., TEDESCHI, J., KITAMURA, W., SUKUZI, H., OSTERMILLER, S., ARAI, E., MOLLER, A. P. & MOUSSEAU, T. A. 2015. Abundance and genetic damage of barn swallows from Fukushima. *Scientific Reports,* 5.

BORYŁO, A., SKWARZEC, B. & FABISIAK, J. 2010. Bioaccumulation of uranium U-234 and U-238 in marine birds. *Journal of Radioanalytical and Nuclear Chemistry,* 284**,** 165-72.

BRITISH TRUST FOR ORNITHOLOGY. 2016. *BTO birdFacts - Great Tit (Parus major)* [Online]. Available: https://blx1.bto.org/birdfacts/results/bob14640.htm [Accessed August 2016].

BROWN, J. E., ALFONSO, B., AVILA, R., BERESFORD, N. A., COPPLESTONE, D. & HOSSEINI, A. 2016. A new version of the ERICA tool to facilitate impact assessments of radioactivity on wild plants and animals. *Journal of Environmental Radioactivity,* 153**,** 141-8.

BROWN, J. E., ALFONSO, B., AVILA, R., BERESFORD, N. A., COPPLESTONE, D., PROHL, G. & ULANOVSKY, A. 2008. The ERICA Tool. *Journal of Environmental Radioactivity,* 99**,** 1371-83.

BRYNILDSEN, L. I. & STRAND, P. 1994. A rapid method for the determination of radioactive cesium in live animals and carcasses, and its practical application in norway after the chernobyl nuclear-reactor accident. *Acta Veterinaria Scandinavica,* 35**,** 401-8.

BURGER, A., GROZA, M., CUI, Y., ROY, U. N., HILLMAN, D., GUO, M., LI, L., WRIGHT, G. W. & JAMES, R. B. 2005. Development of portable CdZnTe spectrometers for remote sensing of signatures from nuclear materials. *Physica Status Solidi,* 2**,** 1586-91.

BUSHBERG, J. T., SEIBERT, J. A., LEIDHOLDT, E. M. & BOONE, J. M. 2011. *The essential physics of medical imaging,* Philadelphia, USA, Wolters Kluwer Health.

CANBERRA INDUSTRIES INC. 2015. *Falcon 5000® portable HPGe-based radionuclide identifier* [Online]. Available: h ttp://www.canberra.com/products/hp_radioprotection/falcon-5000.asp [Accessed July 2015].

CESANA, A. & TERRANI, M. 1989. An empirical method for peak-to-total ratio computation of a gamma-ray detector. *Nuclear Instruments and Methods in Physics Research,* 281**,** 172-5.

CHESSER, R. K. & SUGG, D. W. 2000. Concentrations and dose rate estimates of cesium-134,137 and strontium-90 in small mammals at Chornobyl, Ukraine. *Environmental Toxicology and Chemistry,* 19**,** 305-12.

CLARK, R., BURGESS, P. & CROUDACE, I. Measurement of plutonium contamination through paint using a fidler probe. ASME 2011 14th international conference on environmental remediation and radioactive waste management, 2011 Reims, France.

COOPER, D. M., CHAPMAN, L. D., CARTER, Y., WU, Y., PANAHIFAR, A., BRITZ, H. M., BEWER, B., ZHOUPING, W., DUKE, M. J. & DOSCHAK, M. 2012. Three dimensional mapping of strontium in bone by dual energy K-edge subtraction imaging. *Physics in Medicine and Biology,* 57**,** 5777-86.

COPPLESTONE, D., BERESFORD, N. A., BROWN, J. E. & YANKOVICH, T. 2013. An international database of radionuclide concentration ratios for wildlife: development and uses. *Journal of Environmental Radioactivity,* 126**,** 288-98.

COPPLESTONE, D., BIELBY, S. & JONES, S. R. 2001. Impact assessment of ionising radiation on wildlife. *R&D Publication 128.* Available online: https://www.gov.uk/government/ publications/impact-assessment-of-ionising-radiation-on-wildlife.

COPPLESTONE, D., JOHNSON, M. S., JONES, S. R., TOAL, M. E. & JACKSON, D. 1999. Radionuclide behaviour and transport in a coniferous woodland ecosystem: vegetation, invertebrates and wood mice, Apodemus sylvaticus. *Science of The Total Environment,* 239**,** 95-109.

COPPLESTONE, D., WOOD, M. D., BIELBY, S., JONES, S. R., VIVES, J. & BERESFORD, N. A. 2003. Habitats regulations for Stage 3 assessments: radioactive substances authorisations. *Technical Report P3-101/SP1a.* Bristol, UK: Environment Agency.

COPPLESTONE, D., WOOD, M. D., MERRILL, P. C., ALLOTT, R., JONES, S. R., J. VIVES I BATLLE, N., BERESFORD, N. A. & ZINGER, I. 2005. Impact assessment of ionising radiation on wildlife: Meeting the requirements of the EU birds and habitats directives. *Radioprotection,* 40**,** S893-8.

CURRIE, L. A. 1968. Limits for qualitative detection and quantitative determination. Application to radiochemistry. *Analytical Chemistry,* 40**,** 586-93.

D'AMBROSIO, C. & LEUTZ, H. 2003. Hybrid photon detectors. *Nuclear Instruments and Methods in Physics Research,* 501**,** 463-98.

DAWSON, N. J. & WEBSTER, M. E. D. 1967. The insulative value of mouse fur. *Quarterly Journal of Experimental Physiology and Cognate Medical Sciences,* 52**,** 168-73.

DIDYCHUK, C., BURCHART, P. A., CARLISLE, S. M. & RICHARDSON, R. B. 2014. Retention and excretion of inhaled H-3 and C-14 radiolabeled methane in rats. *Health Physics,* 107**,** 18-35.

DOGDAS, B., STOUT, D., CHATZIIOANNOU, A. F. & LEAHY, R. M. 2007. Digimouse: a 3D whole body mouse atlas from CT and cryosection data. *Physics in Medicine and Biology,* 52**,** 577-87.

EISENBUD, M. & GESELL, T. 1997. *Environmental radioactivity from natural, industrial and military sources,* Michigan, USA, Academic Press.

EKSTRÖM, L. P. & FIRESTONE, R. B. 2004. *WWW table of radioactive isotopes* [Online]. Available: http://ie.lbl.gov/toi/radSearch.asp [Accessed July 2015].

ELDRIDGE, J. S. 1989. Analytical chemistry division annual progress report. Oak Ridge, Tennessee: Oak Ridge National Laboratory.

ENVIRONMENT AGENCY, ENVIRONMENT AND HERITAGE SERVICE, FOOD STANDARDS AGENCY & SCOTTISH ENVIRONMENT PROTECTION AGENCY 2014. Radioactivity in food and the environment, 2013 (RIFE-19). Available from: https://www.food.gov.uk/science/ research/radiologicalresearch/radiosurv/rife.

EUROPEAN ENVIRONMENT AGENCY. 2017. *Soil organic carbon* [Online]. Available: https://www.eea.europa.eu/data-and-maps/indicators/soil-organic-carbon-1/assessment [Accessed February 2017].

EVANS, R. D. 1955. *The atomic nucleus,* New York, USA, McGraw-Hill.

GARLAND, J. A. & WAKEFORD, R. 2007. Atmospheric emissions from the Windscale accident of October 1957. *Atmospheric Environment,* 41**,** 3904-20.

GARTEN, C. T. 1995. Dispersal of radioactivity by wildlife from contaminated sites in a forested landscape. *Journal of Environmental Radioactivity,* 29**,** 137-56.

GASCHAK, S. P., MAKLYUK, Y. A., MAKSIMENKO, A. M., BONDARKOV, M. D., JANNIK, G. T. & FARFAN, E. B. 2011. Radiation ecology issues associated with murine rodents and shrews in the Chernobyl exclusion zone. *Health Physics,* 101**,** 416-30.

GÜRLER, O. & YALÇıN, S. 2005. A practical method for calculation of mass-attenuation coefficients of β particles. *Annals of Nuclear Energy,* 32**,** 1918-25.

GUSS, P., REED, M., YUAN, D., REED, A. & MUKHOPADHYAY, S. 2009. CeBr3 as a room-temperature, high-resolution gamma-ray detector. *Nuclear Instruments and Methods in Physics Research,* 608**,** 297-304.

HALL, E. J. & GIACCIA, A. J. 2006. *Radiobiology for the radiologist,* Philadelphia, USA, Lippincott Williams & Wilkins.

HAMAMATSU PHOTONICS K.K. 2016. Photomultiplier tubes and related products. *Photomultiplier tubes.* Japan: Available from Hamamatsu Photonics K.K.

HENDEE, W. R. & RITENOUR, E. R. 2003. *Medical imaging physics,* New York, USA, Wiley.

HINE, G. J. 2016. *Instrumentation in nuclear medicine,* London, Academic Press.

HINTON, T. G., GARNIER-LAPLACE, J., VANDENHOVE, H., DOWDALL, M., ADAM-GUILLERMIN, C., ALONZO, F., BARNETT, C., BEAUGELIN-SEILLER, K., BERESFORD, N. A., BRADSHAW, C., BROWN, J., EYROLLE, F., FEVRIER, L., GARIEL, J. C., GILBIN, R., HERTEL-AAS, T., HOREMANS, N., HOWARD, B. J., IKAHEIMONEN, T., MORA, J. C., OUGHTON, D., REAL, A., SALBU, B., SIMON-CORNU, M., STEINER, M., SWEECK, L. & VIVES I BATLLE, J. 2013. An invitation to contribute to a strategic research agenda in radioecology. *Journal of Environmental Radioactivity,* 115**,** 73-82.

HOME OFFICE. 2013. *Research and testing using animals* [Online]. Available: h ttps://www.gov.uk/guidance/research-and-testing-using-animals#animals-scientific-procedures-act-1986 [Accessed August 2016].

HORRILL, A. D. & HOWARD, D. M. 1991. Chernobyl fallout in three areas of upland pasture in west Cumbria. *Journal of Radiological Protection,* 11**,** 249-57.

HOWARD, B. J. 2013. A new IAEA handbook quantifying the transfer of radionuclides to wildlife for assessment tools. *Journal of Environmental Radioactivity,* 126**,** 284-7.

HOWARD, B. J., BERESFORD, N. A., ANDERSSON, P., BROWN, J. E., COPPLESTONE, D., BEAUGELIN-SEILLER, K., GARNIER-LAPLACE, J., HOWE, P. D., OUGHTON, D. & WHITEHOUSE, P. 2010. Protection of the environment from ionising radiation in a regulatory context - an overview of the PROTECT coordinated action project. *Journal of Radiological Protection,* 30**,** 195-214.

HOWARD, B. J., BERESFORD, N. A., BURROW, L., SHAW, P. V. & CURTIS, E. J. C. 1987. A comparison of caesium-137 and 134 activity in sheep remaining on upland areas contaminated by Chernobyl fallout with those removed to less active lowland pasture. *Journal of the Society for Radiological Protection,* 7**,** 71-3.

HOWARD, B. J., BERESFORD, N. A., COPPLESTONE, D., TELLERIA, D., PROEHL, G., FESENKO, S., JEFFREE, R. A., YANKOVICH, T. L., BROWN, J. E., HIGLEY, K. A., JOHANSEN, M. P., MULYE, H., VANDENHOVE, H., GASHCHAK, S., WOOD, M. D., TAKATA, H., ANDERSSON, P., DALE, P., RYAN, J., BOLLHÖFER, A., DOERING, C., BARNETT, C. L. & WELLS, C. 2013a.

The IAEA handbook on radionuclide transfer to wildlife. *Journal of Environmental radioactivity,* 121**,** 55-74.

HOWARD, B. J., WELLS, C., BERESFORD, N. A. & COPPLESTONE, D. 2013b. Exploring methods to prioritise concentration ratios when estimating weighted absorbed dose rates to terrestrial Reference Animals and Plants. *Journal of Environmental Radioactivity,* 126**,** 326-37.

HUBBELL, J. H. & SELTZER, S. M. 1996. *Tables of X-Ray mass attenuation coefficients and mass energy absorption coefficients from 1 keV to 20 MeV for elements Z = 1 to 92 and 48 additional substances of dosimetric interest* [Online]. National Institute of Standards and Technology, Gaithersburg, MD. Available: http://physics.nist.gov/xaamdi [Accessed 2015].

IAEA 1989. Measurement of radionuclides in food and the environment - a guidebook. *Technical Reports Series 295.* Vienna: International Atomic Energy Agency.

IAEA 2002. Use of electron paramagnetic resonance dosimetry with tooth enamel for retrospective dose assessment. *IAEA TECDOC 1331.* Vienna, Austria: International Atomic Energy Agency.

IAEA 2010a. Handbook of parameter values for the prediction of radionuclide transfer in terrestrial and freshwater environments. *Technical reports series No. 472.* Vienna: International Atomic Energy Agency.

IAEA 2010b. Radiation biology: a handbook for teachers and students. *Training course series 42.* Vienna: International Atomic Energy Agency.

IAEA 2011. Radioactive particles in the environment: sources, particle characteristics, and analytical techniques. *IAEA-TECDOC-1663.* Vienna: International Atomic Energy Agency.

IAEA 2014. The environmental behaviour of radium: revised edition. *Technical Reports Series No. 476.* Vienna: International Atomic Energy Agency.

ICRP 1977. Recommendations of the ICRP. ICRP Publication 26. *Annals of the ICRP,* 1**,** (3).

ICRP 1979. Limits for Intakes of Radionuclides by Workers. ICRP Publication 30 (Part 1). *Annals of the ICRP,* 2**,** (3-4).

ICRP 1991. 1990 Recommendations of the International Commission on radiological protection. ICRP Publication 60. *Annals of the ICRP,* 21**,** (1-3).

ICRP 2007. The 2007 recommendations of the International Commission on Radiological Protection. ICRP Publication 103. *Annals of the ICRP,* 37**,** (2-4).

ICRP 2008. Environmental protection: the concept and use of Reference Animals and Plants. ICRP Publication 108. *Annals of the ICRP,* 38**,** (4-6).

ISHIDA, K., TANOI, K. & NAKANISHI, T. M. 2015. Monitoring free-living Japanese Bush Warblers (Cettia diphone) in a most highly radiocontaminated area of Fukushima Prefecture, Japan. *Journal of Radiation Research,* 56**,** I24-8.

IYUDIN, A. F., BOGOMOLOV, V. V., SVERTILOV, S. I., YASHIN, I. V., SMOOT, G. F., GREINER, J. & FON KIENLIN, A. 2013. Characteristics of position sensitive detector pixels based on promising inorganic scintillators LaBr3:Ce and CeBr3. *Instruments and Experimental Techniques,* 56**,** 640-8.

JNCC. 2015. *UK BAP priority species* [Online]. Available: h ttp://jncc.defra.gov.uk/page-5717 [Accessed July 2015].

JOHANSEN, M. P., BARNETT, C. L., BERESFORD, N. A., BROWN, J. E., CERNE, M., HOWARD, B. J., KAMBOJ, S., KEUM, D. K., SMODIS, B., TWINING, J. R., VANDENHOVE, H., VIVES I BATLLE, J., WOOD, M. D. & YU, C. 2012. Assessing doses to terrestrial wildlife at a radioactive waste disposal site: inter-comparison of modelling approaches. *The Science of the Total Environment,* 427-428**,** 238-46.

JONES, D. G., APPLETON, J. D., BREWARD, N., MACKENZIE, A. C., SCHEIB, C., BERESFORD, N. A., BARNETT, C. L., WOOD, M. D. & COPPLESTONE, D. 2009. Assessment of naturally occurring radionuclides around England and Wales: Application of the G-BASE dataset to estimate doses to non-human species. *Radioprotection,* 44**,** 629-34.

KAMRANI, A. K. & NASR, E. A. 2010. *Engineering design and rapid prototyping,* London, Springer.

KATHREN, R. L. 1984. *Radioactivity in the environment: sources, distribution, and surveillance,* Michigan, USA, Harwood Academic Publishers.

KAYE, S. V. & DUNAWAY, P. B. 1962. Bioaccumulation of radioactive isotopes by herbivorous small mammals. *Health Physics,* 7**,** 205-17.

KEEVIL, S. F. 2012. Physics and medicine: a historical perspective. *Lancet,* 379**,** 1517-24.

KENDALL, G. M. 2005. Factors affecting cosmic ray exposures in civil aviation. *International Congress Series,* 1276**,** 129-32.

KHANDAKER, M. U. 2011. High purity germanium detector in gamma-ray spectrometry. *International Journal of Fundamental Physical Sciences,* 1**,** 42-6.

KNOLL, G. F. 2010. *Radiation detection and measurement*, John Wiley & Sons.

KOCK, P., RAAF, C. & SAMUELSSON, C. 2014. On background radiation gradients - the use of airborne surveys when searching for orphan sources using mobile gamma-ray spectrometry. *Journal of Environmental Radioactivity,* 128**,** 84-90.

KODAIRA, S., TOLOCHEK, R. V., AMBROZOVA, I., KAWASHIMA, H., YASUDA, N., KURANO, M., KITAMURA, H., UCHIHORI, Y., KOBAYASHI, I., HAKAMADA, H., SUZUKI, A., KARTSEV, I. S., YARMANOVA, E. N., NIKOLAEV, I. V. & SHURSHAKOV, V. A. 2014. Verification of shielding effect by the water-filled materials for space radiation in the International Space Station using passive dosimeters. *Advances in Space Research,* 53**,** 1-7.

KOIKE, T., CHIGA, N., HARUYAMA, T., HOSOMI, K., ICHINOHE, H., KASAMI, K., MATSUSHITA, T., MIZOGUCHI, Y., ONO, H., SHIROTORI, K., TAKEUCHI, T., TAMURA, H. & YAMAMOTO, T. O. 2015. Development of a low-temperature germanium detector via mechanical cooling with a compact pulse-tube refrigerator. *Nuclear Instruments and Methods in Physics Research,* 770**,** 1-7.

KRANE, K. S. 1988. *Introductory nuclear physics*, John Wiley & Sons, Inc.

KRYEMADHI, A., BARNER, L., GROVE, A., MOHLER, J., SISSON, C. & ROTH, A. 2017. Performance of LYSO and CeBr3 crystals readout by silicon photomultiplier arrays as compact detectors for space based applications. *Journal of Instrumentation,* 12**,** C02013.

KUBOTA, Y., TAKAHASHI, H., WATANABE, Y., FUMA, S., KAWAGUCHI, I., AOKI, M., KUBOTA, M., FURUHATA, Y., SHIGEMURA, Y., YAMADA, F., ISHIKAWA, T., OBARA, S. & YOSHIDA, S. 2015. Estimation of absorbed radiation dose rates in wild rodents inhabiting a site severely contaminated by the Fukushima Dai-ichi nuclear power plant accident. *Journal of Environmental Radioactivity,* 142**,** 124-31.

LARSSON, C. M. 2008. An overview of the ERICA Integrated Approach to the assessment and management of environmental risks from ionising contaminants. *Journal of Environmental Radioactivity,* 99**,** 1364-70.

MACDONALD, D. W. 2010. *The encyclopedia of mammals,* Oxford, Oxford University Press.

MAHAJAN, C. S. 2012. Mass attenuation coefficients of beta particles in elements. *Science Research Reporter,* 2**,** 135-41.

MAKLYUK, Y. A., MAKSIMENKO, A. M., GASHCHAK, S. P., BONDARKOV, M. D. & CHIZHEVSKII, I. V. 2007. Long-term dynamics of radioactive Sr-90 and Cs-137 contamination of small mammals in the Chernobyl zone. *Russian Journal of Ecology,* 38**,** 181-9.

MALINOVSKY, G. P., YARMOSHENKO, I. V., ZHUKOVSKY, M. V., STARICHENKO, V. I. & CHIBIRYAK, M. V. 2014. Contemporary radiation doses to murine rodents inhabiting

the most contaminated part of the EURT. *Journal of Environmental Radioactivity,* 129**,** 27-32.

MAYES, R. W., BERESFORD, N. A., LAMB, C. S., BARNETT, C. L., HOWARD, B. J., JONES, B. E., ERIKSSON, O., HOVE, K., PEDERSEN, O. & STAINES, B. W. 1994. Novel approaches to the estimation of intake and bioavailability of radiocaesium in ruminants grazing forested areas. *Science of The Total Environment,* 157**,** 289-300.

MCLEAN, C. M., KOLLER, C. E., RODGER, J. C. & MACFARLANE, G. R. 2009. Mammalian hair as an accumulative bioindicator of metal bioavailability in Australian terrestrial environments. *Science of the Total Environment,* 407**,** 3588-96.

MENEFEE, J., CHO, Y. & SWINEHAR.C 1967. Sodium activated cesium iodide as a gamma ray and charged particle detector. *Ieee Transactions on Nuclear Science,* NS14**,** 464-7.

MENGE, P. R., YANG, K., MCLAUGHLIN, M. & BACON, B. Efficient positioning of silicon photomultipliers on large scintillation crystals. Nuclear science symposium, medical imaging conference and room-temperature semiconductor detector workshop (NSS/MIC/RTSD), 2016. IEEE.

MEREDITH, R. C. K., MONDON, K. J. & SHERLOCK, J. C. 1988. A rapid method for the In vivo monitoring of radiocaesium activity in sheep. *Journal of Environmental Radioactivity,* 7**,** 209-14.

MET OFFICE. 2013. *Weather extremes* [Online]. Available: metoffice.gov.uk/learning/ library/publications/factsheets [Accessed August 2016].

MIDDLETON, G. 2011. Tennesse Department of Environment and Conservation DOE oversight division environmental monitoring report January through December 2011. Oak Ridge, Tennessee: Oak Ridge National Laboratory.

MITCHELL, A. L., BORGARDT, J. D. & KOUZES, R. T. 2009. Skyshine contribution to gamma ray background between 0 and 4 MeV. USA: Pacific Northwest National Laboratory (PNNL), Richland, WA (US).

MORTON, G. A. 1975. The scintillation counter story part II. *IEEE Transactions on Nuclear Science,* 22**,** 26-8.

MOSS, R. & HORRILL, A. D. 1996. Metabolism of radiocaesium in red grouse. *Journal of Environmental Radioactivity,* 33**,** 49-62.

MOSZYŃSKI, M., KLAMRA, W., WOLSKI, D., CZARNACKI, W., KAPUSTA, M. & BALCERZYK, M. 2006. Comparative study of PP0275C hybrid photodetector and XP2020Q photomultiplier in scintillation detection. *Journal of Instrumentation,* 1**,** P05001.

NILSSON, J. M., OSTLUND, K., SODERBERG, J., MATTSSON, S. & RAAF, C. 2014. Tests of HPGe and scintillation-based backpack γ-radiation survey systems. *Journal of Environmental Radioactivity,* 135**,** 54-62.

ORTEC. 2015. *Micro-Detective-HX* [Online]. Available: http://www.ortec-online.com/ Products-Solutions/Hand-Held-Radioisotope-Identifiers-Micro-Detective-HX.aspx [Accessed July 2015].

OUGHTON, D. H., AGUERO, A., AVILA, R., BROWN, J. E., COPPLESTONE, D. & GILEK, M. 2008. Addressing uncertainties in the ERICA Integrated Approach. *Journal of Environmental Radioactivity,* 99**,** 1384-92.

PENTREATH, R. J. 1999. A system for radiological protection of the environment: some initial thoughts and ideas. *Journal of Radiological Protection,* 19**,** 117-28.

PENTREATH, R. J. 2012. Radiation and protection of the environment: The work of Committee 5. *Annals of the ICRP,* 41**,** 45-56.

PODGORSAK, E. B. 2010. *Radiation physics for medical physicists,* Berlin, Springer.

POTAPOV, V. N., VOLKOVICH, A. G., IVANOV, O. P., STEPANOV, V. E., SMIRNOV, S. V. & VOLKOV, V. G. 2006. Development of portable beta spectrometer for Sr-90 activity

measurements in field conditions and its application in rehabilitation activities at RRC Kurchatov Institute. *WM'06 Conference.* Tucson, AZ.

PUBLIC HEALTH ENGLAND 2011. Ionising radiation: dose comparisons. *Radiation and Health protection* www.gov.uk.

PYCKO SCIENTIFIC LIMITED 2014. NitroSPEC HPGe hand held spectrometer *Technical Document.* Available from PYCKO Scientific Limited.

QUARATI, F. G. A., DORENBOS, P., VAN DER BIEZEN, J., OWENS, A., SELLE, M., PARTHIER, L. & SCHOTANUS, P. 2013. Scintillation and detection characteristics of high-sensitivity CeBr3 gamma-ray spectrometers. *Nuclear Instruments and Methods in Physics Research,* 729**,** 596-604.

RENKER, D. & LORENZ, E. 2009. Advances in solid state photon detectors. *Journal of Instrumentation,* 4**,** P04004.

ROBBINS, C. R. 2012. *Chemical and physical behavior of human hair,* London, Springer.

RSA93 1993. Radioactive Substances Act 1993. HMSO: London.

RUSSELL, W. M. S., BURCH, R. L. & HUME, C. W. 1959. *The principles of humane experimental technique,* Michigan, USA, Methuen.

RUSSO, S., BARBARINO, G., DE ASMUNDIS, R. & DE ROSA, G. 2010. The vacuum silicon photomultiplier tube (VSiPMT): A new version of a hybrid photon detector. *Nuclear Instruments and Methods in Physics Research,* 623**,** 291-3.

RYABOKON, N. I., SMOLICH, II, KUDRYASHOV, V. P. & GONCHAROVA, R. I. 2005. Long-term development of the radionuclide exposure of murine rodent populations in Belarus after the Chernobyl accident. *Radiation and Environmental Biophysics,* 44**,** 169-81.

SAENKO, V., IVANOV, V., TSYB, A., BOGDANOVA, T., TRONKO, M., DEMIDCHIK, Y. & YAMASHITA, S. 2011. The Chernobyl accident and its consequences. *Clinical Oncology,* 23**,** 234-43.

SAINT-GOBAIN. 2015. *Plastic scintillator cast sheets* [Online]. Available: http://www. crystals.saint-gobain.com/Cast_Plastic_Scintillator.aspx [Accessed September 2015].

SAKAI, E. 1987. Recent measurements on scintillator-photodetector systems. *IEEE Transactions on Nuclear Science,* 34**,** 418-22.

SALACKA, J. S. & BACRANIA, M. K. 2010. A comprehensive technique for determining the intrinsic light yield of scintillators. *IEEE Transactions on Nuclear Science,* 57**,** 901-9.

SAZYKINA, T. G. & KRYSHEV, I. I. 2006. Radiation effects in wild terrestrial vertebrates - the EPIC collection. *Journal of Environmental Radioactivity,* 88**,** 11-48.

SEMIOSHKINA, N., PROEHL, G., SAVINKOV, A. & VOIGT, G. 2007. The transfer of Cs-137 and Sr-90 from feed to rabbits. *Journal of Environmental Radioactivity,* 98**,** 166-76.

SHAH, K. S., GLODO, J., HIGGINS, W., VAN LOEF, E. V. D., MOSES, W. W., DERENZO, S. E. & WEBER, M. J. 2005. CeBr3 scintillators for gamma-ray spectroscopy. *IEEE Transactions on Nuclear Science,* 52**,** 3157-9.

SHEPPARD, S. C. 2003. An index of radioecology, what has been important? *Journal of Environmental Radioactivity,* 68**,** 1-10.

SMITH, J. T. & BERESFORD, N. A. 2005. *Chernobyl: catastrophe and consequences*, Springer.

SONKAWADE, R. G., KANT, K., MURALITHAR, S., KUMAR, R. & RAMOLA, R. C. 2008. Natural radioactivity in common building construction and radiation shielding materials. *Atmospheric Environment,* 42**,** 2254-9.

SPIERS, F. W. 1946. Effective atomic number and energy absorption in tissues. *British Journal of Radiology,* 19**,** 52-63.

STABIN, M. G. 2007. *Radiation protection and dosimetry: an introduction to health physics*, Springer.

STRUMINSKA-PARULSKA, D. I., BORYLO, A., SKWARZEC, B. & FABISIAK, J. Polonium Po-210, uranium (U-234, U-238) and plutonium (Pu-238, Pu239+240) bioaccumulation in marine birds. 16th International Conference on Heavy Metals in the Environment, 2013 E3S Web of Conferences. EDP Sciences.

STRUMIŃSKA-PARULSKA, D. I., SZYMAŃSKA, K. & SKWARZEC, B. 2015. Determination of Po-210 in hair of domestic animals from Poland and Norway. *Journal of Radioanalytical and Nuclear Chemistry,* 306**,** 71-8.

SUL, W.-S., KIM, H. & CHO, G. 2015. Silicon photomultiplier modules for MRI-compatible PET. *16th international workshop on radiation imaging detectors.* Trieste, Italy: IOP Publishing for Sissa Medialab.

SUNDBERG, J. P., NANNEY, L. B., FLECKMAN, P. & KING, L. E. 2012. Chapter 23 - Skin and Adnexa. *In:* DINTZIS, S. M. (ed.) *Comparative Anatomy and Histology.* San Diego: Academic Press.

TAVERNIER, S., GEKTIN, A., GRINYOV, B. & MOSES, W. W. 2006. *Radiation detectors for medical applications,* Netherlands, Springer.

TAYLOR, M. L., SMITH, R. L., DOSSING, F. & FRANICH, R. D. 2012. Robust calculation of effective atomic numbers: the Auto-Z(eff) software. *Medical Physics,* 39**,** 1769-78.

TETE, N., AFONSO, E., CRINI, N., DROUHOT, S., PRUDENT, A. S. & SCHEIFLER, R. 2014. Hair as a noninvasive tool for risk assessment: do the concentrations of cadmium and lead in the hair of wood mice (Apodemus sylvaticus) reflect internal concentrations? *Ecotoxicology and Environmental Safety,* 108**,** 233-41.

THORNE, M. C. 2003. Background radiation: natural and man-made. *Journal of Radiological Protection,* 23**,** 29-42.

TILLER, B. L. & POSTON, T. M. 1999. Mule deer antlers as biomonitors of strontium-90 on the Hanford Site. *Journal of Environmental Radioactivity,* 47**,** 29-44.

TURCHETTA, R. 2016. *Analog electronics for radiation detection*, CRC Press.

UNSCEAR 2000a. Annex B: Exposures from natural radiation sources. *Sources and effects of ionizing radiation.* New York, USA: United Nations Scientific Committee on the effects of atomic radiation.

UNSCEAR 2000b. Annex C: Exposures from man-made sources of radiation. *Sources and effects of ionizing radiation.* New York, USA: United Nations Scientific Committee on the effects of atomic radiation.

UNSCEAR 2013. Volume 1: Report to the General Assembly, Annex A: Levels and effects of radiation exposure due to the nuclear accident after the 2011 great east-Japan earthquake and tsunami. New York, USA: United Nations Scientific Committee on the effects of atomic radiation.

UPP, D., KEYSER, R. & TWOMEY, T. 2005. New cooling methods for HPGE detectors and associated electronics. *Journal of Radioanalytical and Nuclear Chemistry,* 264**,** 121-6.

VAN LOEF, E., MARKOSYAN, G., SHIRWADKAR, U., MCCLISH, M. & SHAH, K. 2015. Gamma-ray spectroscopy and pulse shape discrimination with a plastic scintillator. *Nuclear Instruments and Methods in Physics Research,* 788**,** 71-2.

VIVES I BATLLE, J., BALONOV, M., BEAUGELIN-SEILLER, K., BERESFORD, N. A., BROWN, J., CHENG, J. J., COPPLESTONE, D., DOI, M., FILISTOVIC, V., GOLIKOV, V., HORYNA, J., HOSSEINI, A., HOWARD, B. J., JONES, S. R., KAMBOJ, S., KRYSHEV, A., NEDVECKAITE, T., OLYSLAEGERS, G., PROHL, G., SAZYKINA, T., ULANOVSKY, A., VIVES LYNCH, S., YANKOVICH, T. & YU, C. 2007. Inter-comparison of absorbed dose rates for non-human biota. *Radiation and Environmental Biophysics,* 46**,** 349-73.

VIVES I BATLLE, J., BEAUGELIN-SEILLER, K., BERESFORD, N. A., COPPLESTONE, D., HORYNA, J., HOSSEINI, A., JOHANSEN, M., KAMBOJ, S., KEUM, D. K., KUROSAWA, N., NEWSOME, L.,

OLYSLAEGERS, G., VANDENHOVE, H., RYUFUKU, S., VIVES LYNCH, S., WOOD, M. D. & YU, C. 2011. The estimation of absorbed dose rates for non-human biota: An extended intercomparison. *Radiation and Environmental Biophysics,* 50**,** 231-51.

WAKEFORD, R. 2007. The Windscale reactor accident: 50 years on. *Journal of Radiological Protection,* 27**,** 211-15.

WAKEFORD, R. 2011. And now, Fukushima. *Journal of Radiological Protection,* 31**,** 167-76.

WANG, B., YANG, W., MCKITTRICK, J. & MEYERS, M. A. 2016. Keratin: Structure, mechanical properties, occurrence in biological organisms, and efforts at bioinspiration. *Progress in Materials Science,* 76**,** 229-318.

WEARNE, S. 2012. The removal of post-chernobyl sheep controls. Food Standards Agency.

WHICKER, F. W. & SCHULTZ, V. 1982. *Radioecology: nuclear energy and the environment Vol. I*, CRC Press.

WOOD, M. D. 2010. *Assessing the impact of ionising radiation in temperate coastal sand dune ecosystems : measurement and modelling.* PhD thesis, University of Liverpool.

WOOD, M. D., BERESFORD, N. A., BARNETT, C. L., COPPLESTONE, D. & LEAH, R. T. 2009a. Assessing radiation impact at a protected coastal sand dune site: an intercomparison of models for estimating the radiological exposure of non-human biota. *Journal of Environmental Radioactivity,* 100**,** 1034-52.

WOOD, M. D., BERESFORD, N. A., YANKOVICH, T. L., SEMENOV, D. V. & COPPLESTONE, D. 2011. Addressing current knowledge gaps on radionuclide transfer to reptiles. *Radioprotection,* 46**,** S521-7.

WOOD, M. D., LEAH, R. T., JONES, S. R. & COPPLESTONE, D. 2009b. Radionuclide transfer to invertebrates and small mammals in a coastal sand dune ecosystem. *The Science of the Total Environment,* 407**,** 4062-74.

YANG, G., BOLOTNIKOV, A. E., FOCHUK, P. M., KOPACH, O., FRANC, J., BELAS, E., KIM, K. H., CAMARDA, G. S., HOSSAIN, A., CUI, Y., ADAMS, A. L., RADJA, A., PINDER, R. & JAMES, R. B. 2013. Post-growth thermal annealing study of CdZnTe for developing room-temperature X-ray and gamma-ray detectors. *Journal of Crystal Growth,* 379**,** 16-20.

YANG, P., HARMON, C. D., DOTY, F. P. & OHLHAUSEN, J. A. 2014. Effect of humidity on scintillation performance in Na and Tl activated CsI crystals. *Ieee Transactions on Nuclear Science,* 61**,** 1024-31.

YOO, H., JOO, S., YANG, S. & CHO, G. 2015a. Optimal design of a CsI(Tl) crystal in a SiPM based compact radiation sensor. *Radiation Measurements,* 82**,** 102-7.

YOO, W. J., SHIN, S. H., LEE, D. E., JANG, K. W., CHO, S. & LEE, B. 2015b. Development of a small-sized, flexible, and insertable fiber-optic radiation sensor for gamma-ray spectroscopy. *Sensors,* 15**,** 21265-79.

YU, C., LEPOIRE, D., ARNISH, J., CHENG, J. J., HLOHOWSKIJ, I., KAMBOJ, S., KLETT, T., DOMOTOR, S., HIGLEY, K., GRAHAM, R., NEWKIRK, P. & HARRIS, T. 2003. The RESRAD-BIOTA code for application in biota dose evaluation: Providing screening and organism-specific assessment capabilities for use within an environmental protection framework. *Protection of the Environment from Ionising Radiation,* 17**,** 283-9.

ZHANG, L., MAO, R., YANG, F. & ZHU, R.-Y. 2014. LSO/LYSO crystals for calorimeters in future hep experiments. *IEEE Transactions on Nuclear Science,* 61**,** 483-8.

10 Appendices

10.1 Tabulated properties of environmentally important radionuclides

Radionuclides with a half-life of under one day are ignored. Abundances under 2% are not included. Beta emissions display maximum energy. Undeclared fractions pass through the body without being absorbed. [1] - (Environment Agency et al., 2014); [2] - (Eisenbud and Gesell, 1997); [3] - http://www.nndc.bnl.gov/ensdf/; [4] - Y=years, D=days, H=hours, M=minutes; [5] - (ICRP, 1979); [6] - s=bone surface; [7] - fractional emission per decay; [8] - per 100 decays.

Column groups: **Decays to[3]** (Daughter, Stable?); **Principal Organ[5]** (WB, Bone[6], Kidney, Liver, Spleen, Thyroid, Stomach); **Total emission per decay[7]** (Alpha, Beta, Gamma); **Beta Emissions[3]** (Primary Peak keV, Abundance %[8], Secondary Peak keV, Abundance %[8]); **Gamma Emissions[3]** (Primary Peak keV, Abundance %[8], Secondary Peak keV, Abundance %[8]).

Nuclide[1,2]	Half-life[3,4]	Daughter	Stable?	WB	Bone[6]	Kidney	Liver	Spleen	Thyroid	Stomach	Alpha	Beta	Gamma	Beta Primary Peak (keV)	Beta Abundance (%)[8]	Beta Secondary Peak (keV)	Beta Abundance (%)[8]	Gamma Primary Peak (keV)	Gamma Abundance (%)[8]	Gamma Secondary Peak (keV)	Gamma Abundance (%)[8]
^{3}H	12.32 Y	^{3}He	Y	1.00								1.00		18.60	100.00						
^{14}C	5.70E+03 Y	^{14}N	Y	1.00								1.00		156.47	100.00						
^{32}P	14.27 D	^{32}S	Y	0.40	0.30							1.00		1710.66	100.00						
^{35}S	87.37 D	^{35}Cl	Y	0.20								1.00		167.30	100.00						
^{40}K	1.25E+09 Y	^{40}Ca	Y	1.00								0.89	0.11	1311.07	89.14			1460.88	10.66		
^{41}Ar	1.10E+02 M	^{41}K	Y									1.00	0.99	1198.30	99.16			1293.64	99.16		
^{60}Co	5.27 Y	^{60}Ni	Y	0.45			0.05					1.00	2.00	317.88	99.88			1332.49	99.98	1173.23	99.85
^{85}Kr	10.74 Y	^{85}Rb	Y	Skin and whole body external								1.00	0.00	687.00	99.56						
^{90}Sr	28.79 Y	^{90}Y	N		1.00							1.00		546.00	100.00						
^{90}Y	64.00 H	^{90}Zr	Y	0.10	0.50		0.15					1.00		2280.00	99.99						
^{95}Nb	34.99 D	^{95}Mo	Y	0.26	0.71							1.00	1.00	159.70	99.97			765.80	99.81		
^{95}Zr	64.03 D	^{90}Nb	N	0.50	0.50							1.00	0.99	366.90	54.46	399.40	44.34	756.73	54.38	724.19	44.27
^{99}Tc	2.11E+05 Y	^{99}Ru	Y	0.83			0.03		0.04	0.10		1.00	0.00	293.50	100.00						
^{106}Ru	3.72E+02 D	^{106}Rh	N	0.85								1.00		39.40	100.00						
^{106}Rh	1.31E+02 M	^{106}Pd	Y	0.85										920.00	85.00			511.70	85.50	1046.70	30.35
^{110m}Ag	2.50E+02 D	^{110}Cd	Y	0.20			0.80					1.00	3.26	83.74	68.60	530.00	31.30	657.76	95.61	884.68	74.96
^{125}I	59.40 D	^{125}Te	Y						0.30				0.07					35.50	6.70		
^{125}Sb	2.76 Y	^{125}Te	Y	0.50	0.20		0.10					1.00	0.91	303.30	40.30	621.90	13.60	427.87	29.60	600.60	17.65
^{129}I	1.57E+07 Y	^{129}Xe	Y						0.30			1.00	0.08	149.00	100.00			39.58	7.51		
^{131}I	8.03 D	^{131}Xe	Y						0.30			1.00	1.01	606.30	89.60			364.49	81.50	636.99	7.16
^{134}Cs	2.07 Y	^{134}Ba	Y	1.00								1.00	2.23	658.00	70.17	415.40	2.45	604.72	97.62	795.86	85.46
^{137}Cs	30.08 Y	^{137}Ba	Y	1.00								1.00	0.85	514.03	94.70	1176.00	5.30	661.66	85.10		
^{144}Ce	2.85E+02 D	^{144}Pr	N	0.15	0.20		0.60					1.00	0.13	318.20	76.50	184.70	19.60	133.52	11.09	80.12	1.36
^{144}Pr	17.28 M	^{144}Nd	N		0.25	0.05	0.60							2996.00	97.90			696.51	1.34		
^{155}Eu	4.75 Y	^{155}Gd	Y		0.40	0.06	0.40					1.00	0.55	147.40	47.00	166.20	25.00	86.55	30.70	105.31	21.12
^{210}Po	1.38E+02 D	^{206}Pb	Y	0.70			0.10	0.10	0.10		1.00		0.00								
^{214}Pb	26.80 M	^{214}Bi	N		0.55	0.02	0.25							670.00	45.90	1030.00	11.00	351.93	35.60	295.22	18.42
^{218}Po	3.10 M	^{214}Pb	N	0.70			0.10	0.10	0.10												
^{222}Rn	3.82 D	^{218}Po	N			0.30												510.00	0.08		
^{224}Ra	3.66 D	^{220}Rn	N		1.00s													240.99	4.10		
^{226}Ra	1.60E+03 Y	^{222}Rn	N		1.00						1.00		0.04					186.21	3.64		
^{228}Ac	6.15 H	^{228}Th	N		0.45		0.45							1165.00	29.90	1738.00	11.65	911.20	25.80	968.97	15.80
^{228}Ra	5.75 Y	^{228}Ac	N		1.00									39.10	40.00	39.50	10.00	13.52	2.00		
^{228}Th	1.91 Y	^{224}Ra	N	0.16	0.70s						1.00		0.02					84.37	1.19		
^{230}Th	7.54E+04 Y	^{226}Ra	N	0.16	0.70s						1.00		0.00								
^{231}Th	25.52 H	^{231}Pa	N	0.16	0.70s									290.20	40.00	305.00	32.00	25.64	14.12	84.21	6.60
^{232}Th	1.40E+10 Y	^{228}Ra	N	0.16	0.70s						1.00		0.00								
^{234m}Pa	1.16 M	^{234}U	N		0.40	0.02	0.15					1.00	0.02	2290.00	97.57	1224.00	1.00				
^{234}Th	24.10 D	^{234m}Pa	N	0.16	0.70s							1.00	0.08	198.50	78.00	273.00	14.00	63.29	3.67	92.38	2.13
^{234}U	2.46E+05 Y	^{230}Th	N	0.12		0.22	0.12				1.00		0.00								
^{235}U	7.04E+08 Y	^{231}Th	N	0.12		0.22	0.12				1.02		0.84					185.72	57.03	143.76	10.97
^{236}U	2.34E+07 Y	^{232}Th	N	0.12		0.22	0.12											49.46	0.08		
^{237}Np	2.14E+06 Y	^{233}Pa	N		1.00s													29.37	14.12	86.48	12.44
^{238}Pu	87.70 Y	^{234}U	N		0.45s		0.45				1.00		0.00								
^{238}U	4.47E+09 Y	^{234}Th	N	0.12		0.22	0.12				1.00		0.00								
^{239}Pu	2.41E+04 Y	^{235}U	N		0.45s		0.45				1.00		0.00								
^{240}Pu	6.56E+03 Y	^{236}U	N		0.45s		0.45				1.00		0.00								
^{241}Am	4.33E+02 Y	^{237}Np	N		0.45s		0.45				1.00		0.38					59.54	35.90	26.34	2.27
^{241}Pu	14.33 Y	^{241}Am	N		0.45s		0.45					1.00		20.78	100.00						

10.2 Activity connections required to reach a screening level.

The following tables detail the radionuclide activity concentrations (Bq kg^{-1}) that would result in a 10 µGy h^{-1} screening dose rate in each of the indicated reference organism. Concentrations calculated using data from RIFE (Environment Agency et al., 2014). All values are averaged across all sites where soil activity concentrations were available.

	Amphibian				Bird				Large Mammal			
	Max	Min	Average	SD	Max	Min	Average	SD	Max	Min	Average	SD
Ag-110m	1.31E+02	7.58E+01	1.03E+02	3.89E+01	2.24E+02	1.26E+02	1.75E+02	6.97E+01	7.47E+01	3.19E+01	5.33E+01	3.03E+01
Am-241	1.31E+02	1.34E+01	6.92E+01	3.92E+01	7.74E+01	7.41E+00	3.20E+01	2.27E+01	1.54E+01	1.35E+00	6.51E+00	4.99E+00
C-14	3.21E+04	1.24E+04	2.05E+04	8.29E+03	5.50E+04	1.75E+04	3.41E+04	1.56E+04	1.83E+04	5.80E+03	1.05E+04	5.50E+03
Ce-144	1.52E+00	1.52E+00	1.52E+00	-	5.15E+01	5.15E+01	5.15E+01	-	8.56E-01	8.56E-01	8.56E-01	-
Co-60	1.09E+02	2.99E+00	3.23E+01	4.34E+01	1.90E+01	3.85E-01	5.19E+00	7.76E+00	7.20E+01	1.09E+00	1.91E+01	2.97E+01
Cs-134	6.06E+01	8.60E+00	3.58E+01	2.14E+01	1.92E+02	2.01E+01	9.43E+01	6.45E+01	2.99E+02	2.34E+01	1.41E+02	1.06E+02
Cs-137	1.24E+04	5.30E+02	7.06E+03	3.53E+03	2.60E+04	1.66E+03	1.63E+04	7.40E+03	2.81E+04	7.92E+03	2.26E+04	5.80E+03
Eu-155	1.17E+02	2.97E+01	5.51E+01	3.56E+01	3.37E+03	9.47E+02	1.69E+03	9.79E+02	6.67E+01	1.08E+01	2.77E+01	2.23E+01
H-3	1.37E+03	1.02E+02	7.27E+02	5.00E+02	2.05E+03	2.59E+02	1.27E+03	7.22E+02	6.84E+02	1.15E+02	3.88E+02	2.35E+02
I-125	7.45E+02	7.45E+02	7.45E+02	-	1.26E+03	1.26E+03	1.26E+03	-	2.32E+02	2.32E+02	2.32E+02	-
I-129	1.18E+01	1.18E+01	1.18E+01	-	2.81E+01	2.81E+01	2.81E+01	-	6.62E+00	6.62E+00	6.62E+00	-
I-131	5.35E+02	5.35E+02	5.35E+02	-	9.07E+02	9.07E+02	9.07E+02	-	1.67E+02	1.67E+02	1.67E+02	-
Nb-95	1.45E+01	5.18E+00	9.83E+00	6.58E+00	1.02E+02	5.09E+01	7.65E+01	3.63E+01	8.27E+00	2.92E+00	5.59E+00	3.78E+00
Pu-238	1.03E+01	4.12E-01	5.01E+00	4.99E+00	4.26E+00	1.60E-01	2.06E+00	2.07E+00	2.06E+01	2.32E-01	7.63E+00	1.13E+01
Pu-240	1.48E+01	3.37E+00	9.49E+00	5.75E+00	6.02E+00	1.32E+00	3.87E+00	2.38E+00	2.06E+01	1.90E+00	9.85E+00	9.66E+00
Ru-106	6.25E+01	3.95E+01	5.10E+01	1.63E+01	1.60E+02	9.44E+01	1.27E+02	4.65E+01	4.12E+01	2.22E+01	3.17E+01	1.34E+01
S-35	4.45E+02	9.75E+01	2.69E+02	1.52E+02	6.29E+02	1.72E+02	4.26E+02	2.14E+02	2.08E+02	5.13E+01	1.34E+02	7.79E+01
Sb-125	9.41E-01	9.41E-01	9.41E-01	-	2.41E+00	2.41E+00	2.41E+00	-	6.21E-01	6.21E-01	6.21E-01	-
Sr-90	6.50E+03	1.16E+03	2.87E+03	2.09E+03	8.56E+03	2.59E+03	4.38E+03	2.41E+03	3.85E+03	8.27E+02	1.80E+03	1.20E+03
Tc-99	4.60E+03	4.60E+03	4.60E+03	-	8.21E+03	8.21E+03	8.21E+03	-	4.65E+03	4.65E+03	4.65E+03	-
Th-228	3.44E+00	3.44E+00	3.44E+00	-	8.72E+00	8.72E+00	8.72E+00	-	2.39E+00	2.39E+00	2.39E+00	-
Th-230	7.53E-01	7.53E-01	7.53E-01	-	1.91E+00	1.91E+00	1.91E+00	-	5.23E-01	5.23E-01	5.23E-01	-
Th-232	3.01E+00	3.01E+00	3.01E+00	-	7.63E+00	7.63E+00	7.63E+00	-	2.09E+00	2.09E+00	2.09E+00	-
U-234	1.90E+02	1.75E+01	9.17E+01	7.04E+01	1.89E+02	1.03E+01	7.20E+01	7.68E+01	1.92E+02	1.15E+01	7.84E+01	7.59E+01
U-235	1.03E+01	6.34E-01	4.76E+00	3.69E+00	1.00E+01	3.74E-01	3.75E+00	3.94E+00	1.05E+01	4.19E-01	4.22E+00	3.91E+00
U-238	1.80E+02	1.65E+01	9.59E+01	7.12E+01	1.78E+02	9.75E+00	7.89E+01	7.65E+01	1.82E+02	1.09E+01	8.58E+01	7.53E+01
Zr-95	4.21E+01	4.21E+01	4.21E+01	-	7.43E+01	7.43E+01	7.43E+01	-	4.29E-02	4.29E-02	4.29E-02	-

	Small Mammal				Reptile				Annelid			
	Max	Min	Average	SD	Max	Min	Average	SD	Max	Min	Average	SD
Ag-110m	9.56E+01	4.28E+01	6.92E+01	3.73E+01	1.74E+02	9.03E+01	1.32E+02	5.93E+01	1.56E+02	9.42E+01	1.25E+02	4.37E+01
Am-241	1.98E+01	1.65E+00	8.53E+00	6.34E+00	8.09E+01	7.10E+00	4.13E+01	2.59E+01	1.48E+02	5.11E+00	9.13E+01	4.98E+01
C-14	2.35E+04	7.29E+03	1.36E+04	7.00E+03	4.27E+04	1.70E+04	2.68E+04	1.12E+04	1.23E+04	3.03E+03	7.45E+03	3.78E+03
Ce-144	1.05E+00	1.05E+00	1.05E+00	-	1.69E+00	1.69E+00	1.69E+00	-	4.36E-01	4.36E-01	4.36E-01	-
Co-60	9.24E+01	1.53E+00	2.46E+01	3.81E+01	1.42E+02	2.30E+00	4.02E+01	5.72E+01	7.00E+00	3.17E-01	2.31E+00	2.74E+00
Cs-134	3.84E+02	3.29E+01	1.85E+02	1.36E+02	9.90E+01	1.19E+01	5.54E+01	3.61E+01	9.67E+00	9.61E-01	5.58E+00	4.03E+00
Cs-137	3.97E+04	4.07E+03	2.97E+04	1.01E+04	1.56E+04	5.30E+02	1.01E+04	4.39E+03	2.60E+03	2.78E+01	1.25E+03	8.98E+02
Eu-155	8.55E+01	1.52E+01	3.62E+01	2.84E+01	1.56E+02	3.28E+01	6.91E+01	5.10E+01	2.43E+01	1.60E+00	1.05E+01	8.39E+00
H-3	8.75E+02	1.05E+02	4.77E+02	3.27E+02	1.88E+03	8.13E+01	9.32E+02	7.14E+02	1.43E+03	3.03E+01	6.90E+02	6.03E+02
I-125	3.26E+02	3.26E+02	3.26E+02	-	7.48E+02	7.48E+02	7.48E+02	-	3.44E+02	3.44E+02	3.44E+02	-
I-129	8.10E+00	8.10E+00	8.10E+00	-	1.31E+01	1.31E+01	1.31E+01	-	1.32E+00	1.32E+00	1.32E+00	-
I-131	2.34E+02	2.34E+02	2.34E+02	-	5.37E+02	5.37E+02	5.37E+02	-	2.47E+02	2.47E+02	2.47E+02	-
Nb-95	1.06E+01	3.57E+00	7.08E+00	4.96E+00	1.93E+01	5.76E+00	1.25E+01	9.56E+00	6.29E+01	5.43E+00	3.41E+01	4.06E+01
Pu-238	1.06E+01	2.84E-01	4.50E+00	5.41E+00	6.74E+00	3.76E-01	3.59E+00	3.18E+00	6.68E+00	2.59E-01	3.25E+00	3.23E+00
Pu-240	1.06E+01	2.33E+00	7.31E+00	4.39E+00	1.26E+01	3.08E+00	7.47E+00	4.80E+00	9.69E+00	2.13E+00	6.17E+00	3.81E+00
Ru-106	5.29E+01	2.72E+01	4.01E+01	1.82E+01	8.12E+01	4.39E+01	6.26E+01	2.64E+01	2.17E+00	6.05E-01	1.39E+00	1.10E+00
S-35	2.62E+02	6.79E+01	1.72E+02	9.63E+01	6.11E+02	1.31E+02	3.56E+02	2.14E+02	4.00E+02	1.15E+02	2.76E+02	1.24E+02
Sb-125	7.97E-01	7.97E-01	7.97E-01	-	1.22E+00	1.22E+00	1.22E+00	-	8.06E+00	8.06E+00	8.06E+00	-
Sr-90	4.84E+03	1.01E+03	2.31E+03	1.50E+03	2.75E+03	3.99E+02	1.17E+03	9.19E+02	2.50E+02	1.69E+01	1.35E+02	8.28E+01
Tc-99	4.60E+03	4.60E+03	4.60E+03	-	4.84E+03	4.84E+03	4.84E+03	-	7.72E+02	7.72E+02	7.72E+02	-
Th-228	1.23E+00	1.23E+00	1.23E+00	-	1.53E+01	1.53E+01	1.53E+01	-	2.40E+01	2.40E+01	2.40E+01	-
Th-230	2.69E-01	2.69E-01	2.69E-01	-	3.34E+00	3.34E+00	3.34E+00	-	5.26E+00	5.26E+00	5.26E+00	-
Th-232	1.08E+00	1.08E+00	1.08E+00	-	1.34E+01	1.34E+01	1.34E+01	-	2.10E+01	2.10E+01	2.10E+01	-
U-234	1.91E+02	1.48E+01	7.95E+01	7.46E+01	1.91E+02	1.67E+01	9.42E+01	6.95E+01	2.41E+02	4.05E+01	1.51E+02	7.11E+01
U-235	1.04E+01	5.37E-01	4.14E+00	3.84E+00	1.03E+01	7.81E-01	4.81E+00	3.65E+00	1.09E+01	2.55E+00	7.48E+00	3.29E+00
U-238	1.80E+02	1.40E+01	8.54E+01	7.48E+01	1.80E+02	1.90E+01	9.61E+01	7.16E+01	1.84E+02	4.60E+01	1.33E+02	6.06E+01
Zr-95	5.67E-02	5.67E-02	5.67E-02	-	5.68E+01	5.68E+01	5.68E+01	-	3.61E+00	3.61E+00	3.61E+00	-

	Arthropod				Flying Insect				Mollusc			
	Max	Min	Average	SD	Max	Min	Average	SD	Max	Min	Average	SD
Ag-110m	7.49E+00	4.04E+00	5.76E+00	2.44E+00	1.15E+01	7.50E+00	9.52E+00	2.86E+00	1.72E+02	1.00E+02	1.36E+02	5.09E+01
Am-241	1.06E+02	7.46E+00	6.45E+01	3.77E+01	1.57E+02	8.72E+00	1.05E+02	5.29E+01	1.33E+02	4.08E+00	8.03E+01	4.50E+01
C-14	1.48E+04	5.43E+03	9.19E+03	3.98E+03	2.28E+04	7.58E+03	1.46E+04	6.28E+03	1.35E+04	3.04E+03	8.08E+03	4.29E+03
Ce-144	5.01E-01	5.01E-01	5.01E-01	-	5.86E-01	5.86E-01	5.86E-01	-	6.11E+00	6.11E+00	6.11E+00	-
Co-60	4.39E+00	1.30E-01	1.30E+00	1.75E+00	6.11E+00	2.57E-01	1.97E+00	2.39E+00	7.54E+00	3.38E-01	2.47E+00	2.96E+00
Cs-134	1.52E+01	2.33E+00	9.62E+00	6.37E+00	2.44E+01	3.80E+00	1.55E+01	1.04E+01	5.34E+00	4.73E-01	3.00E+00	2.20E+00
Cs-137	3.28E+03	5.98E+01	1.90E+03	1.02E+03	7.85E+03	7.77E+01	3.57E+03	2.59E+03	1.32E+03	1.24E+01	6.51E+02	4.66E+02
Eu-155	1.02E+01	1.45E+00	4.38E+00	3.46E+00	1.58E+01	1.69E+00	7.19E+00	5.17E+00	2.68E+01	1.58E+00	1.14E+01	9.35E+00
H-3	1.87E+03	4.98E+01	9.38E+02	7.77E+02	2.65E+03	6.47E+01	1.43E+03	1.18E+03	1.57E+03	2.70E+01	7.35E+02	6.60E+02
I-125	6.40E+02	6.40E+02	6.40E+02	-	1.52E+03	1.52E+03	1.52E+03	-	4.03E+02	4.03E+02	4.03E+02	-
I-129	6.61E+00	6.61E+00	6.61E+00	-	7.72E+00	7.72E+00	7.72E+00	-	1.50E+00	1.50E+00	1.50E+00	-
I-131	4.59E+02	4.59E+02	4.59E+02	-	1.09E+03	1.09E+03	1.09E+03	-	2.90E+02	2.90E+02	2.90E+02	-
Nb-95	4.74E-01	8.79E-02	2.81E-01	2.73E-01	7.30E-01	1.03E-01	4.16E-01	4.44E-01	6.92E+01	5.34E+00	3.73E+01	4.52E+01
Pu-238	9.21E+00	5.63E-01	5.14E+00	4.35E+00	1.20E+01	6.58E-01	6.50E+00	5.67E+00	2.34E+01	1.00E+00	1.14E+01	1.13E+01
Pu-240	1.94E+01	4.62E+00	1.11E+01	7.57E+00	2.36E+01	5.39E+00	1.37E+01	9.24E+00	3.43E+01	8.20E+00	2.20E+01	1.31E+01
Ru-106	3.60E+00	1.57E+00	2.58E+00	1.44E+00	5.02E+00	1.83E+00	3.42E+00	2.25E+00	2.33E+00	5.95E-01	1.46E+00	1.23E+00
S-35	6.08E+02	1.38E+02	3.74E+02	2.11E+02	8.49E+02	2.15E+02	5.75E+02	2.82E+02	4.41E+02	1.27E+02	2.93E+02	1.32E+02
Sb-125	3.28E+00	3.28E+00	3.28E+00	-	4.56E+00	4.56E+00	4.56E+00	-	8.67E+00	8.67E+00	8.67E+00	-
Sr-90	2.31E+03	2.25E+02	9.97E+02	7.83E+02	3.23E+03	2.63E+02	1.50E+03	1.07E+03	3.48E+02	2.31E+01	1.98E+02	1.17E+02
Tc-99	2.47E+03	2.47E+03	2.47E+03	-	2.48E+03	2.48E+03	2.48E+03	-	7.72E+00	7.72E+00	7.72E+00	-
Th-228	2.19E+01	2.19E+01	2.19E+01	-	2.84E+01	2.84E+01	2.84E+01	-	2.14E+01	2.14E+01	2.14E+01	-
Th-230	4.78E+00	4.78E+00	4.78E+00	-	6.21E+00	6.21E+00	6.21E+00	-	4.69E+00	4.69E+00	4.69E+00	-
Th-232	1.91E+01	1.91E+01	1.91E+01	-	2.49E+01	2.49E+01	2.49E+01	-	1.88E+01	1.88E+01	1.88E+01	-
U-234	1.92E+02	2.05E+01	1.16E+02	6.66E+01	1.92E+02	2.66E+01	1.34E+02	6.82E+01	2.42E+02	3.61E+01	1.49E+02	7.13E+01
U-235	1.06E+01	1.31E+00	5.83E+00	3.48E+00	1.06E+01	1.82E+00	6.65E+00	3.44E+00	1.07E+01	2.75E+00	7.28E+00	3.16E+00
U-238	1.82E+02	2.33E+01	1.11E+02	6.90E+01	1.82E+02	3.03E+01	1.22E+02	6.68E+01	1.84E+02	4.10E+01	1.30E+02	5.98E+01
Zr-95	3.48E+00	3.48E+00	3.48E+00	-	5.41E+00	5.41E+00	5.41E+00	-	3.99E+00	3.99E+00	3.99E+00	-

	Rabbit (soil data only)				Rabbit (soil and rabbit data)			
	Max	Min	Average	SD	Max	Min	Average	SD
Ag-110m	9.56E+01	4.28E+01	6.92E+01	3.73E+01	1.45E+02	8.29E+01	1.14E+02	4.37E+01
Am-241	1.21E+01	1.65E+00	6.22E+00	5.36E+00	1.99E+02	1.68E-01	1.05E+02	9.05E+01
C-14	2.35E+04	1.05E+04	1.70E+04	9.16E+03	5.64E+04	2.75E+04	4.19E+04	2.04E+04
Ce-144	1.05E+00	1.05E+00	1.05E+00	-	1.30E+02	1.30E+02	1.30E+02	-
Co-60	1.16E+01	1.08E+01	1.12E+01	5.74E-01	1.01E+02	2.82E+01	6.47E+01	5.17E+01
Cs-134	9.69E+01	9.69E+01	9.69E+01	-	2.82E+01	2.82E+01	2.82E+01	-
Cs-137	3.36E+04	2.21E+04	2.78E+04	4.70E+03	4.63E+02	8.29E+01	2.59E+02	1.56E+02
Eu-155	8.55E+01	2.18E+01	4.31E+01	3.67E+01	5.61E+01	2.79E+01	3.82E+01	1.56E+01
H-3	8.75E+02	1.40E+02	4.20E+02	3.20E+02	8.29E+03	2.82E+03	6.48E+03	2.48E+03
I-129	8.10E+00	8.10E+00	8.10E+00	-	2.82E+01	2.82E+01	2.82E+01	-
Nb-95	1.06E+01	3.57E+00	7.08E+00	4.96E+00	1.16E+02	2.82E+01	7.21E+01	6.21E+01
Pu-238	2.62E+00	2.84E-01	1.45E+00	1.65E+00	3.95E-01	1.23E-01	2.59E-01	1.92E-01
Pu-240	9.00E+00	2.33E+00	5.66E+00	4.72E+00	3.24E+00	8.05E-02	1.66E+00	2.23E+00
Ru-106	2.72E+01	2.72E+01	2.72E+01	-	2.09E+02	2.09E+02	2.09E+02	-
S-35	2.45E+02	1.12E+02	1.79E+02	9.39E+01	1.59E+03	9.95E+02	1.29E+03	4.22E+02
Sr-90	2.14E+03	1.01E+03	1.52E+03	5.76E+02	2.31E+02	5.64E+01	1.51E+02	8.85E+01
U-234	6.65E+01	5.07E+01	5.86E+01	1.12E+01	9.25E+01	3.08E+01	6.17E+01	4.37E+01
U-235	3.59E+00	2.66E+00	3.12E+00	6.55E-01	3.70E+00	1.78E+00	2.74E+00	1.36E+00
U-238	6.21E+01	5.20E+01	5.70E+01	7.13E+00	8.64E+01	2.04E+01	5.34E+01	4.67E+01

10.3 Allowable shield thicknesses for a range of scintillator sizes

Depth (cm)	Width (cm)	length (cm)													
		2	3	4	5	6	7	8	9	10	11	12	13	14	15
1.5	1.5	4.97	4.81	4.66	4.52	4.39	4.26	4.14	4.03	3.92	3.82	3.72	3.63	3.54	3.46
	2.0	4.89	4.73	4.58	4.43	4.30	4.17	4.05	3.94	3.83	3.73	3.63	3.54	3.45	3.37
	2.5	4.81	4.65	4.49	4.35	4.22	4.09	3.97	3.85	3.75	3.64	3.55	3.45	3.37	3.28
	3.0	4.73	4.57	4.41	4.27	4.14	4.01	3.89	3.77	3.66	3.56	3.47	3.37	3.29	3.20
	3.5	4.65	4.49	4.34	4.19	4.06	3.93	3.81	3.69	3.59	3.48	3.39	3.29	3.21	3.12
	4.0	4.58	4.41	4.26	4.12	3.98	3.85	3.73	3.62	3.51	3.41	3.31	3.22	3.13	3.05
	4.5	4.50	4.34	4.19	4.04	3.91	3.78	3.66	3.54	3.44	3.33	3.24	3.15	3.06	2.98
	5.0	4.43	4.27	4.12	3.97	3.84	3.71	3.59	3.47	3.36	3.26	3.17	3.08	2.99	2.91
	5.5	4.37	4.20	4.05	3.90	3.77	3.64	3.52	3.40	3.30	3.19	3.10	3.01	2.92	2.84
2.0	1.5	4.82	4.66	4.51	4.37	4.23	4.10	3.98	3.87	3.76	3.66	3.56	3.47	3.38	3.29
	2.0	4.74	4.58	4.42	4.28	4.15	4.02	3.90	3.78	3.67	3.57	3.47	3.38	3.29	3.21
	2.5	4.66	4.49	4.34	4.20	4.06	3.93	3.81	3.70	3.59	3.49	3.39	3.30	3.21	3.13
	3.0	4.58	4.41	4.26	4.12	3.98	3.85	3.73	3.62	3.51	3.41	3.31	3.22	3.13	3.05
	3.5	4.50	4.34	4.18	4.04	3.90	3.78	3.65	3.54	3.43	3.33	3.23	3.14	3.06	2.97
	4.0	4.42	4.26	4.11	3.96	3.83	3.70	3.58	3.46	3.36	3.26	3.16	3.07	2.98	2.90
	4.5	4.35	4.19	4.03	3.89	3.75	3.63	3.51	3.39	3.29	3.18	3.09	3.00	2.91	2.83
	5.0	4.28	4.12	3.96	3.82	3.68	3.56	3.44	3.32	3.22	3.11	3.02	2.93	2.84	2.76
	5.5	4.21	4.05	3.89	3.75	3.61	3.49	3.37	3.25	3.15	3.05	2.95	2.86	2.78	2.70
2.5	1.5	4.68	4.52	4.37	4.22	4.08	3.96	3.83	3.72	3.61	3.51	3.41	3.32	3.23	3.14
	2.0	4.60	4.43	4.28	4.14	4.00	3.87	3.75	3.63	3.52	3.42	3.32	3.23	3.14	3.06
	2.5	4.51	4.35	4.20	4.05	3.92	3.79	3.67	3.55	3.44	3.34	3.24	3.15	3.07	2.98
	3.0	4.43	4.27	4.12	3.97	3.84	3.71	3.59	3.47	3.36	3.26	3.17	3.07	2.99	2.91
	3.5	4.36	4.19	4.04	3.89	3.76	3.63	3.51	3.40	3.29	3.19	3.09	3.00	2.91	2.83
	4.0	4.28	4.12	3.96	3.82	3.68	3.56	3.44	3.32	3.22	3.11	3.02	2.93	2.84	2.76
	4.5	4.21	4.04	3.89	3.75	3.61	3.48	3.36	3.25	3.14	3.04	2.95	2.86	2.78	2.70
	5.0	4.14	3.97	3.82	3.68	3.54	3.41	3.29	3.18	3.08	2.98	2.88	2.79	2.71	2.63
	5.5	4.07	3.90	3.75	3.61	3.47	3.35	3.23	3.12	3.01	2.91	2.82	2.73	2.65	2.57
3.0	1.5	4.55	4.39	4.23	4.08	3.95	3.82	3.69	3.58	3.47	3.37	3.27	3.17	3.09	3.00
	2.0	4.46	4.30	4.15	4.00	3.86	3.73	3.61	3.49	3.39	3.28	3.19	3.09	3.01	2.92
	2.5	4.38	4.22	4.06	3.92	3.78	3.65	3.53	3.41	3.31	3.20	3.11	3.02	2.93	2.85
	3.0	4.30	4.14	3.98	3.84	3.70	3.57	3.45	3.34	3.23	3.13	3.03	2.94	2.86	2.77
	3.5	4.22	4.06	3.90	3.76	3.62	3.49	3.37	3.26	3.15	3.05	2.96	2.87	2.78	2.70
	4.0	4.15	3.98	3.83	3.68	3.55	3.42	3.30	3.19	3.08	2.98	2.89	2.80	2.72	2.64
	4.5	4.07	3.91	3.75	3.61	3.48	3.35	3.23	3.12	3.01	2.91	2.82	2.73	2.65	2.57
	5.0	4.00	3.84	3.68	3.54	3.41	3.28	3.16	3.05	2.95	2.85	2.76	2.67	2.59	2.51
	5.5	3.93	3.77	3.61	3.47	3.34	3.21	3.10	2.99	2.88	2.78	2.69	2.61	2.52	2.45
3.5	1.5	4.43	4.26	4.10	3.96	3.82	3.69	3.56	3.45	3.34	3.23	3.14	3.04	2.96	2.87
	2.0	4.34	4.17	4.02	3.87	3.73	3.60	3.48	3.36	3.26	3.15	3.06	2.96	2.88	2.80
	2.5	4.25	4.09	3.93	3.79	3.65	3.52	3.40	3.29	3.18	3.08	2.98	2.89	2.80	2.72
	3.0	4.17	4.01	3.85	3.71	3.57	3.44	3.32	3.21	3.10	3.00	2.91	2.82	2.73	2.65
	3.5	4.09	3.93	3.78	3.63	3.49	3.37	3.25	3.13	3.03	2.93	2.83	2.75	2.66	2.58
	4.0	4.02	3.85	3.70	3.56	3.42	3.29	3.18	3.06	2.96	2.86	2.77	2.68	2.60	2.52
	4.5	3.94	3.78	3.63	3.48	3.35	3.22	3.11	2.99	2.89	2.79	2.70	2.61	2.53	2.45
	5.0	3.87	3.71	3.56	3.41	3.28	3.16	3.04	2.93	2.83	2.73	2.64	2.55	2.47	2.39
	5.5	3.80	3.64	3.49	3.35	3.21	3.09	2.97	2.86	2.76	2.67	2.58	2.49	2.41	2.34

Maximum thickness of lead to keep overall shield weight below 10 kg. Each thickness displayed results from the specific scintillator length, width and depth. All shield thicknesses are in cm.

10.4 Tables of ϕ_{ratio} for modelled organisms

Depth (cm)	Width (cm)	2	3	4	5	6	7	8	9	10	11	12	13	14	15
								length (cm)							
1.5	1.5	48.95	55.19	58.61	60.44	61.32	61.27	60.91	53.71	47.64	42.71	38.45	34.94	31.84	29.27
	2.0	54.40	61.15	64.82	66.34	67.24	67.14	66.71	58.80	52.12	46.72	42.05	38.20	34.81	31.99
	2.5	58.33	65.42	68.83	70.81	71.73	71.58	71.09	62.25	55.52	49.44	44.77	40.41	37.05	33.84
	3.0	61.15	68.47	71.96	73.98	74.90	74.71	74.19	64.94	57.55	51.56	46.68	42.13	38.62	35.27
	3.5	63.12	70.58	74.58	76.16	77.08	76.86	76.30	66.78	59.54	53.01	47.98	43.30	39.69	36.25
	4.0	64.82	71.96	75.99	78.05	78.47	78.23	77.65	68.37	60.57	54.26	48.80	44.32	40.37	37.09
	4.5	58.31	65.07	68.68	70.08	70.88	70.65	70.11	61.34	54.68	48.67	44.05	40.00	36.43	33.47
	5.0	53.07	59.19	62.44	63.69	64.40	64.18	63.69	55.72	49.35	44.20	40.00	36.32	33.08	30.39
	5.5	48.83	54.09	57.04	58.17	58.81	58.60	58.14	50.86	45.32	40.34	36.50	33.15	30.19	27.73
2.0	1.5	50.87	57.16	60.58	62.37	62.83	62.73	62.32	54.93	48.69	43.65	39.28	35.68	32.51	29.70
	2.0	56.41	63.22	66.49	68.39	69.26	69.10	68.63	60.08	53.25	47.72	42.93	39.00	35.53	32.65
	2.5	60.38	67.14	70.97	72.94	73.37	73.17	72.65	63.98	56.69	50.79	45.69	41.50	37.80	34.74
	3.0	63.22	70.20	74.14	76.16	76.58	76.35	75.78	66.73	59.12	52.96	47.63	43.26	39.40	36.20
	3.5	65.20	72.76	76.32	78.36	78.77	79.00	77.91	68.60	60.76	54.43	48.95	44.45	40.74	37.20
	4.0	66.49	74.14	78.21	79.78	80.67	80.39	79.76	69.78	62.19	55.70	50.10	45.49	41.43	38.06
	4.5	60.14	67.01	70.22	72.05	72.39	72.58	72.00	62.99	56.13	49.96	45.21	41.05	37.38	34.35
	5.0	54.71	60.93	63.82	65.47	65.76	65.93	65.40	57.20	50.98	45.37	41.05	37.27	33.94	31.18
	5.5	50.01	55.66	58.28	59.78	60.03	60.18	59.69	52.21	46.52	41.66	37.46	34.01	31.17	28.63
2.5	1.5	51.06	57.25	60.59	61.94	62.35	62.60	61.78	54.43	48.24	43.23	38.90	35.33	32.19	29.40
	2.0	56.54	62.86	66.44	68.28	68.68	68.50	68.00	59.52	52.73	47.25	42.50	38.60	35.16	32.31
	2.5	60.09	67.11	70.87	72.34	73.18	72.96	72.41	63.36	56.13	50.28	45.22	41.07	37.64	34.37
	3.0	62.86	70.13	74.00	75.50	76.35	76.10	75.51	66.07	58.52	52.41	47.43	42.81	39.23	36.05
	3.5	65.18	72.20	76.15	77.66	78.51	78.24	77.62	68.33	60.52	54.20	48.74	44.26	40.31	37.03
	4.0	66.44	74.00	77.52	79.53	79.89	80.09	79.45	69.50	61.94	55.12	49.88	45.29	41.24	37.89
	4.5	60.07	66.45	70.02	71.81	72.13	71.85	71.27	62.73	55.54	49.74	45.01	40.87	37.45	34.40
	5.0	54.62	60.40	63.62	65.24	65.51	65.26	64.72	56.96	50.75	45.45	40.87	37.10	34.00	31.23
	5.5	49.91	55.16	58.09	59.56	59.80	59.94	59.44	52.31	46.32	41.47	37.52	34.07	31.22	28.68
3.0	1.5	51.03	57.11	60.01	61.30	62.05	61.89	61.06	53.79	47.66	42.70	38.41	34.67	31.78	29.02
	2.0	56.09	62.65	66.16	67.53	67.90	67.69	67.18	58.79	52.41	46.65	42.22	38.11	34.93	31.89
	2.5	59.93	66.85	70.10	71.96	72.32	72.07	71.52	62.57	55.77	49.64	44.92	40.79	37.15	34.14
	3.0	62.65	69.82	73.17	75.08	75.43	75.16	74.57	65.64	58.13	52.06	46.82	42.51	38.96	35.57
	3.5	64.53	71.86	75.27	77.21	77.55	77.26	76.64	67.45	59.73	53.50	48.41	43.95	40.02	36.77
	4.0	66.16	73.17	77.09	78.56	79.39	79.08	78.44	69.03	61.13	54.74	49.53	44.97	41.21	37.86
	4.5	59.43	66.09	69.18	70.93	71.67	71.38	70.79	62.30	55.16	49.40	44.69	40.58	37.18	34.16
	5.0	54.03	60.06	62.85	64.43	65.09	64.82	64.28	56.57	50.40	45.13	40.83	37.07	33.97	31.21
	5.5	49.35	54.85	57.38	58.81	59.41	59.16	59.03	51.95	45.99	41.18	37.26	34.04	30.99	28.65
3.5	1.5	50.22	55.79	58.57	60.17	60.50	60.33	59.51	52.40	46.43	41.33	37.41	33.76	30.95	28.26
	2.0	55.15	61.16	64.54	65.85	66.18	65.96	65.45	57.26	51.04	45.43	41.12	37.10	34.01	31.24
	2.5	58.53	65.23	68.35	70.14	70.47	70.22	69.66	61.32	54.31	48.64	43.74	39.72	36.17	33.23
	3.0	61.16	68.10	71.33	73.16	73.49	73.21	72.62	63.92	56.60	50.69	45.87	41.65	37.93	34.84
	3.5	62.97	70.07	73.82	75.22	75.54	75.72	75.10	65.68	58.53	52.41	47.12	43.06	39.21	36.02
	4.0	64.54	71.33	75.12	77.01	77.33	77.01	76.86	67.21	59.89	53.63	48.52	44.05	40.37	37.08
	4.5	57.95	64.42	67.82	69.09	69.80	69.51	69.36	60.65	54.04	48.39	43.78	39.75	36.42	33.46
	5.0	52.68	58.53	61.61	62.75	63.39	63.51	62.98	55.42	49.37	44.21	40.00	36.31	33.27	30.56
	5.5	48.11	53.44	56.24	57.64	57.85	57.96	57.47	50.57	45.05	40.59	36.72	33.34	30.55	28.24

Table shows ϕ_{ratio} for vole calculated for each scintillator length, width and depth. Results are grouped by depth.

Depth (cm)	Width (cm)	length (cm)													
		2	3	4	5	6	7	8	9	10	11	12	13	14	15
1.5	1.5	0.14	0.16	0.17	0.16	0.13	0.11	0.10	0.09	0.08	0.07	0.06	0.06	0.05	0.05
	2.0	0.16	0.18	0.19	0.17	0.15	0.13	0.11	0.10	0.09	0.08	0.07	0.06	0.06	0.05
	2.5	0.17	0.19	0.20	0.19	0.16	0.13	0.12	0.10	0.09	0.08	0.07	0.07	0.06	0.06
	3.0	0.18	0.20	0.21	0.19	0.16	0.14	0.12	0.11	0.09	0.08	0.08	0.07	0.06	0.06
	3.5	0.16	0.18	0.19	0.17	0.14	0.12	0.11	0.09	0.08	0.07	0.07	0.06	0.06	0.05
	4.0	0.14	0.16	0.17	0.15	0.13	0.11	0.10	0.08	0.07	0.07	0.06	0.05	0.05	0.05
	4.5	0.13	0.14	0.15	0.14	0.12	0.10	0.09	0.08	0.07	0.06	0.05	0.05	0.04	0.04
	5.0	0.12	0.13	0.14	0.13	0.11	0.09	0.08	0.07	0.06	0.05	0.05	0.04	0.04	0.04
	5.5	0.11	0.12	0.12	0.11	0.10	0.08	0.07	0.06	0.06	0.05	0.04	0.04	0.04	0.03
2.0	1.5	0.15	0.17	0.18	0.16	0.14	0.12	0.10	0.09	0.08	0.07	0.06	0.06	0.05	0.05
	2.0	0.16	0.18	0.19	0.18	0.15	0.13	0.11	0.10	0.09	0.08	0.07	0.06	0.06	0.05
	2.5	0.18	0.20	0.21	0.19	0.16	0.14	0.12	0.10	0.09	0.08	0.07	0.07	0.06	0.06
	3.0	0.18	0.20	0.22	0.20	0.17	0.14	0.12	0.11	0.10	0.09	0.08	0.07	0.06	0.06
	3.5	0.16	0.18	0.19	0.18	0.15	0.13	0.11	0.10	0.09	0.08	0.07	0.06	0.06	0.05
	4.0	0.15	0.16	0.17	0.16	0.13	0.11	0.10	0.09	0.08	0.07	0.06	0.06	0.05	0.05
	4.5	0.13	0.15	0.15	0.14	0.12	0.10	0.09	0.08	0.07	0.06	0.06	0.05	0.05	0.04
	5.0	0.12	0.13	0.14	0.13	0.11	0.09	0.08	0.07	0.06	0.06	0.05	0.05	0.04	0.04
	5.5	0.11	0.12	0.13	0.12	0.10	0.08	0.07	0.06	0.06	0.05	0.05	0.04	0.04	0.04
2.5	1.5	0.15	0.17	0.18	0.16	0.14	0.12	0.10	0.09	0.08	0.07	0.06	0.06	0.05	0.05
	2.0	0.16	0.18	0.19	0.18	0.15	0.13	0.11	0.10	0.09	0.08	0.07	0.06	0.06	0.05
	2.5	0.17	0.20	0.21	0.19	0.16	0.14	0.12	0.10	0.09	0.08	0.07	0.07	0.06	0.06
	3.0	0.18	0.20	0.22	0.20	0.17	0.14	0.12	0.11	0.10	0.09	0.08	0.07	0.06	0.06
	3.5	0.16	0.18	0.19	0.17	0.15	0.13	0.11	0.10	0.08	0.08	0.07	0.06	0.06	0.05
	4.0	0.14	0.16	0.17	0.16	0.13	0.11	0.10	0.09	0.08	0.07	0.06	0.06	0.05	0.05
	4.5	0.13	0.15	0.15	0.14	0.12	0.10	0.09	0.08	0.07	0.06	0.06	0.05	0.05	0.04
	5.0	0.12	0.13	0.14	0.13	0.11	0.09	0.08	0.07	0.06	0.06	0.05	0.05	0.04	0.04
	5.5	0.11	0.12	0.13	0.12	0.10	0.08	0.07	0.06	0.06	0.05	0.05	0.04	0.04	0.04
3.0	1.5	0.15	0.17	0.17	0.16	0.14	0.12	0.10	0.09	0.08	0.07	0.06	0.06	0.05	0.05
	2.0	0.16	0.18	0.19	0.18	0.15	0.13	0.11	0.10	0.09	0.08	0.07	0.06	0.06	0.05
	2.5	0.17	0.19	0.20	0.19	0.16	0.13	0.12	0.10	0.09	0.08	0.07	0.07	0.06	0.06
	3.0	0.18	0.20	0.21	0.20	0.16	0.14	0.12	0.11	0.10	0.09	0.08	0.07	0.06	0.06
	3.5	0.16	0.18	0.19	0.17	0.15	0.12	0.11	0.09	0.08	0.08	0.07	0.06	0.06	0.05
	4.0	0.14	0.16	0.17	0.15	0.13	0.11	0.10	0.08	0.08	0.07	0.06	0.06	0.05	0.05
	4.5	0.13	0.14	0.15	0.14	0.12	0.10	0.09	0.08	0.07	0.06	0.05	0.05	0.05	0.04
	5.0	0.12	0.13	0.14	0.13	0.11	0.09	0.08	0.07	0.06	0.06	0.05	0.05	0.04	0.04
	5.5	0.11	0.12	0.13	0.12	0.10	0.08	0.07	0.06	0.06	0.05	0.05	0.04	0.04	0.04
3.5	1.5	0.15	0.16	0.17	0.16	0.13	0.11	0.10	0.09	0.08	0.07	0.06	0.06	0.05	0.05
	2.0	0.16	0.18	0.19	0.17	0.14	0.12	0.11	0.09	0.08	0.07	0.07	0.06	0.06	0.05
	2.5	0.17	0.19	0.20	0.18	0.15	0.13	0.11	0.10	0.09	0.08	0.07	0.07	0.06	0.05
	3.0	0.18	0.20	0.21	0.19	0.16	0.14	0.12	0.10	0.09	0.08	0.08	0.07	0.06	0.06
	3.5	0.16	0.17	0.18	0.17	0.14	0.12	0.11	0.09	0.08	0.07	0.07	0.06	0.06	0.05
	4.0	0.14	0.16	0.16	0.15	0.13	0.11	0.09	0.08	0.07	0.07	0.06	0.05	0.05	0.05
	4.5	0.13	0.14	0.15	0.14	0.11	0.10	0.09	0.07	0.07	0.06	0.05	0.05	0.04	0.04
	5.0	0.11	0.13	0.13	0.12	0.10	0.09	0.08	0.07	0.06	0.05	0.05	0.04	0.04	0.04
	5.5	0.10	0.12	0.12	0.11	0.09	0.08	0.07	0.06	0.06	0.05	0.05	0.04	0.04	0.03

Table shows ϕ_{ratio} for small bat calculated for each scintillator length, width and depth. Results are grouped by depth.

| Depth (cm)	Width (cm)	length (cm)													
		2	3	4	5	6	7	8	9	10	11	12	13	14	15
1.5	1.5	0.29	0.33	0.35	0.36	0.37	0.37	0.32	0.28	0.25	0.22	0.20	0.18	0.17	0.15
	2.0	0.33	0.37	0.39	0.40	0.40	0.40	0.35	0.31	0.27	0.25	0.22	0.20	0.18	0.17
	2.5	0.35	0.39	0.41	0.43	0.43	0.43	0.37	0.33	0.29	0.26	0.24	0.21	0.20	0.18
	3.0	0.37	0.41	0.43	0.45	0.45	0.45	0.39	0.34	0.30	0.27	0.25	0.22	0.20	0.19
	3.5	0.38	0.42	0.45	0.46	0.46	0.46	0.40	0.35	0.31	0.28	0.25	0.23	0.21	0.19
	4.0	0.39	0.43	0.46	0.47	0.47	0.47	0.41	0.36	0.32	0.29	0.26	0.23	0.21	0.20
	4.5	0.35	0.39	0.41	0.42	0.43	0.43	0.37	0.32	0.29	0.26	0.23	0.21	0.19	0.18
	5.0	0.32	0.36	0.38	0.38	0.39	0.39	0.34	0.29	0.26	0.23	0.21	0.19	0.17	0.16
	5.5	0.29	0.33	0.34	0.35	0.35	0.35	0.31	0.27	0.24	0.21	0.19	0.17	0.16	0.15
2.0	1.5	0.31	0.34	0.36	0.38	0.38	0.38	0.33	0.29	0.26	0.23	0.21	0.19	0.17	0.16
	2.0	0.34	0.38	0.40	0.41	0.42	0.42	0.36	0.32	0.28	0.25	0.23	0.21	0.19	0.17
	2.5	0.36	0.40	0.43	0.44	0.44	0.44	0.38	0.34	0.30	0.27	0.24	0.22	0.20	0.18
	3.0	0.38	0.42	0.45	0.46	0.46	0.46	0.40	0.35	0.31	0.28	0.25	0.23	0.21	0.19
	3.5	0.39	0.44	0.46	0.47	0.47	0.48	0.41	0.36	0.32	0.29	0.26	0.23	0.21	0.20
	4.0	0.40	0.45	0.47	0.48	0.49	0.48	0.42	0.37	0.33	0.29	0.26	0.24	0.22	0.20
	4.5	0.36	0.40	0.42	0.43	0.44	0.44	0.38	0.33	0.30	0.26	0.24	0.22	0.20	0.18
	5.0	0.33	0.37	0.38	0.39	0.40	0.40	0.34	0.30	0.27	0.24	0.22	0.20	0.18	0.16
	5.5	0.30	0.33	0.35	0.36	0.36	0.36	0.31	0.27	0.24	0.22	0.20	0.18	0.16	0.15
2.5	1.5	0.31	0.34	0.36	0.37	0.38	0.38	0.33	0.29	0.25	0.23	0.20	0.19	0.17	0.15
	2.0	0.34	0.38	0.40	0.41	0.41	0.41	0.36	0.31	0.28	0.25	0.22	0.20	0.19	0.17
	2.5	0.36	0.40	0.43	0.44	0.44	0.44	0.38	0.33	0.30	0.26	0.24	0.22	0.20	0.18
	3.0	0.38	0.42	0.45	0.45	0.46	0.46	0.40	0.35	0.31	0.28	0.25	0.23	0.21	0.19
	3.5	0.39	0.43	0.46	0.47	0.47	0.47	0.41	0.36	0.32	0.29	0.26	0.23	0.21	0.19
	4.0	0.40	0.45	0.47	0.48	0.48	0.48	0.42	0.37	0.33	0.29	0.26	0.24	0.22	0.20
	4.5	0.36	0.40	0.42	0.43	0.43	0.43	0.38	0.33	0.29	0.26	0.24	0.22	0.20	0.18
	5.0	0.33	0.36	0.38	0.39	0.39	0.39	0.34	0.30	0.27	0.24	0.22	0.20	0.18	0.16
	5.5	0.30	0.33	0.35	0.36	0.36	0.36	0.31	0.28	0.24	0.22	0.20	0.18	0.16	0.15
3.0	1.5	0.31	0.34	0.36	0.37	0.37	0.37	0.32	0.28	0.25	0.22	0.20	0.18	0.17	0.15
	2.0	0.34	0.38	0.40	0.41	0.41	0.41	0.35	0.31	0.28	0.25	0.22	0.20	0.18	0.17
	2.5	0.36	0.40	0.42	0.43	0.44	0.43	0.38	0.33	0.29	0.26	0.24	0.21	0.20	0.18
	3.0	0.38	0.42	0.44	0.45	0.45	0.45	0.39	0.35	0.31	0.27	0.25	0.22	0.21	0.19
	3.5	0.39	0.43	0.45	0.46	0.47	0.46	0.40	0.36	0.31	0.28	0.25	0.23	0.21	0.19
	4.0	0.40	0.44	0.46	0.47	0.48	0.48	0.41	0.36	0.32	0.29	0.26	0.24	0.22	0.20
	4.5	0.36	0.40	0.42	0.43	0.43	0.43	0.37	0.33	0.29	0.26	0.24	0.21	0.20	0.18
	5.0	0.33	0.36	0.38	0.39	0.39	0.39	0.34	0.30	0.27	0.24	0.21	0.20	0.18	0.16
	5.5	0.30	0.33	0.35	0.35	0.36	0.36	0.31	0.27	0.24	0.22	0.20	0.18	0.16	0.15
3.5	1.5	0.30	0.34	0.35	0.36	0.36	0.36	0.31	0.28	0.24	0.22	0.20	0.18	0.16	0.15
	2.0	0.33	0.37	0.39	0.40	0.40	0.40	0.34	0.30	0.27	0.24	0.22	0.20	0.18	0.16
	2.5	0.35	0.39	0.41	0.42	0.42	0.42	0.37	0.32	0.29	0.26	0.23	0.21	0.19	0.17
	3.0	0.37	0.41	0.43	0.44	0.44	0.44	0.38	0.34	0.30	0.27	0.24	0.22	0.20	0.18
	3.5	0.38	0.42	0.44	0.45	0.45	0.46	0.40	0.35	0.31	0.28	0.25	0.23	0.21	0.19
	4.0	0.39	0.43	0.45	0.46	0.47	0.46	0.40	0.35	0.32	0.28	0.26	0.23	0.21	0.20
	4.5	0.35	0.39	0.41	0.42	0.42	0.42	0.37	0.32	0.28	0.25	0.23	0.21	0.19	0.18
	5.0	0.32	0.35	0.37	0.38	0.38	0.38	0.33	0.29	0.26	0.23	0.21	0.19	0.18	0.16
	5.5	0.29	0.32	0.34	0.35	0.35	0.35	0.30	0.27	0.24	0.21	0.19	0.18	0.16	0.15

Table shows ϕ_{ratio} for large bat calculated for each scintillator length, width and depth. Results are grouped by depth.

Depth (cm)	Width (cm)	length (cm)													
		2	3	4	5	6	7	8	9	10	11	12	13	14	15
1.5	1.5	2.41	2.72	2.89	2.98	3.02	3.02	3.00	2.64	2.35	2.10	1.89	1.72	1.57	1.44
	2.0	2.68	3.01	3.19	3.27	3.31	3.31	3.28	2.89	2.57	2.30	2.07	1.88	1.71	1.58
	2.5	2.87	3.22	3.39	3.49	3.53	3.52	3.50	3.06	2.73	2.43	2.20	1.99	1.82	1.67
	3.0	3.01	3.37	3.54	3.64	3.69	3.68	3.65	3.20	2.83	2.54	2.30	2.07	1.90	1.74
	3.5	3.11	3.47	3.67	3.75	3.79	3.78	3.76	3.29	2.93	2.61	2.36	2.13	1.95	1.78
	4.0	3.19	3.54	3.74	3.84	3.86	3.85	3.82	3.37	2.98	2.67	2.40	2.18	1.99	1.83
	4.5	2.87	3.20	3.38	3.45	3.49	3.48	3.45	3.02	2.69	2.40	2.17	1.97	1.79	1.65
	5.0	2.61	2.91	3.07	3.14	3.17	3.16	3.14	2.74	2.43	2.18	1.97	1.79	1.63	1.50
	5.5	2.40	2.66	2.81	2.86	2.90	2.88	2.86	2.50	2.23	1.99	1.80	1.63	1.49	1.37
2.0	1.5	2.50	2.81	2.98	3.07	3.09	3.09	3.07	2.70	2.40	2.15	1.93	1.76	1.60	1.46
	2.0	2.78	3.11	3.27	3.37	3.41	3.40	3.38	2.96	2.62	2.35	2.11	1.92	1.75	1.61
	2.5	2.97	3.31	3.49	3.59	3.61	3.60	3.58	3.15	2.79	2.50	2.25	2.04	1.86	1.71
	3.0	3.11	3.46	3.65	3.75	3.77	3.76	3.73	3.29	2.91	2.61	2.34	2.13	1.94	1.78
	3.5	3.21	3.58	3.76	3.86	3.88	3.89	3.84	3.38	2.99	2.68	2.41	2.19	2.01	1.83
	4.0	3.27	3.65	3.85	3.93	3.97	3.96	3.93	3.44	3.06	2.74	2.47	2.24	2.04	1.87
	4.5	2.96	3.30	3.46	3.55	3.56	3.57	3.54	3.10	2.76	2.46	2.23	2.02	1.84	1.69
	5.0	2.69	3.00	3.14	3.22	3.24	3.25	3.22	2.82	2.51	2.23	2.02	1.84	1.67	1.54
	5.5	2.46	2.74	2.87	2.94	2.96	2.96	2.94	2.57	2.29	2.05	1.84	1.67	1.53	1.41
2.5	1.5	2.51	2.82	2.98	3.05	3.07	3.08	3.04	2.68	2.38	2.13	1.91	1.74	1.58	1.45
	2.0	2.78	3.09	3.27	3.36	3.38	3.37	3.35	2.93	2.60	2.33	2.09	1.90	1.73	1.59
	2.5	2.96	3.30	3.49	3.56	3.60	3.59	3.56	3.12	2.76	2.48	2.23	2.02	1.85	1.69
	3.0	3.09	3.45	3.64	3.72	3.76	3.75	3.72	3.25	2.88	2.58	2.34	2.11	1.93	1.77
	3.5	3.21	3.55	3.75	3.82	3.87	3.85	3.82	3.36	2.98	2.67	2.40	2.18	1.98	1.82
	4.0	3.27	3.64	3.82	3.92	3.93	3.94	3.91	3.42	3.05	2.71	2.46	2.23	2.03	1.87
	4.5	2.96	3.27	3.45	3.54	3.55	3.54	3.51	3.09	2.73	2.45	2.22	2.01	1.84	1.69
	5.0	2.69	2.97	3.13	3.21	3.23	3.21	3.19	2.80	2.50	2.24	2.01	1.83	1.67	1.54
	5.5	2.46	2.72	2.86	2.93	2.94	2.95	2.93	2.58	2.28	2.04	1.85	1.68	1.54	1.41
3.0	1.5	2.51	2.81	2.95	3.02	3.05	3.05	3.01	2.65	2.35	2.10	1.89	1.71	1.56	1.43
	2.0	2.76	3.08	3.26	3.32	3.34	3.33	3.31	2.89	2.58	2.30	2.08	1.88	1.72	1.57
	2.5	2.95	3.29	3.45	3.54	3.56	3.55	3.52	3.08	2.75	2.44	2.21	2.01	1.83	1.68
	3.0	3.08	3.44	3.60	3.70	3.71	3.70	3.67	3.23	2.86	2.56	2.30	2.09	1.92	1.75
	3.5	3.18	3.54	3.71	3.80	3.82	3.80	3.77	3.32	2.94	2.63	2.38	2.16	1.97	1.81
	4.0	3.26	3.60	3.80	3.87	3.91	3.89	3.86	3.40	3.01	2.69	2.44	2.21	2.03	1.86
	4.5	2.93	3.25	3.41	3.49	3.53	3.51	3.49	3.07	2.72	2.43	2.20	2.00	1.83	1.68
	5.0	2.66	2.96	3.09	3.17	3.20	3.19	3.16	2.78	2.48	2.22	2.01	1.83	1.67	1.54
	5.5	2.43	2.70	2.82	2.90	2.92	2.91	2.91	2.56	2.26	2.03	1.83	1.68	1.53	1.41
3.5	1.5	2.47	2.75	2.88	2.96	2.98	2.97	2.93	2.58	2.29	2.03	1.84	1.66	1.52	1.39
	2.0	2.72	3.01	3.18	3.24	3.26	3.25	3.22	2.82	2.51	2.24	2.02	1.83	1.67	1.54
	2.5	2.88	3.21	3.37	3.45	3.47	3.46	3.43	3.02	2.67	2.39	2.15	1.96	1.78	1.64
	3.0	3.01	3.35	3.51	3.60	3.62	3.60	3.58	3.15	2.79	2.50	2.26	2.05	1.87	1.72
	3.5	3.10	3.45	3.63	3.70	3.72	3.73	3.70	3.23	2.88	2.58	2.32	2.12	1.93	1.77
	4.0	3.18	3.51	3.70	3.79	3.81	3.79	3.78	3.31	2.95	2.64	2.39	2.17	1.99	1.83
	4.5	2.85	3.17	3.34	3.40	3.44	3.42	3.41	2.99	2.66	2.38	2.16	1.96	1.79	1.65
	5.0	2.59	2.88	3.03	3.09	3.12	3.13	3.10	2.73	2.43	2.18	1.97	1.79	1.64	1.50
	5.5	2.37	2.63	2.77	2.84	2.85	2.85	2.83	2.49	2.22	2.00	1.81	1.64	1.50	1.39

Table shows ϕ_{ratio} for bird calculated for each scintillator length, width and depth. Results are grouped by depth.

10.5 RMS30 operating instructions

Introduction: The RMS30 unit from John Caunt Scientific (JCS) has been modified to work with the four scintillators included with the live-monitor. The setup of the electronic components for this live-monitor is detailed in Figure 10.1. Cables are labelled to indicate port attachment.
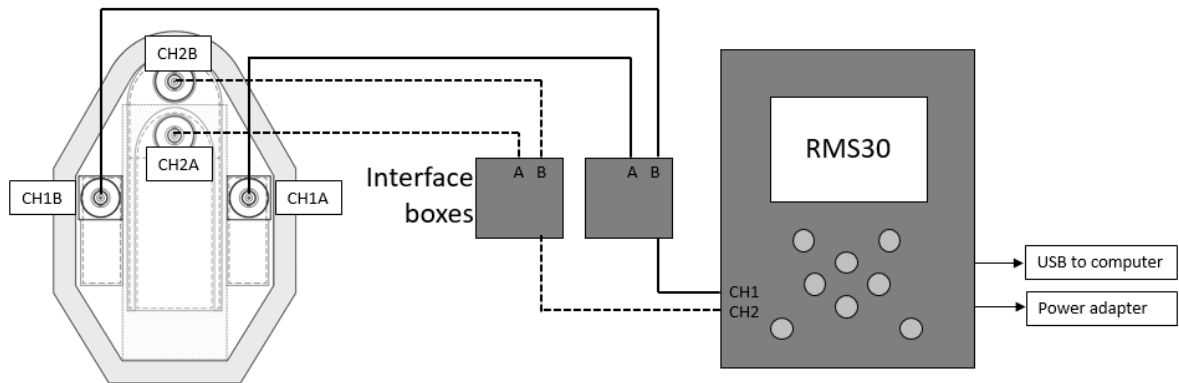
Figure 10.1: Diagram of live-monitor electrical connections

Operation: The RMS30 is turned on by pressing and holding the ⏻ button (ensure all required scintillators are connected before turning on). Pressing and holding the same button will turn off the RMS30. The main interface will appear as shown in Figure 10.2. There are four readable outputs, one for each scintillator, displayed on the main interface. The total counts for the two gamma scintillators are displayed on the top row (CH1A and CH1B for inputs A and B respectively) and the total counts for the two beta scintillators are displayed of the bottom row (CH2A and CH2B for inputs A and B respectively). If one or more of the scintillators are not connected to the RMS30 then a not connected message will display for the respective channel. Do **NOT** remove or add any scintillator device to the RMS30 whilst it is powered on. The unit will operate for approximately 10 hours and can be recharged by using the supplied power adapter.
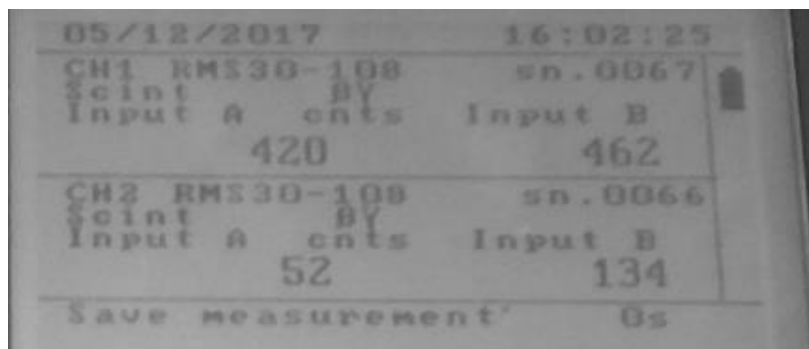
Figure 10.2: RMS30 interface

Menu options: Pressing the down button will provide the following functions:

- Start count
- Change sample time
- Change CH1 HV, LLD & ULD
- Change CH2 HV, LLD & ULD
- Connect to a PC (USB mode)

The RMS30 initialises with the menu set to "start count".

Measurement: Ensure the required scintillators are connected and the unit is powered on. Press (✓) when on the menu option "start count" to start a measurement. The measurement will count for the defined sample time. At any time during this measurement the user can press (✗) to cancel and return to the initial interface. Once the measurement is complete the user is given the option to save to the internal memory. Pressing (✓) will save the measurement data and pressing (✗) will discard the data. This option allows the user to later copy the measurements to a computer.

Change sample time: The sample time period can be changed by navigating the menu and selecting "change sample time". The up and down buttons then scroll through the pre-set values (from 1 to 10,000 seconds). Select the required sample time and then press (✓) to save this value.

Energy calibration: The scintillators can be calibrated via the "Change CH1 HV, LLD & ULD" and "Change CH2 HV, LLD & ULD" menu options. Select the required option by pressing (✓). Continue to press (✓) to cycle through the options: HV (high voltage), LLD (lower level discriminator), ULD (upper level discriminator), and enable window. This will first cycle through input A and then the same options for input B. This procedure is the same for CH1 and CH2. Each interface box contains two sockets for attaching to an oscilloscope if a more detailed energy calibration is required.

PC connection: The saved measurements can be accessed by connecting the RMS30 to a computer (using the USB cable), powering on the unit, and selecting "Connect to a PC" from the menu. The data files are then accessible from the computer. Data is saved into a .csv file and a new file is created each time the RMS30 is powered on.

10.6 Ethical approval

University of **Salford**
MANCHESTER

14 February 2017

Ross Fawkes

Dear Ross,

RE: ETHICS APPLICATION STR1617-24– New detectors for the Live-monitoring of radionuclides in wildlife

Based on the information you provided, I am pleased to inform you that your application STR1617-24 has been approved.

If there are any changes to the project and/ or its methodology, please inform the Panel as soon as possible by contacting S&T-ResearchEthics@salford.ac.uk

Yours sincerely,

Prof Mohammed Arif
Chair of the Science & Technology Research Ethics Panel
Professor of Sustainability and Process Management
School of Built Environment
University of Salford
Maxwell Building, The Crescent
Greater Manchester, UK M5 4WT
Phone: + 44 161 295 6829
Email: m.arif@salford.ac.uk
www.salford.ac.uk/ethics

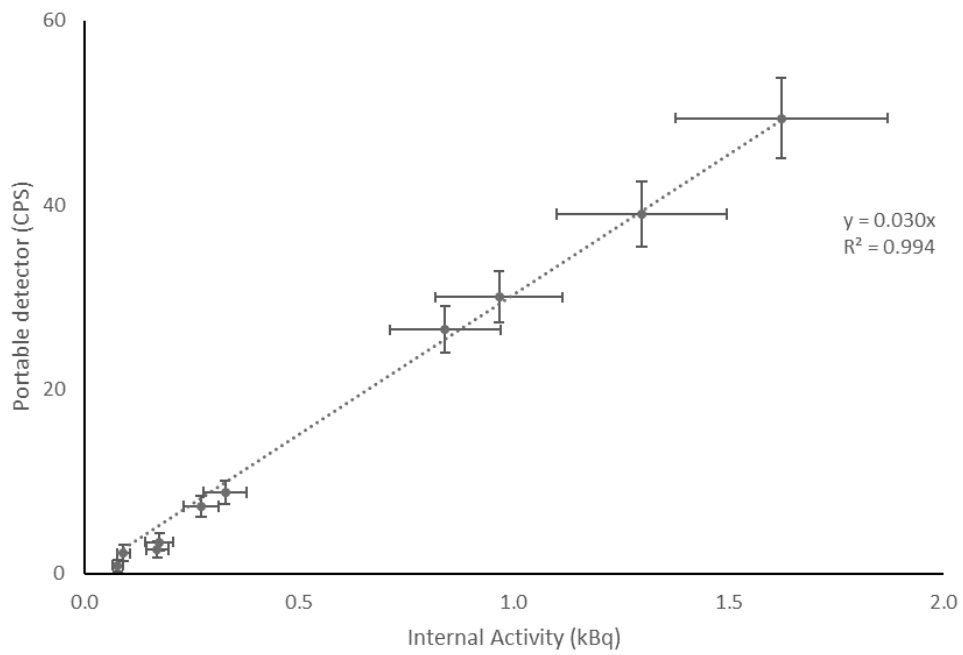## 10.7 Laboratory measurements of small organisms using portable detector

Figures showing correlation between the portable detector count rate and known animal internal activity (verified through alternative means). Uncertainties shown are the expanded uncertainties. For the portable detector this includes the uncertainty in the measurement (Currie, 1968), the horizontal and rotational movement, and the scintillator response rates .
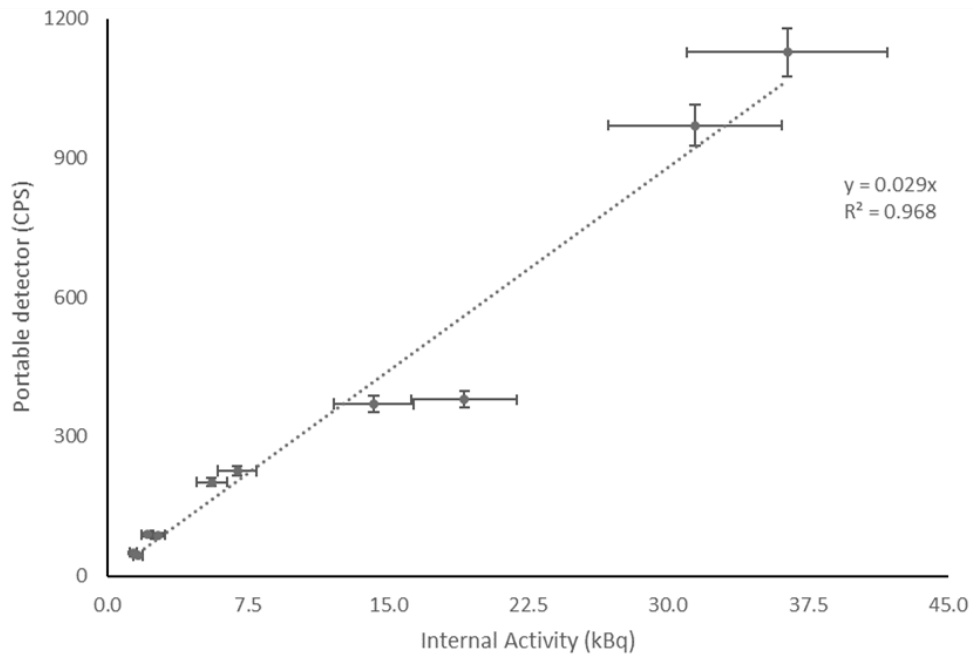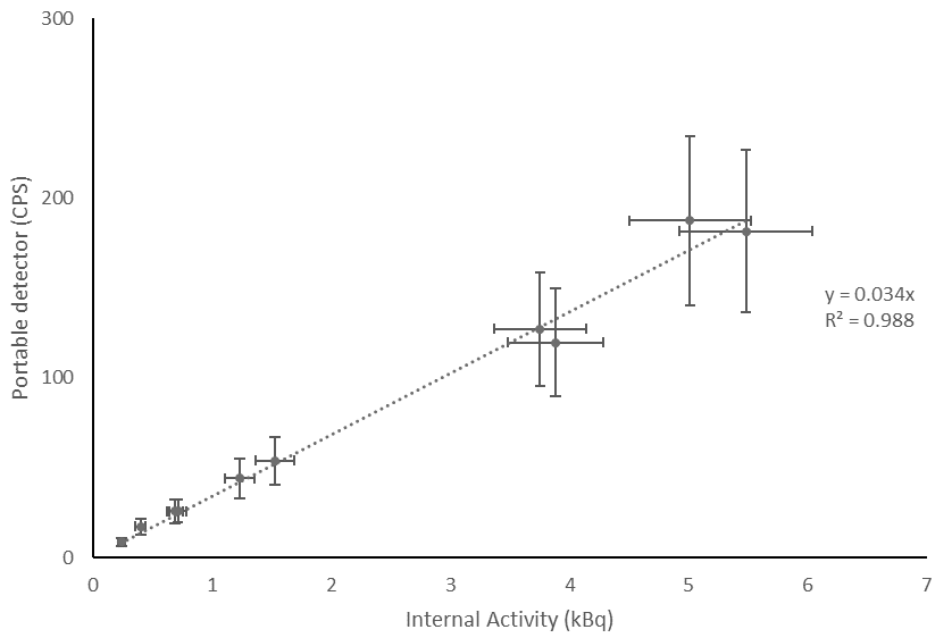

Mouse measured ^{137}Cs count rate (laboratory) compared to internal activity.
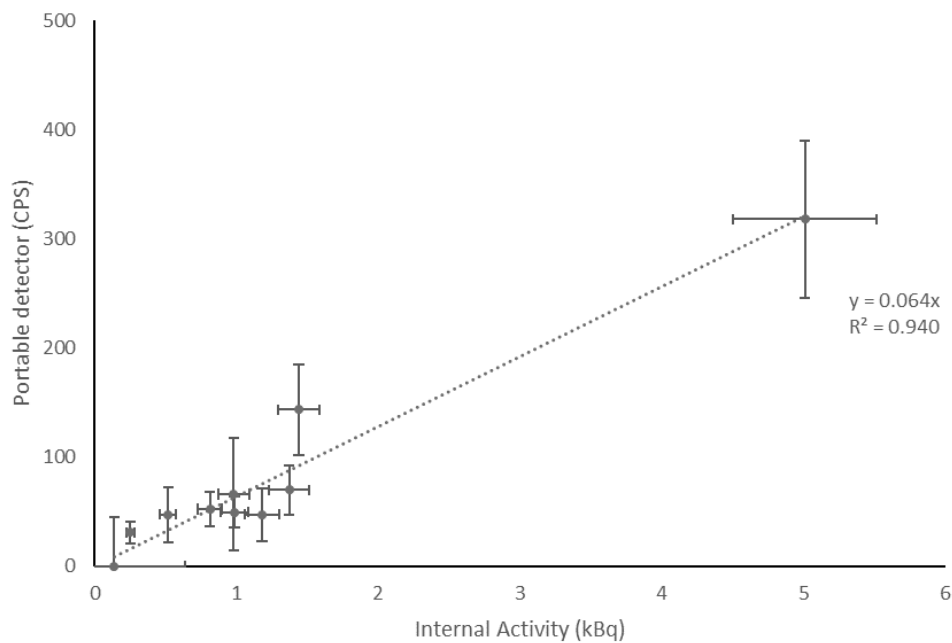
Mouse measured ^{90}Sr count rate (laboratory) compared to internal activity.

Bird measured ^{137}Cs count rate (laboratory) compared to internal activity.

Bird measured ^{90}Sr count rate (laboratory) compared to internal activity.